NASA Contractor Report 3826

Initialization of a Mesoscale Model for April 10, 1979, Using Alternative Data Sources

Michael W. Kalb

CONTRACT NAS8-34767
AUGUST 1984

NASA

NASA Contractor Report 3826

Initialization of a Mesoscale Model for April 10, 1979, Using Alternative Data Sources

Michael W. Kalb

Universities Space Research Association
Columbia, Maryland

Prepared for
George C. Marshall Space Flight Center
under Contract NAS8-34767

National Aeronautics
and Space Administration

Scientific and Technical
Information Branch

1984

ACKNOWLEDGMENTS

I wish to thank Dr. David D. Houghton the the University of Wisconsin-Madison for his expert guidance and advice throughout this research. The assistance of Dr. Dong-Kyou Lee, Dr. Donald J. Perkey, Dr. Carl Kreitzberg, and Dr. Chia-Bo Chang is gratefully acknowledged. This research was supported under NSF Grant ATM-8005369 and NASA Contracts NAS5-21965 and NAS8-34767. Model calculations were performed with the support of the Scientific Computing Division at NCAR, which is sponsored by the National Science Foundation.

Table of Contents

List of Figures

List of Tables

INITIALIZATION OF A MESOSCALE MODEL FOR APRIL 10, 1979 USING ALTERNATIVE DATA SOURCES

Michael W. Kalb*

1. Introduction

1.1 Research Objectives

This research examines several aspects of initializing a limited area mesoscale atmospheric prediction model with real data obtained from unconventional sources. SESAME (Severe Environmental Storms and Mesoscale Experiment) radiosonde data and satellite derived temperature soundings are used in conjunction with sub-synoptic scale surface wind analyses to specify the initial mass and momentum fields in the LAMPS (Limited Area Mesoscale Prediction System) model (Perkey, 1976).

Three fundamental issues are addressed:

(1) Can high density satellite temperature data be assimilated into a mesoscale model to produce forecasts which verify favorably with real observations or a control forecast?

(2) How do forecasts made with satellite temperatures compare with those using "special" radiosonde temperatures, data sources which presumably contain equivalent sub-synoptic structure?

(3) How important is initial specification of realistic low level winds for accurate initial development of mesoscale structures and the

*Universities Space Research Association Visiting Scientist at NASA Marshall Space Flight Center.

forecast existence and locations of those structures?

1.2 Background Discussion

This study is based on a set of mesoscale model forecasts for April 10, 1979, a day chosen to take advantage of data from the SESAME regional scale observing system which produced radiosonde data every three hours for a twenty-four hour period and with a 200 km average station separation. The sub-synoptic scale observing capability of this data and the convective nature of the precipitation on this day made this case particularly favorable for study with a mesoscale prediction model. The SESAME radiosondes provided a unique source of data for both model initialization and verification. The availability of TIROS-N satellite temperature soundings over the SESAME domain on April 10 made this day the only candidate of three special observing periods for investigating the relative information content of high density satellite and simultaneous high density radiosonde temperatures.

Service A surface wind data is employed in some of the model forecasts to construct wind fields capable of accurately depicting low level moisture convergence and advection. Observed surface winds have also been used

in other modeling studies. Lee (1981) used hourly surface winds in the LAMPS model, however, his experiments were not designed to test the impact of surface winds, but rather cloud motion winds inserted at about 1 km. It was found that initial small scale low level divergence did not persist beyond several hours of model integration. The horizontal scales of those initial divergence features at about 850 mb were much smaller than those inserted at low levels in the present study.

Fiorino and Warner (1981) inserted surface winds into a hurricane model, but due to their experimental design were unable to demonstrate any impact. Those winds were not observed but calculated or modified with a diagnostic PBL model.

The inclusion of divergence in the initialization of large scale models has generally shown no impact on generation of meteorological "noise" or on the long term evolution of forecast mass and wind fields (Houghton, et al., 1971; Dey and McPherson, 1977; Lejenäs, 1977). However, results with non-linear normal mode initialization (Daley, 1981) have shown great potential for including realistic divergence while suppressing high frequency gravity waves.

Although it seems that the inclusion of divergence in a mesoscale model must be important, the manner in which it can be successfully done remains elusive. Rao and Fishman (1975) proposed a scheme for including divergence in a mesoscale model based on a Matsuno type forward–backward integration method; however, they never reported having initialized, run, and verified a model using their technique.

Tarbell (1979) studied the impact of initial divergence on the evolution of precipitation in a six-level version of the Penn State model. The divergent components were not derived kinematically but calculated from a "mesoscaled" omega equation. Spatial distribution of small scale vertical motions were obtained by including a diabatic heating term based on observed precipitation rates. The end result was that the initial divergence had some impact (with respect to a control forecast) on the total precipitation, but only for about the first six hours.

Satellite vertical temperature profiles represent a new data source and relatively few attempts have been made to fully exploit their meteorological information content (e.g. Mills and Hayden, 1982). Efforts at the University of Wisconsin indicate that high density

satellite temperature soundings when properly processed may be useful for defining sub-synoptic structure (hundreds of km) despite their low vertical resolution (~2 km) (Smith, et al., 1979; Smith, et al., 1981; Seaman, et al., 1977). In many previous studies satellite temperature and geopotential data have been obtained with the NESS operational 250 km separations and inserted into models to correct a first guess analysis (Hayden, 1973; Sumi, 1977; Ghil, et al., 1979; Atlas, et al., 1982). In the present study high density TIROS-N temperature data fully specify the mass field in a mesoscale model without benefit of a first guess objective analysis.

Hillger and Vonder Haar (1979) found via structure function analysis that "high resolution satellite soundings provide information about spatial variations of temperature structure equivalent to that provided by high density radiosondes." Individual case studies have shown that high horizontal resolution satellite temperature data compensate for low vertical resolution by their ability to define horizontal gradients. Streit (1981) in an analysis of April 10, 1979 found that TIROS-N data was useful in locating the diffluence of the polar and subtropical jet streams over Mexico.

While map locations of satellite height and temperature gradients are good, their magnitudes and directional orientations may be in considerable error. A recent study by Schlatter (1982) contained statistical results from TIROS-N temperature data indicating this to be the case. Kalb (1979) found significant errors in TIROS-N geopotential gradients in certain regions for many individual cases. Those soundings were produced with similar data spacing and editing techniques as the soundings of the present study. For a single case, Broderick (1980) found operationally derived TIROS-N data to accurately depict the locations of vertically integrated temperature (and thus geopotential) gradients through the depth of the troposphere as verified by radiosonde data. However, the satellite did not clearly define the tropopause or show the observed tilt of the cold air with height.

In this particular case, the good quality of the TIROS-N satellite temperature and height data is documented through direct comparison with simultaneous (2100 GMT) SESAME / AVE I radiosonde data over the same area. This unique congruity in space and time of high density satellite soundings and high density radiosonde data offers an excellent opportunity to explore their

respective impacts on a mesoscale prediction model which is capable of resolving sub-synoptic scales in the initial data. Since the model is run approximately over the SESAME regional domain during the April 10, 1979 observing period, real data verification for the model is available every three hours.

In this study the term mesoscale refers to typical length scales from 35 km (as defined by the model grid spacing) to 1000 km. These lengths fall within the "meso-α" (200-2000 km) and "meso-β" (20-200 km) ranges as proposed by Orlanski (1975). Phenomena exhibiting these scales would have time scales ranging from one hour to one day.

1.3 Synoptic Summary

April 10 is the date of the Wichita Falls tornado outbreak which resulted in over 50 deaths and nearly 400 million dollars in property damage (Moller, 1980). The synoptic scale events which led to the conditions favorable for severe weather included a north-south oriented upper level baroclinic trough centered over the Western Rocky Mountains at 1200 GMT on April 10. The trough developed a negative tilt as its axis rotated toward the Texas Panhandle region during the next twelve hours (Figure 1). An upper

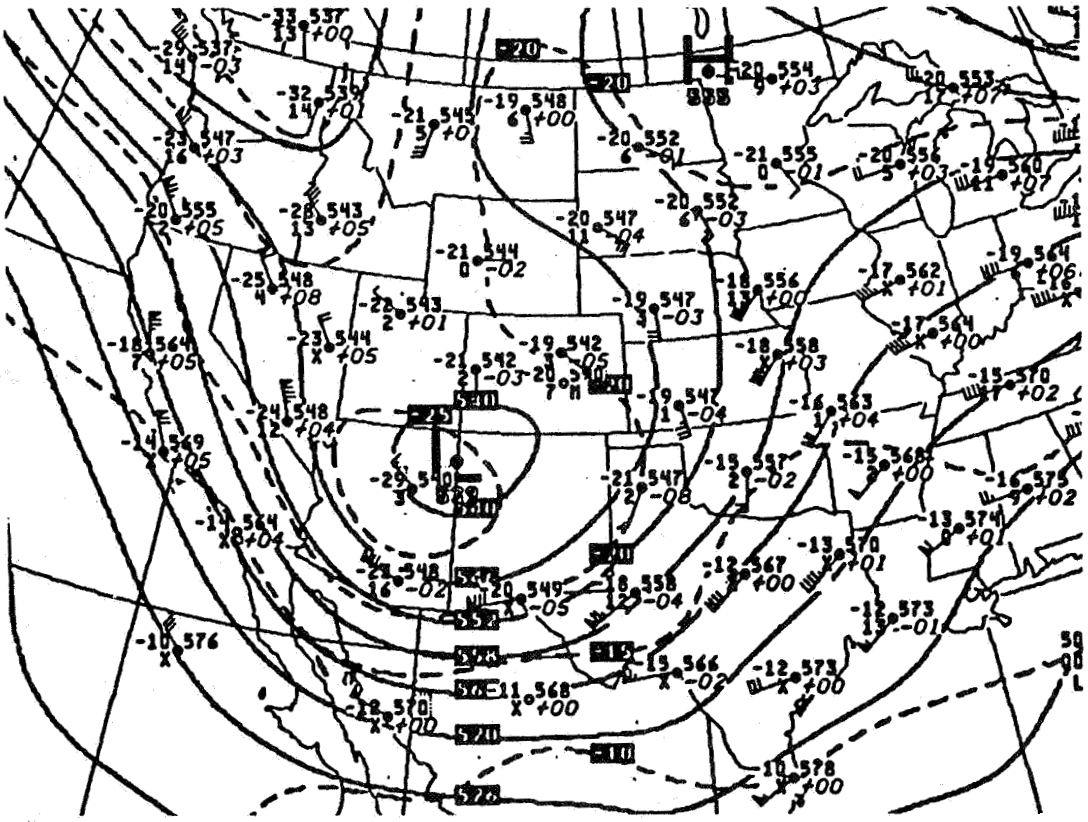

Figure 1: 500 mb height analysis at 0000 GMT April 11, 1979.

level jet streak propagated around the trough via Mexico and entered Southwest Texas by 2100 GMT.

At the surface a 988 mb low located in North-central Colorado at 1200 GMT moved to the southeastern part of the state where it remained almost stationary until 0900 GMT on the 11th. However, a cold front extending southward from the low into Mexico entered Texas from the west at 1800 GMT. As the cold front pushed eastward into central Texas during the next six

hours, a warm front moved northward from the Gulf of Mexico to the Texas/Oklahoma border by 2100 GMT providing most of Texas with an abundant supply of warm air and low level moisture. Southerly 850 mb winds pumped additional moisture into Oklahoma. A low level capping inversion created by dry, hot air from the Mexican Plateau at 700 mb prevented moist convection in central Texas until 0100 GMT.

The 500 mb jet, vertical directional wind shear and low level moisture are combined in the SWEAT index (Miller, 1972) for 0000 GMT in Figure 2. The SWEAT index plot which is based on SESAME radiosonde observations delineates areas with the greatest potential for severe weather (values greater than 300 indicate where severe weather becomes likely). Most notable is a rapid increase in values along the surface cold front and dry line which runs through Central Texas and the Panhandle. A squall line developed along this zone around 0135 GMT (Figure 3). Total totals index plots showed values greater than 50 over most of Texas, Oklahoma, Kansas, and the Gulf states indicating instability with heavy thunderstorm potential over a large area.

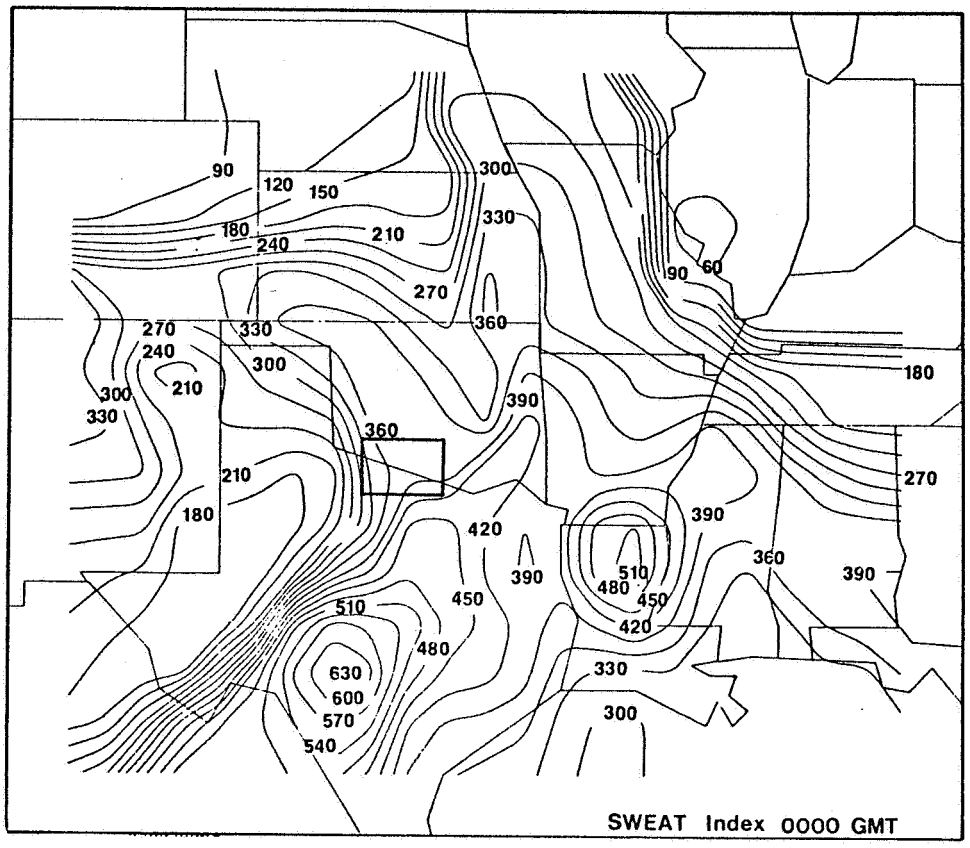

Figure 2: SWEAT index at 0000 GMT April 11, 1979. Box indicates tornado outbreak area.

The first tornado occurred at 2100 GMT near Cornwell, Texas to begin the Red River Valley outbreak in which at least one tornado was on the ground at any time during the next five hours (see Figure 4). This severe weather area has been linked to strong isallobaric convergence associated with an indirect circulation about the exit region of the 500 mb jet (Kocin, et al., 1982). Intense low level convergence supplied the moisture necessary to sustain the

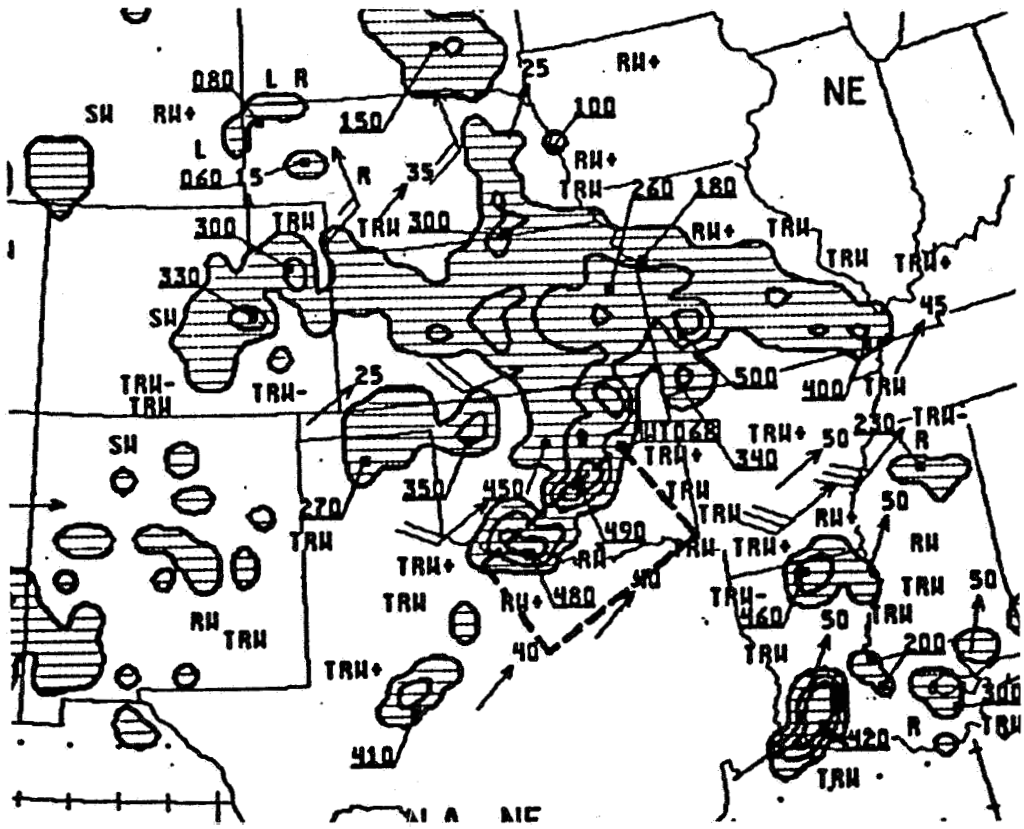

Figure 3: NMC radar summary for 0135 GMT April 11, 1979.

convection in the Red River Valley. In addition, the 2100 GMT SESAME radiosonde analyses reveals a low level short wave trough through the area.

A second outbreak struck central Texas at 0300 GMT and lasted for three hours in association with the squall line which had formed earlier. Tornadic activity subsided after 0600 GMT, but during the night general convective precipitation spread from Oklahoma into Missouri, Illinois, Iowa and Nebraska. The

following day, the low began to occlude resulting in wide spread precipitation over much of the Midwest.

This modeling study focuses only on the period of most intense severe weather from 2100 to 0600 GMT.

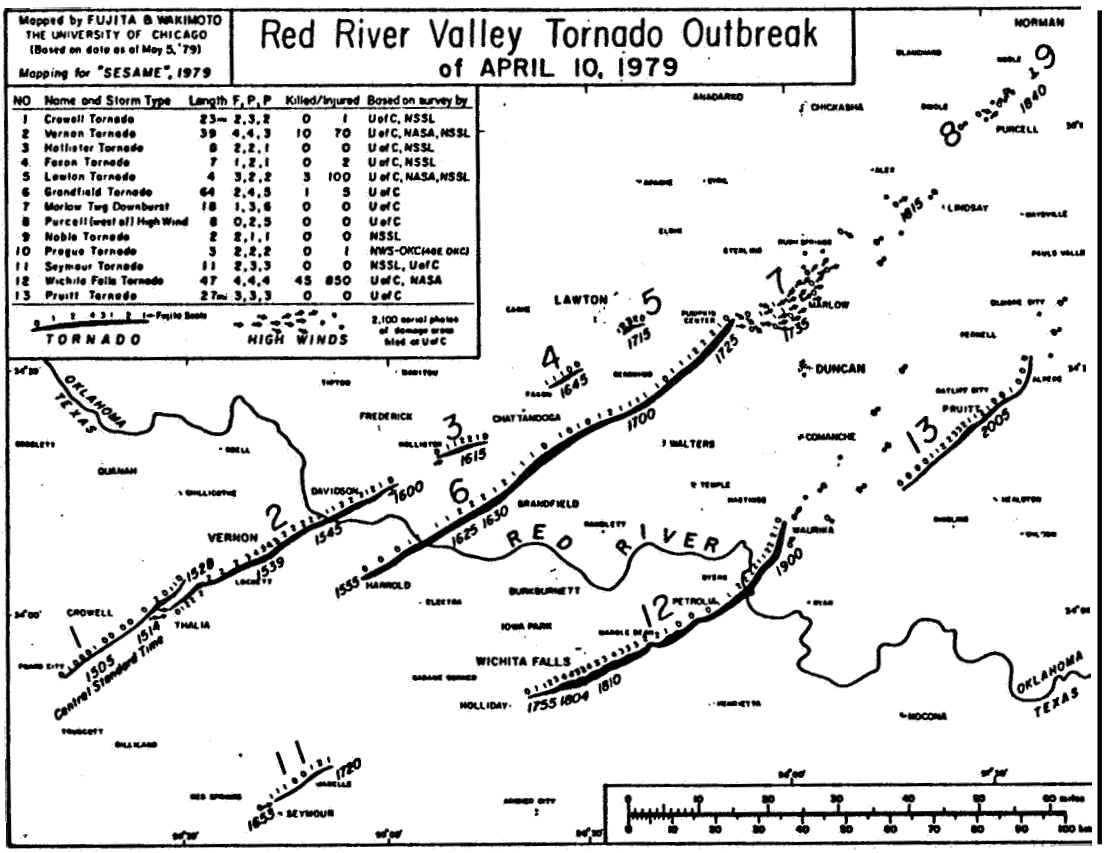

Figure 4: Tornado paths in the Red River Valley Outbreak. Area corresponds to the box in Figure 2. (reproduced from Alberty, et al., 1980).

2, The Model

The **LAMPS** model is a fifteen level hydrostatic primitive equation convective model with options for variable grid spacing **(35** Km, 70 km or 140 **km)** and nesting of the finer resolution grids within the coarser. The vertical coordinate is a terrain following height coordinate h_σ **("sigma-height")** defined by

$$(2.1) \qquad h_\sigma = \frac{Z-E}{H-E} H\delta + Z\,(1-\delta) \qquad \begin{matrix}\delta=1 \text{ if } h_\sigma < H \\ \delta=0 \text{ if } h_\sigma \geq H\end{matrix}$$

where Z is height above sea level and E is terrain height. **If** h_σ is greater than H = **5250** meters then. $h_\sigma = Z$ (See Figure **5).** The model levels are h_σ =0., 25., 375., 750., 1250., 2000., 3000., 4500., 6000., 7500., 9000., 10500., 12000., 14000., and 16000. meters. Note that vertical resolution increases at the lower levels.

The prognostic model variables are u, v, θ, q and π. In addition rain water and cloud water are predicted. The variable π is related to pressure by

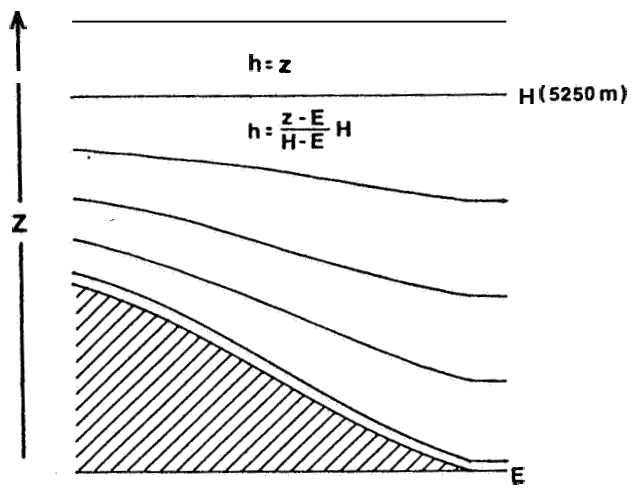

Figure 5: Model vertical coordinate system. Z is the geometric height above sea level, E is the terrain height and h is the model vertical coordinate.

$$(2.2) \qquad \pi = C_p \left(\frac{p}{1000}\right)^{R/C_p}$$

Other symbols have their usual meteorological meanings.

Vertical velocity ($\dot{h}$) is diagnosed from a form of the continuity equation (2.3) which includes a diabatic

(2.3)

$$\frac{\partial}{\partial h_\sigma}\left(\frac{\pi}{p}\dot{h}_\sigma\right) = -\vec{\nabla}\cdot\rho\vec{V} - \frac{1}{p}\frac{\partial \pi}{\partial t} + p\left(\underset{(a)}{\frac{\dot{Q}}{\theta\pi}} + \underset{(b)}{\frac{v\tan\phi}{a}} + \underset{(c)}{\delta\frac{\dot{E}}{H-E}}\right)$$

heating term (a), a curvature correction term (b) and a

terrain correction term (c) which is zero when $h_\sigma \geq H$. Vertical motion is constrained to be zero at the top and bottom of the model. This still allows for upslope surface winds since the $h_\sigma = 0$ surface by definition follows the terrain. Equation (2.3) is solved numerically in Appendix E.

π is predicted only at the model top and is diagnosed at all lower levels down to the surface with a hydrostatic equation

$$\frac{\partial \pi}{\partial h_\sigma} = \frac{-\alpha g}{\theta} \quad \text{where } \alpha = \frac{1}{\rho} . \tag{2.4}$$

Both surface winds and temperatures are diagnosed.

Each prognostic equation contains a fourth derivative diffusion term to smooth computational errors and eliminate small scale features which can not be adequately handled numerically by the model. For example, the u-component equation in z coordinates would be written.

$$\frac{du}{dt} = fv - \frac{1}{\rho} \frac{\partial p}{\partial x} + \frac{uv\tan\phi}{a} + \left.\frac{du}{dt}\right|_s \tag{2.5}$$

where the term with subscript s represents accelerations due to sub-grid scale process. This term is subdivided into three components

$$(2.6) \qquad \left.\frac{du}{dt}\right|_s = \left.\frac{du}{dt}\right|_{cu} - \frac{\partial}{\partial z}\left(K_m \frac{\partial u}{\partial z}\right) - K_m^4 \nabla^4 u$$

The first term on the right hand side of (2.6) contains accelerations arising from the convective parameterization. The second term represents the effects of eddy stresses in the boundary layer, and the last term is the diffusion term which is only a means to control numerical errors. The vertical variation of K_m is given by Perkey (1976).

The surface layer employs Monin-Obukhov similarity theory. K - theory describes the remainder of the boundary layer. Boundary layer height is not predicted and changes in time in a very simple fashion.

Precipitation in the LAMPS model is partitioned into a stable and convective part. Precipitation resulting from grid scale processes constitutes the stable category. The other part is parameterized by a one dimensional sequential convective plume model as

described by Rreitzberg and Perkey **(1976).** The main advantage of this scheme over other convective parameterizations is its ability to initiate convection at any level in the atmosphere through release of layer potential instability $(\frac{\partial}{\partial z}(Lq_s + C_p T_v + gz) \leq \Theta)$ and to fuel that convection with a supply of moisture from an arbitrary level (Perkey, **1976).** Other convective parameterization schemes such as Kuo **(1974)** are more attuned for use in the tropics since they are based on deep convection in which the influx of moisture to supply convection derives from a large scale, low level moisture convergence field.

The LAMPS convective plume model can also give realistic vertical profiles of convective latent heating based on the vertical profiles of parameterized condensation and evaporation. Other schemes have incorporated pre-specified profiles of diabatic convective heating (e.g. Anthes, et. al., **1982).** The vertical distribution of diabatic heating or cooling can have important effects on future development just from simple static stability considerations. A study by Gyakum **(1981)** as referenced in the National Storm Program Document (1983) suggested that the lower the level (height) of maximum diabatic heating in the

atmosphere, the more rapid would be the development of a meso- α cyclone.

The horizontal space differencing in the model is fourth order accurate while the vertical differencing is second-order accurate. The time differencing is second order accurate leap frog, i.e., for an arbitrary variable Φ at time n,

$$\Phi^{n+1} = \Phi^{n-1} + \left(\frac{\partial \Phi}{\partial t}\right)^n 2\Delta t$$

A slight time smoother is applied to avoid a computational mode inherent in leap frog schemes. This involves updating values at n-1 according to

$$\Phi^{n-1} = \Phi^n + \frac{\nu}{2} \left(\Phi^{n-1} + \Phi^{n+1} - 2\Phi^n\right)$$

where ν is a parameter which depends on the variable Φ.

The lateral boundary conditions on u, v, θ_v, π and q are time varying based on SESAME analyses of these variables at 1200 GMT April 10, 1979, 0000 GMT and 1200 GMT April 11. It is through these time dependent boundary conditions that larger scale

factors outside the model grid can influence the interior. Time tendencies on the domain boundaries are not applied directly but affect the interior through a four grid row buffer zone. The tendencies along any one of these rows is a weighted sum of the specified boundary row tendencies and those generated by the model itself. The weights applied to each row effectively eliminate reflection of waves generated by the model grid back into the domain. (Perkey and Kreitzberg, 1976).

The domain used for this study covers an area approximating the **SESAME** regional domain. The geographical limits are **105.0** to **86.13** degrees west longitude and 29.0 to **42.4375** degrees north latitude. The north-south grid spacing is **0.3125** degrees; the east-west spacing is **0.385** degrees. These parameters define a **44** x 50 grid with average **35** km horizontal resolution. Figure 6 shows the domain limits along with the model terrain. The time step for the model **is 40** seconds. **A** nine-hour forecast requires approximately **2.5 CRAY-1** computer hours.

All model variables were output to physical tape for every half hour of each forecast at every model

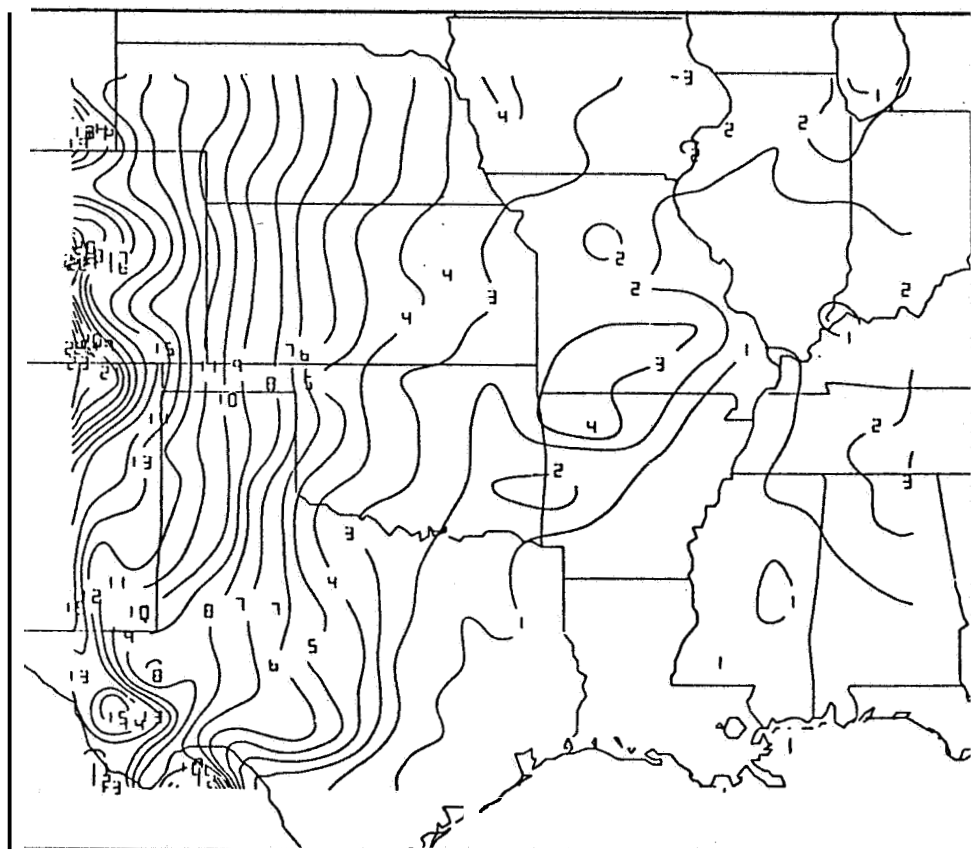

Figure 6: Terrain used in model. Contours are heights above sea level labelled in hundreds of meters.

grid point. These tapes can be processed to produce maps at mandatory pressure levels or vertical cross-sections. Several parameters were also output for every model time step at the sixteen locations indicated in Figure 7. These variables included vertical velocity and wind speed at model level 9 (≃500 mb), surface pressure, and divergence at levels 5 and 12 (≃850 mb and ≃250 mb). Instantaneous time

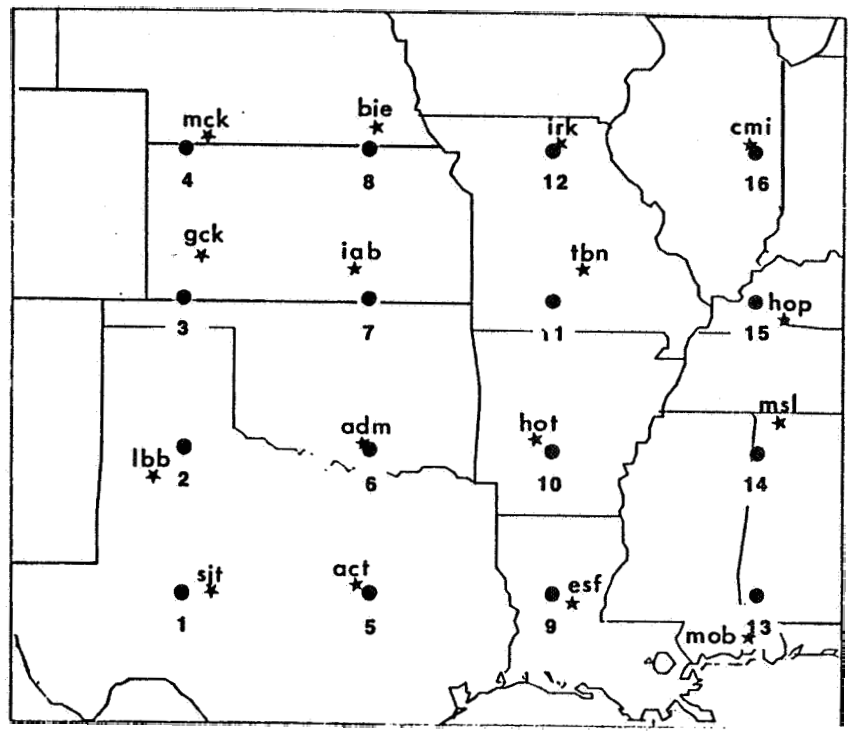

Figure 7: Locations where model diagnostics were collected every time step (●). Stars (★) are locations of hourly reporting surface stations used for verification.

rates of change of these variables provide diagnostics which are useful for monitoring the level of gravity wave noise during the initialization/adjustment phase of the forecasts.

3. Data

3.1 Data Acquisition

The meteorological observations used to construct the model initial state were from three sources: hourly suface data, SESAME radiosonde data and TIROS-N satellite temperature soundings. The surface data consisted of wind, temperature, dew point and

pressure. These were available hourly through the Service A network from 1800 GMT (April 10) to 0600 GMT (April 11) with the single exception of 0500 GMT.

SESAME radiosonde observations were reported every three hours from 1200 GMT to 1200 GMT April 10-11. The distance between stations was about 200 km which is only half the distance as for conventional radiosondes. At any given time, approximately thirty-five out of forty soundings were available. Radiosonde data outside the model and SESAME domain were obtained for 2100 GMT using a weighted average of the conventional 1200 and 0000 GMT observations. Each radiosonde reported geopotential height, wind speed and direction, temperature and dew point every 25 mb. Only mandatory level data were used in order to give the radiosonde the same vertical resolution as the satellite data. No vertical smoothing of the radiosonde data was done and no attempt was made to compensate for down wind balloon drift. Height corrections were required for several radiosonde to account for mis-calibrated barometers (Barnes, 1981). These corrections were implemented only when the height adjustment at 100 mb was greater than ten meters.

For each mandatory level, wind speeds and

directions were converted to u and v components. Dew points were converted to vapor pressures and then to specific humidities using Teten's formula, which is the empirical approximation

$$e = 6.11 \times 10^{(7.5T_d)/(T_d+237.3)} \quad (T_d \text{ in } {}^0C)$$

and the relation $q \simeq .622\ e\ /\ P$. The specific humidities (q) were used to compute virtual temperatures.

Geopotential heights were computed below ground using an altimeter setting approach. The hypsometric equation used a mean layer temperature which was assumed to be the U.S. Standard Atmosphere temperature at the midpoint of the layer from sea level to the terrain height.

The satellite data consisted of eighty-nine vertical temperature profiles at mandatory pressure levels over the model domain. These were obtained from the TIROS-N polar orbiting satellite and processed at the University of Wisconsin using a man-computer interactive technique in which an operator attempts to

select cloud-free fields of view (20 X 20 km) for making temperature retrievals from satellite sensed infrared (IR) radiance measurements. The selection is based on inspection of video images of cloud cover and IR radiance patterns. In areas with partial cloud cover, clear-column radiances can be deduced from adjacent fields of view (Smith and Woolf, 1976). In totally cloudy regions temperatures may be retrieved from radiances in the microwave channels which are not affected by cloud water. Satellite heights were not used directly since the surface pressures used as the reference level data for the height assignments were from 2000 GMT rather than 2100 GMT when the soundings were made. In view of rapid pressure changes in active parts of the domain, surface pressures from 2100 GMT were used to recalculate the satellite heights. To give the satellite and radiosonde the same reference, radiosonde altimeter settings were objectively analyzed to a grid and interpolated to the satellite locations. New surface pressures could then be calculated for the satellite terrain.

The satellite derived moisture was not used. The specific humidities used to compute satellite virtual temperatures were obtained at the mandatory levels by

analyzing the 2100 GMT SESAME radiosonde humidity values (q) to a grid and interpolating to the satellite sounding locations as was done for the altimeter settings. These values, along with the original satellite temperatures and new surface pressures were used to generate new satellite geopotential height observations.

The areal coverage of satellite and radiosonde observations at 2100 GMT is shown in Figure 8. The satellite had several data void regions. A large cloud mass over Oklahoma associated with heavy rainfall prevented soundings from being made in this critical area, resulting in significant satellite-radiosonde temperature and height differences (see Appendix A). However, both observing systems produced similar analyses there in terms of the depiction of the low level short wave and large geopotential gradients at the upper levels. The data void in Southwestern Texas demarcates the western edge of the TIROS-N orbit.

Two faulty satellite soundings in Colorado were edited creating a data void there. To help in this region with the objective analysis, two SESAME soundings were included along the western boundary of

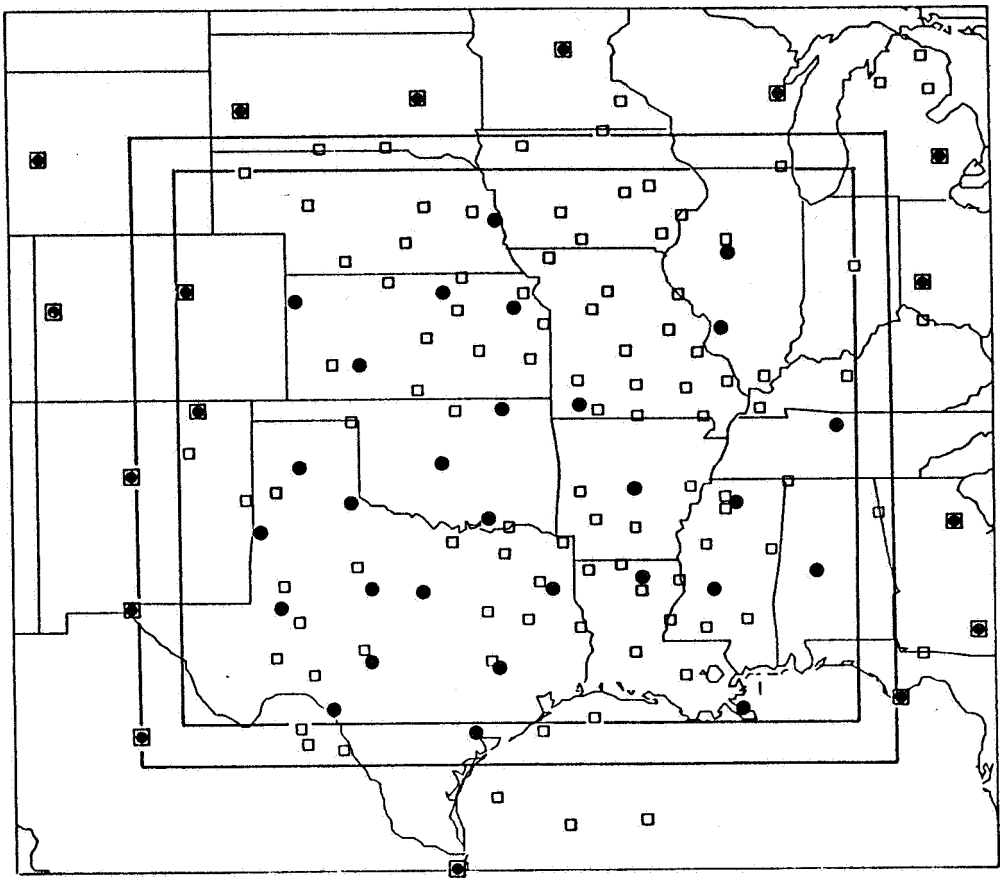

Figure 8: Mesoscale model domain (inner box) showing coverage of satellite data (□) and radiosonde data (●) on April 10, 1979 at 2100 GMT. The outer boundary represents the analysis domain. The notation ◉ denotes radiosonde data which were included in the satellite data base.

the model domain as indicated in Figure 8. Except for these two observations, data in the interior of the domain was provided only by the satellite. Outside the model domain, the conventional radiosonde observations were included in both the SESAME and satellite data sets.

3.2 Interpolation and Analysis

Each radiosonde and satellite mandatory level profile of T, q, u and v was interpolated linearly in height (Z) to the fifteen model sigma-height surfaces (h_σ) subject to two constraints. First the vertical distance between two consecutive mandatory levels had to be less than 4000 meters in order to interpolate to an intervening sigma-height level, otherwise the value was set to missing. The second constraint required that the observed surface values of T, u, v and q be the values at the model's surface as well. Values at h_σ = 25, 375, and 750 meters were obtained by linearly interpolating between the surface (model level 1) and model level 5 (1250 meters).

With each sounding variable interpolated in the vertical, a Barnes objective analysis (Barnes, 1973) was performed on the model surfaces with a one degree latitude/longitude grid. Since the model horizontal resolution is about .32 degrees, a two dimensional cubic spline was used to interpolate the one degree analyses to the model grid.

Because the satellite or radiosonde terrain was not the same as the model terrain, the surface pressure at every model grid point had to be derived. This was

done by first calculating a radiosonde-model terrain difference field AZ and using a standard lapse rate to find a corredted temperature for the model terrain, that is

$$T_{model,\ sfc} = T_{Raob,\ sfc} + (Z_{Raob,\ sfc} - Z_{model,\ sfc}) * .006$$

where temperature, T, is in degrees Kelvin, Z is in meters and the lapse rate (.006) is in degrees Kelvin per meter. Finally, a mean temperature, $(T_{model,\ sfc} + T_{Raob,\ sfc})/2$, was used in the hypsometric equation to get a model surface pressure. With this new reference level, the hypsometric equation was integrated upward to obtain pressures at every model level. With hydrostaticity assured, T, q and p were used (with the help of eqn (2.2) and the potential temperature equation) to compute θ_v and Π for each model grid point.

3.3 Special Procedures

3.3.1 Satellite Moisture Observations

Since in this study the intention is to compare satellite and radiosonde forecasts only on the basis of their temperature information, the following procedure was used to obtain specific humidity values at satellite locations which when analyzed give the radiosonde analysis. The first step in this process (see Figure 9) was to analyze the radiosonde moisture (q) observations over a domain large enough to include all the satellite locations. That analysis was interpolated to the satellite locations on the mandatory pressure surfaces to generate initial estimates for "satellite moisture" observations. These observations were analyzed in turn to the radiosonde analysis grid for comparison of the two fields in terms of absolute, relative and RMS differences. The difference field was interpolated back to and added to the satellite observations to create new ones. The process was repeated until the difference fields were sufficiently small.

It is estimated in Appendix C that an inherent lower bound on the relative measurement error for specific humidity at low levels is at least 6.4%.

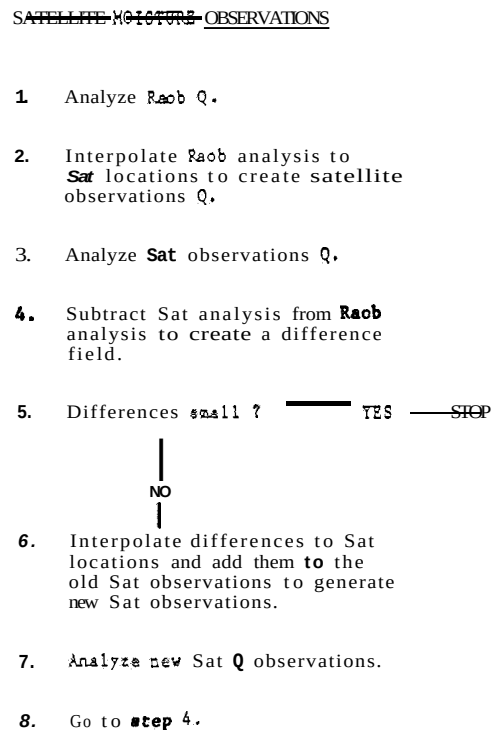

Figure 9: Algorithm for obtaining specific humidity measurements at satellite observation locations.

Thus, the satellite moisture values which were extracted from radiosonde moisture analyses were deemed "accurate" at a grid point when the "satellite"-radiosonde specific humidity differences represented a relative error less than 6%. At levels below 500 mb, most relative errors were less than 2%. Absolute and RMS differences were also considered at the upper levels (higher than 700 mb) where relative errors could be as high as 100%, but with absolute errors less than

0.05 gm kg^{-1}.

The satellite and radiosonde specific humidity fields were very close (see Appendix A), but could never be exactly the same by this procedure since each observing system sampled the same physical distribution of moisture, but at different locations and with different data densities. This limitation is seen in the reduction of RMS differences between satellite and radiosonde fields after four iterations (see Figure 10).

Even though the satellite and radiosonde had essentially the same specific humidity analyses, their relative humidities differed due to differences in temperature. Over limited areas the satellite relative humidity exceeded 100%. The remedy for this situation was to violate the previous attempt to preserve and match the total water contents by reducing satellite specific humidity as required to produce 100% relative humidity.

Only two areas of the domain were affected. They were both of limited areal extent, and since both were confined to relatively shallow layers, the total loss of water was small. It was estimated that the total loss of precipitable water anywhere in the domain was

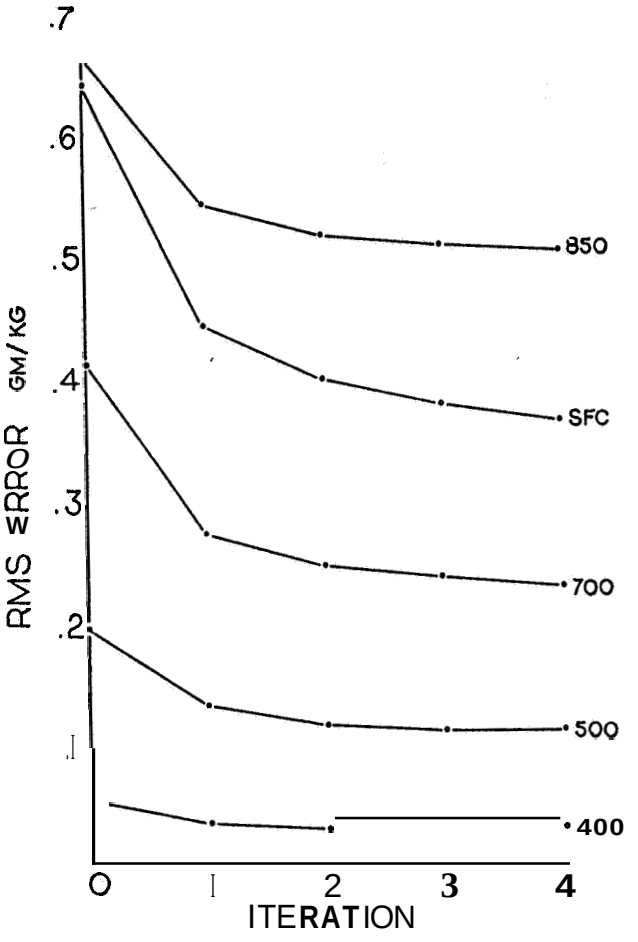

Figure 10: RMS differences between satellite and radiosonde analyses of specific humidity as a function of height (pressure) and number of iterations of the algorithm in Figure 9.

less than 0.04 cm. One of these areas was over a weather active region of Oklahoma. The greatest loss in a column there was no greater than 0.03 cm, representing less than 10% of the total in the affected layers.

3.3.2 Balanced Winds

The balance equation is used in meteorology to diagnose a relation between a wind and pressure field such that the wind is non-divergent while incorporating several important accelerations which influence large scale atmospheric motions. It is frequently used for initializing wind and pressure fields in numerical prediction models. Because the divergence of the winds is zero, generation of gravity wave modes is kept to a minimum; a desirable feature since energy associated with spurious gravity waves can be aliased into and seriously contaminate the slower and larger scale modes which describe meteorologically important phenomena.

The use of the balance relationship in this study means that the initial wind fields are dependent only on the temperature structure in the radiosonde or satellite data. The full non-linear balance equation is written in Cartesian coordinates with spherical terms neglected:

$$f\nabla^2\psi = \nabla^2\Phi - \frac{\partial f}{\partial y}\frac{\partial \psi}{\partial y} - 2\frac{\partial^2\psi}{\partial x^2}\frac{\partial^2\psi}{\partial y^2} + 2\left(\frac{\partial^2\psi}{\partial x \partial y}\right)^2 \tag{3.1}$$

where Φ is geopotential, f is the coriolis parameter and ψ is the stream function of the balanced wind. This equation is solved numerically on pressure surfaces for ψ by successive under-relaxation (See Appendix D for details of the numerics) using the geopotential stream function, $-\Phi/f$, as a first guess field and to calculate boundaries. In areas where the equation was non-elliptic the winds were constrained to have zero absolute vorticity. Others have forced the equation to be elliptic when necessary by altering the height fields (Asselin, 1967), however such height adjustments can be greater than one hundred meters (Ellsaeser, 1968) and would require a hydrostatic adjustment in the temperature fields. Balanced winds below the terrain (required for vertical interpolation to the terrain) were based on geopotential heights obtained hypsometrically assuming a standard lapse rate between sea level and the terrain height.

A problem arose in calculating balanced winds at the southern boundary of the model domain where speeds may exceed 150 m sec^{-1} at the upper levels. While winds near the Gulf of Mexico were relatively fast, the geopotential gradients (and thus balanced speeds) were

exaggerated by analysis error resulting from a lack of data in Mexico and the Gulf. The use of one-sided differencing on the boundaries may have amplified the effect of an already tight gradient which is perpendicular to the boundary (west to east flow).

To alleviate this problem, the balanced winds near the southern boundary were altered so that the boundary grid row winds were replaced by the winds one degree north of that row. The winds between the new boundary row and those two degress north of it were obtained by linear interpolation between them.

The balanced winds were calculated with second order accurate finite differencing on a one degree latitude/longitude grid. Upon horizontal interpolation to the model grid, the winds acquired a small randomly distributed divergence due partly to interpolation error, but mainly because the model code calculates divergence with a fourth-order accurate scheme. The divergent components were removed by relaxing the equation $\nabla^2\psi = \zeta$ for ψ where ψ is the non-divergent stream function of the interpolated winds and ζ is their relative vorticity. All calculations were done with fourth-order accurate finite differencing with more stringent convergence requirements than used in

the original solution on the one degree grid. The new balanced winds were then obtained from the relations

$$u = -\frac{\partial \psi}{\partial y} \text{ and } v = \frac{\partial \psi}{\partial x}.$$

The u and v balanced wind components were vertically interpolated to the model sigma-height coordinates. Surface values were obtained by vertical interpolation between two mandatory pressure levels, one above and one below the terrain height. Finally, a wind adjustment program was run over the entire domain to remove any net vertically integrated mass divergence which could have arisen from vertical interpolation errors.

A sample comparison between geostrophic, balanced and observed 400 mb isotachs is shown in Figure 11. The importance of the flow curvature correction in the balanced winds is obvious from their much reduced speeds in the southwestern portions of the domain. The balanced winds are much closer to the observed winds than are the geostrophic winds, but the balanced and observed winds still have large differences.

3.3.3 Omega Equation

To obtain inital quasi-geostrophic (QG) divergence fields for insertion into the model, a QG vertical motion equation was derived for the model coordinates

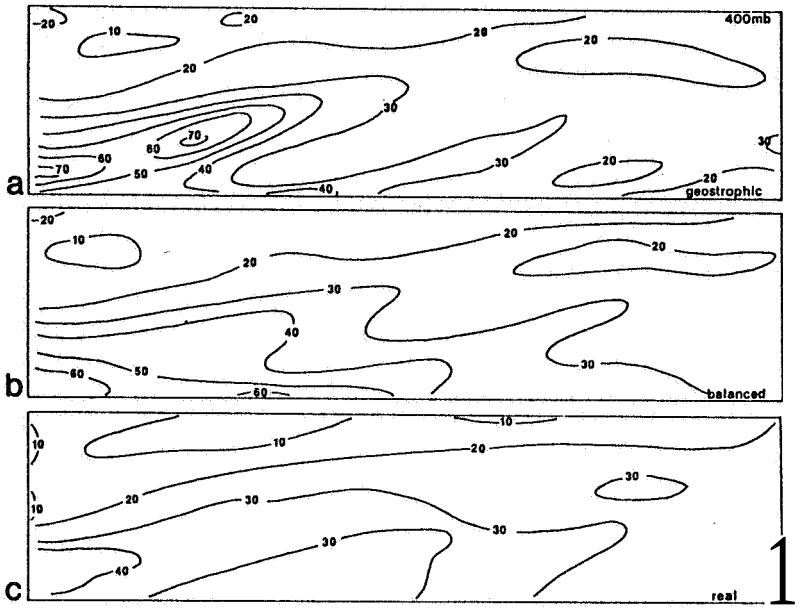

Figure 11: Comparison of geostrophic winds, balanced winds and observed winds (isotachs in m sec^{-1}) for the same *400* mb geopotential height analysis. The rectangular areas represent the zonally stretched model domain.

based on an equivalent equation in Z coordinates by Lee (1981).

$$g\ (\sigma_1-\sigma_2)\ \nabla^2(\rho w) + f_o^2\ \frac{\partial^2(\rho w)}{\partial z^2} =$$

$$f_o\ \frac{\partial}{\partial z}\ \{(\rho\vec{V}_g)\cdot\vec{\nabla}\ (\frac{1}{\rho f_o}\ \nabla_z^2\ p+\ f)\} + \frac{fR}{C_p}\ \nabla_z^2\ (\vec{V}_g\cdot\vec{\nabla}\rho)$$

$$\sigma_1 = \frac{\partial \ln\theta}{\partial z}\ ;\ \sigma_2 = \frac{C_p}{C_v}\ \frac{\partial \ln p}{\partial z}$$

This equation was transformed term by term (appendix E) to give a formulation consistent with the sloped model height surfaces, and solved by SOR to obtain vertical velocities. The forcing functions were smoothed and the terrain adjusted to facilitate solution by insuring that the scale of phenomena was consistent with QG theory. If the terrain height, E (in meters), at any grid point i,j exceeded 1000 meters it was altered according to

$$E_{ij} = 10000 + (E_{ij} - 1000)/5.$$

This was considered preferable to applying a strong smoother because simple numerical smoothing can not eliminate large areas with heights significantly above one kilometer. Where the terrain height was altered in the above manner, temperatures below the original terrain were obtained hypsometrically using a standard lapse rate; and below H, model data had to be interpolated to new h_σ surfaces.

The boundary conditions used zero vertical motion at the model top and on the lateral boundaries. For the lower boundary conditions surface vertical velocities were computed so as to be consistent with observed surface winds and the adjusted terrain slopes.

Given the QG vertical velocities, the vertical

motion equation (2.3) was solved for the divergent wind components which were added to the balanced winds in experiment C. The numerics, which is also shown in Appendix E, required that the local rate of change of density be ignored. Only every third model grid point was used to solve the "omega" and "continuity" equations in order to keep computer costs reasonable. The final divergent components were obtained by interpolating horizontally to the full resolution model grid.

3.3.4 Specification of Low Level Winds

Hourly surface wind data was used in this study to construct a low level wind field approximately 2000 meters deep where accurate advection of low level moisture is critical for development of convective precipitation (Ulanski and Garstang, 1978; Doneaud, et. al., 1981). Inclusion of mesoscale divergence is of primary importance since formation of convective storms at a location is often preceded by intense local moisture convergence (Newman, 1972). Such a correlation was found by Homan and Vincent (1982) and Moore (1982) for convection that occurred on April 10, 1979 over the SESAME regional domain.

The surface wind data influenced a layer up to

model level 6 (h_σ =2000) which represented the top of an artificial boundary layer unrelated to that specified by the model itself. The winds at level 6 consisted of balanced winds or balanced winds with divergent components obtained from an omega equation. The u and v components at model levels 2 through 5 were obtained by linear interpolation between the surface and level 6, resulting in an Ekman type turning of the low level winds with height.

3.3.5 Wind Adjustment

Vertical motion in the LAMPS model is constrained to be zero at the top (16 km). If this condition is not satisfied at the initial time step, large external gravity waves can be excited which can greatly modify the forecast mass fields, To insure initially small vertical velocities at the model top, a "wind adjustment" scheme (LAMPS standard software) was employed, similar to the procedure used by Washington and Baumhefner (1975), which removes net vertically integrated mass divergence. In the process, winds at all levels have their divergent components altered according to a pre-selected weighting function. The details of the method are found in Lee (1981).

In model runs initialized with real winds at all

levels, the divergence adjustments were applied between level 6 and the model top. For runs initialized with balanced winds plus observed low level winds, the adjustments were also confined to the upper levels in order to keep the low level divergence patterns intact. Finally, for model runs with balanced intial winds at all levels the adjustments were made below level 6. At the lowest levels the balanced winds were vertically interpolated to sigma-height surfaces based partly on geopotential height analyses which were calculated below the terrain. Since the low level balanced winds were therefore subject to the greatest uncertainty they were chosen to bear the brunt of the wind adjustment procedure.

4. Experimental Design

The experiments are divided into two blocks as shown in Figure 12. Block I consists of model forecasts statically initialized at 1800 GMT April 10 with SESAME radiosonde data. The differences between model runs are based upon how the initial wind fields were specified. The Block II experiments were all initialized at 2100 GMT with balanced winds above model level 6. These experiments employ various combinations of satellite versus radiosonde temperatures, observed versus balanced surface winds, and static versus dynamic initialization of low level winds.

The purpose of the Block I experiments was to determine a simple and reliable initialization technique. Experiment A was a three hour forecast initialized with observed SESAME radiosonde winds at all levels, while experiment B used balanced winds at all levels. Comparison of A and B provided an assessment of the models' ability to mutually adjust the mass and highly unbalanced momentum fields of April 10. Comparison of experiments B and C examines the forecast impact of including a quasi-geostrophic divergence in the initial wind fields. Model run D repeated experiment B to provide a twelve hour forecast

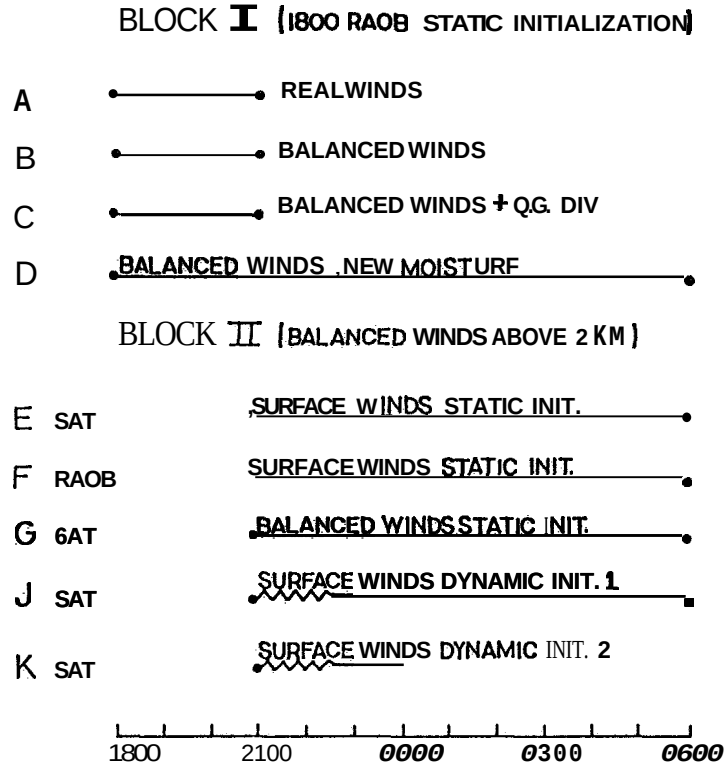

Figure 12: Schematic of experimental design. Capital letters denote individual model forecasts. Lengths of forecasts are indicated by the time scale on the horizontal axis.

which partly serves as a control by which the Block II experiments can be evaluated. It differs from experiment B in that it used an updated moisture analysis (q) to correct for an inadvertant underestimation of total available moisture in experiments A, B and C.

The Block II experiments were designed to examine the impacts of satellite and radiosonde temperature

data, and observed low level winds in the LAMPS model, Model forecasts **E** and **F** provide the most direct comparison of radiosonde and satellite data. Both have the same surface pressures, surface winds, moisture analyses and use the same static initialization technique. Differences in the outcomes of these experiments are caused by differences in their initial temperature structure. Satellite run G differs from **E** only in that G is initialized with balanced winds at low levels, Comparison of these forecasts determines if the initial observed low level winds are "remembered" by the model and have any lasting impact on model evolution. Satellite runs J and K employ two different dynamic initializations to force the model to utilize the observed low level winds during the initialization/adjustment period (the first 1-1/2 hour).

5. Initialization

5.1 Preliminary Initialization Runs

5.1.1 Noise Diagnostics

It has been understood for over three decades that the synoptic scale atmosphere is engaged in an unending attempt to achieve geostrophic equilibrium through mutual adjustments in the mass and momentum fields (Bolin, 1953; Haltiner and Williams, 1980, pp. 42-52). In this adjustment process, fast moving inertia-gravity waves are generated which have low amplitudes and are rapidly dispersed. According to theory of large scale mid-latitude dynamics, the atmosphere is assumed to be in an approximate or *'quasi*'-geostrophic state in which slight ageostrophic imbalances are resolved by adjustment of the mass and wind fields via broad scale divergence and vertical motions. In this view gravity waves play a minor role. As a result the earliest numerical models were based on quasi-geostrophic equations which precluded the existence of inertia-gravity waves.

In the primitive equations (PE) inertia-gravity waves are valid solutions. While the degree of ageostrophic imbalance in the broad scale atmosphere is generally small, when the mass and wind distributions

are specified independently from observations and used to initialize a PE model, the imbalances, either real or due to inaccurate observations result in inertia-gravity waves. These can misrepresent the energy in the slower meteorological modes and adversely affect a numerical forecast. The energy in gravity wave modes can be reduced by diagnosing the wind field from geopotential height (or vice-versa) using the balance equation (experiment B). An analysis by Phillips (1960) suggested that the inclusion of a quasi-geostrophic divergence field with the balanced winds (experiment C) would further reduce the presence of gravity wave "noise" in the initial state.

Since the quality of a model forecast may depend critically on the quality of the initialization, this section will examine the level of gravity wave activity in experiments A, B and C resulting from initialization with real winds, balanced winds and balanced winds with quasi-geostrophic divergence. Although the magnitudes of pressure perturbations and vertical motions associated with gravity waves may be small, the fact that their time rates of change are large provides a means for detecting their presence in the model initializations. The gravity waves are monitored from

diagnostics involving local time tendencies of surface pressure and mid-level vertical velocity.

A useful noise level statistic, PS, is defined to be the domain averaged local rate of change of surface pressure (Warner, et. al, 1978) and is calculated as

$$PS = \frac{1}{N} \sum_{i=1}^{N} \left| \frac{\partial P_{sfc,i}}{\partial t} \right|$$

where the average is taken over the N=16 verification points in Figure 7. PS is plotted as a function of model time in Figure 13 for every time step of the real (A) and balanced wind (B) forecasts. For the real wind, PS starts out at 7 mb hr^{-1} during the first thirty time steps compared to 4 mb hr^{-1} for the balanced winds. After thirty-five time steps, real wind values drop to about 4 mb hr^{-1} and to about 1.3 mb hr^{-1} at 150 time steps. However, superimposed on the decline are oscillations with amplitudes of 1 - 2 mb hr^{-1} and with a period of about ten minutes, consistent with the Brunt-Vaisalla frequency for buoyant oscillations usually associated with small scale internal gravity waves. The ten minute oscillations are not in phase everywhere in the domain as the curve

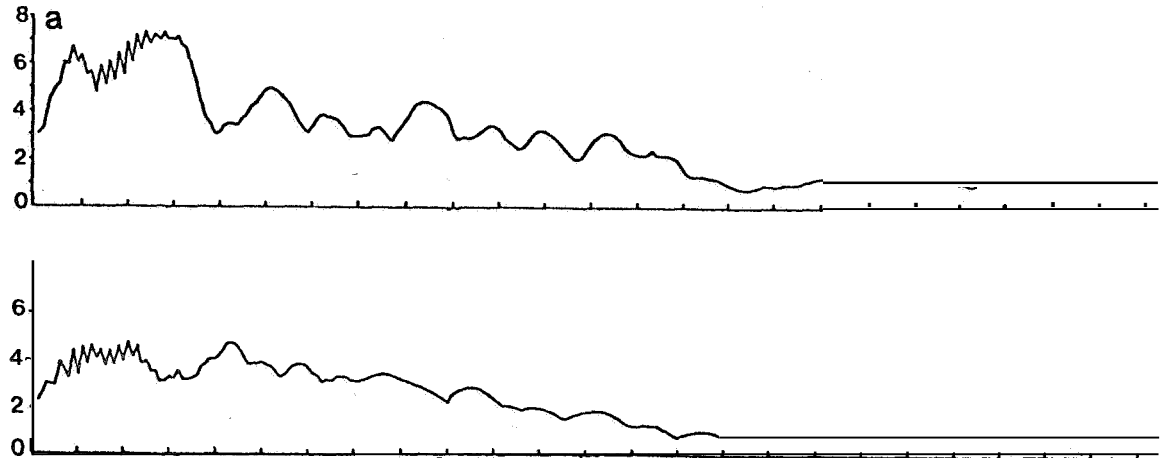

Figure 13: Time series of domain averaged surface pressure tendency for each time step of a three-hour forecast (1800 - 2100 GMT) initialized with (a) real winds, (b) balanced winds. Units of ordinate are mb hr^{-1} . Number of model time steps is shown on the abscissa.

in Figure 13 implies, rather the statistic PS tends to be dominated by a few grid points with the largest amplitudes in the western part of the domain. Oscillations in PS €or the balanced wind case do not have the same high amplitudes or regularity as the real winds, but for both cases PS levels off to ∿ 1 mb hr^{-1} after 150 time steps (∿ 1-1/2 hr) which is regarded as the end of the initialization/adjustment period of the model forecasts.

A more dramatic comparison between real and balanced wind initialization noise is seen in the local rate of change of mid-level (h_σ =6000 meters) vertical

velocity at a single location, This parameter has been used by Lejenas (1977). Point 2 (see Figure 7) was chosen for this illustration because the largest ageostrophic imbalances were found in that vicinity. Values of $\partial w/\partial t$ are plotted in Figure 14 for every time step of experiments A, B and C. For all three cases the first hour was characterized by ten minute oscillations with the amplitudes for the real winds being twice as large as the others and about a mean value of 25 cm sec^{-1} hr^{-1}. The "balanced" oscillations were about a zero mean. The $2\Delta t$ oscillations which appear every thirty time steps result from restoration of hydrostatic balance after implementation of the convective parameterization.

Comparison of $\partial w/\partial t$ for the two balanced wind cases indicates that no discernible reduction of noise was achieved by including quasi-geostrophic divergence in the initial conditions. The vertical velocities (see Figure 15) from which the divergence was derived were less than 1 cm sec^{-1} over most of the model domain. The three hour forecast vertical motions for experiments B and C showed differences at 6000 meters no greater than 3 cm sec^{-1} anywhere in the domain (Figure 16); therefore, after experiment C the

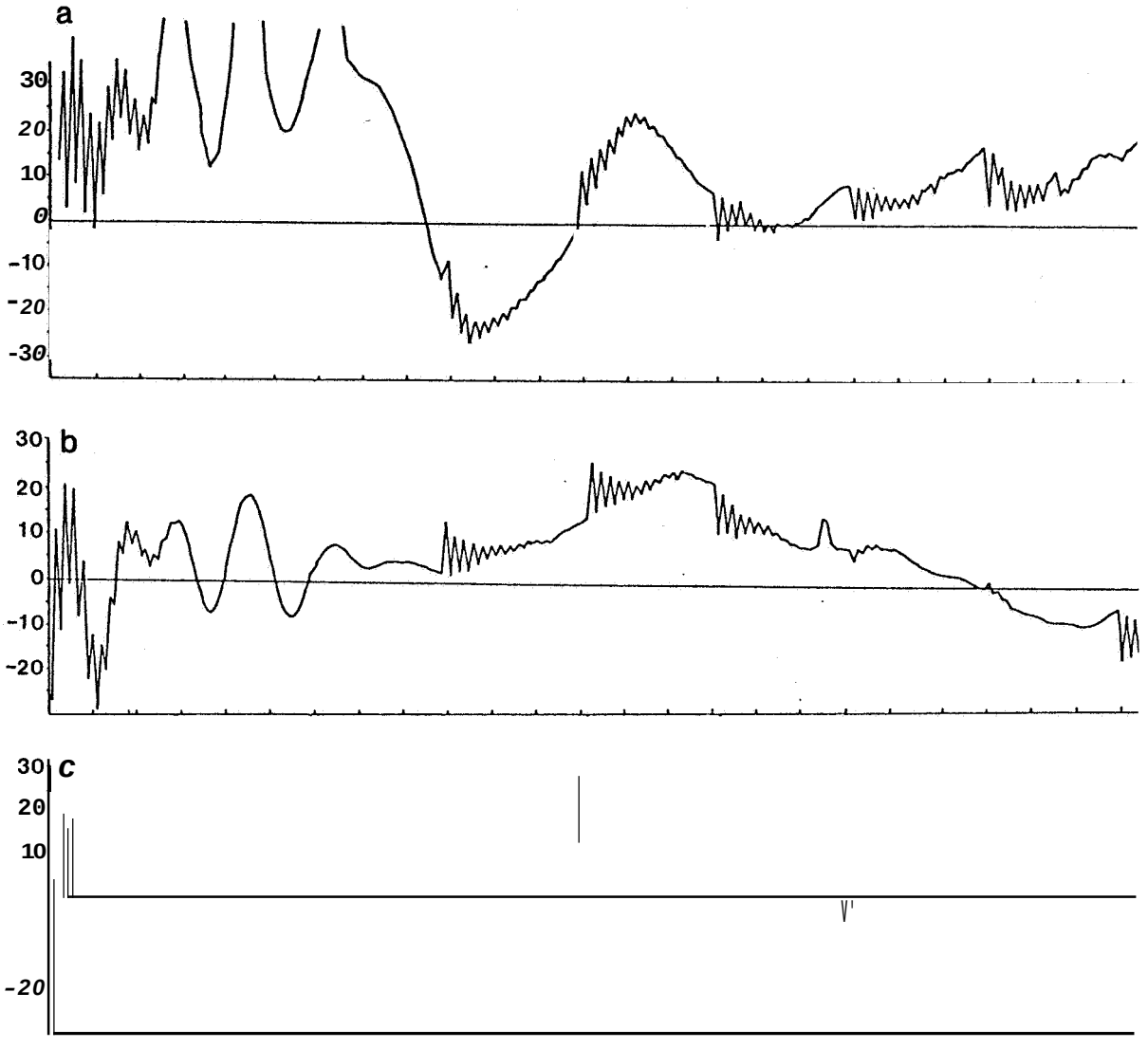

Figure 14: Time series of model level 9 vertical velocity tendency at point 2 for every time step of a three-hour forecast initialized with (a) real winds, (b) balanced winds, and (c) balanced winds with quasi-geostrophic divergence. Units on ordinate are cm $sec^{-1} hr^{-1}$. Number of model time steps is shown on the abscissa.

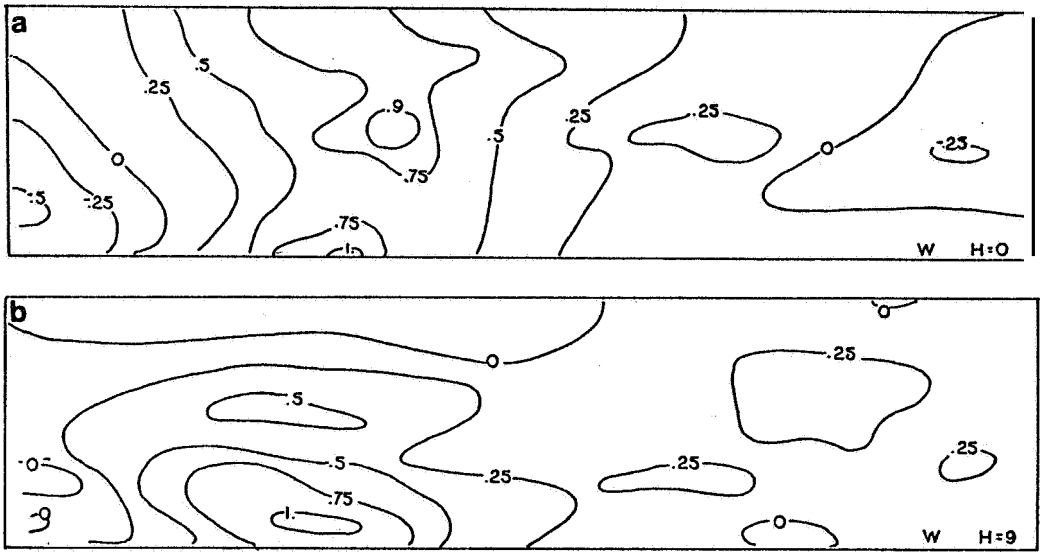

Figure 15: Horizontal zonally stretched domain maps of vertical velocity at the initial time (1800 GMT) for (a) lower boundary conditions, (b) quasi-geostrophic values at model level 9. Units are cm sec^{-1} .

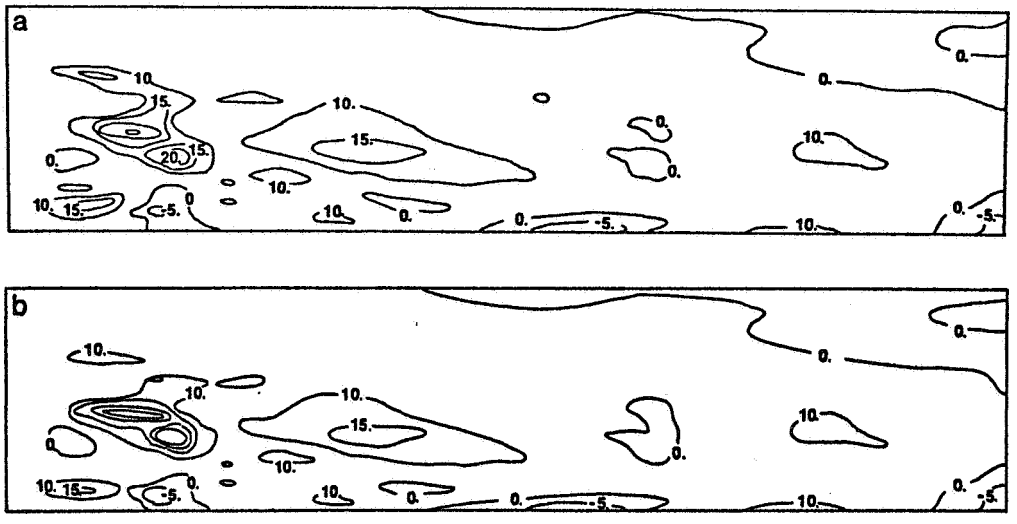

Figure 16: Horizontal zonally stretched domain maps of level 9 vertical velocity for three-hour forecasts initialized with (a) balanced winds, (b) balanced winds plus QG divergence. Units are cm sec^{-1} .

inclusion of QG divergence was abandoned for negligible impact on the model.

To summarize the results of the noise indicators, the balanced wind initialization clearly reduced model shock below the levels in the real wind forecast. The inclusion of quasi-geostrophic divergent components in the initial state with balanced winds was not found to have any beneficial effect on either suppression of initialization generated gravity waves or on lower spatial and temporal frequency features in the model forecast fields.

5.1.2 Forecast Fields

Even though the use of balanced wind and pressure fields reduce initial model shock, it does not follow that they must produce a better forecast than real winds. Adjustments do take place in the atmosphere in response to real mass/winds imbalances and may result in divergence and vertical motions related to observed weather on sub-synoptic scales. April 10, 1979 is a good example. The basic problem with the balanced wind (which really applies to the synoptic scale by its derivation) is that it removes smaller scale wind features that represent imbalances in the quasi-geostrophic framework, but which for the real atmosphere and possibly the primitive equations may represent information essential for accurate development of real phenomena. Balanced winds may also be sufficiently unrealistic as to distort magnitudes of advection. On the other hand real winds inherently incorporate the "essential" information, but also contain errors that can generate spurious high frequency gravity waves in a PE model which can adversely affect a forecast. This section will focus on experiments A and B to examine the impacts of the adjustment process on some of the forecast model fields

that resulted from initialization with real and balanced winds.

Arnold (1982) performed an analysis on the ageostrophic accelerations in the observed SESAME radiosonde winds for April 10. His results are pertinent because they provide an incisive illustration of the model adjusting to a non-geostrophic wind field to produce corresponding vertical motion and divergence patterns. Arnold computed the ratio, R, of the isallobaric acceleration to inertial advective acceleration $(\partial \vec{V}_g/\partial t / \overline{V \cdot \nabla V_g})$ at 500 mb for the period 1800 to 2100 GMT on April 10, and plotted the values over the SESAME domain. His figure which is reproduced in Figure 17d shows where R is small by shading. The elongated shaded area along the Texas/Oklahoma border corresponds well to the initial outbreak of convection as seen in the 1835 GMT radar summary data (appendix B).

The smaller values of R show where the magnitude of the inertial advective components of the ageostropic wind are larger than the isallobaric components. It is in these regions that the geostrophic adjustments are large. Divergence at 700 mb (Figure 17b) for experiment A (real winds), after one hour of

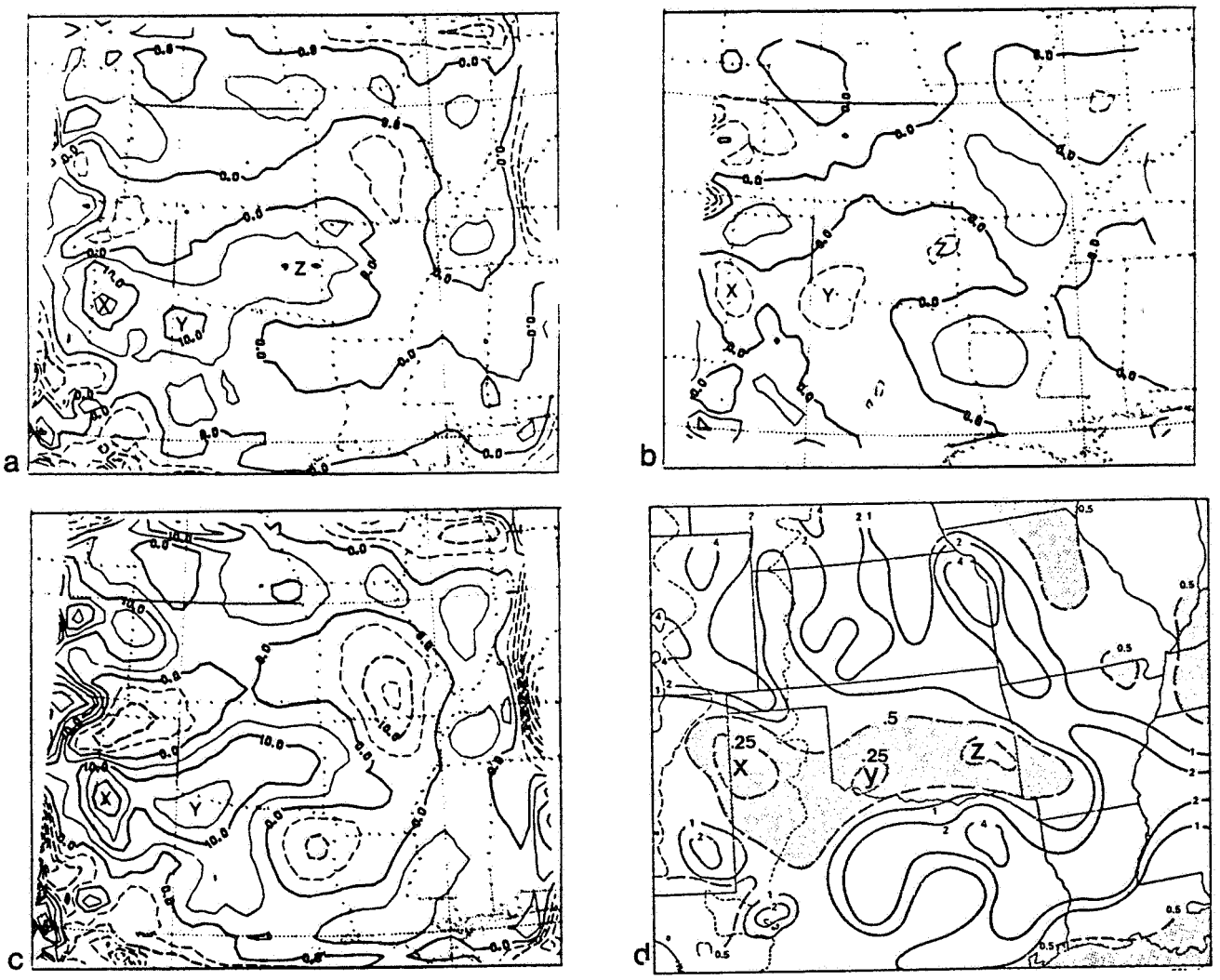

Figure 17: (a) 1900 GMT 700 mb vertical motion forecast from real wind initial state. Contour interval is 5 cm sec^{-1}. (b) same as (a) except for divergence (interval 2.5x $10^{-5}sec^{-1}$). (c) same as (a) except for 500 mb. (d) Ratio of magnitudes of isallobaric to inertial advective components of ageostrophic wind for 1800 - 2100 GMT (After Arnold, 1982).

integration, shows an elongated region of convergence corresponding to the shaded area in Figure 17d. Three convergent cells ($< -2.5 \times 10^{-5}$ sec^{-1}) marked "x", "y" and "z" are positioned almost exactly where R is a minimum. The 700 mb vertical motion at the same places show maxima greater than 10 cm sec^{-1}. The 5 cm sec^{-1} contour encloses approximately the same area as the R=0.5 contour. At 500 mb the same vertical motion patterns are found. The model has clearly responded in a region of large observed ageostrophic wind to produce low level convergence and upward motion in an area where the observed convective development would require it.

A comparison of balanced and real wind forecasts of 500 mb vertical velocity (at 2100 GMT) was made using an observed 500 mb omega field for verification. The observed field which is based on SESAME radiosonde data is reproduced from Vincent and Carney (1982) in Figure 18a. The primary feature is a broad area of upward motion over the Texas/Oklahoma border (A). To the north and south are downward cells (B and C), and to the west is a narrow downward band (E) running the length of the Texas Panhandle. The real wind forecast shows several of the same

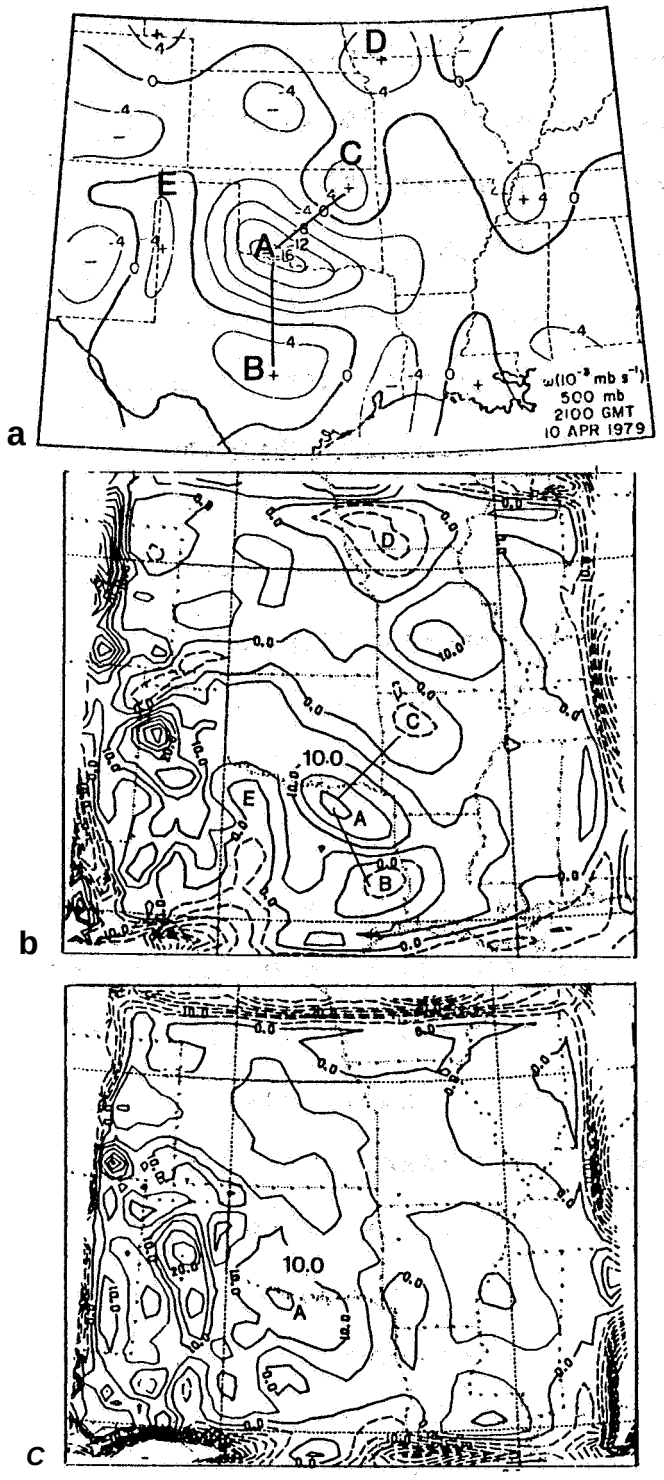

Figure 18: (a) 2100 GMT observed 500 mb "omega" field (After Vincent and Carney, 1982). (b) real wind forecast A 500 mb vertical velocity for 2100 GMT (contour interval 5 cm sec^{-1}). *(c)* same as (b) except for balanced wind forecast B.

features. Their relative positions are similar (see Figure 18b) to those observed, however, they are all consistently displaced about 200 km too far to the east. This is an indication that the high initialization noise levels in experiment A may be having a detrimental effect on the forecast. In the balanced wind run vertical velocity cells B, C, D and E are absent; however, the main cell A does exist and is situated well with respect to the observed one.

An examination of three hour forecasts of mean sea level pressure (MSLP) patterns discloses serious difficulties with the real wind initialization. The initial 1800 GMT MSLP, as diagnostically determined in the model (Figure 19), shows a low in Colorado with isobars extending in the north-south direction along the surface cold front. After three hours there is no evidence of a low pressure system moving into the domain as was observed. In Southeastern Colorado, where the low should have been, surface pressure actually increased and instead, the lowest pressure was found at the western edge of the Texas Panhandle. A six hour forecast showed this low pressure area propagating northeastward. The height fields at the mandatory levels also showed the initial low " washing

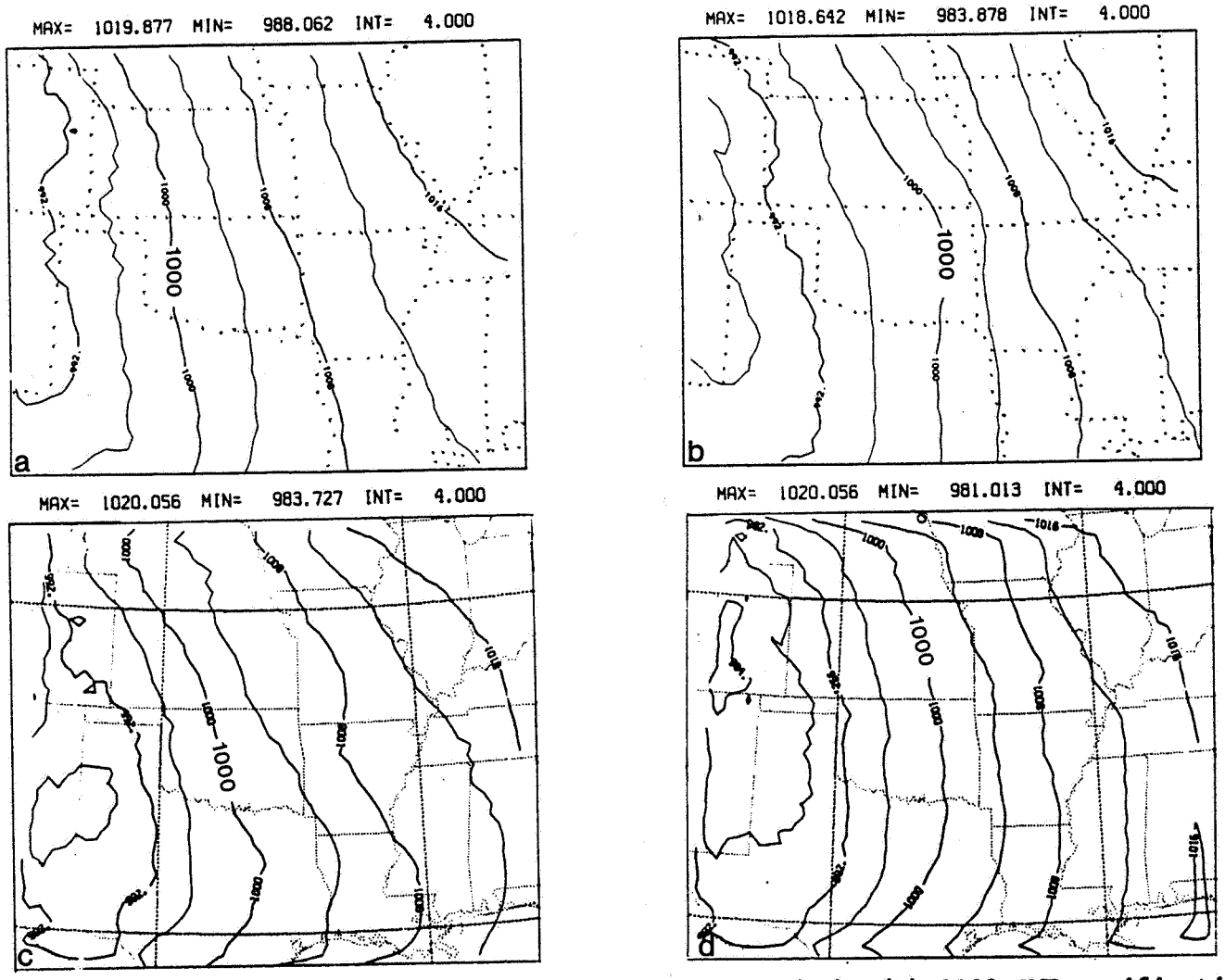

Figure 19: (a) initial 1800 GMT model sea level pressure (mb). (b) 2100 GMT verification sea level pressure. (c) Three-hour forecast sea level pressure from real wind initial state. (d) same as (c) except for balanced wind initial state.

out" in Colorado.

The balanced wind forecast MSLPs are about 2 mb too low in most areas of the domain (compare Figures 19b and 19d). The overall integrity of the isobar patterns was preserved. This forecast accurately moved the low into Southeastern Colorado as observed. The forecast lowest pressure was approximately 981 mb compared to an NMC observed 985 mb (see Appendix B, Figure B1). However, it is noted that model and NMC sea level pressure values are not expected to verify exactly since the mean temperature used by the National Weather Service for reduction to sea level is an average of the current and previous twelve hour surface temperatures. The model code incorporates only the current surface temperature into the sea level pressure calculation.

The superior initialization was achieved with balanced winds, Since both model runs A and B had the same initial mass fields and time dependent boundary conditions, the failure of the real winds to properly develop the low pressure system must be due to the deleterious effects of intense gravity wave generation during initialization. The severe toll of the adjustment process in experiment A could also be seen

in ten-minute output by highly distorted height fields as the model was initialized.

5.2 Dynamic Initialization of Low Level Winds

In recognition that the model may either ignore or reject the initial low level winds based on observed surface data, a dynamic initialization was used to force the model to accept the low level wind information for a period equal to the initialization phase of the forecasts. As detailed earlier,, the rationale for this approach was to include realistic low level divergence patterns which might impact on the initial development and evolution of convective precipitation. These procedures, which are the basis for experiments J and K, are described in this section.

In the dynamic initialization, u and v wind components at every grid point (i,j) at the lowest six levels (k) are linearly combined with the model predicted values at the same grid points according to a weight $\beta(t,z)$ which is a function of model time and height. The u-component equation is

$$U^{n}_{ijk} = U^{n}_{ijk}\,(1-\beta(n,k)) + U^{obs}_{ijk}\,(\beta(n,k))$$

for time step n = 1 to 156 (approximately **1-1/2** hours) and model level k = 1 to 6. u^n_{ijk} is the model predicted value at a given time step. It is updated by the initial constant u^{obs}_{ijk}.

It is important to note that the initial low level winds (in Block II experiments) were not based on 2100 GMT surface data, but on the average of the **2200** and **2300** GMT surface winds. This was done so that the surface winds that influence the initialization are those which would be valid at the end of the adjustment period. This time offset was not considered important for the statically initialized Block II experiments because the observed surface winds changed very Little over this period. The surface wind analyses for **2230** GMT are shown in Figure **20.**

The weighting factor β was chosen to be a decreasing function of model time going from 1.0 to 0.0 during the initialization phase. This forces the initially specified low level winds into the model strongly at the beginning and then reduces their influence to zero at the end of the initialization.

In experiment K, the weight β was a decreasing function of model height as well **as** time (Figure **21).**

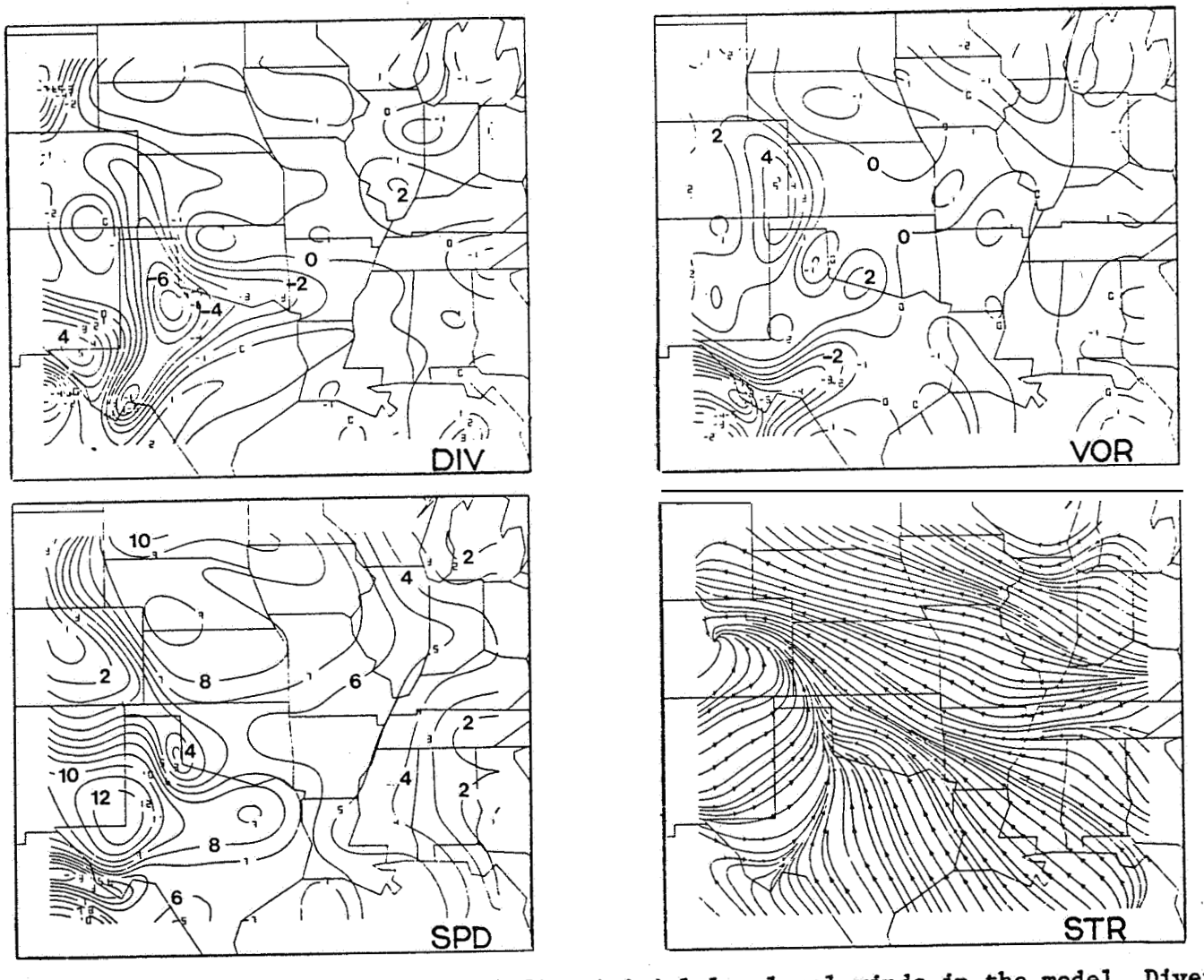

Figure 20: Surface wind analyses used to define initial low level winds in the model. Divergence and relative vorticity are in units of 10^{-5} sec^{-1}. Speeds are in m sec^{-1}.

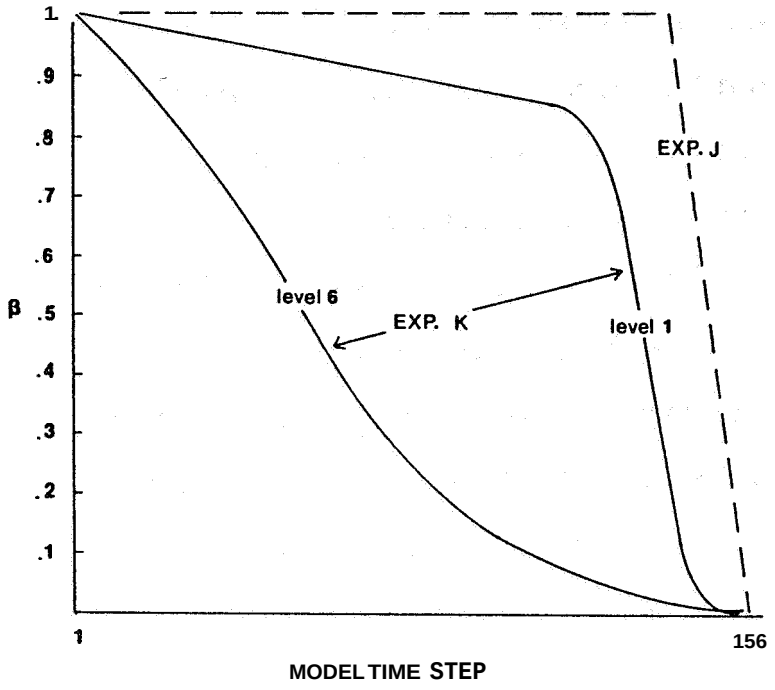

Figure 21: Weight (β) assigned to initial low level winds in the dynamic initialization of experiments J and K. The length of the initialization is represented as the 156 time steps on the abscissa.

At level 6 the weight given to the initial winds falls off rapidly with time, while the lowest level winds receive more than eighty-five percent of the total weight until near the end of the initialization. The β-function values for a given time at levels 2 through 5 are obtained by linear interpolation between values at the surface and level 6. The shapes of the

functions are somewhat arbitrary but reasonable if the goal is to ease the model forecast away from the initial low level winds in both time and height. The function values at level 6 were derived by fitting a fourier series to points extracted from hand-drawn curves. At level 1, a mixed linear and fourier series fitting interpolation was used.

In experiment J the weighting function was the same for all model levels (k = 1 to 6) and was held constant for one hundred thirty-five time steps with a value of 1.0 (Figure 21). During the ensuing twenty-one time steps, @ decreased linearly to zero. Experiment J essentially held the low level winds constant for the entire initialization. Results and comparisons of experiments J and K are discussed in the next chapter.

6. Model Results

6.1. Mass Fields

6.1.1 General Features

The model forecast mass fields are investigated with inter-comparisons between model cases and with observed mean sea level pressure (MSLP) and **SESAME** geopotential height fields. The first part of the discussion focuses on general aspects of the mass field evolution. The second part will investigate the generation and evolution of specific mesoscale features in the height fields.

The quality of the model forecast sea level pressure fields is examined in terms of two attributes which characterize the observed mean sea level pressure patterns. (See Figure B1 of Appendix B). The first is the elongation of the isobars along the surface cold front and the second is the small change in the central pressure of the storm over the forecast period (~1 mb over nine hours). Values of the forecast lowest sea level-pressure for each model run (Figure 22) and maps of the sea level pressure patterns at the final forecast time for each case (Figure 23) will be used in the discussion which follows.

The first hour and a half of all model runs is

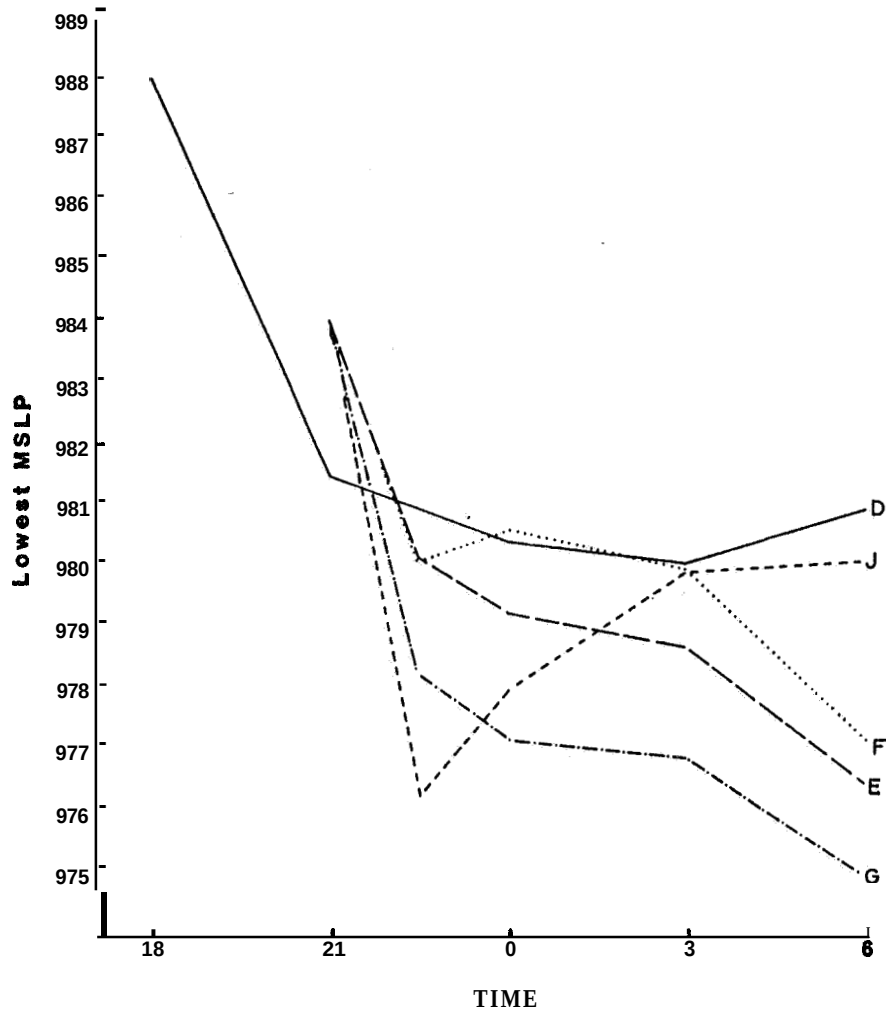

Figure 22: Time traces of the lowest forecast sea level pressures for case D and the Block II experiments.

characterized by rapid falls of the domain lowest pressure ($\sim$ 2-1/2 mb hr^{-1}) as seen in Figure 22. Both satellite case E and case F showed initial drops of 4 mb. Although pressure increases for case F between

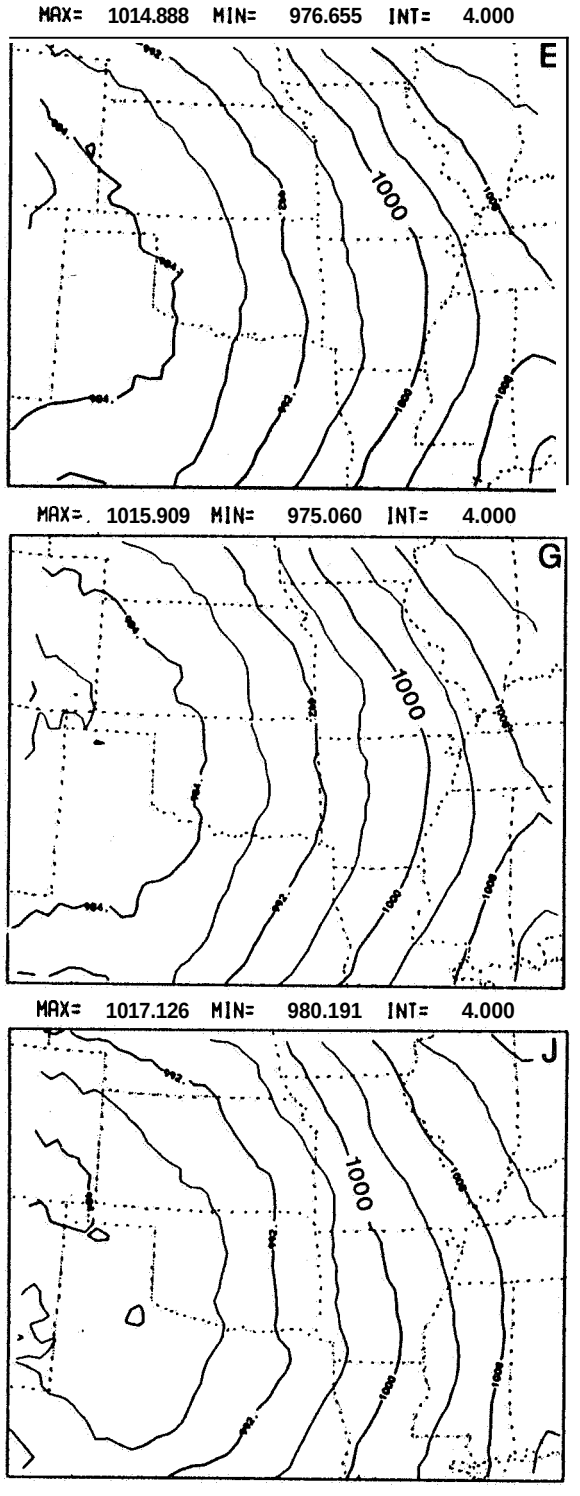

Figure 23: Final forecast (0600 GMT) sea level pressure fields for cases E, G, J, F and D. Units of contours are millibars.

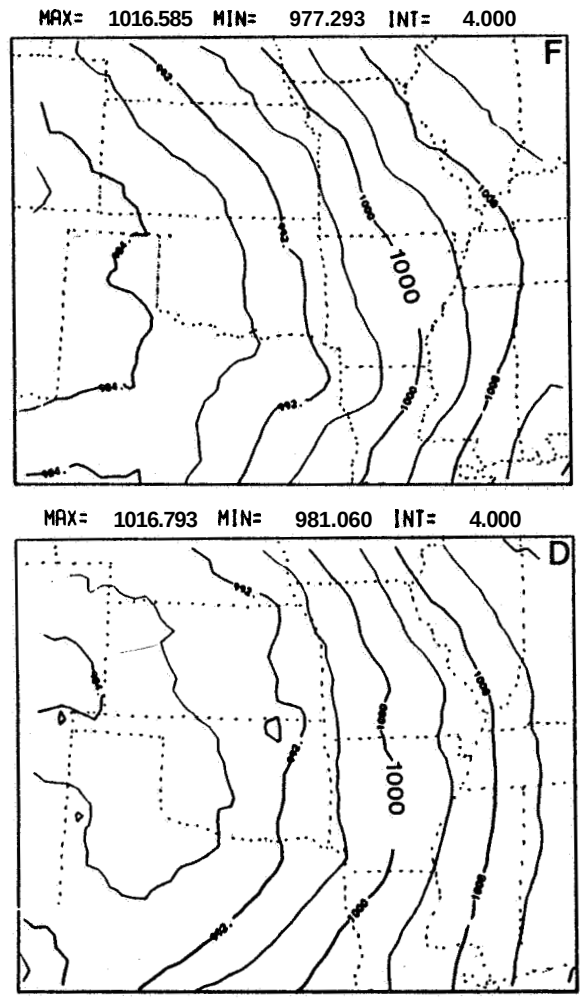

Figure 23: (continued)

2230 and 0000 GMT, both the satellite and radiosonde values decrease steadily at about the same rate (after 0000 GMT) for the remainder of the forecasts with the satellite pressure about 1 mb lower. For both cases, by 0600 GMT all isobars are shifted eastward relative

to the observed isobars (compare Figures 23 and 24) indicating pressure forecasts which are generally too low. The deviations from observed pressure are greater in the western part of the domain.

Comparison of the final pressure fields for cases G and E shows great similarity with both having large eastward bulges in the isobar patterns. In case G the lowest **MSLP** dropped almost six millibars during the initialization and remained about two millibars lower than in case E for the entire forecast period.

Holding the low level winds constant during the initialization period (J) resulted in a much improved

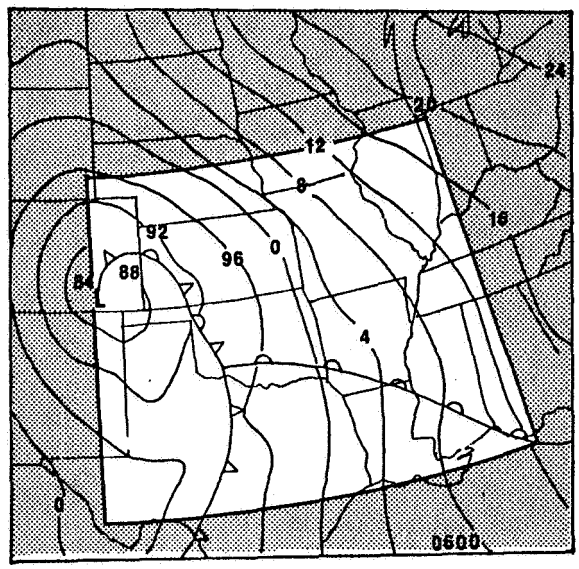

Figure *24:* Verification mean sea level pressure field for 0600 GMT April 11. Un-shaded area corresponds to the model domain.

pressure pattern forecast with isobars extending southward from the low along the approximate position of the surface cold front. Despite an initial 8 mb drop in the lowest MSLP, the model quickly recovered to give a final value only 4 mb lower than at the initial time, the smallest total drop of the Block II experiments. At the end of the forecast, sea level pressures for case J are 2 to 4 mb higher over the model domain than in cases F, G, and E.

The excellent MSLP forecast made in case D shows the same features as case J at 0600 GMT; however, D did not include observed low level winds in any form. Thus, the dynamic initialization with observed low level winds, while improving the quality of the Block II experiments, is not essential (depending on the initial conditions) for producing a good mass Eield forecast. Case D experienced significant drops in lowest MSLP during the first three hours but leveled off to give a value only 3 mb lower than observed at 0600 GMT. Because cases D and F are based on SESAME radiosonde data from successive observing times (1800 GMT for case D and 2100 GMT for case F), ideally, they should produce similar forecasts. The fact that they do not reflects a model sensitivity to the initial

conditions and possibly to the length of the model forecasts.

For all experiments, the forecast sea level pressures were lower than observed over most of the domain, with the largest discrepancies in the West where the lowest pressures were. The same phenomenon is evident at the upper levels as well. However, while the position of the synoptic scale low is close to the one observed, the relative rates of intensification and eastward propagation of the low (at the surface and aloft) between cases is different.

These differences are illustrated by comparing the expected changes over time of a lowest height value in the model domain to actual changes computed in the model forecasts for the same time periods. The height change value was computed as an average of the changes of the domain lowest geopotential heights at 850, 700 and 500 mb for the periods 2100 to 0000 GMT and from 0000 to 0600 GMT (April 11). The model forecast changes were determined from the maximum/minimum height values provided by the model output software for each mandatory level pressure-height field.

The expected changes in the minimum height value for the same periods were determined in two ways. The

first method computed changes in height from the time dependent boundary condition fields nearest the low pressure center based on values at 1200, 0000 and 1200 GMT (April 10-11). Thus, expected changes by this method for 2100 to 0000 GMT were based on the first twelve hour time tendencies. Likewise, changes from 0000 to 0600 GMT were based on the second set of twelve hour tendencies. The second method computed changes in the lowest height from values at the center of the synoptic scale low pressure system in independently analyzed SESAME height fields at 2100, 0000 and 0600 GMT. 0300 GMT was not used in order to be consistent with the time resolution afforded by the boundary conditions. For the model output and boundary condition fields, it was assumed that the model grid point with the lowest height represented the center of the low. Since the actual low pressure system was positioned only near (inside or outside) the western boundary of the domain, the lowest valued grid point may not have been at the center, but it was close, and its changes over time reflect either development or propagation of the low pressure into the model domain.

The results of this analysis are presented graphically in Figure 25 which shows the averaged (850-

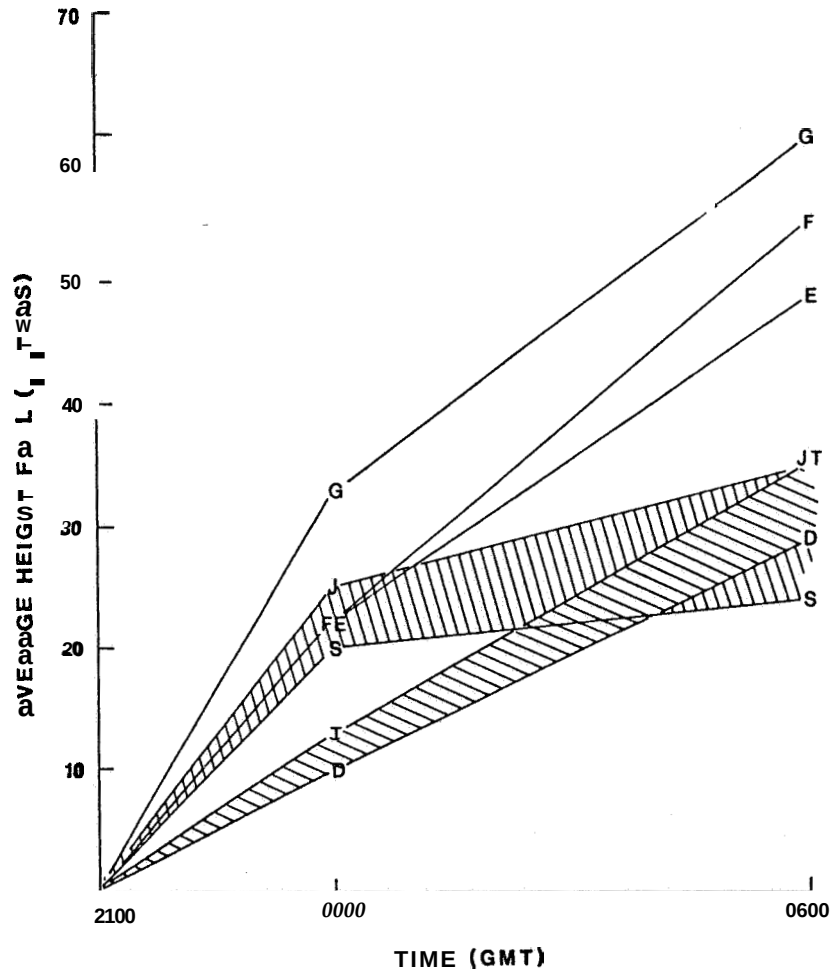

Figure 25: Time changes of domain lowest average height (850 - 500 mb) from the reference time 2100 GMT. Individual cases are identified on each curve. S and T refer to time changes expected from independent SESAME height analyses and time dependent boundary fields respectively.

500 mb) changes of lowest geopotential heights relative to the reference time of 2100 GMT. Each curve is labelled with a letter identifying the model run. The curves T and S represent height falls expected from the

twelve hour time tendencies and from the SESAME observations respectively. From 2100 to 0000 GMT the lowest height in case D fell only 9 meters compared to 21 meters for cases E and F, and 33 meters for case G. Case D shows greater consistency with the time dependent boundary values, while E, F and J are more consistent with the observed changes.

Even though all Block II experiments were subject to the same time dependent boundary conditions for the same length of time, large differences developed between case J and cases E, F and G from 0000 to 0600 GMT. The latter cases experienced total height falls of 49 (E) to 62 (G) meters compared to an observed drop (S) of 24 meters, and 35 meters for both case J and the time dependent boundary fields. The impact of the dynamic initialization with low level observed winds was to produce more realistic height falls. The use of balanced winds at all levels (G) caused over-development of the low and faster eastward propagation of the height and pressure fields at all times. The static initialization with observed low level winds (E, F) was of benefit in reducing these height falls only during the first three hours.

The rates of change of the lowest heights with

time (slopes of lines) in case J are most consistent with the SESAME observations. Only case D (twelve hour forecast) was consistent with the time boundary tendencies for the entire nine hour period analyzed. These results are in agreement with the superior sea level pressure forecasts achieved in experiments J and D.

There are several reasons why the boundary condition mass fields might not be expected to match the model evolution. First, boundary conditions twelve hours apart can not include changes which occur on smaller time scales. The use of balanced winds initially at levels above 2000 meters omits some initial state mass/wind structure which would be essential for a PE model to completely simulate the observed mass field evolution. Finally, the boundary conditions may be imperfectly posed due to the inherent difficulties of accurately prescribing boundary values from observations.

6.1.2 Mesoscale Features

Care was taken in preparing the data in this study to include sub-synoptic scale short waves in the initial state in order to see how they would be handled by the model forecasts. The major short waves were

confined to the low levels. The initial and forecast 700 mb height fields are presented in Figures 26, 27 and 28 for experiments F, E and J respectively. Both the satellite and radiosonde show three very similar short waves in the initial data. A main short wave, marked "M", along the Texas/Oklahoma border at 2100 GMT is the only one of the three which is retained throughout the model forecasts.

The response of the model toward these features was to either eliminate them or reduce their amplitude during the initialization. A substantial loss of amplitude is evident for the main short wave in all model forecasts; however, in each case it rotated around the large scale trough into Central or Northern Oklahoma by 0000 GMT. Continuity of the propagation is verified by height fields at 2130 and 2230 GMT.

Steady northward propagation of the main short wave is obvious after 0000 GMT. Its position at a given time is approximately the same in both the radiosonde and satellite forecasts, however the amplitude is slightly larger in radiosonde case F. After the short wave reaches Northern Oklahoma, the length of the wave front increases. At this point in the radiosonde forecast (F), the width of the short

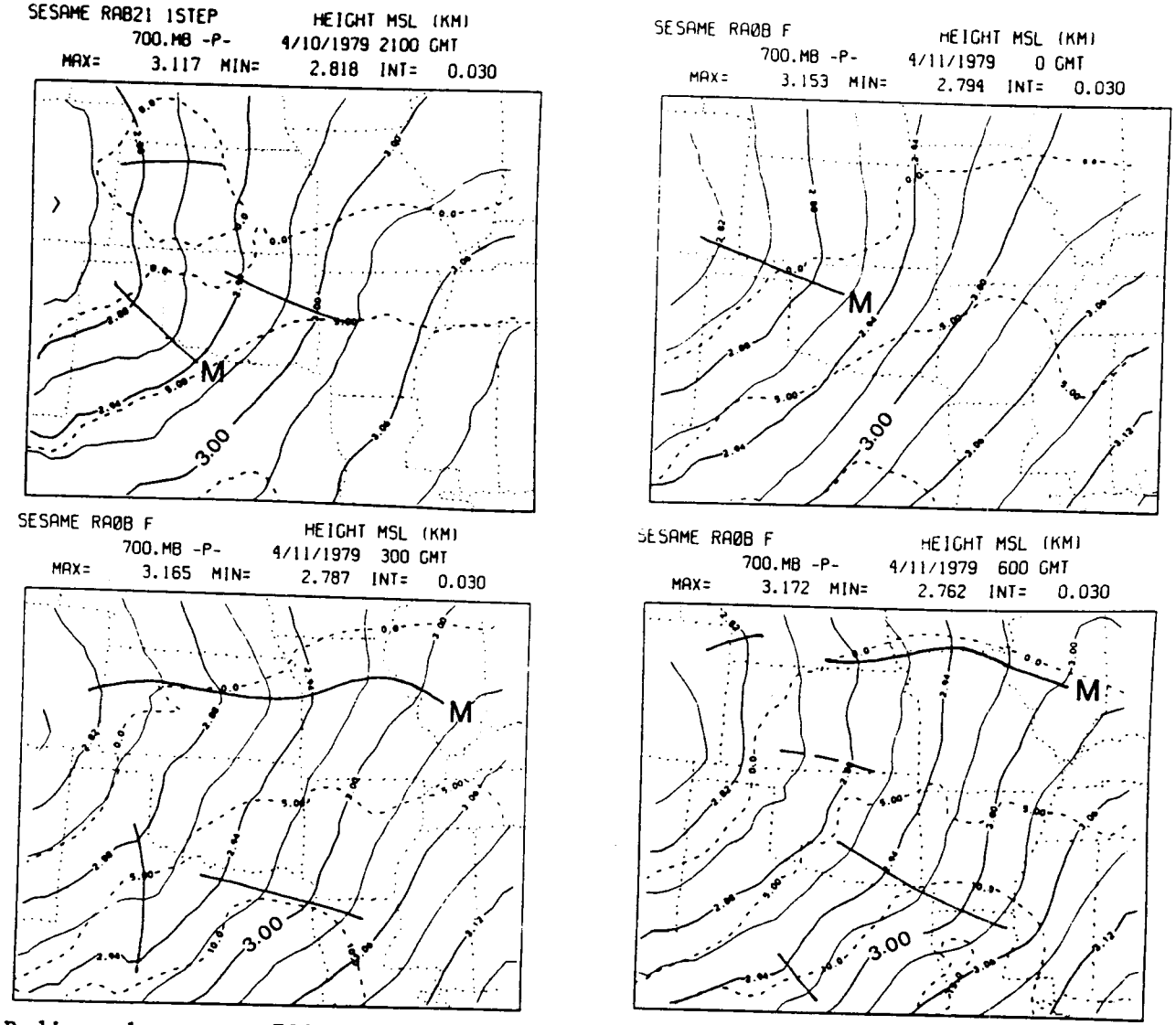

Figure 26: Radiosonde case F 700 mb forecast heights. Location of the main short wave "M" trough axis is indicated. Units and times are shown above each map. Dashed lines are isotherms (°C).

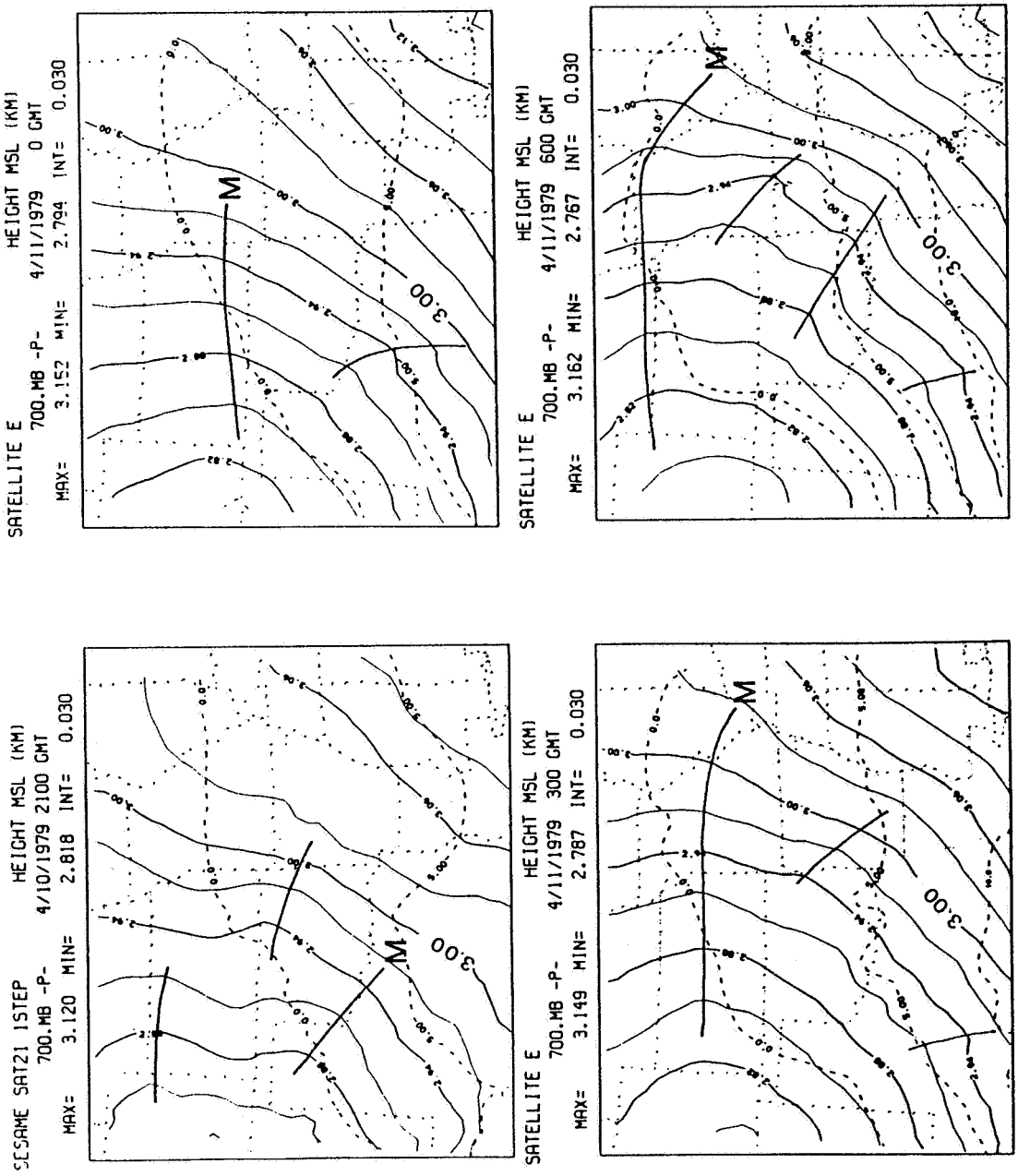

Figure 27: Same as Figure 26, except for satellite case E.

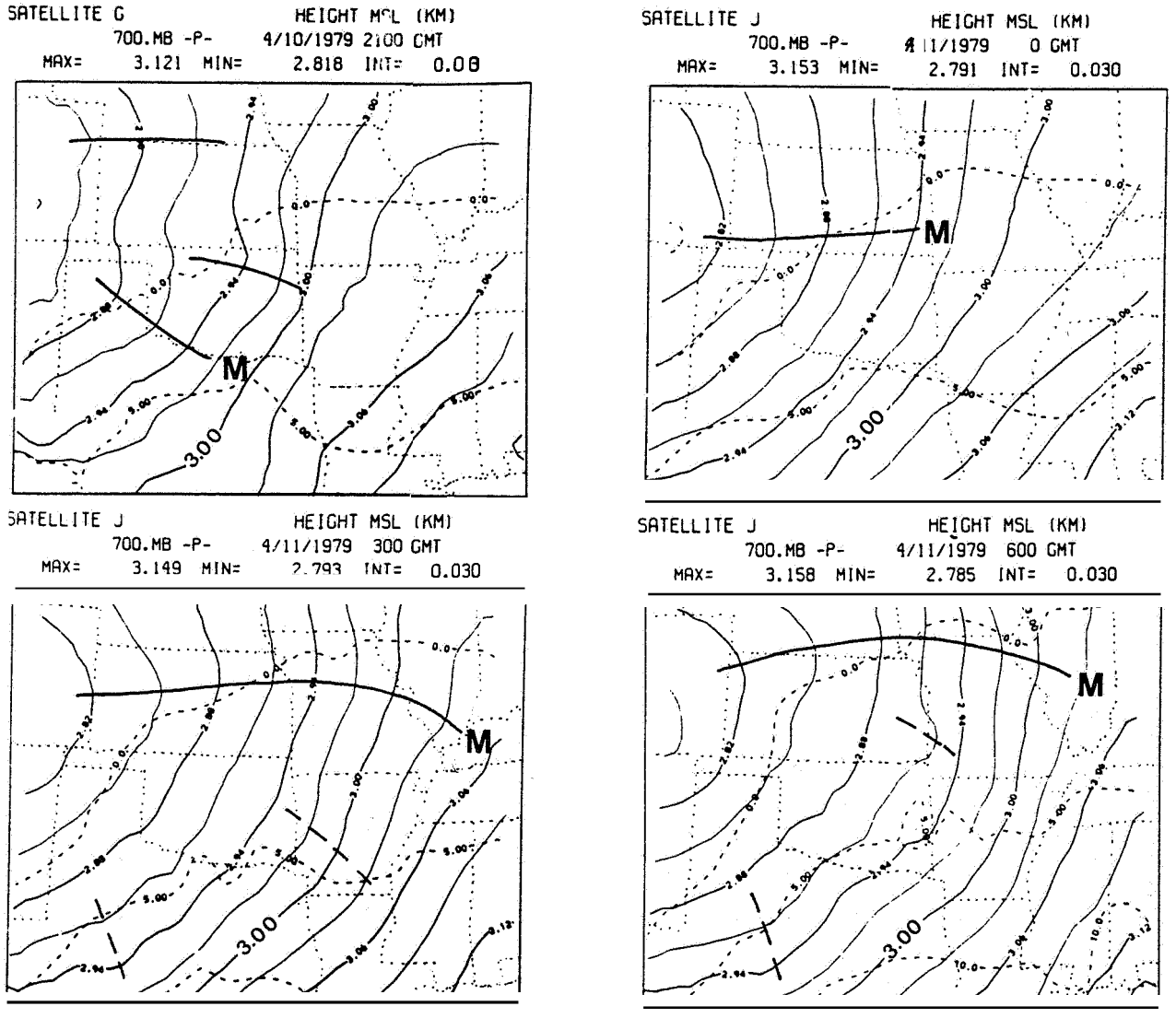

Figure 28: Same as Figure 26, except for satellite case J.

wave decreases as the wave becomes associated with a precipitation band of similar dimensions. The precipitation band, which will be discussed in detail in a later section, propagates northward with the short wave with a uniform speed of about 18 m sec^{-1}. The maximum amplitude of the short wave in all forecasts occurs at 0300 GMT. A short wave with locations and spatial dimensions very similar to those of the short wave in the model forecasts is evident in the 700 mb SESAME height analyses (see Appendix B). Both the observed and forecast short waves lose amplitude as they propagate into Nebraska.

After the initialization phase and by 0000 GMT, each model run eliminated much of the small scale structure in the initial states. In case F, for example, except for the main short wave, the 700 mb height analysis is smooth. Thus, the presence of additional short waves after 0000 GMT demonstrates the model's ability to generate mesoscale short wave features of its own accord.

The main short wave has vertical as well as horizontal structure. Overlaying the height analyses from different levels reveals maximum amplitude of the short wave at 700 mb with weaker signals at 850 and 500

mb, and shows a slight down wind tilt with height. For example, consider case D which produced two significant short waves which were picked up by the model first at 0000 GMT. The speed, locations and dimensions of one of these waves (Figure 29) is similar to the main short wave in the Block II experiments even though case D was initialized three hours earlier with different initial data. The short wave in question is found at 850 and 700 mb at 0000 GMT and moves northward at about 15 m sec^{-1}. By 0300 GMT the trough axis is also evident at 500 mb. The location of the axes with respect to one another indicates that the trough is tilted to the north with height. The second short wave shows the same tilt at 850 and 700 mb, however that one propagates only very slowly into Oklahoma. The model 700 mb height analysis at 0300 GMT (Figure 29b) shows the mesoscale width of the short waves. The vertical structure of the main short wave in Block II cases is examined in more detail later with a discussion of the divergence, vertical velocity and precipitation patterns associated with it.

Anthes, et. al. (1981) suggested that initialization with mesoscale data may not be essential for producing accurate mesoscale model forecasts. This

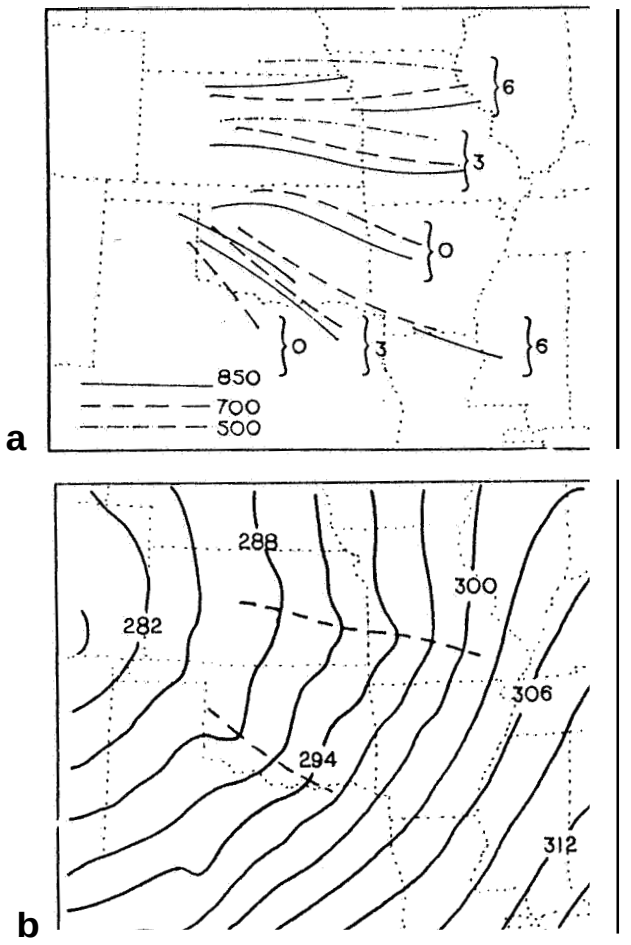

Figure 29: Panel (a) shows isochrones (labelled in hours GMT) of 850, 700 and 500 mb radiosonde case D forecast short wave trough axes. Panel (b) shows the 700 mb forecast height field (dekameters) at 0300 GMT.

is based on the fact that many mesoscale phenomena are by-products of synoptic scale interactions. The best example is a frontal zone which typically is formed from the confluence of two larger scale flows. By the same token mesoscale phenomena are generally

inadequately observed or their internal structure and relationship to larger scales are poorly understood. Thus, if observations intended to describe a particular mesoscale phenomenon are inserted into even a perfect mesoscale model, the phenomenon may be unrecognized and is likely to be eliminated or severely misrepresented during the initialization/adjustment process.

Despite these arguments, in this study at least one of the initial low level short waves was retained by the model and went on to have a significant positive impact on the precipitation forecasts. The initial loss of amplitude in the main short wave however, may derive from the inconsistency of using balanced winds in the vicinity of a short wave feature. As noted earlier, the balance relation is based on assumptions of large scale and non-divergence and therefore is unable to include the large observed divergence and vertical motion fields which were probably at least partially related to the main short wave at 2100 GMT.

There is evidence of some adjustment activity in the form of an external wave which seems to have its origin in the vicinity of the main short wave, This is revealed in plots of local pressure tendency at the surface and model top at 2130 GMT (Figure 30). Large

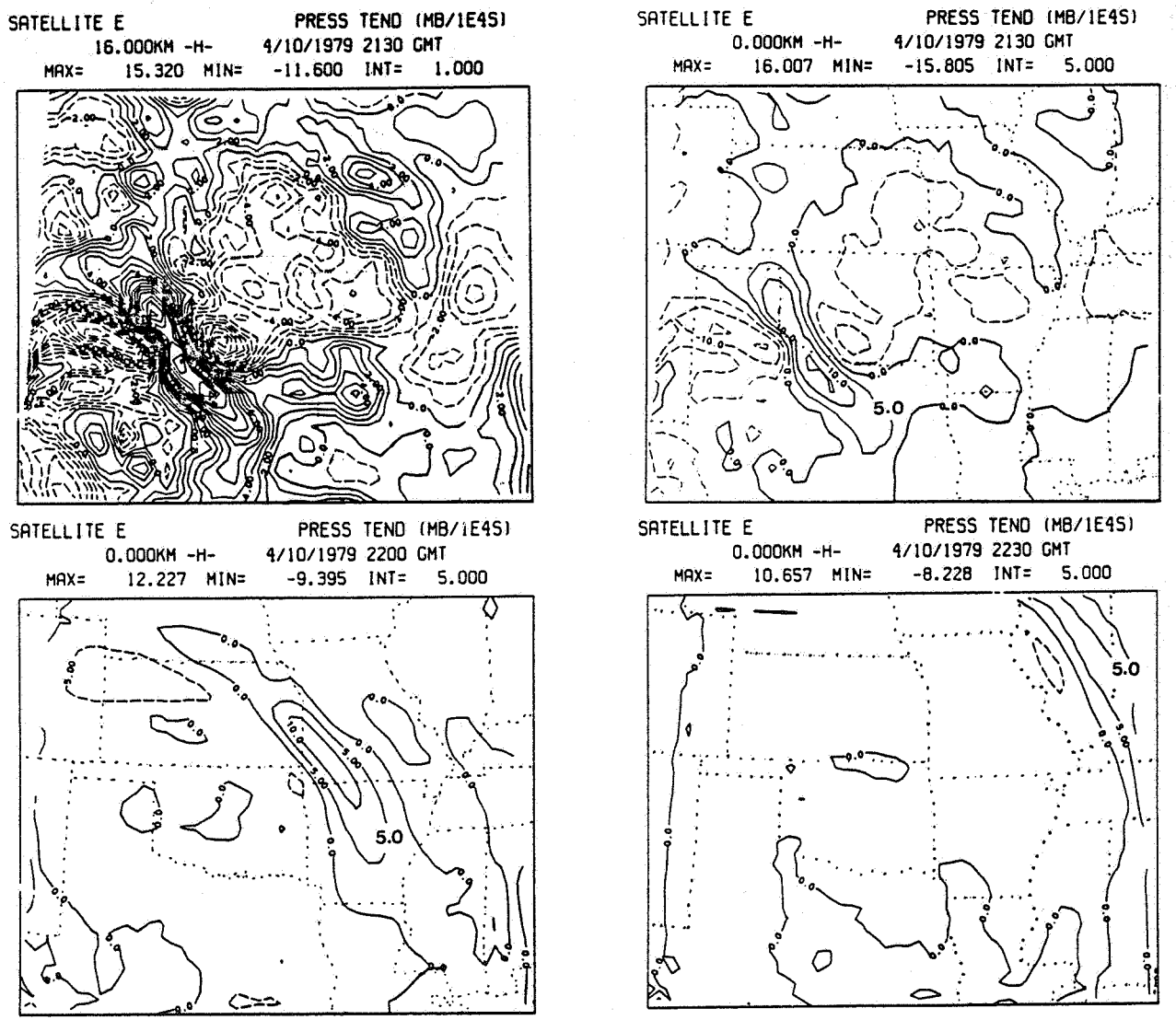

Figure 30: Maps of instantaneous pressure tendency showing an external wave propagating from the Texas Panhandle region. Units, times and levels are given above each panel.

positive values in a northwest-southeast oriented band in the Texas Panhandle area at both levels suggest an external perturbation for satellite case E. Subsequent half-hourly plots confirm this by showing the wave front expanding as it propagates north eastward at about 350 m sec^{-1}. Since this wave appeared in all Block II experiments (see Figure 31), its generation can not be attributed to satellite data or to the inclusion of low level winds. It can only be hypothesized that it is associated with a model perceived mass/wind imbalance in the southwest portion of the domain. In all cases the external wave propagated out of the domain without affecting precipitation and was absorbed at the lateral boundaries.

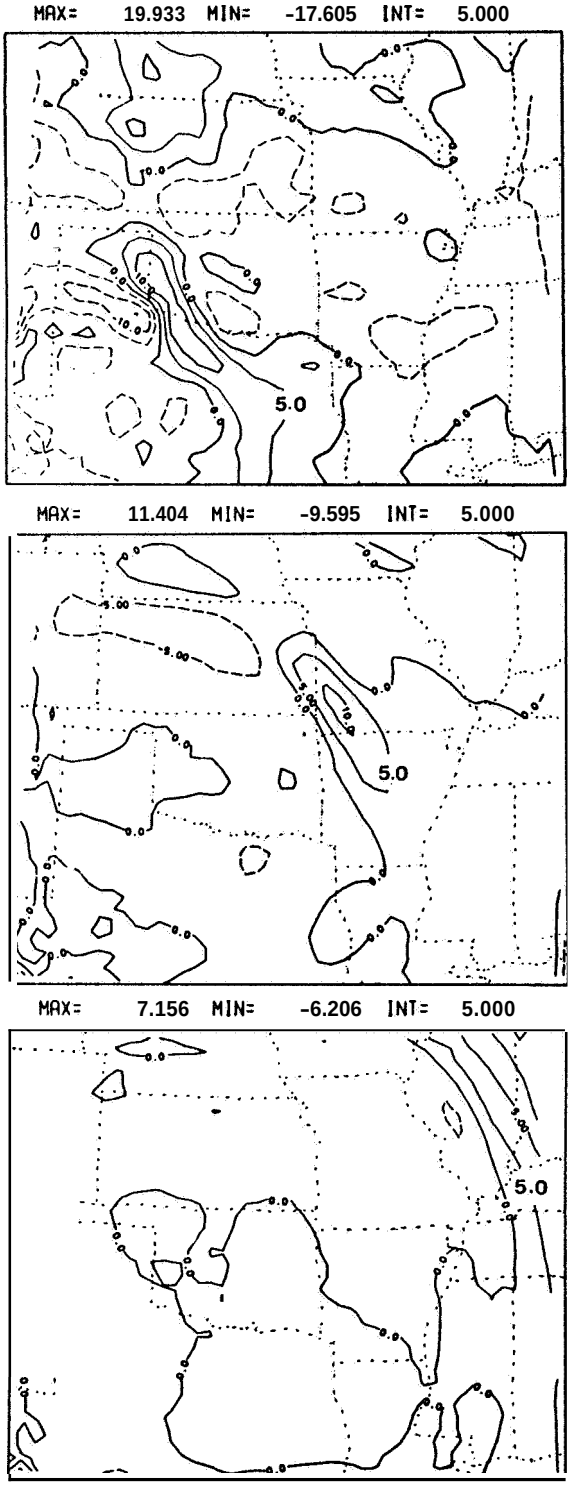

Figure 31: Same as Figure 30, except for radiosonde case F.

6.2 Precipitation

6.2.1 Mesoscale Structure

This section examines the precipitation forecasts of the Block II experiments and case D. The first part of the discussion will focus on the mesoscale structure of the preciptiation generated by the model with emphasis on the short wave system in case F. The remainder of the section provides a more general inter-comparison of model forecasts in terms of precipitation patterns and total accumulations.

The association of the case F 700 mb short wave with a mesoscale precipitation band is illustrated in Figure 32 which shows stable (grid scale) precipitation rate fields for every hour and a half beginning with 0130 GMT. The short wave axis "M" is superimposed to show that the stable precipitation band propagates northward with the short wave and lies directly over the trough axis. The forecast convective precipitation starting with 2230 GMT is also seen to coincide with the short wave' (Figure 33). The convective rainfall rates are comparable to the stable rates, but the convective preciptitation occurs over a wider area around the short wave trough axis. Maximum precipitation rates, like the maximum amplitude of the

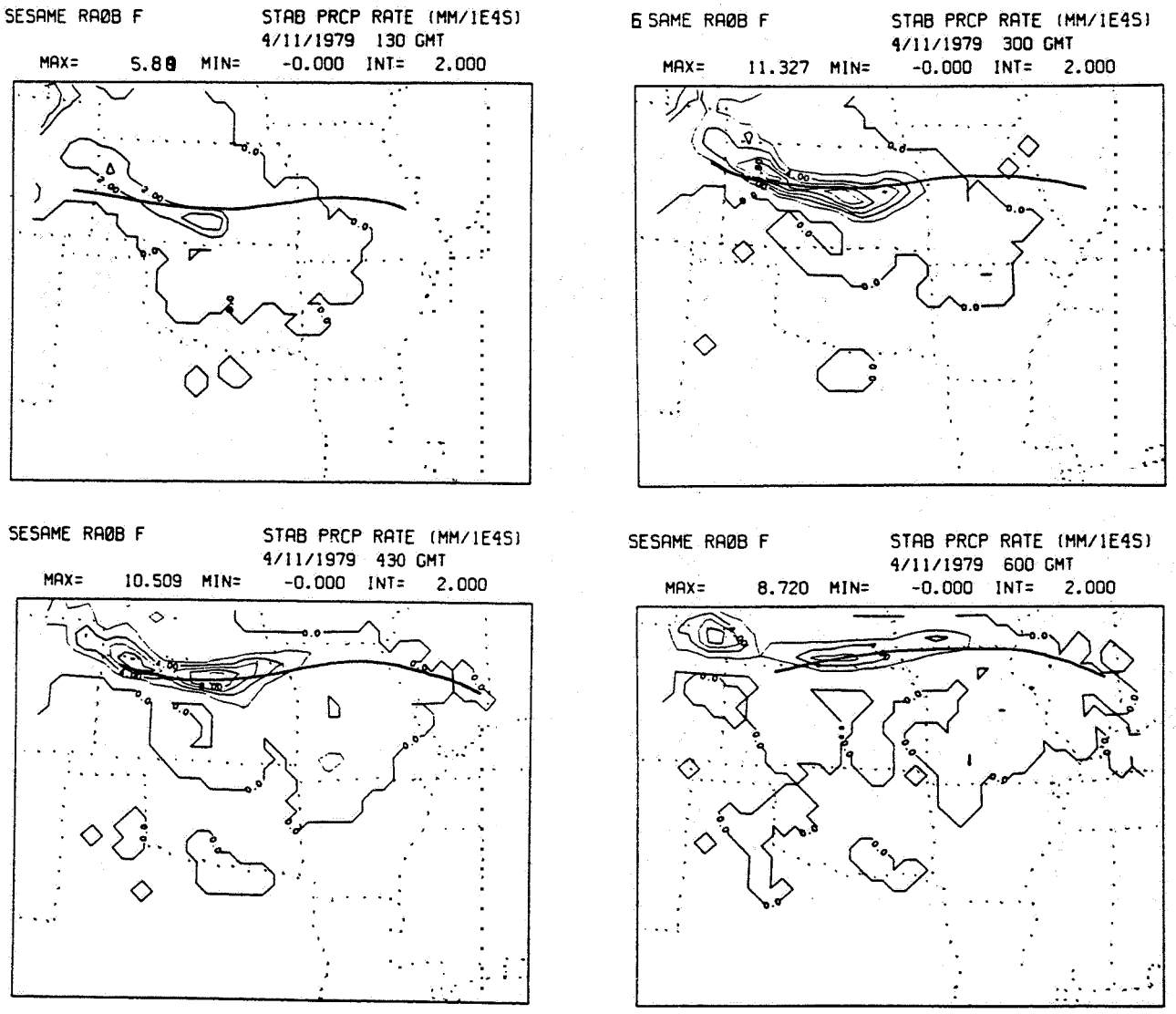

Figure 32: Stable precipitation rates for radiosonde forecast F. The position of the 700 mb short wave is superimposed. Units and times are shown above each panel.

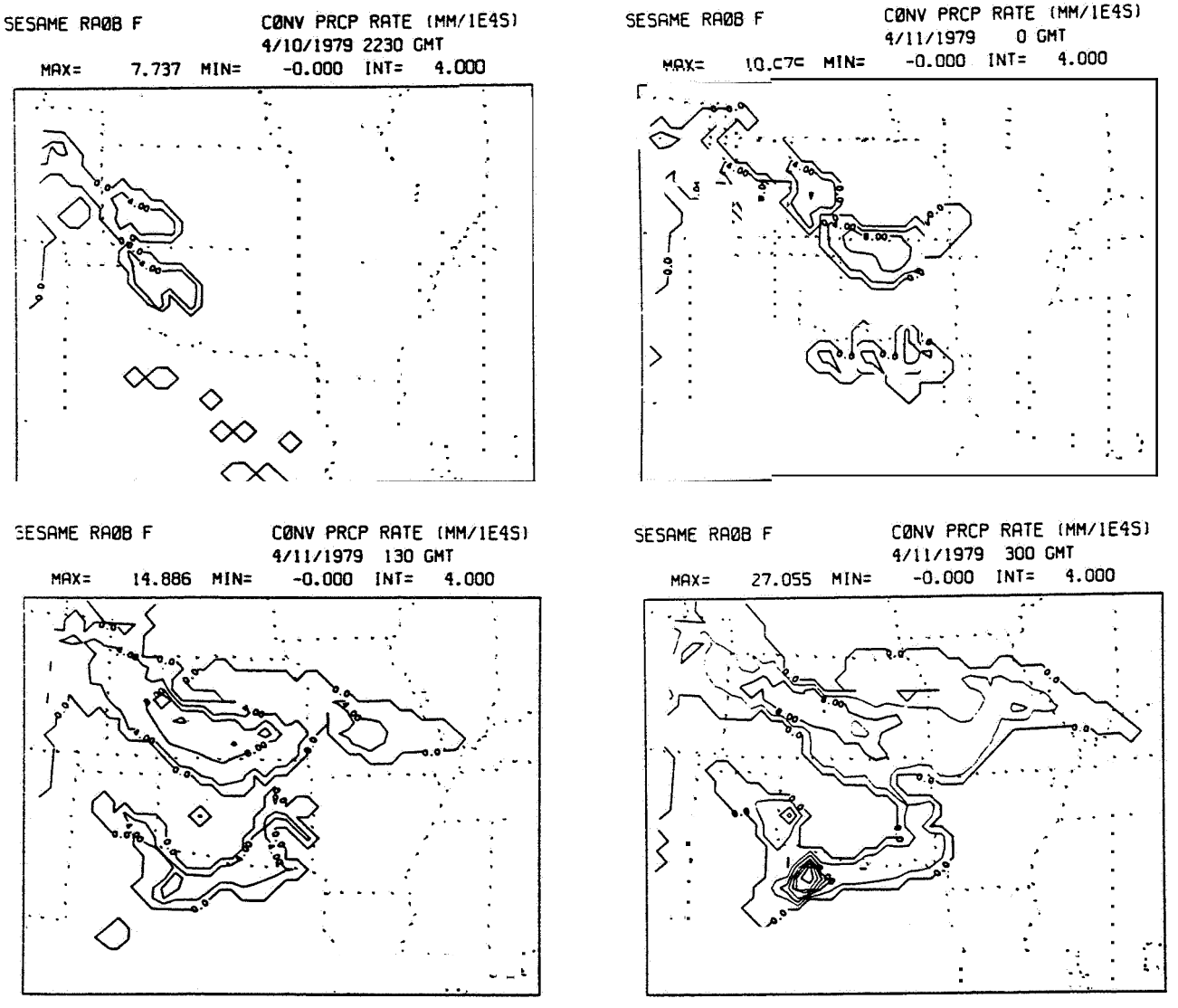

Figure 33: Same as Figure 32, except for convective precipitation.

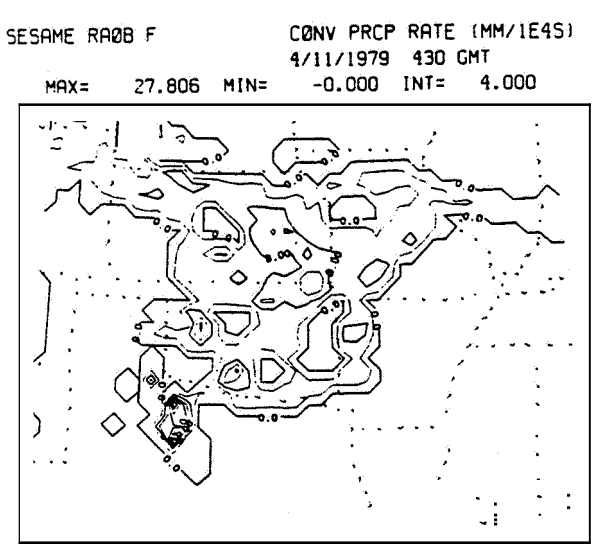

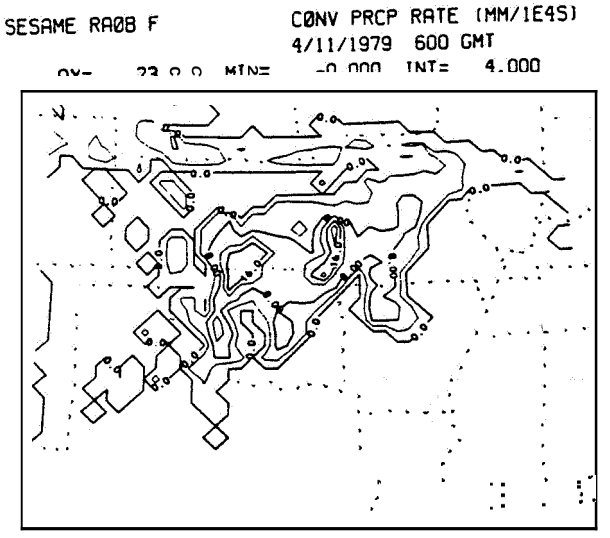

Figure 33: (continued)

short wave, occur at 0300 GMT.

A time series of vertical cross-sections along the line A'-B' (Figure 34) shows the evolution of the stable precipitation band in more detail. The contours in Figure 35 represent the amount of stable precipitation in millimeters which fell through a given level within the past half hour of the times indicated. The initial generation of the precipitation occurred around 0000 GMT between 400 and 600 mb and over a relatively broad area. The width of the precipitation area became smaller between 0000 and 0130 GMT as precipitation rates increased and water reached the surface. The band did not move until after 0130 GMT. Since each tic mark on the abscissa represents 35 km, the speed of the band can be estimated to be about 18 m sec^{-1} and its width less than 200 km.

Similar cross-sections for convective precipitation {not shown) reveals that at 0000 GMT significant convective precipitation had already formed just to the rear (left, upwind) of the weaker stable precipitation. It may be speculated that moistening of the large scale environment from detrainment of vapor and cloud water in the convective parameterizaton may be responsible in part for initiating the stable

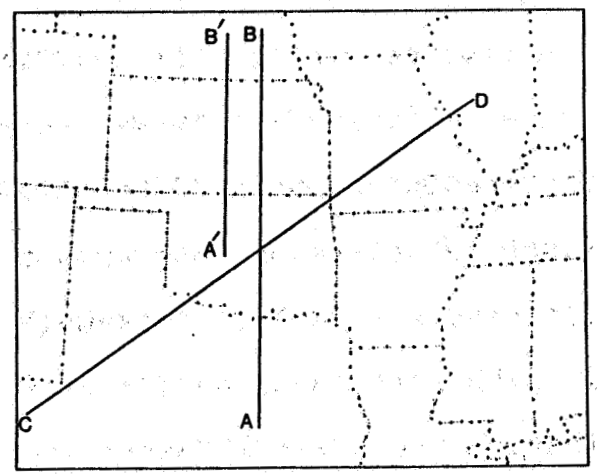

Figure *34:* Locations of vertical cross-sections used in this study.

precipitation in the mid-troposhpere. The overhanging stable precipitation extending downwind at the upper levels from the major precipitation area resulted most likely from lifting and condensation of moisture advected adiabatically along inclined isentropic surfaces. A convective component of the total precipitation as observed to propagate northward with the stable band, and was found to its rear, but produced relatively small accumulations.

The basic kinematic features of the short wave system are presented. The direct correspondence of the 700 mb short wave trough axis with mesoscale bands of

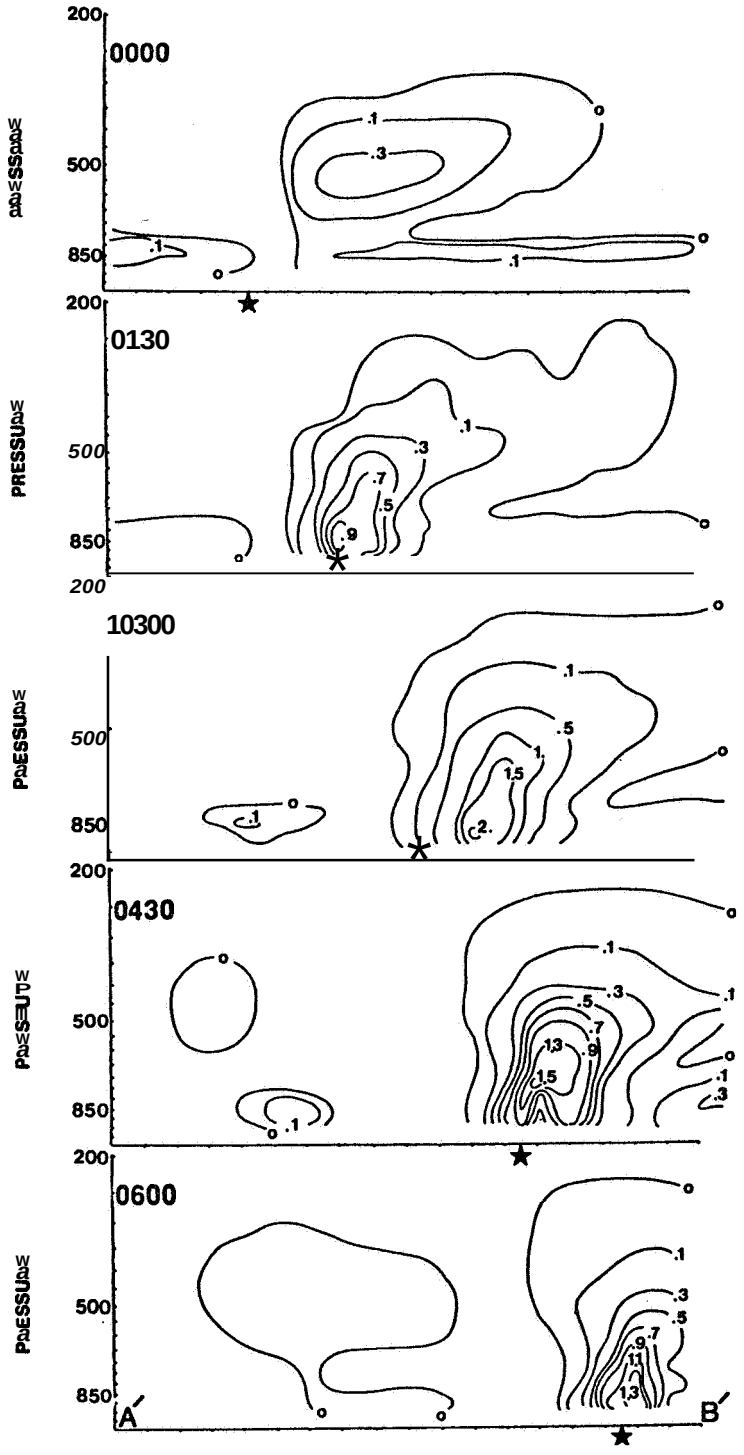

Figure 35: Time series of vertical cross-sections (A'- B') for half-hourly stable precipitaion accumulations (mm). Vertical velocity maximum *in* the short wave is shown by ★.

convergence, upward motion and cyclonic relative vorticity is seen in Figure 36. A time series of vertical cross-sections of vertical motion and divergence along the line A-B (see Figure 37) helps to highlight the three dimensional structure. The first manifestation of the short wave appeared at 0000 GMT as a narrow band of vertical velocity at the 650 km distance (★) with a maximum positive value of 16 cm sec^{-1} near 500 mb. This zone propagated northward as seen in the sequence of diagrams. As it did so, the width constricted and vertical velocity maxima exceeded 35 cm sec^{-1} from 0100 through 0300 GMT before the short wave system began to decay.

The vertical motion is supported by a well developed divergence pattern that consists of a vertical narrow convergence band which precedes the short wave and a divergence band which follows it. The two bands are parallel to one another and tilt downwind with height over a distance of 300 km. The tilt gives low level convergence overlain by divergence at the short wave through. The entire system which extends to the tropopause near 10 km is shown Schematically in Figure 38.

The destabilizing effect of diabatic heating is

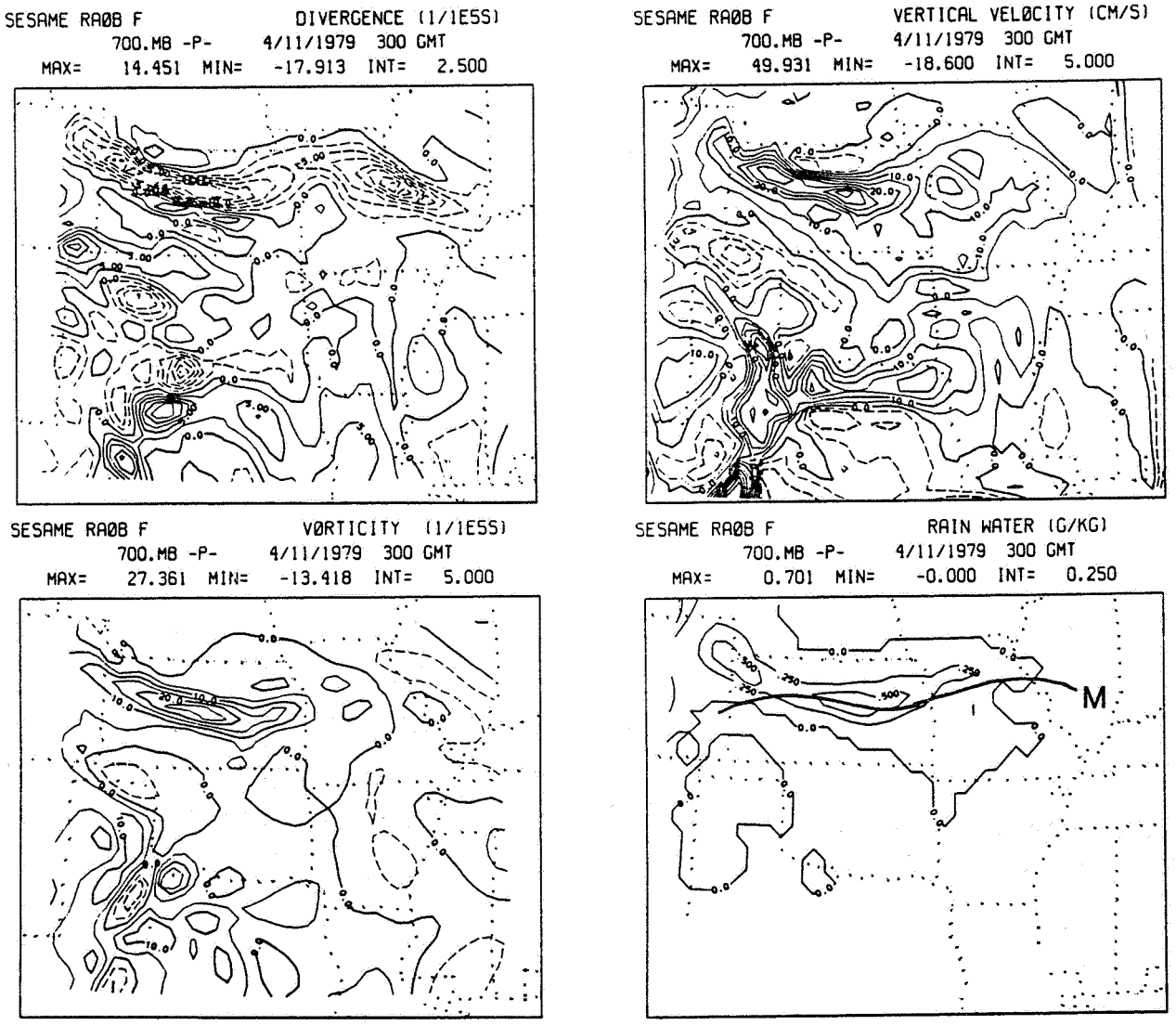

Figure 36: Maps showing correspondence of convergence, upward motion, cyclonic relative vorticity and rain water with the 700 mb main short wave trough axis. Units and times are given.

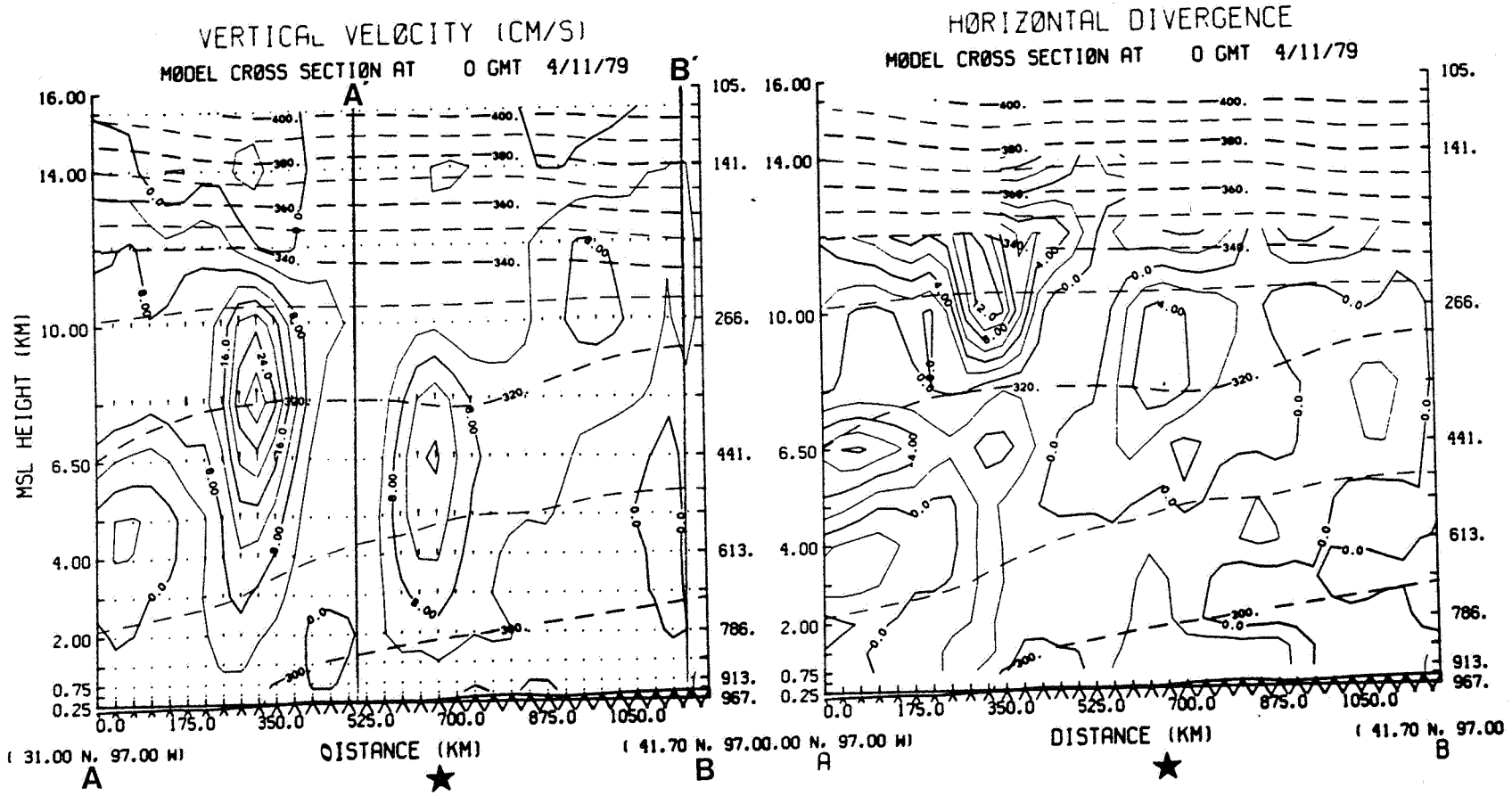

Figure 37: Vertical cross-sections A-B for vertical velocity and divergence at two hour intervals from 0000 to 0600 GMT. Units are shown above each panel. The location of cross-section A' - B' is shown on the first diagram. Dashed lines are isentropic surfaces (°K). The vertical velocity maximum associated with the short wave is indicated by a star (★) on the horizontal axis.

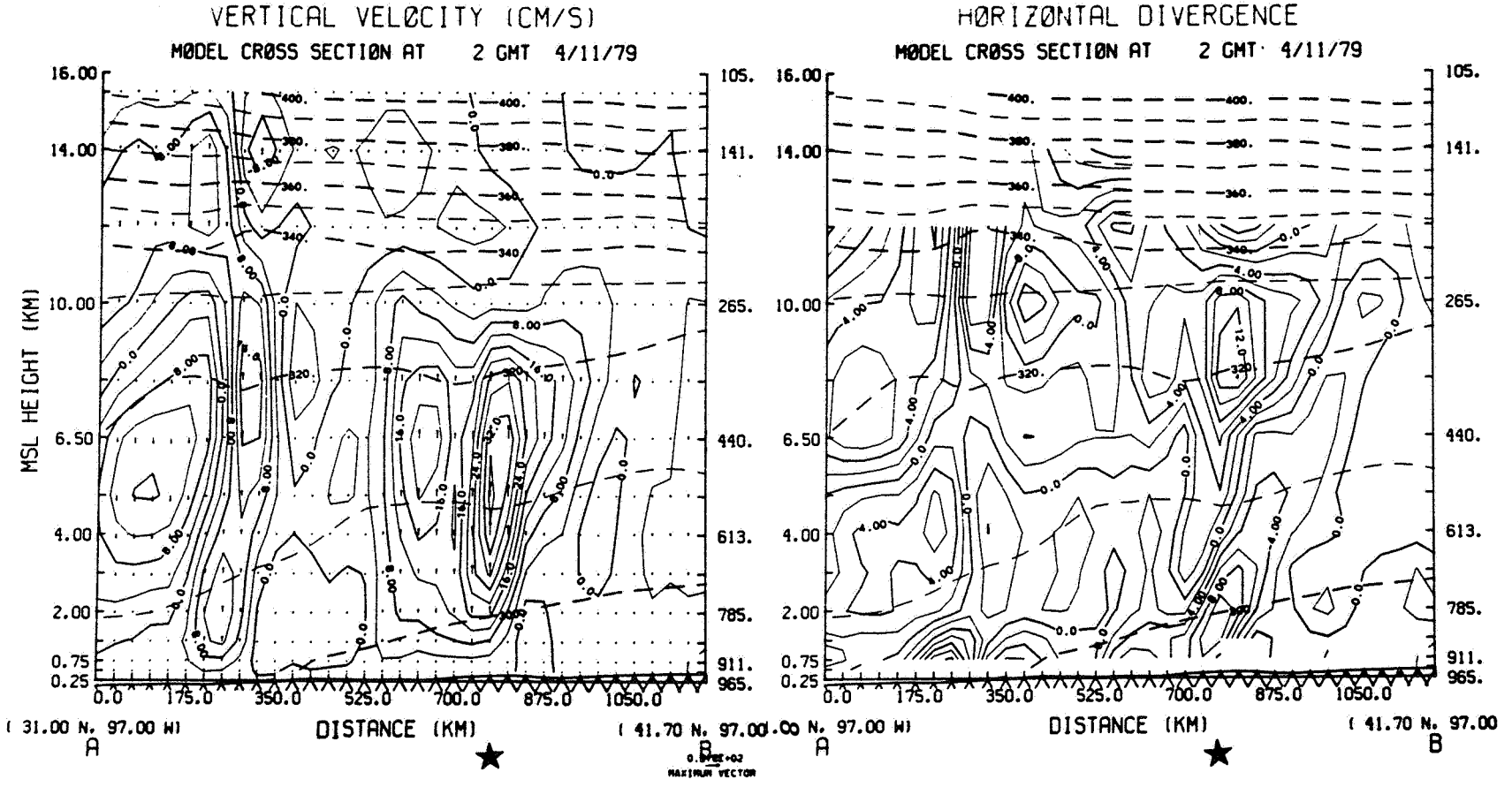

Figure 37: (continued)

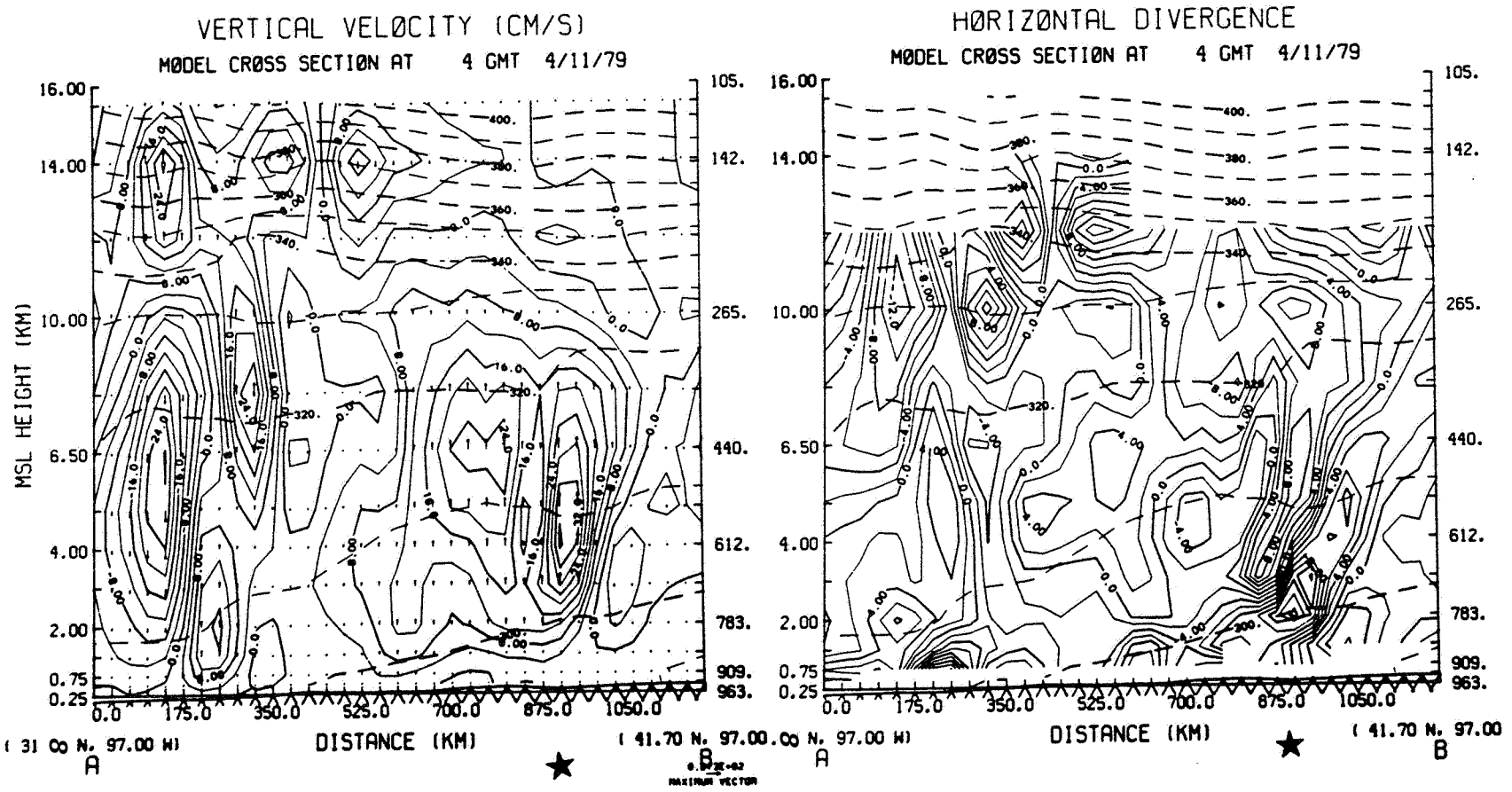

Figure 37: (continued)

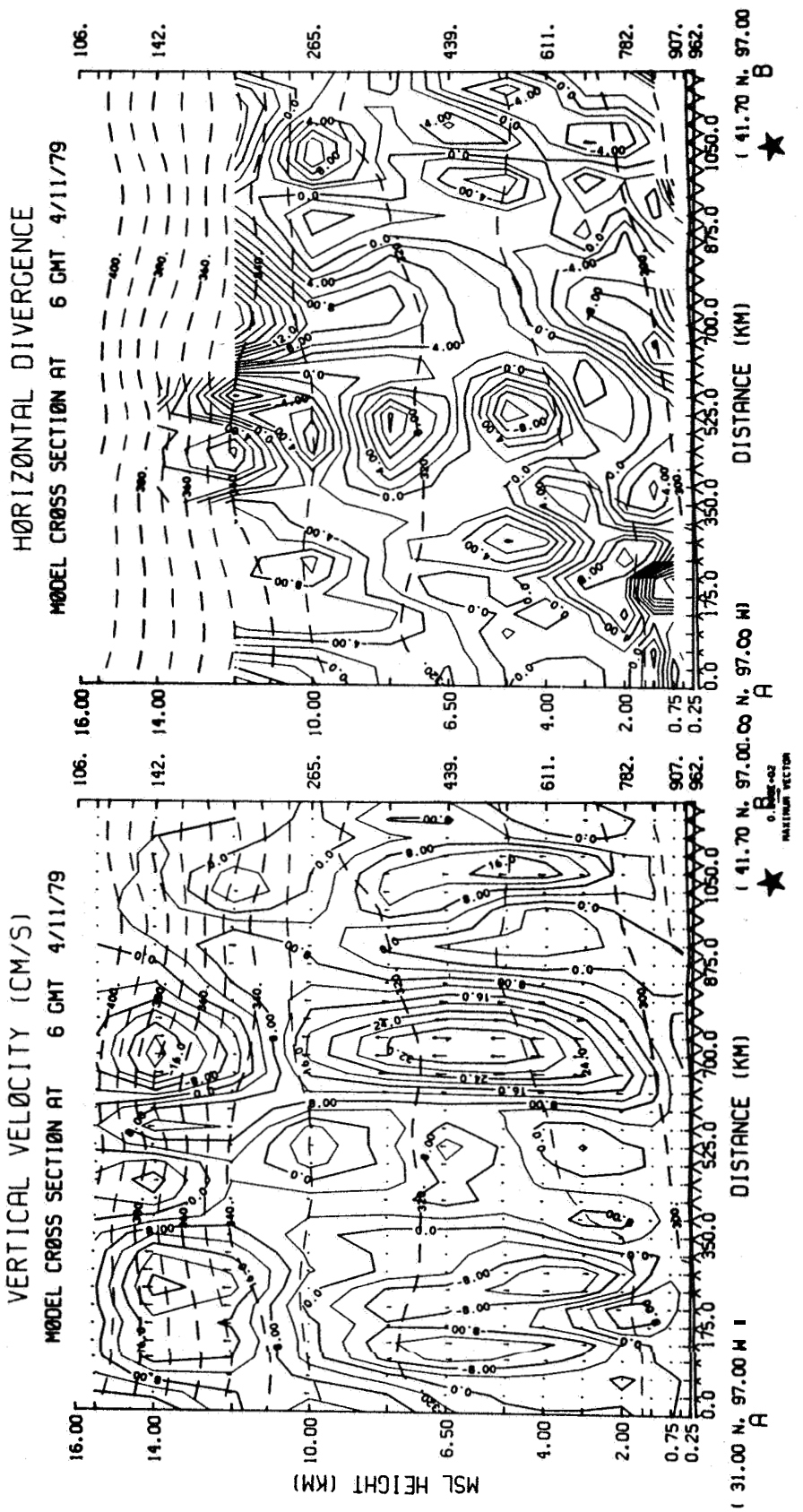

Figure 3T: (continued)

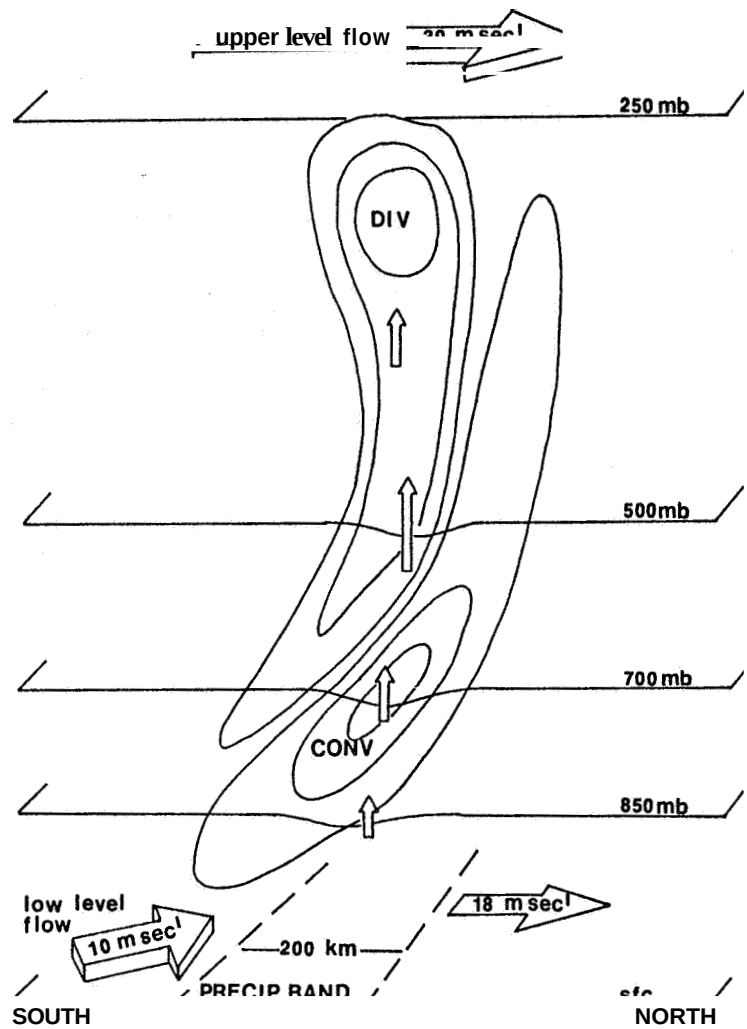

Figure 38: Schematic showing basic structure of the model short wave system of experiment F.

seen in the cross-section at 0400 GMT where the 310° K isentropic surface dips downward at the vertical velocity maximum. Upward motion above the rain level

resulted in adiabatic cooling, forcing the 320° K surface upward directly over the short wave. At the peak intensity of the short wave system, the maximum rain water (as depicted in Figure 36) is found between 700 and 500 mb.

The location of the vertical velocity maximum is marked with a star (★) in Figure 35 and is observed to move northward with a nearly constant speed. The stable rain area was stationary until 0130 GMT when the short wave (vertical velocity maximum) approached it and organized it into a narrow band. Precipitation processes may have also played a role in constricting the width of the short wave.

Examination of the SESAME radiosonde data reveals the existence of an observed 700 mb short wave trough which propagated northward with time (see Appendix B, Figure B2) and was associated with a mesoscale precipation band just as in the radiosonde model forecast F. The observed short wave appeared to be stationary from 2100 to 0000 GMT but showed up sharply at 0300 GMT in almost exactly the same location and with the same spatial dimensions on the numerically simulated short wave. Both the observed and modeled waves lose amplitude after 0300 GMT. It must be noted

that even with the SESAME data spacing, the short wave which is obviously less than 300 km wide, may still be poorly resolved: thus, its exact shape and location is subject to some uncertainty. In Figure 39 the observed short wave at 0300 GMT is superimposed with the surface precipitation reports for the same time to show the correlation of the observed short wave trough with an observed mesoscale precipitation band.

Hourly radar summaries in Appendix B show very clearly the northward propagation of a narrow short wave precipitation band originating in Oklahoma around 2000 GMT and ending up in Nebraska at 0600 GMT. Its position is very close to the model forecast precipitation band and short wave. Figure 40 displays isochrones of the 700 mb short wave trough axes at three hour intervals for model forecasts E and F. These are compared to lines drawn through the center of the radar precipitation band at about the same times. The positions of the radiosonde and satellite short waves are close at all times as they propagate northward at the same speed. The radar band has comparable locations and speeds of movement. The correspondence between the radar bands and SESAME 700 mb short waves should be noted from analyses presented

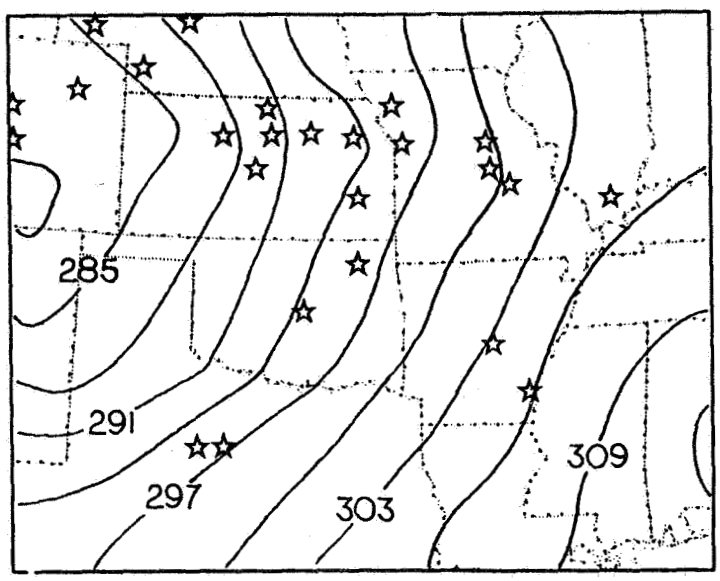

Figure 39: SESAME observed 700 mb height analysis (dekameters) at 0300 GMT April 11, 1979. Surface reports of precipitation, ☆, are superimposed to show the correlation of the observed short wave with an observed precipitation band.

in Appendix B.

At approximately 2100 GMT a squall line was observed to develop southwest of the tornado outbreak area (see radar analyses Appendix B) and increase in length by building progressively northeastward through Oklahoma as the precipitation band moved northward, Eastward translation of this squall line was only about 100 km during the following nine hours. Because of the several hours required to produce significant

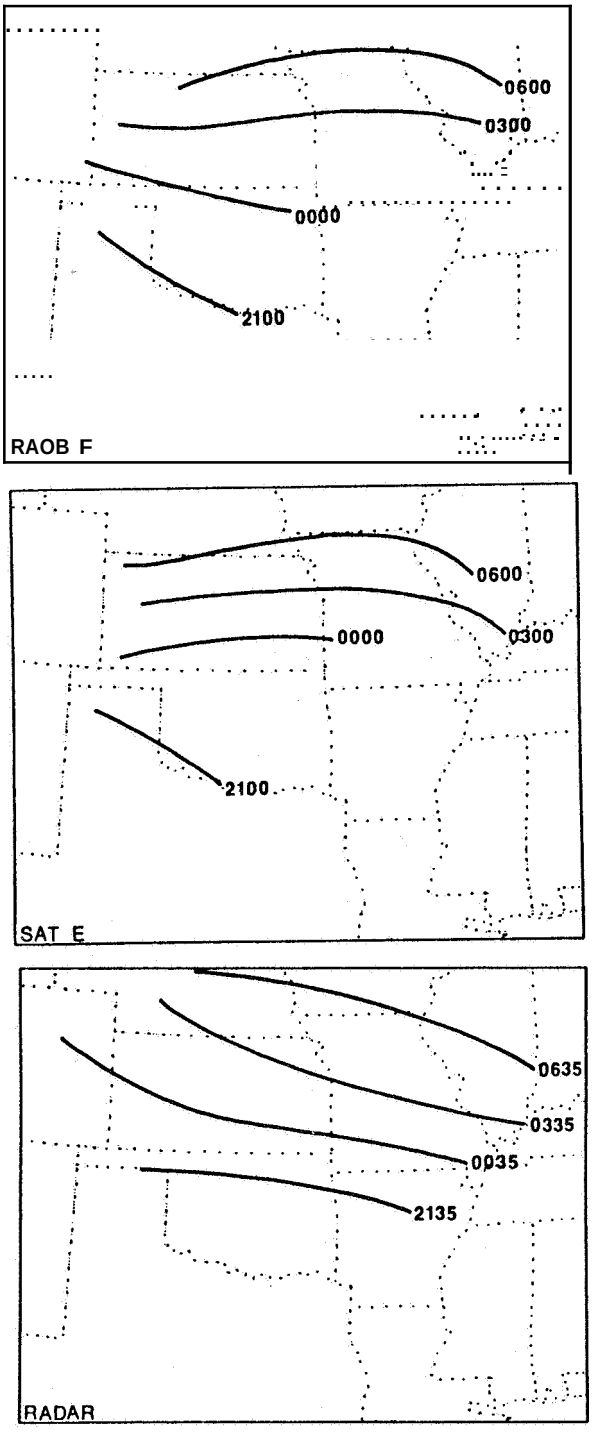

Figure *40:* Isochrones for the 700 mb short wave trough axis in cases E and F. Bottom panel shows locations of the radar precipitation band at approximately the same times.

precipitation in the model, none was forecast in the observed severe weather area until 0000 GMT (Figure 33) when in reality the heavy convection had already been in existence there for several hours. It is noteworthy that the precipitation which was forecast (case F) was almost entirely convective and was confined to a narrow band at 0130 and 0300 GMT (Figure 33) suggestive of the April 10 squall line. However, its orientation was about thirty degrees clockwise fxom that of the observed squall line. The areal expansion of the model convective precipitation associated with this band after 0300 GMT is consistent with the radar analyses after 0335 GMT.

While none of the model forecasts was able to simulate the development of the squall line Earther south in Central Texas after 0000 GMT, there is some evidence that the radiosonde initialized forecasts were tending in that direction, The 700 mb relative humidity analyses for cases F and D at 0600 GMT (Figure 41) show tongues of relatively moist air extending down into Texas very close to the observed squall line position. The relative humidities were all less than 50%, that is, saturation was never achieved in these bands. In case F the moist band was associated with

Figure 41: Forecast 700 mb relative humidity at 0600 GMT for cases F, D and J. Areas with relative humidity greater than 60% are shaded.

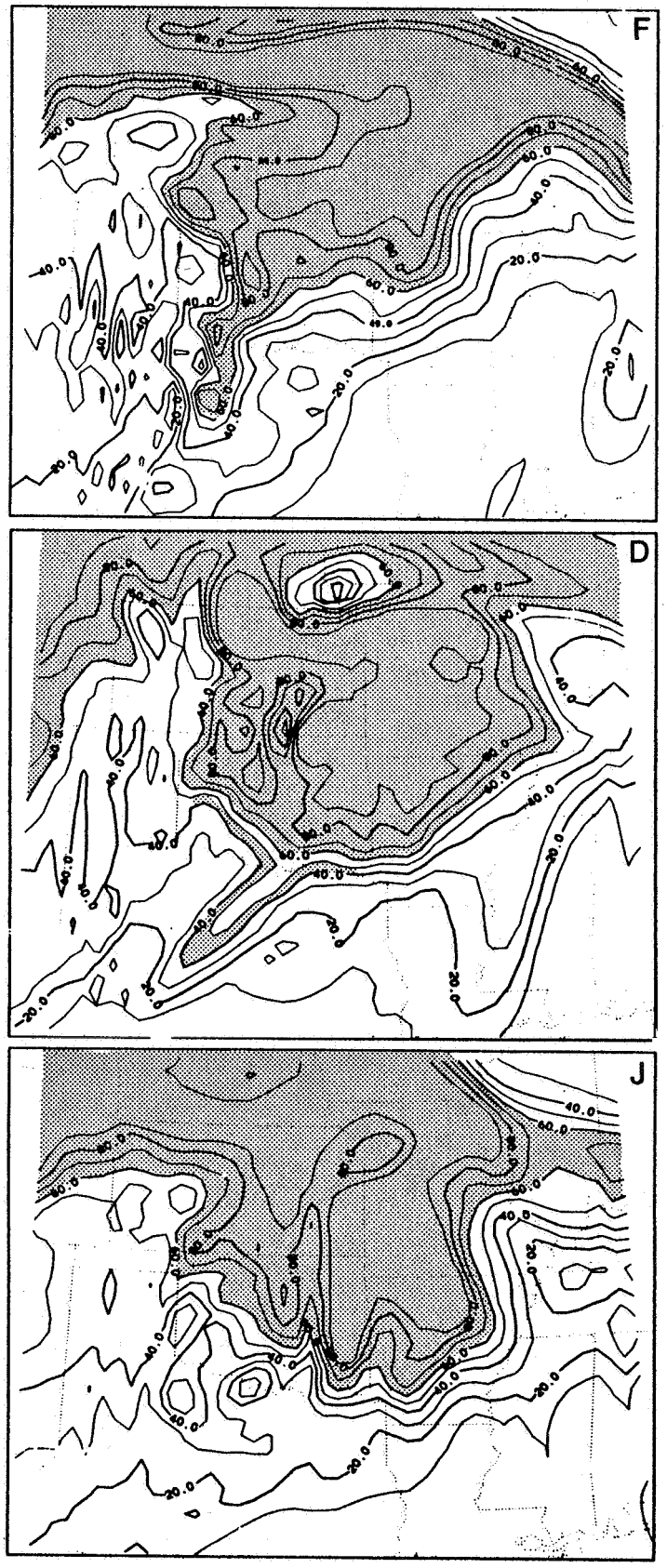
F
D
J

low level convergence along the surface dry line and resultant upward transport of the low level moisture. In terms of position, the case D moist tongue is situated best relative to the observed squall line. The satellite forecase J, which typifies all the satellite runs, shows no evidence of this moist tongue.

The evolution of precipitation for the satellite cases was very much different than for the radiosonde forecast **F.** Convective precipitation rates in cases E and J are shown in Figures **42** and **43** along with the 700 mb forecast short wave axes. These figures show that the satellite short waves had only a weak association with a convective precipitation band. Most of the precipitation in the satellite forecasts was convective. In fact the only significant stable precipitation which fell in the satellite cases occurred after 0300 GMT and was confined to a small but intense (rates $\geq$ 10 mm hr^{-1}) region in Southwestern Missouri and Northern Arkansas (see Figure **44).** The initial outbreak of convective precipitation along the Texas/Oklahoma border occurred early in the satellite forecasts, whereas no significant precipitation developed in the radiosonde forecast for the first three hours.

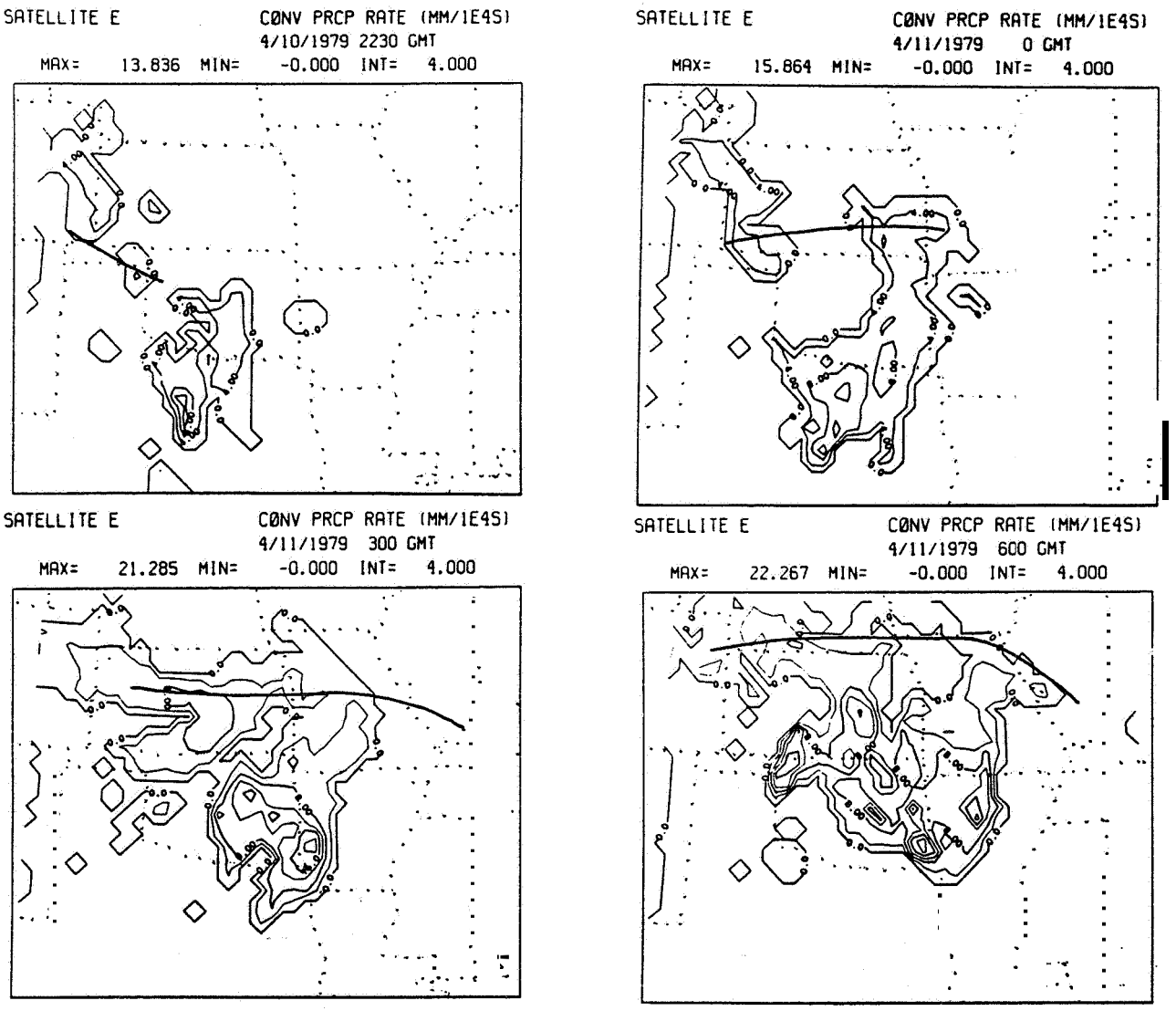

Figure 42: Convective precipitation rates for satellite case E. Locations of the 700 mb short wave trough axis is indicated. Units and times are shown above each map.

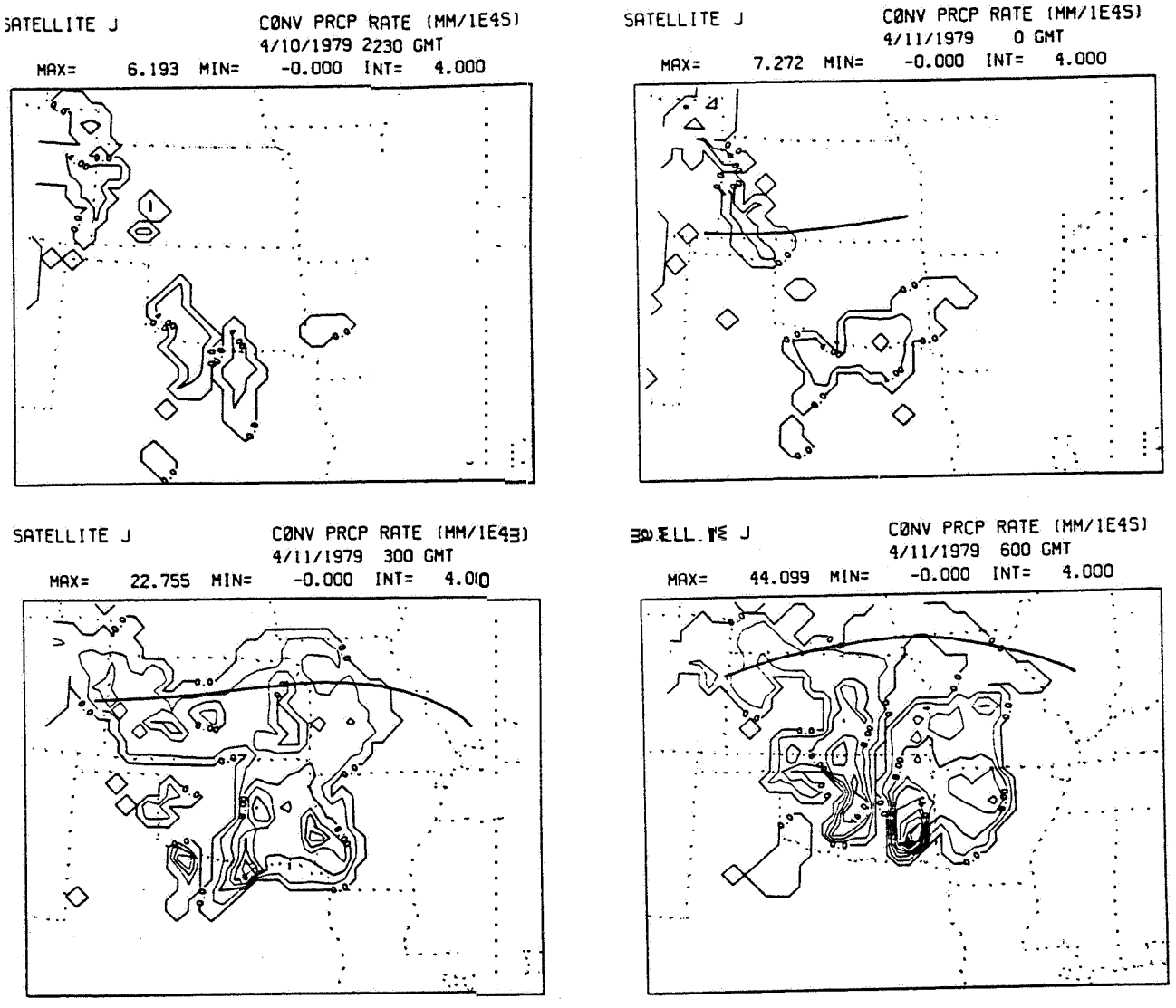

Figure 43: Same as Figure 42, except for satellite case J.

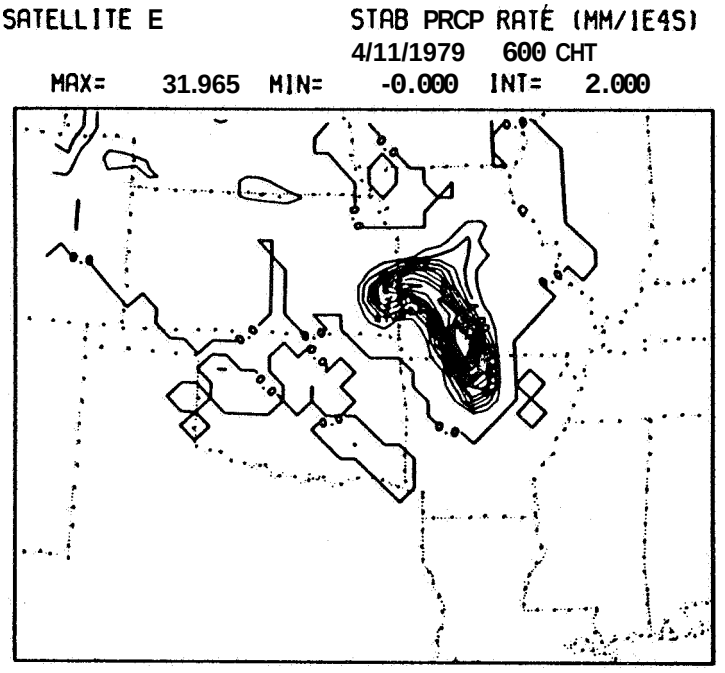

Figure 44: Stable precipitation rates at 0600 GMT for satellite case E.

All forecast precipitation rates can be compared to the observed rates computed by Vincent and Carney (1982) which have been reproduced in Appendix B. These precipitation rates, expressed in mm hr^{-1}, are averages over one degree latitude/longitude boxes and therefore do not have the resolution to accurately depict fine detail in the observed precipitation fields; however, they do show the general features. The satellite precipitation rates when converted to mm hr^{-1}

(↶ divide by 3) are comparable to the observed magnitudes. Between 0000 and 0300 GMT the satellite convective precipitation shows the same orientation as observed with a wide band running from Texas to Illinois, however the satellite band is located too far to the east.

The effect of holding the low level "observed" winds constant during the intitialization (case J, Figure 43) was to retard convective precipitation over Oklahoma, Kansas and Missouri for the first several hours (compared to case E). By 0300 GMT cases E and J were similar with both exhibiting northward movement of the weak short wave precipitation band and the southwest to northeast orientation of the "squall line" precipitation. However, in case J the latter was constricted to a narrower zone and was found farther west, and therefore closer to the observed precipitation. By 0600 GMT the convective precipitation for the satellite cases had changed its character as it moved completely out of Texas. Any banded structure it may have had earlier disappeared. The only significant difference between experiments E and J was that in J the convection had split into two separate areas over Oklahoma.

Up to this point there has been little mention of

cases D, G and K. Radiosonde case D is discussed in detail later because it had some exceptional features which merit a separate examination. Precipitation fields in cases E and G were very similar, especially in the convective mode, which suggests that only a minor impact resulted from static initialization with balanced rather than observed low level winds. Since the short wave features in E and G were also very similar, experiment G did not merit a special or detailed analysis.

Model forecast K was only run for three hours when differences between J and K in the mass and precipitation fields were found to be trival. It was felt that the expenditure of the substantial computer time required to complete the forecast was not justified. Because the influence of the observed winds in case K dies off rapidly with height, but slowly in time for the lowest level winds, it is only the winds below 750 meters which have a signficant weight assigned to them over the entire initialization period (recall Figure 21). Thus the similarity of cases J and K indicates that it is primarily the lowest level winds which held the impact potential for the pressure and precipitation forecasts.

6.2.2 Domain Accumulations

Attention is now turned to the total accumulated precipitation at the end of the model forecasts. Because little precipitation accumulated in the model prior to 0000 GMT (except for case D which had a three hour lead on other experiments), it is fair to compare the total model accumulations (Figure 45) to the observed surface accumulated precipitation from 0000 to 0600 GMT (Figure 46).

Major features in the observed field are also found in the satellite forecasts including the convective precipitation band associated with the squall line which ran diagonally through Oklahoma. The maximum accumulations over Oklahoma are most consistent with the satellite forecast J which has values from 30 to 40 mm within a narrow band. The diagonal band in cases in cases E and G is too broad, and even in case J it is found too far East. A second verifiable feature is the wide area of precipitation covering Kansas, Nebraska, Wyoming and Colorado. It must be noted that most of the satellite case precipitation which fell in this region was in the convective mode, whereas the surface observations showed mostly steady type rain. Never-the-less, the total accumulations were similar to

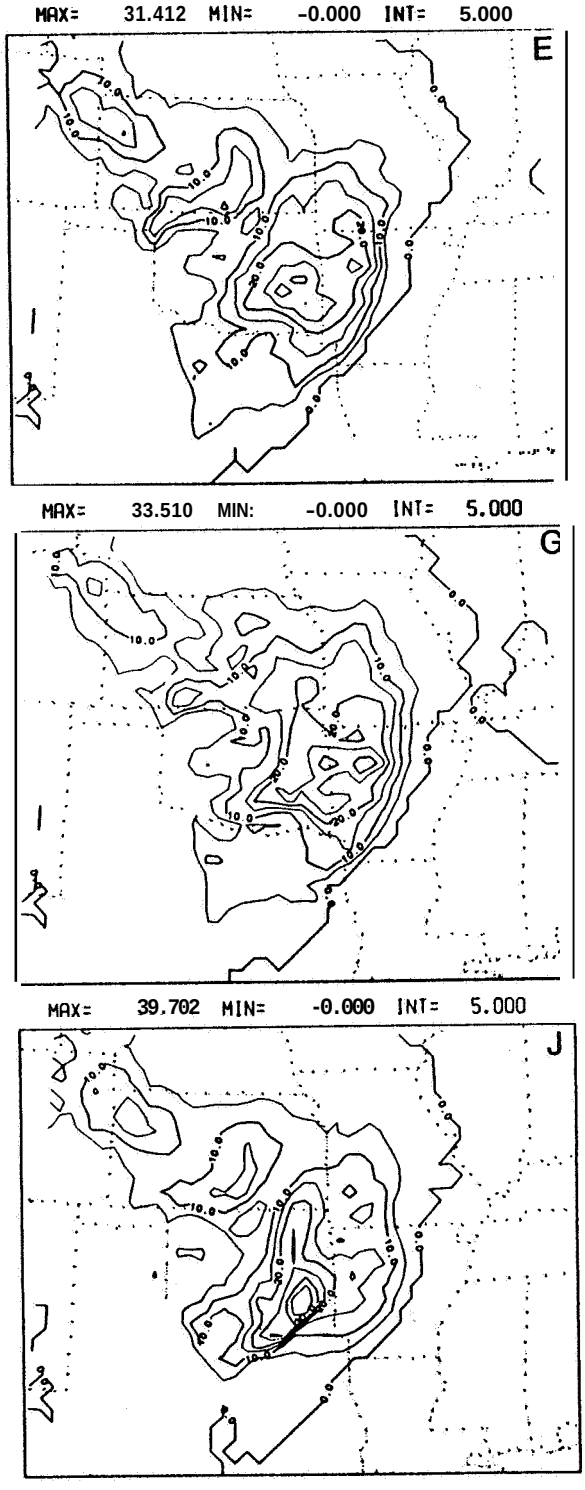

Figure 45: Total forecast precipitation accumulations (mm) for the model cases indicated in the upper right hand corner of each map.

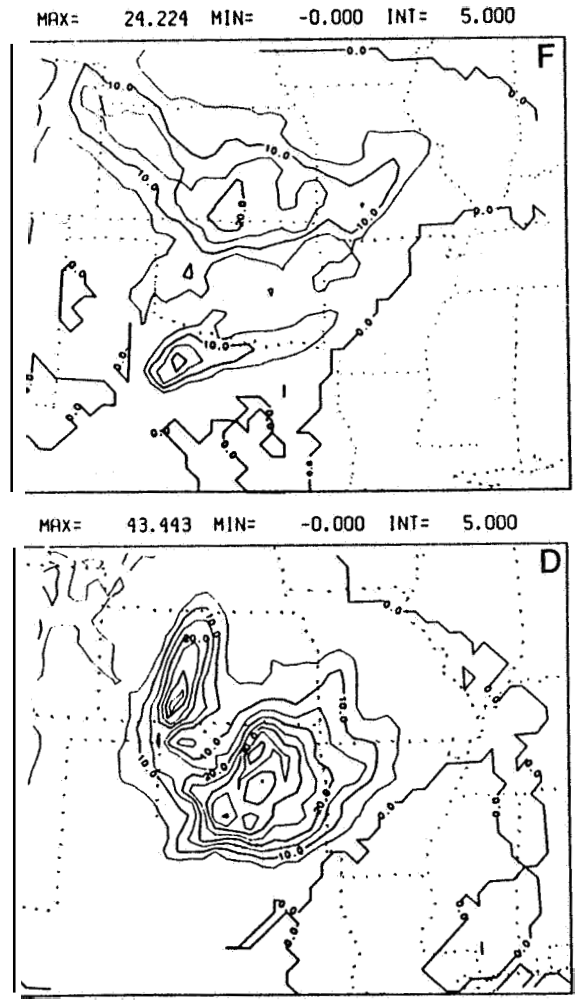

Figure *45:* **(continued)**

those observed (0.1 to 10 mm with pockets of up to 20 mm).

Intercomparisons of the satellite forecasts shows the impact of including low level observed winds. The

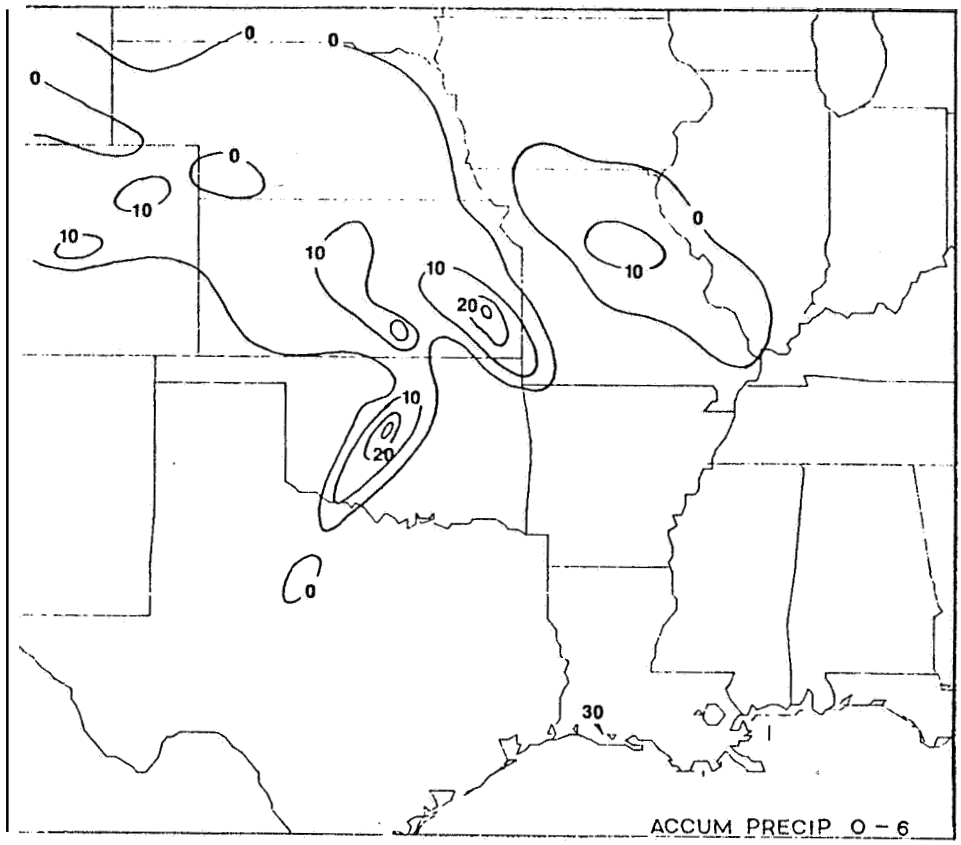

Figure *46:* Observed surface accumulated precipitation (mm) for the period 0000 - 0600 GMT April 11.

differences between cases with static initialization using real low level winds (E) and using balanced low level winds (G) are small. Continous insertion of the wind data (J), however, had the long term effect of confining the precipitation over Oklahoma to a narrower and more intense band.

The total precipitation accumulations for radiosonde case F are different from those in the satellite forecasts with most being accounted for by the combined stable and convective modes associated with the propagating short wave. The short wave precipitation band is also reflected in the observed accumulations. The only other significant precipitation in case F occurred along the Texas/Oklahoma border in the convective mode.

The twelve hour radiosonde forecast (D, 1800-0600 GMT) accumulation patterns resemble those of satellite case E the most, with precipitation found mainly in two areas. The largest one, over Oklahoma, is well situated with respect to observations but shows only a weak orientation from southwest to northeast. Most of the precipitation in this broad area was convective. Even though there was a low level short wave similar to that in case F, it was not accompanied by large precipitation amounts.

The total accumulated precipitation for the entire domain as a function of time is summarized for each case in Table 1. The numbers in the table are computed as $\sum_{i=1}^{N} (\overline{accum}_i \times NGP_i)$, where the expression in parentheses is the total number of grid points with

TOTAL PRECIPITATION

	18:00	21:00	22:00	00:00	03:00	06:00	
Forecast E	-	0	414	1246	3381	6220	(convective)
	-	0	0	74	371	1149	(stable)
	-	0	414	1328	3693	7230	(total)
Forecast P	-	0	133	494	2218	4761	
	-	0	0	55	523	1126	
	-	0	133	542	2618	5678	
Forecast G	-	0	384	1199	3422	6725	
	-	0	0	41	167	775	
	-	0	384	1240	3496	1335	
Poreeaet J	-	0	416	815	2624	5685	
	-	0	0	59	258	961	
	-	0	416	886	2816	6562	
Forecast D	0	558	749	1453	3472	6265	
	0	53	93	248	666	1360	
	0	605	836	1656	4025	7389	

Table 1: Whole domain precipitation accumulations as a function of time for each model forecast. Numbers represent the summation of accumulated precipitation (mm) over all model grid points.

accumulations falling within an interval, i, multiplied by the average accumulation for that interval. The summation is over N=12 intervals, each 5 mm wide (0.1-5, 6 - 10, . . . 40 - 45, 46 - 50, and 51+ mm). This quantity, which is proportional to the total amount of water reaching the surface, is computed for stable, convective and total precipitation.

The amount of precipitation depended heavily on the initial data (satellite versus radiosonde) and the

method of handling the low level winds. Despite having the same initial surface winds, surface pressure, and moisture analyses, the radiosonde case F generated 21% less total precipitation than satellite case E (5678 compared to 7230). Most of this difference accrued in the convective mode. Because of initially different relative humidities, after the first hour the radiosonde case had produced only about 30% as much precipitation as the satellite (E). For the remainder of the radiosonde forecast, basic differences in model evolution related to wind and temperature in the initial states resulted in lower precipitation accumulations at all times.

Differences in precipitation accumulations between satellite cases during the first hour were related to the low level convergence. After one hour cases J and E (same initial winds) had the same acculumations (415), but case G which had a very small initial low level convergence produced only 384 units (mm). The large low level convergences which developed after 2200 GMT in cases G and E resulted in greater moisture convergence and upward motion than in case J, so that by 0000 GMT the total rainfall amount for J (with a constant but relatively weak low level convergence

field) was 29% less than for case E. By the end of the forecast, the effect of holding the low level winds constant during the initialization was to reduce total precipitation by 9%. The impact of initializing statically with balanced low level winds (G vs. E) was to only slightly increase the convective precipitation, but to reduce the grid scale precipitation by half. Case G had the lowest accumulated stable precipitation at all times.

The accumulated precipitation amounts for the first three hours of radiosonde case D are most similar to those in the first three hours of case F. Despite the fact that case D had a three hour lead on the Block II experiments, its total accumulation ended up only slightly larger than in any other forecast.

6.2.3 Case D Convective Complex

Discussion of experiment D has been postponed until now in order to give it special consideration. Although this case did not give the best precipitation forecast, it did produce a convective precipitation area associated with temperature and wind patterns which resemble those found in a mesoscale convective complex (MCC). The satellite forecast precipitation area had similar features, but the adherence to the strict definition of an MCC was not as good. A brief summary of the MCC phenomenon is provided.

Mesoscale convective complexes have only been recently recognized, mainly through satellite observations, as a distinct self-sustaining meso-α convective precipitation system found frequently in the Central United States in the spring and summer months (Maddox, 1980). Such a system is characterized by mean mesoscale ascent over areas as large as several hundred thousand square kilometers in response to the statistical sum effects of the convective thunderstorms which comprise it. The vertical circulation is driven by mid-level latent heating, and results in mean low and mid-level convergence and a cold anticyclonic outflow at the convective cloud tops near 200 mb. The

aggregate of all thunderstorms anvils forms a large, thick cirrus cloud shield which provides the means for defining and detecting the presence of an MCC from a geostationary satellite.

The first and essential criterion for defining an MCC (Maddox, 1980) is that the area encompassed by specific cloud top IR blackbody isotherms be greater than 100,000 km^2 for -32 ° C or greater than **50,000** km^2 for -52° C. Their shape must be nearly circular in order to avoid misclassification of squall lines as MCCs. The minimum duration is six hours; however, since they may last as long as twenty-four hours with little reduction in the intensity of the precipitation associated with them, MCCs may be partially responsible for the nocturnal maximum which characterizes convective precipitation in the great Plains and Midwest U.S. during the summer months.

The generation of MCCs has not been linked to a specific synoptic scale forcing, and the existence of a mesoscale (a or β) forcing is unproven. However, the presence of an MCC does influence the synoptic scale by perturbing the large scale wind and temperature fields. The specific features of a mature MCC which cause this include a positive temperature anomaly at

middle levels (500 to 300 mb) and a cold temperature anomaly at the convective cloud tops near 200 mb. The cold temperature anomaly is associated with a high pressure dome which induces an upper level divergent outflow that in turn also acquires anticyclonic vorticity in repsonse to coriolis acceleration. The positive pressure anomaly at the convective tops changes the local pressure gradients and may result in increased wind speeds, especially on the north side of an MCC imbedded in a westerly flow. All of the above phenomena have been observed by Fritsch and Maddox (1981) and to some extent have been generated in numerical simulations by Fritsch and Brown (1982) and Chang, et al., (1982).

These same features were also forecast in experiment D in association with the large convective precipitation area over Oklahoma. A set of figures (Figure 47) on the next three pages shows the close connection of an intensifying and growing convection area with perturbations in the temperature and wind fields. At 500 mb the temperature anomaly produced by the convection is less than +4.0 degrees celsius but is seen to expand in area as the precipitation area enlarges. At 300 mb the maximum positive temperature

Figure 47: Sequence of maps showing the evolution of a convective precipitation system whose temperature and wind structure resembles that of a mesoscale convective complex (MCC). Units and times are given above each panel.

SESAME CØNTRØL D CBNV PRCP RRTE (MM/1E4S)
4/11/1979 0 GMT
MAX= 18.957 MIN= -0.000 INT= **4.000**

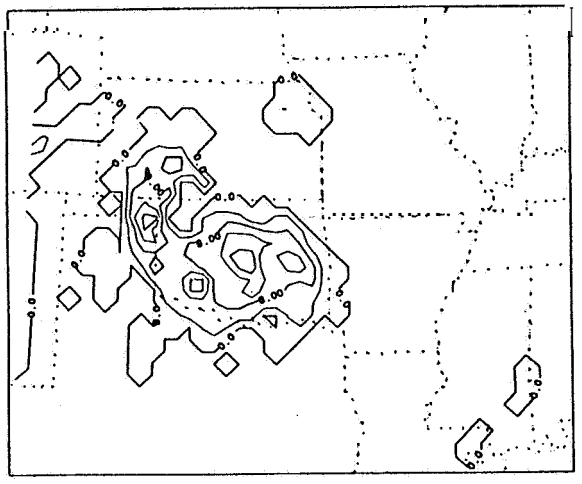

SESRME CBNTRBL D TEMPERATURE (DEC C)
500.MB -P- 4/11/1979 0 CMT
MAX= -9.987 MIN= -22.792 INT= 2.500

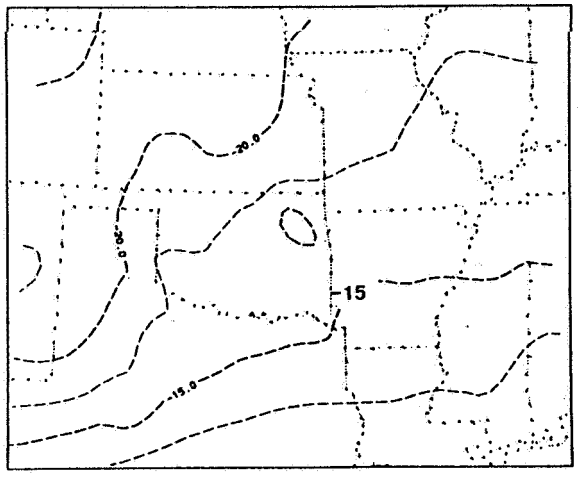

4/11/1979 300 GMT
MAX= 34.484 MIN= -0.000 INT= **4.000**

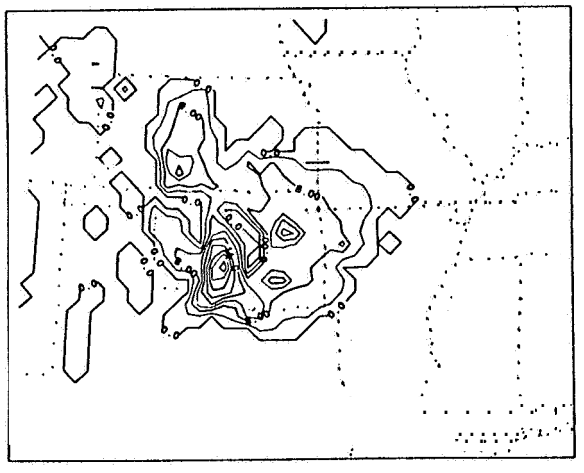

500.MB -P- 4/11/1979 300 GMT
MAX= -9.267 MIN= -23.467 INT= 2.500

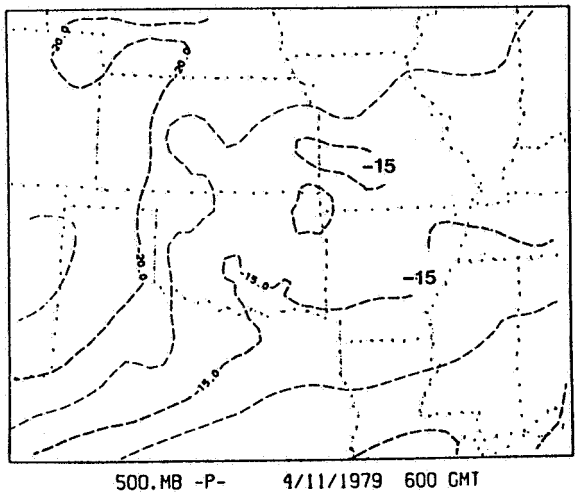

4/11/1979 600 GMT
MAX= 28.605 MIN= -0.000 INT= 4.000

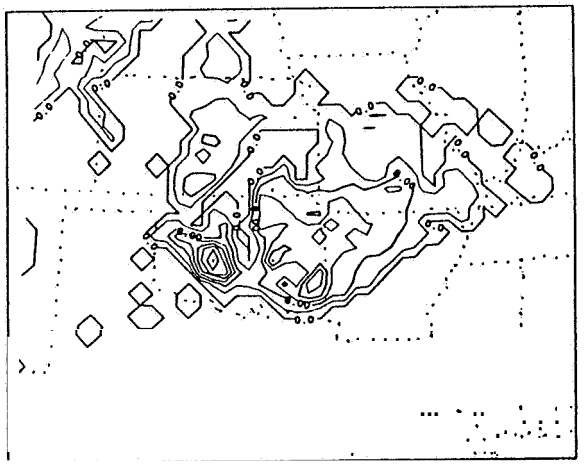

500.MB -P- 4/11/1979 600 GMT
MAX= -8.516 MIN= -24.213 INT= 2.500

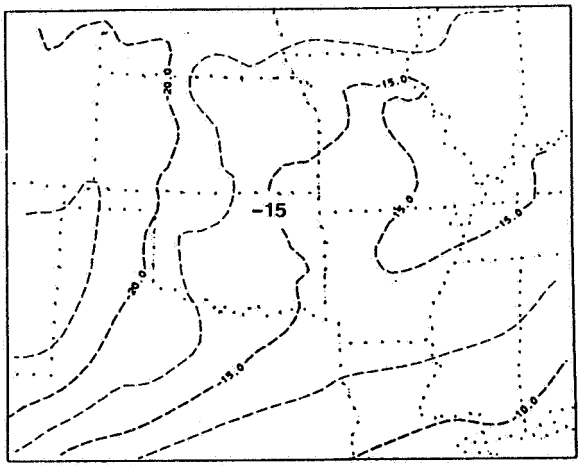

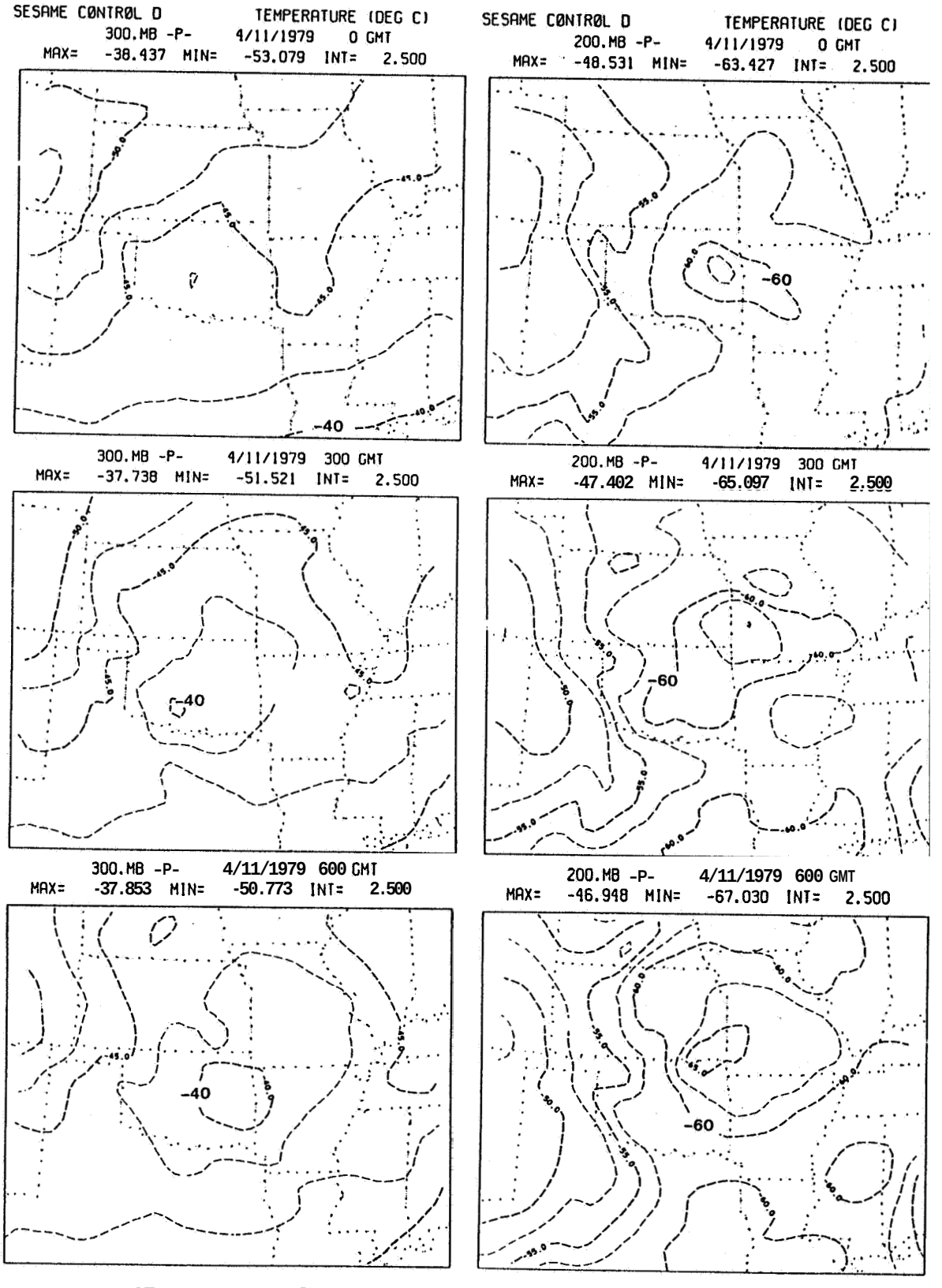

Figure *47:* (continued)

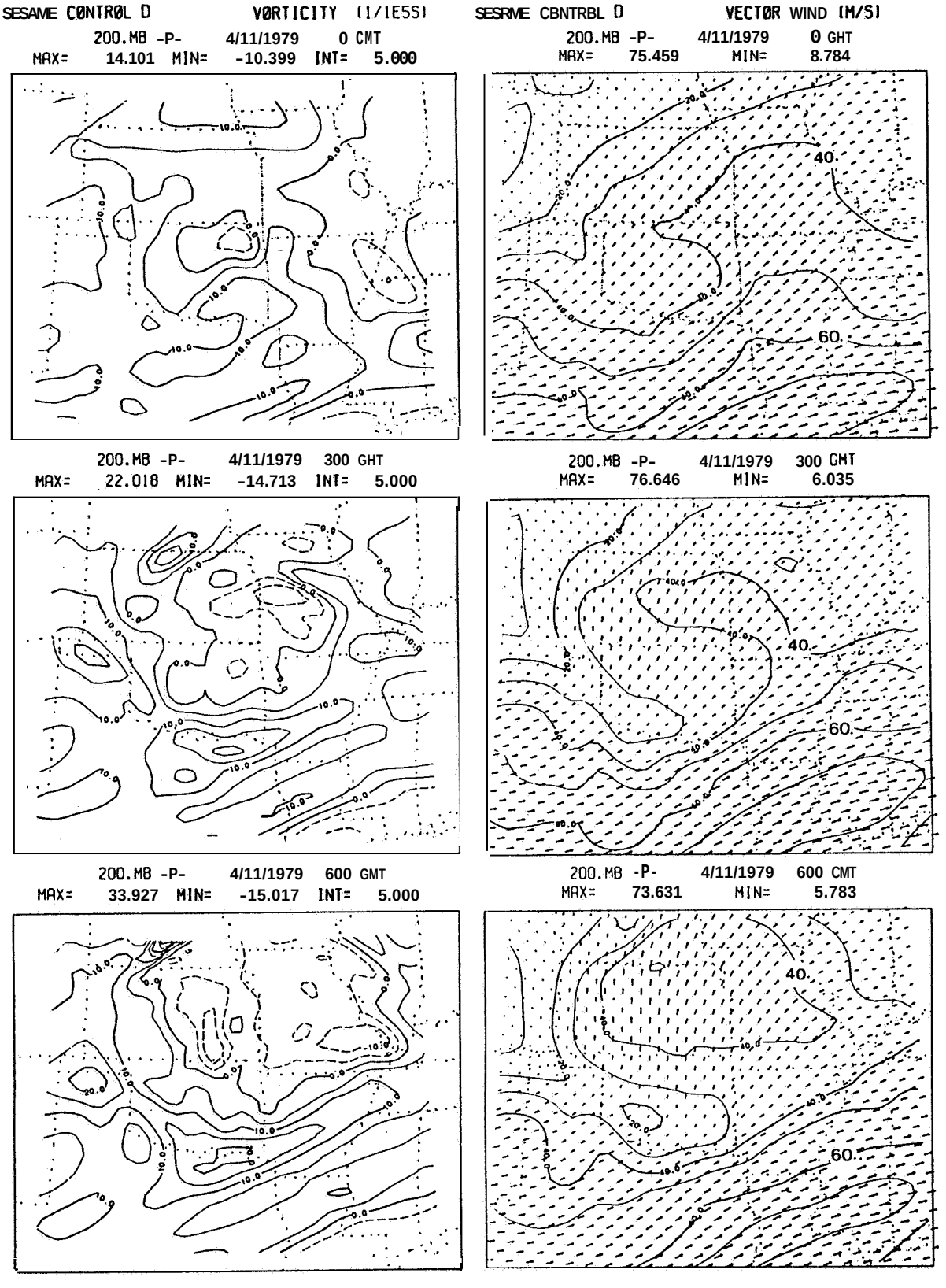

Figure *47:* (continued)

anomalies are found lying directly over the convective area, while at 200 mb the temperature perturbations are negative as observed in an MCC.

The flow at 200 mb becomes divergent and the relative vorticity maps show the anticyclonic rotation of the outflow generated from the precipitation region. The wind vectors and isotachs show the perturbed flow and enhancement of wind speeds by as much as 10 m sec^{-1} over an area just to the north and west of the negative temperature anomaly at 0600 GMT.

While the system is not examined in detail in this thesis, it is suggested that because its structure is very similar to that of an MCC, diagnostic studies on the model uutput for this case should be performed in hope of gaining insight into the generation and evolution of observed convective complexes.

6.3 Wind and Moisture

6.3.1 Boundary Layer Winds and Moisture

This section of the study examines major aspects of the evolution of low level wind fields with emphasis on their impact on the low level moisture. A significant finding concerning model initialization with "observed" low level winds is that generally much of the potential impact on the forecasts is tempered by the model's ability to rapidly develop low level flow patterns similar to those observed. It is also found that the lowest level wind speeds evolve mainly in response to the pressure field.

Evidence for these statements is seen in Figure 48 which compares initial and three hour forecast surface stream lines and isotachs for case E (statically initialized observed surface winds) and case G (balanced surface winds). At the initial time speeds and directions are very different with speeds for E typically 5 m sec^{-1} and those for G as high as 20 m sec^{-1} in the center of the domain. After three hours, experiment G developes the confluence (and as will be seen, convergence) zone in the West. While the speeds are reduced by about a factor of two, the isotach pattern is similar to that at the initial time with a

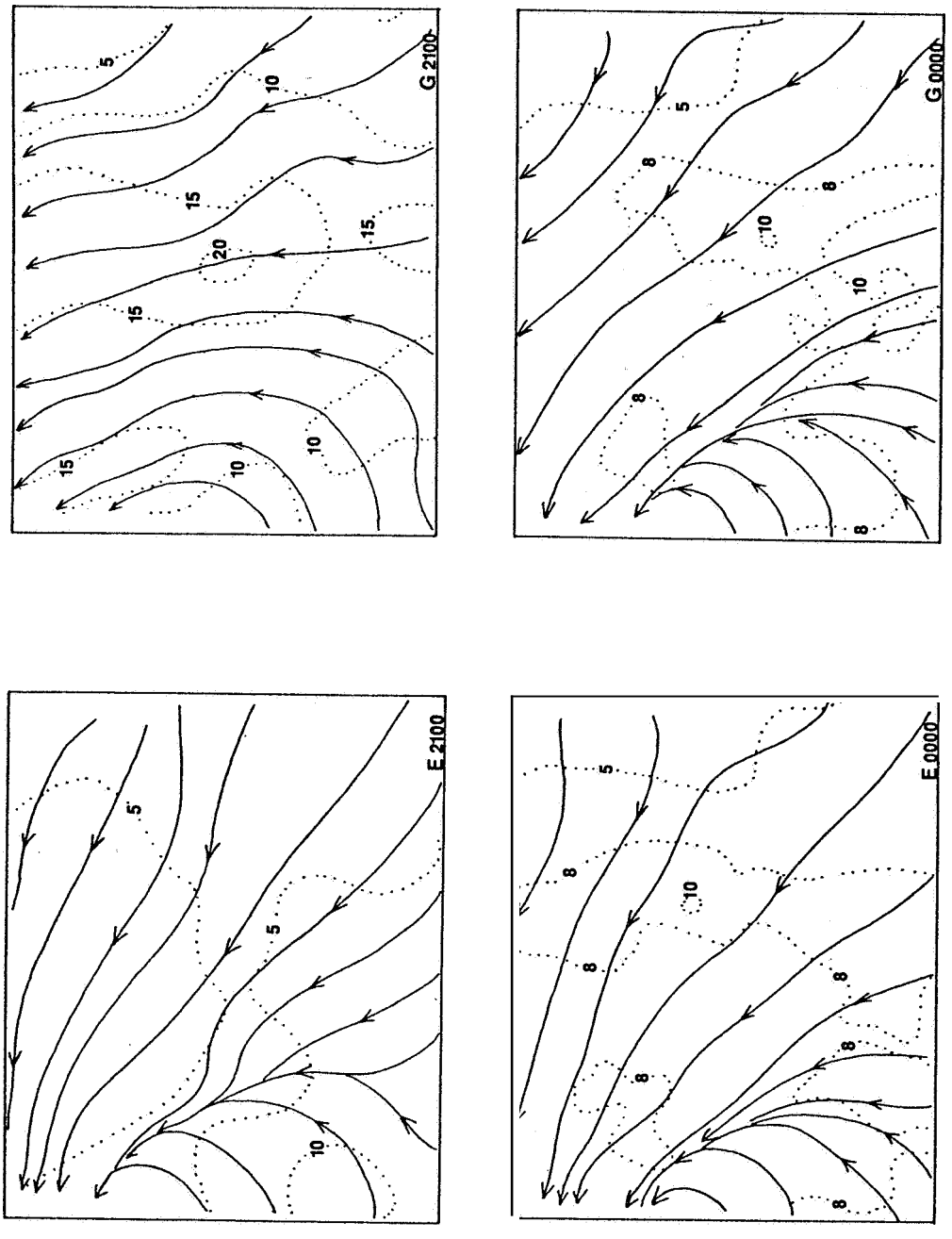

Figure 48: Streamlines and isotachs (m sec^{-1}, dashed) at initial time and at 0000 GMT for cases E and G. Times and cases are indicated in the lower right corner of each panel.

band of relatively fast winds running north-south through the center of the domain, For case E the confluent streamlines are found in the same location but resemble those in G. Likewise, a band of large speeds developed in the center of the domain in response to the pressure field.

The surface divergence patterns for these same cases are shown in Figure 49 for 2100 and 2230 GMT. The initial divergence in case E lines up well with surface frontal positions (see Appendix B) while that for case G is small and unorganized. The divergence in case G results from the vertical interpolation of the balanced winds to the model terrain and from the wind adjustment program. After the one and a half hour initialization period both runs produced a narrower and more intense convergence zone oriented north to south through Central Texas. The great similarity between the two forecasts indicates that the resultant low level wind field has little or nothing to do with the winds inserted there initially.

The convergence band is not confined only to the lowest layers, The same can be seen at 850 mb with slightly stronger convergence (Figure 50). It is also associated with vertical motions up to 500 mb, Figure

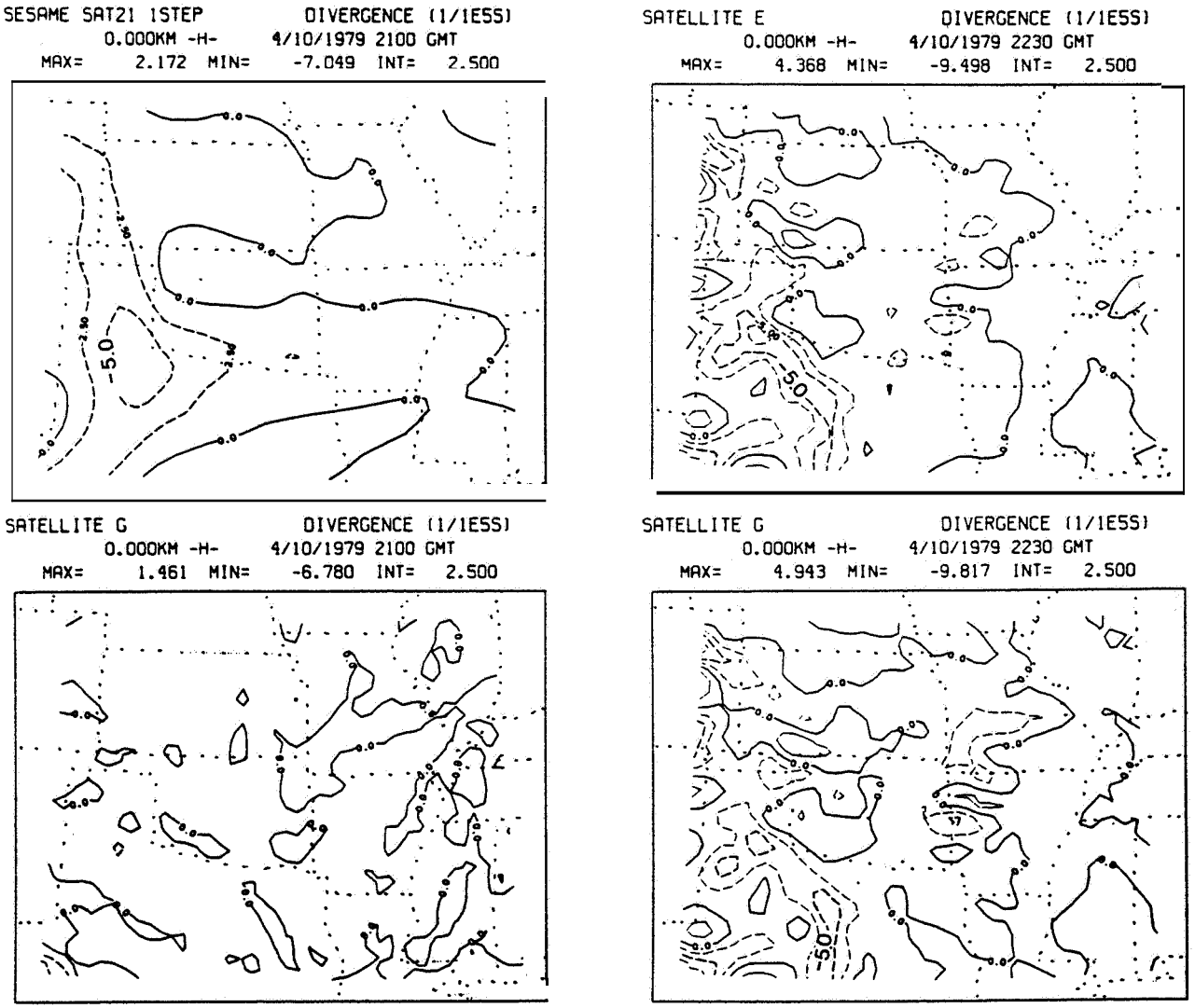

Figure 49: Surface divergence for satellite cases E and G initially and after the 1-1/2 hour initialization period. Units and times are shown above each map.

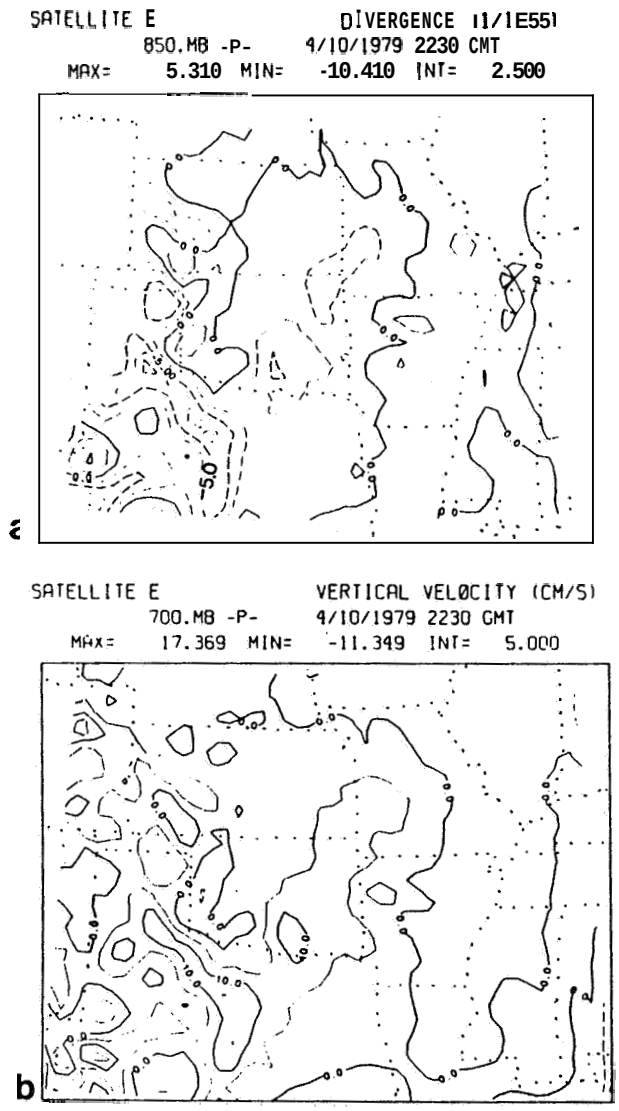

Figure 50: Maps showing correspondence of upper level convergence (a) and upward motion (b) with the low level convergence band. Units and times are indicated.

50b shows 700 mb vertical velocities as great as 10 cm sec^{-1} in this band. The convergence band is a persistent feature of all model forecasts and has a strong influence on the intensification of the low level dry line. The impact on 700 mb relative humidity has already been noted in the discussion pertaining to Figure 41.

In satellite case J, the low level winds were held constant so that the enforced divergence was the same as that in Figure 49 for one and a half hours. Yet after the initialization phase and during the subsequent hour and a half the low level divergence field evolved into one very similar to those in cases E and G (see Figure 51). The persistence of some of the smallest scale features in all cases, particularly in Missouri and Arkansas and along the western boundary in the high terrain, shows some effect of the terrain on forcing of surface divergence.

The convergence band moves only very slowly eastward in all forecasts and the only major difference between the satellite and radiosonde runs is that in the former, the convergence band pushes farther eastward into Southern Texas. This will be evident later. The impact of the confluent/convergent zone on

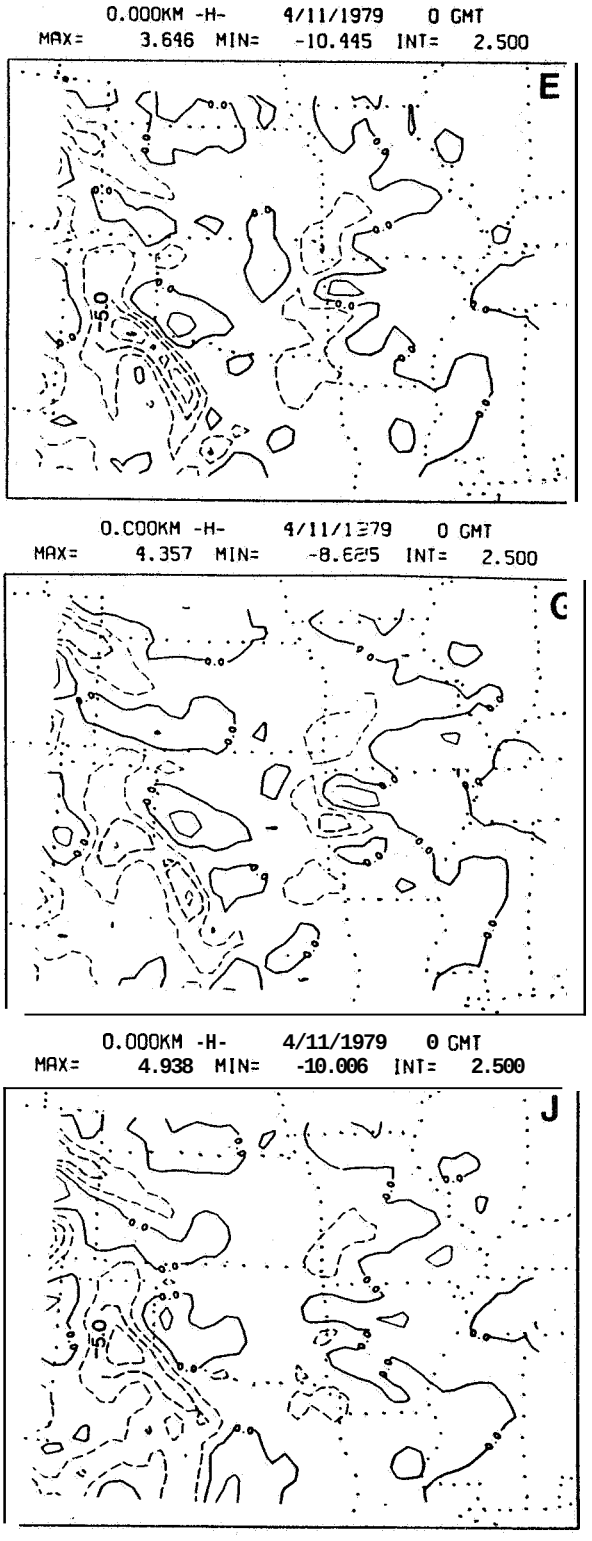

Figure 51: Forecast 0000 *GMT* surface divergence for cases E, G and J.

the surface specific humidity forecasts is seen in case F (Figure 52) to have produced rapid intensification of the low level dry line. Although the magnitude of the gradient may be unrealistic, the intensification of the moisture gradient was also forecast in the Penn State model (Anthes, et al., 1982) and in the Australian model (Mills and Hayden, 1982) for April 10. This dry line is qualitatively consistent with the advection of cool, dry air behind the cold front as it moved into Texas.

It was originally hypothesized that it might be possible to have a positive impact on model precipitation forecasts by including a low level wind field which forces an observed moisture convergence field (as was done in case J). This was tested by examining the moisture flux convergence in each model run during the initialization phase. Moisture flux divergence $\vec{\nabla} \cdot \rho q \vec{V}$ can be broken into two terms as follows

$$\vec{\nabla} \cdot \rho q \vec{V} = \rho q \underset{(1)}{(\vec{\nabla} \cdot \vec{V})} + \underset{(2)}{\vec{V} \cdot \vec{\nabla} (\rho q)}$$

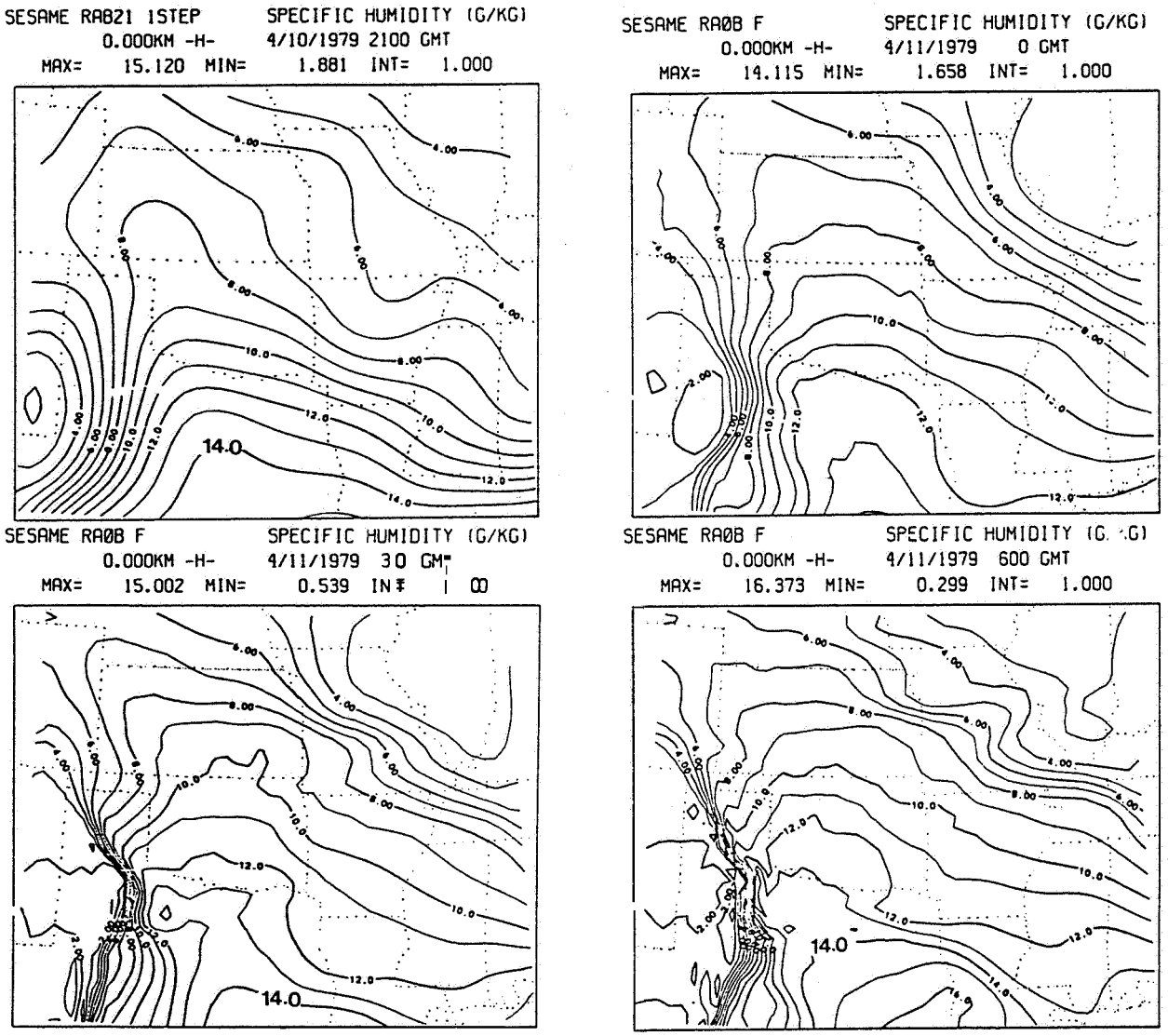

Figure 52: Time sequence of maps showing intensification of the surface dry line in radiosonde case F. Units and times are shown above each panel.

ρ is air density and q is specific humidity. The velocity divergence term (1) was found to be at least an order of magnitude larger than the moisture advection term (2) except in the immediate vicinity of the convergence band where the moisture gradient is very large. Therefore, term 1 was integrated trapezoidally over model height from the surface to h_σ = 1250 meters, and over time for the initialization period for each model forecast. That is,

$$X = \int_{t=0}^{t = 1.5 \text{ hr}} \int_{h_\sigma=0}^{h_\sigma = 1250} pq\,(\vec{\nabla} \cdot \vec{V})\,dh\,dt$$

The quantity X represents the total amount of water vapor accumulated in a column 1250 meters thick during the model initialization. The X values were converted from gm m^{-2} to an equivalent depth of water in millimeters and plotted in Figure 53 for cases J, E, G and F.

Case J accumulations exhibit the same patterns as the constant divergence field with maximum values over 9 mm just southeast of the Texas Panhandle. Accumulations in case E and G are heavily influenced by

Figure 53: Maps of low level moisture flux convergence integrated over the initialization period and over the bottom 1250 meters in the model. Units are mm. Each case is identified by a letter in the upper right hand corner of each panel. Values greater than +2 mm are shaded; greater than +5 mm darkly shaded.

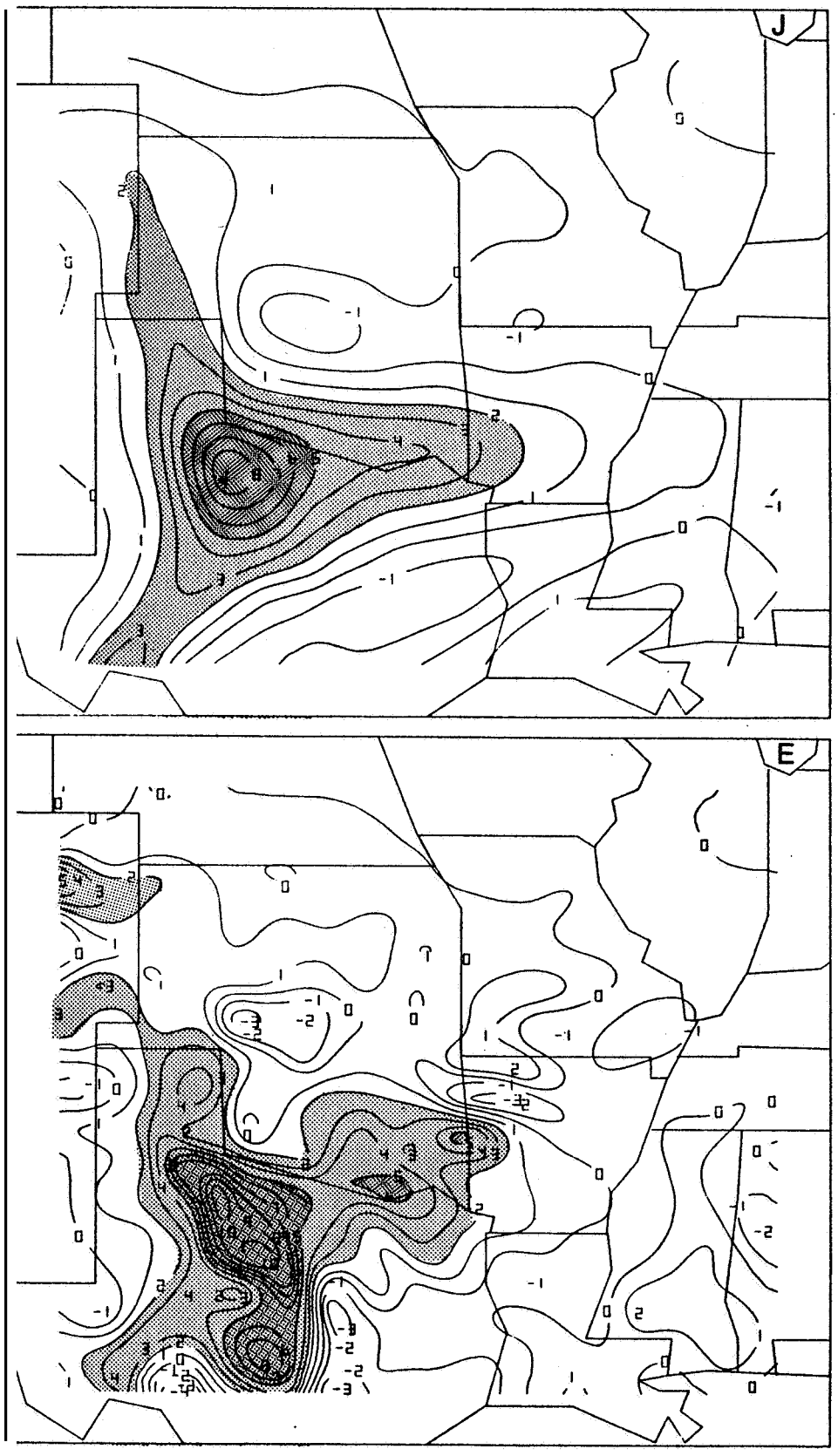
J
E

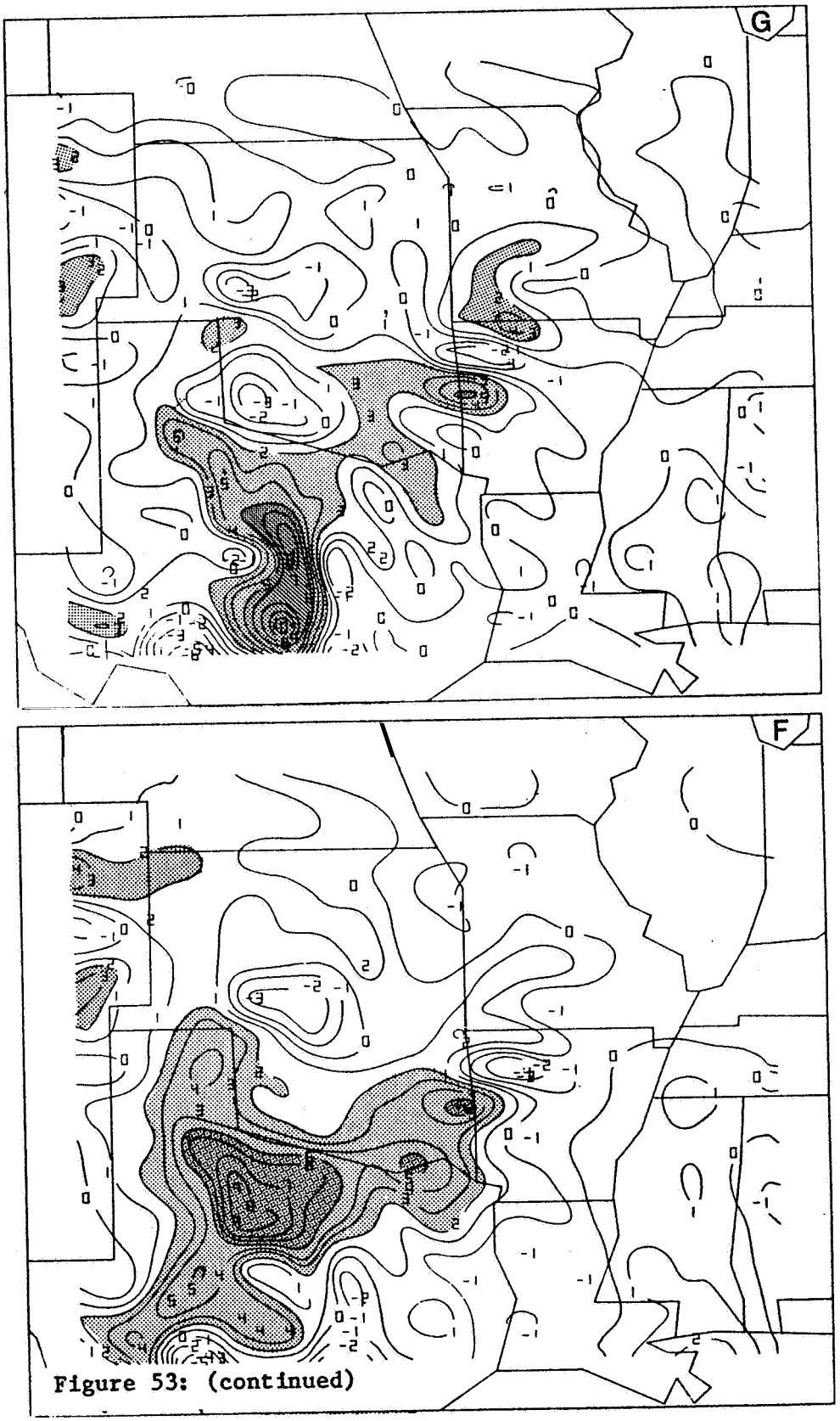

Figure 53: (continued)

the rapidly developing convergence band discussed earlier, although in case E the impact of the observed surface winds is evident. The radiosonde case F resembles E in terms of accumulations along the Texas/Oklahoma border since both had approximately the same low level winds initially. However, case F also resembles J in terms of the single maximum near the severe weather initial outbreak area and the north-south moisture convergence band which bends backwards into Southwestern Texas rather than developing strongly in the central part of the state.

There are clear differences between experiments in terms of low level moisture accumulations due to convergence. While it is obvious that the constant insertion had an impact on the precipitation forecasts (compare E and J in Figures 42, 43 and 45), the effect of forcing low level moisture convergence may have been overwhelmed by other factors. A direct correspondence can not be found between patterns in Figure 53 and specific patterns in the precipitation forecasts for the same cases.

6.3.2 Free atmosphere winds

Vertical profiles of total kinetic energy (TKE) at each model level for experiments E, F, G and J provide

an overview of the evolution of the model wind fields. The TKE for each level is given by the sum of $\frac{1}{2}\rho|\vec{v}|^2$ at all horizontal grid points. Three curves in each Panel of Figure 54 show the TKE as a function of time at 2100, 0000 and 0600 GMT. At the initial time the kinetic energy in the satellite cases is greater than that for radiosonde case F with a peak value of 680 x 10^3 kg m^2 sec^{-2} compared to 530 x 10^3 kg m^2 sec^{-2}. The maximum occurs around 12 km and the fastest winds are confined to a shallower layer in the satellite initial states. The larger TKE in the upper levels for the satellite reflects larger geopotential gradients. The initial gradient differences are greater over certain areas of the model domain such as along the cross-section C-D (see Figure 34). Geostrophic winds tangential to this cross-section in Figure 55 show the largest gradients at 12 km for the satellite versus about 9 km for the SESAME radiosondes.

The evolution of TKE with time demonstrates that there are significant differences between model runs. In all four experiments, wind speeds increase substantially at the tropopause level between 2100 and 0000 GMT as the upper level jet enters the southwestern part of the domain in accordance with time dependent

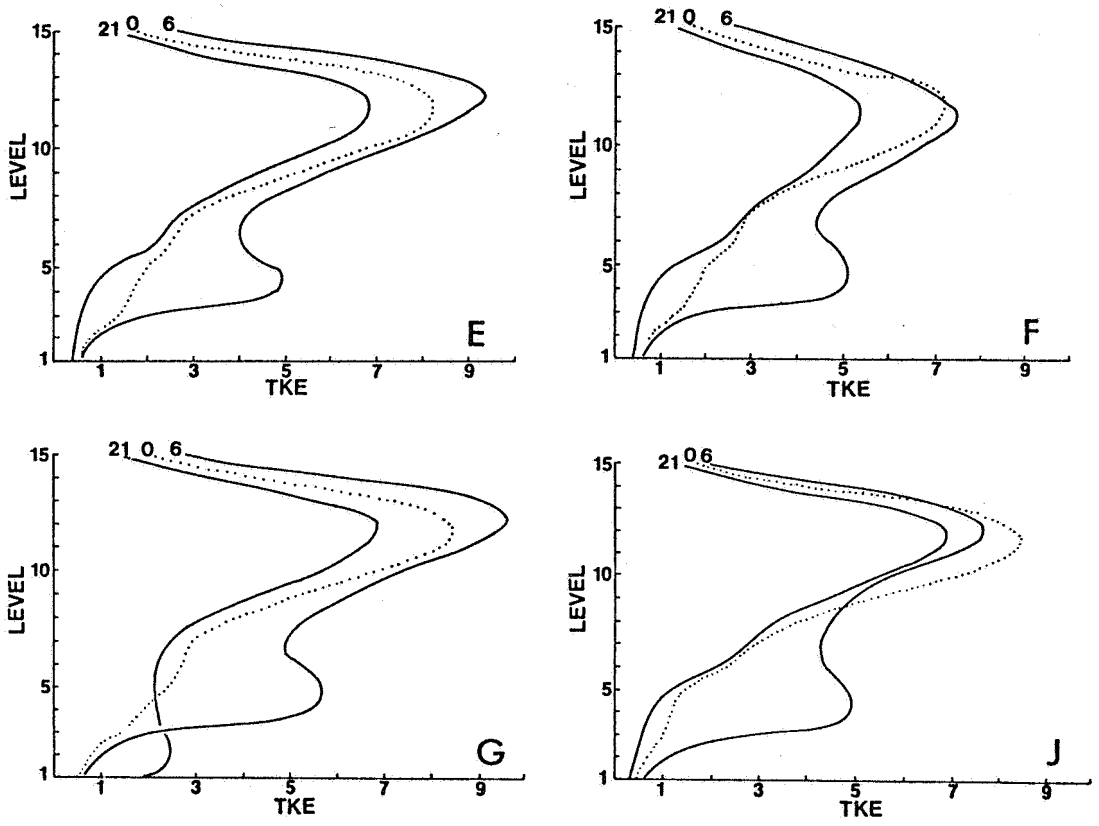

Figure 54: Vertical profiles of total kinetic energy (TKE) at each model level for cases E, F, G and J. Times for each curve are labelled in GMT hours. Units of abscissa are 10^5 kg m^2 sec^2 .

boundary conditions. Below level 6 (h_σ = 2000 meters) in experiments E and F there are increases of TKE during the first three hours, however, in case J the increase is smaller because of the initial constraints on the low level winds. For case G, eddy stresses in the boundary layer reduce the inviscid balanced wind

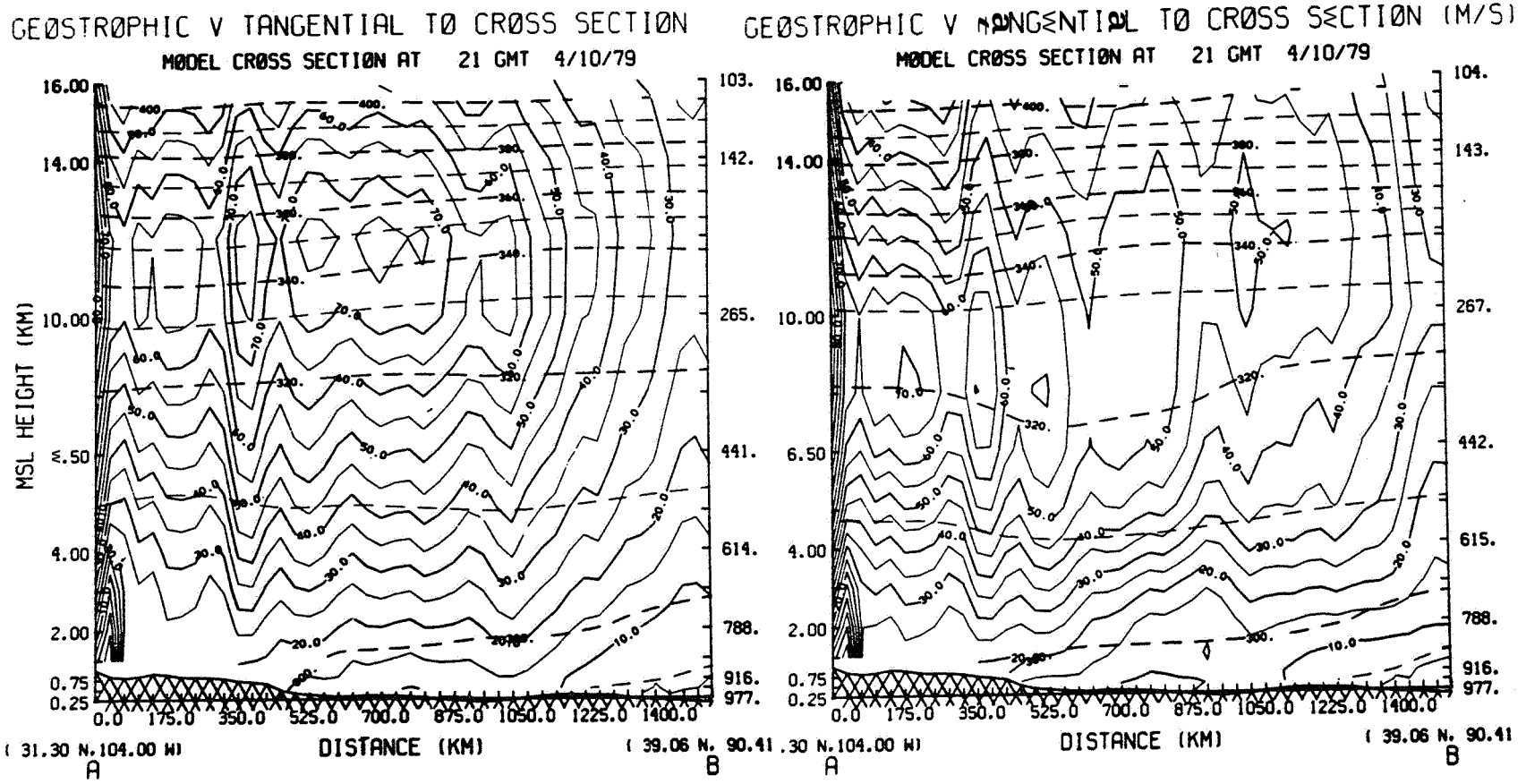

Figure 55: Vertical cross-section of geostrophic wind speed tangential to the line C-D (see Fig. 34) for the satellite case E (left) and radiosonde case F at the initial time.

speeds so that the TKE for the lower levels ends up about the same as in the other experiments.

Holding the low level winds constant during the initialization had an impact on wind fields near the tropopause which did not show up until long after the initialization had ended. As the upper level jet propagated across the southern part of the domain from 0000 to 0600 (see left hand side of Figure 57), experiments E and G showed concurrent increases of TKE. Experiment J is the only one in which TKE decreased during the same period. Thus, at the end of the forecasts, peak values for G and E were about 920 x 10^3 compared to 730 x 10^{-3} kg m^2 sec^{-2} for cases J and F.

After 0000 GMT in all experiments the TKE between the surface and level 7 underwent rapid increases due to two processes. First is the effect of vertical momentum transport by convection and mean motions. This is most evident in the upper level wind fields. The effect of the convective component is not as readily seen in the low level wind fields because the total downward displacement of air parcels (and thus momentum transport) due to convection induced subsidence is small compared to parcel displacements in the updraft. For example, in case F vertical motions

associated with parameterized convection has distorted what would have been smooth isotach patterns at 300 mb over the Texas/Oklahoma border (see Figure 56b). Wind speeds there as low as 35 m sec^{-1} resulted from upward transport (advection) of low momentum. In the region of the main short wave a band of relatively low wind speed moved eastward out of Colorado along the convective (and stable) precipitation area associated with upward vertical motion in the short wave. The effects are also found over the convective precipitation areas in other experiments. The main point is that just as low momentum is transported upward by the convective parameterizaton, "faster" momentum is transported downward helping to explain the increase in TKE after 0000 GMT in the lower levels.

The second and probably primary factor which contributes to the low level maximum in TKE is a low level jet (LLJ) and broad area of fast winds which is generated near 850 mb in response to mass readjustment around the exit region of the upper level (300 mb) jet (see Figure 57). In Figure 58 a rectangular box is drawn over the low level jet at 0600 GMT with shaded and unshaded areas bisecting the low level wind maximum. The shaded part encompasses the low level

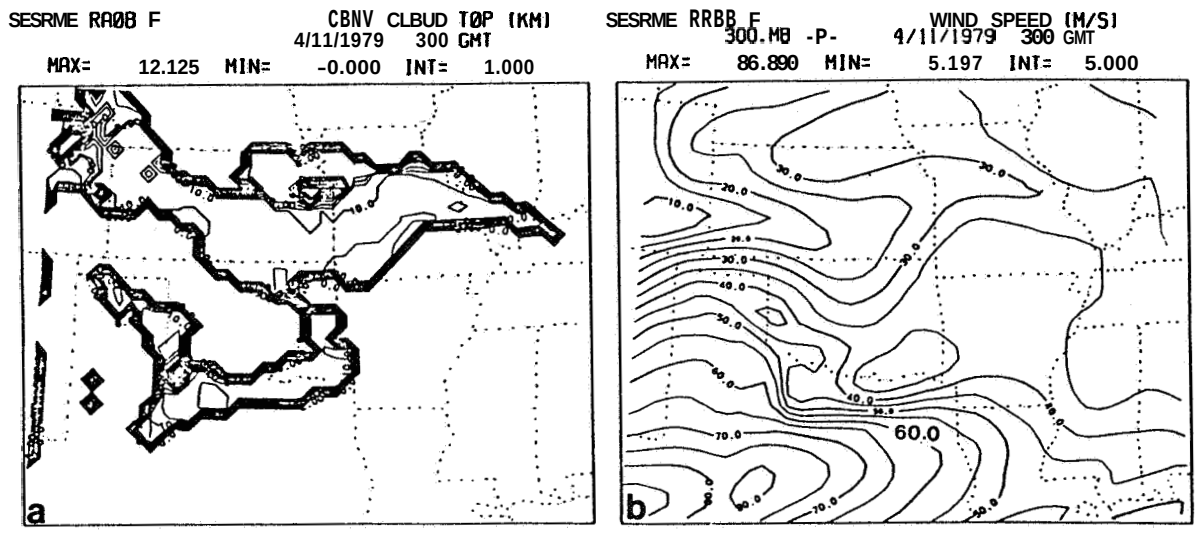

Figure 56: Maps illustrating the effect of convective (location of convection shown in panel a) upward transport of low momentum on upper level isotach patterns. Units and times are given above each panel.

convergence and upward motion which is expected to the left hand side of the exit region of an upper level propagating jet maximum. The unshaded portion shows the expected divergence and downward motion.

How realistic is the forecast low level jet? The SESAME 850 mb winds (see Appendix B, Figure B3) show the LLJ which has been previously linked to isallobaric adjustment about the 500 mb jet streak which propagated around the upper level through into Texas (Kocin, et al., 1982). The observed 850 mb LLJ moves from Central

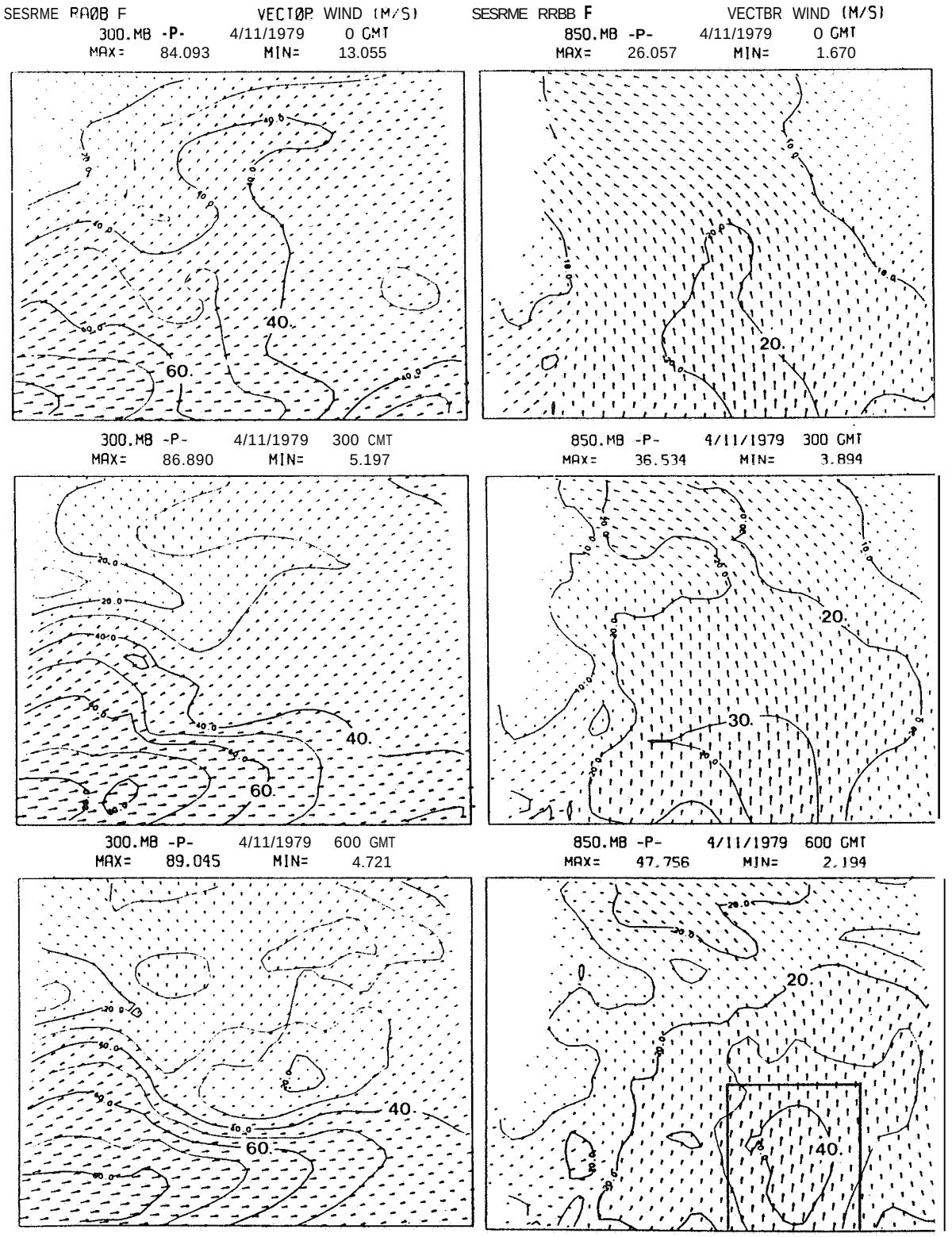

Figure 57: Time sequence of maps showing the generation of a low level (850 mb) jet about the exit region of an upper level (300 mb, left hand panels) for radiosonde case F. Units and times given.

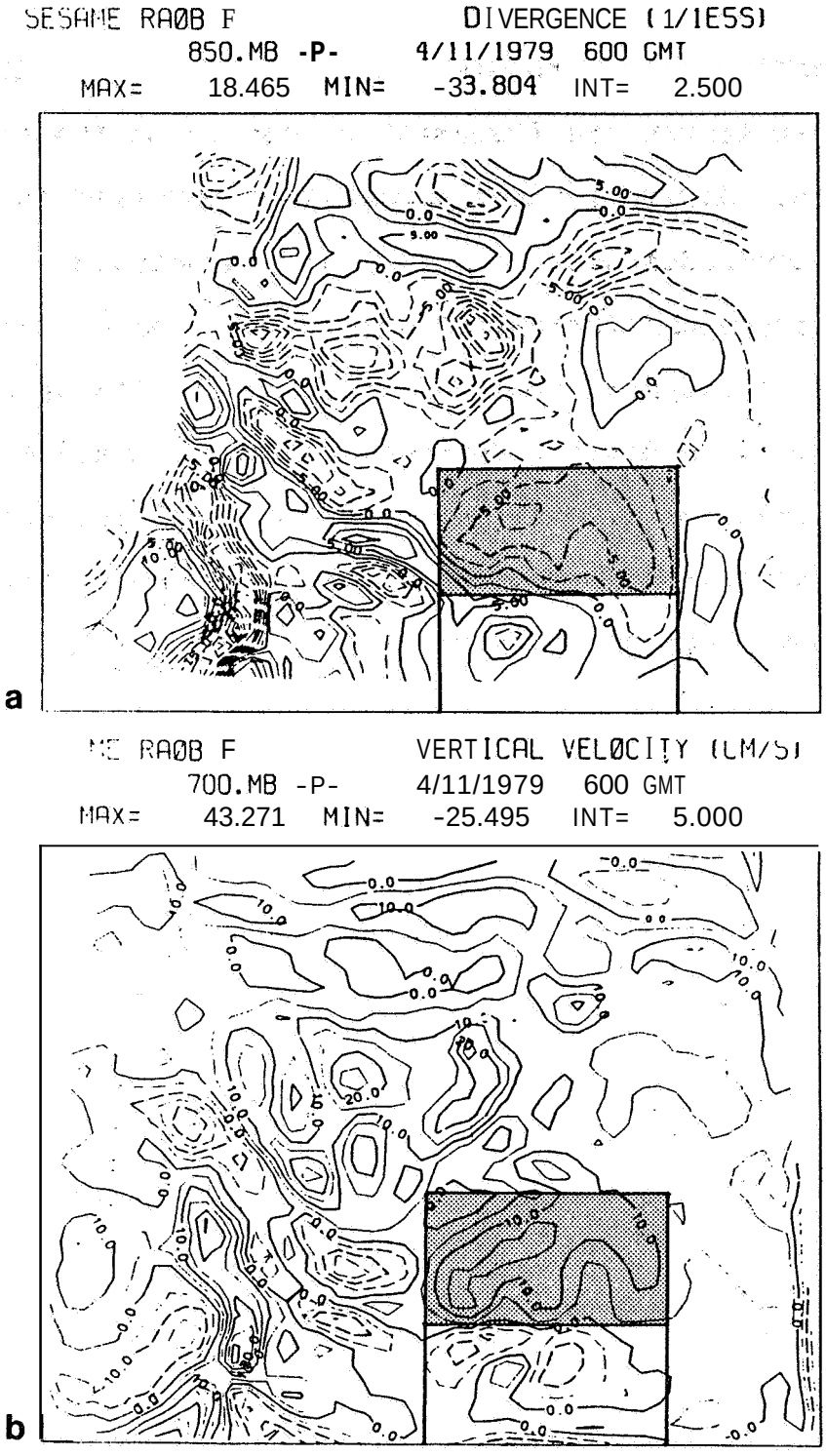

Figure 58: Maps showing the correlation of divergence (a) and vertical motion (b) with the location of the low level jet. Shaded and un-shaded halves of the rectangle bisect the 850 mb wind maximum. Units and times are given above each panel.

to Eastern Oklahoma between 0000, 0300 GMT, and it is found over Western Mississippi by 0600 GMT situated close to the one forecast in case F for the same time. However, since there is no observed equivalent to the model's 300 mb jet, one can not argue that the observed and forecast LLJ's are the same. Never-the-less it is proposed that the forecast low level jet be studied in detail from model output since its formation constitutes a complete numerical simulation of the adjustment processes associated with an upper troposphere propagating jet streak.

7. Summary and Conclusions

A fine mesh (35 km) limited area numerical prediction model (LAMPS) was initialized using sub-synoptic scale data from unconventional sources. SESAME radiosonde data and high density TIROS-N satellite vertical temperature profiles from April 10, 1979, 2100 GMT were used individually and in conjunction with low level wind fields constructed from hourly surface wind observations.

The main goal was to examine the utility of satellite temperature data for initializing a mesoscale model by comparing the forecast results with those from similar experiments employing radiosonde data and with observational verification. By using wind fields based on the non-linear balance relationship and giving the satellite initial states essentially the same moisture analysis as the radiosonde initial state, the only differences between the two are related to differences in their temperature structure. This study also investigated the impact of realistic (observed) low level winds on the model forecast by inserting them into the model at the first time step or continuously during a 1-1/2 hour initialization period. (The length of the initialization period was determined based on

domain averaged local pressure tendency statistics.) It was hypothesized that starting the model with these winds would force a low level moisture convergence which could have a positive impact on the precipitation forecasts.

A preliminary set of three-hour forecasts was made based on SESAME radiosonde data from 1800 GMT on April 10. These were designed to test model initialization with (A) observed radiosonde winds, (B) balanced winds, and (C) balanced winds plus a quasi-geostrophic (QG) divergence. The QG divergence, which was obtained by solving the QG "Omega" equation in model coordinates, was not found to have any significant impact on either model evolution or on suppression of the initial generation of high frequency gravity waves. Balanced winds substantially reduced initial "noise" levels over those for the real wind forecast and provided a smoother, more accurate mass field at the end of the initialization period. The balanced wind case was run out to 0600 GMT on April 11 (twelve hour forecast, D) and produced reasonable mass and precipitation fields.

The real winds generated vertical motion patterns during the initialization which were found to be consistent with geostrophic adjustment theory, and

after three hours of model integration, some of the forecast vertical motion features could be seen in observed vertical motion patterns. However, the forecast vertical motion features were located about 200 km too far east. The prevalence of high amplitude gravity waves in the real wind initialization resulted in highly distorted mass fields, and the synoptic scale low pressure system over Colorado was not properly maintained by the model.

Two of the main experiments (E,F) were designed to provide a direct comparison of model performances of SESAME radiosonde temperature and high density satellite temperature data. The satellite data consisted of 89 TIROS-N temperature soundings over the model domain, with two SESAME soundings being included along the western boundary to remedy a void in the satellite coverage. These two experiments (as well as other model forecasts) were compared in terms of mass fields, precipitation and wind structure. Both the initial states had the same moisture, surface pressure and were statically initialized with low level winds (below 2000 meters) obtained on model surfaces by linear interpolation between observed surface wind analyses and balanced winds at 2000 meters. Thus, the

low levels included an Ekman type turning with height.

Most of the smaller scale features in the initial mass fields were eliminated during model initialization, however one major 700 mb short wave was retained by the model and went on to have a significant impact on precipitation. This short wave which was present in both the radiosonde and satellite forecasts propagated around the 700 mb synoptic scale trough from Southern Oklahoma to Nebraska from 2100 to 0600 GMT (April 11).

In the radiosonde forecast (F), as the shortwave reached Northern Oklahoma around 0000 GMT, it organized recently initiated precipitation (both convective and stable modes) into a narrow band. Then both the short wave and precipitation propagated northward at about 18 m sec^{-1}, reaching peak precipitation rates around 0300 GMT, and had largely dissipated by 0600 GMT. The propagating short wave had a distinct vertical structure with maximum vertical motions of about 35 cm sec^{-1} near 500 mb. It was preceded by a convergent band and followed immediately by a divergent band which were parallel to each other and sloped down wind with height. The entire width of the system was about 200-300 km.

This short wave precipitation band has not been seen in model simulations by other investigators, but verifies excellently with a similar band evident in the NMC hourly radar summaries in terms of location, rate of movement and spatial dimensions, The observed precipitation band is seen to be associated with a 700 mb short wave in the SESAME height analyses, just as in the radiosonde forecast F.

Along the Texas/Oklahoma border the radiosonde forecast convective precipitation was initiated around 0000 GMT and by 0300 had been organized into a narrow band suggestive of the April 10 squall line, However, it did not extend far southward into Central Texas as observed and was oriented about 30 degrees clockwise from the real squall line. After 0300 GMT the orientation and location of the model forecast convective precipitation was generally consistent with the observations.

Although the satellite 700 mb short wave forecast location and movements are almost identical to those of the radiosonde forecast short wave, it shows only a weak association with a convective precipitation band. More significant for the satellite forecast is an area of heavy convection over Oklahoma which covers

a much broader area than radar observations indicate. However this area shows the same NE–SW orientation as the observations. Thus, there are significant differences between the radiosonde and satellite precipitation forecasts. Overall, the radiosonde forecast (F) generated 20% less total precipitation than its comparable satellite forecast (E).

Differences between the satellite and radiosonde forecasts must be related to differences in their temperature structure. The ramifications of different initial temperature fields include different initial relative humidities and static stability. In addition, the satellite balanced winds (which depend on temperature) are on the averge **14%** faster near the tropopause than those in the radiosonde initial state. All these differences feed back into the model to produce very different precipitation forecasts. When compared with observations both the satellite and radiosonde cases produced some very realistic precipitation patterns and amounts. On the basis of the short wave precipitation, however, it is concluded that the radiosonde data gave the best overall forecast.

The impact of the surface wind data was examined

with the help of two additional satellite forecasts. One was initialized with balanced winds at the low levels (G) and the other held the observed surface and low level winds constant during the initialization period (J). The potential importance of including low level wind observations was tempered because of the model's ability to quickly generate realistic low level streamlines from balanced winds. However, their evolution is controlled to a large extend by adjustment to the pressure field since isotach patterns that resulted after the static initialization with real winds (E) resembled the balanced wind isotach patterns (G).

The result of using balanced winds at the low levels initially (versus static initialization with observed low level winds) was to make the field propagate slightly faster to the east. While the forecast precipitation patterns were about the same, the total amount of the stable (grid scale) precipitation was reduced by half. However, an increase in the convective amounts gave this case slightly more total precipitation.

Holding the low level winds constant during the initialization (J) affected the forecasts of wind,

pressure and precipitation. The most dramatic of these was a substantial improvement of the sea level pressure forecast by reducing large pressure falls experienced in other experiments. This case was the only one of the satellite experiments whose surface isobar patterns reflected the trough along the approximate position of the observed surface cold front at 0600 GMT.

The continuous insertion of low level winds had an impact on the upper level winds which did not appear until long after the initialization period (1-1/2 h) had ended. The result was a substantial reduction in mean wind speed near the tropopause between 0000 and 0600 GMT. The other forecasts showed increases during the same period as the upper level jet propagated into the model domain. Since the high level winds in the model retain the initial faster than observed "balanced" wind speeds, the reduction of speed for the case in question is regarded as a significant, but poorly understood improvement.

The effect on precipitation was to retard the intensities (rates) of the convective mode for at least the first three hours. At the end of the forecast the result was a 9% reduction of total domain accumulations (compared to the static initialization forecast). The

convective precipitation area over Oklahoma was constricted to a narrower band and was found farther westward closer to the observed squall line precipitation area.

For the Block II experiments, low level moisture flux convergence was integrated over time and height for each model grid point to obtain patterns of water vapor which accumulated via low level wind fields in a column 1250 meters thick during the 1-1/2 hour model initialization. The patterns clearly reflected differences between the experiments in terms the evolution of the low level winds. However, no definite correlation could be seen between low level accumulations of water vapor due to forced moisture convergence and resultant precipitation patterns. Since the forced wind insertion simultaneously affected precipitation, pressure and upper level winds, it is difficult to say that the forecast precipitation impacts were directly related to low level moisture convergence. The secondary effects may have been more important in altering the precipitation forecast.

In addition to the 700 mb short wave system which was seen in the radiosonde and satellite forecasts, the model also produced other mesoscale phenomena such as

the intensification of the low level dry line over Texas. This feature has been predicted in model simulations by others and is consistent with a cold front which pushed eastward into Texas during the forecast period. An 850 mb low level jet was generated by isallobaric enhancement of the low level flow about the exit region of the upper level jet (300 mb) which propagated through the domain via Texas. At the end of the model forecasts the southerly low level jet's position is almost identical to that of a low level jet evident in the SESAME 850 mb wind field at 0600 GMT; however, the two may be caused by different physical processes. Although radiosonde case D (twelve hour forecast) did not give the best precipitation forecast, it produced the most pronounced convective precipitation system over Oklahoma with the characteristics that define a Mesoscale Convective Complex (MCC). These include a warm core in mid-troposphere and a cold anticyclonic outflow dome at the top of the convection. Criteria for size and duration are also satisfied. The generation of the low level jet and the MCC-type convective system was unexpected. However, the numerical simulations of each merit special study from model output diagnostics which

are avaiable every half hour with 35 km resolution.

Results of this study suggest that to obtain accurate mesoscale model forecasts, it may be necessary in many situations to initialize with sub-synoptic scale data. Implicit in this statement is the need for fine mesh model grids capable of resolving sub-synoptic scale structure. This study demonstrated that high horizontal resolution satellite temperature profile data can be assimilated into a limited area mesoscale model to produce forecasts which verify favorably with mesoscale observations or forecasts with radiosonde data. In addition, this study demonstrated that a reasonable mesoscale forecast is possible incorporating only balanced winds for the motion field in the initial conditions.

Appendix A - Comparison of Initial Satellite and Radiosonde Fields

This appendix presents comparisons of the TIROS-N satellite and SESAME radiosonde fields of geopotential height, temperature and specific humidity for 2100 GMT on April 10, 1979. The height and temperature fields are compared statistically in Tables A1, A2, and A3. The sample size is the number of grid points on the one degree latitude/longitude grid used for the objective analysis. The RMS satellite-radiosonde temperature differences (Table A1) are similar in magnitude to values cited for co-located satellite and radiosonde vertical temperature profiles (Gruber and Watkins, 1982) with average RMS differences of about 1.5 K° and with a maximum around 2.0 K° near the tropopause level at 200 mb.

The satellite shows a cold bias between 700 and 400 mb which is reflected by lower mean satellite heights from 500 to 250 mb. RMS height differences (Table A2) increase with height up to 250 mb with a 25 meter value. The largest height differences, such as the 80 meters at 250 mb, occur over the satellite data void over Oklahoma in an inherently high gradient area.

The gradients of the satellite and radiosonde

LEVEL	MEAN	RMS	MAX
100 mb	.85	1.52	-4.2
150	-.63	1.30	-3.8
200	-1.13	2.21	-6.8
250	.96	1.41	3.8
300	.65	1.16	4.1
400	-.70	1.53	4.9
500	-.12	1.39	-4.1
700	-.92	1.17	-3.7
850	.67	1.94	6.1
sfc	1.40	1.52	3.9

Table A1: Statistical comparison of satellite - radiosonde temperature difference fields (°K).

LEVEL	MEAN	RMS	MAX
100 mb	3.6	17.3	-55
150	-4.8	17.9	-46
200	-3.1	21.7	-64
250	-7.9	25.6	-81
300	-13.3	25.3	-80
400	-13.9	18.0	-53
500	-7.7	10.6	-33
700	4.6	8.3	30
850	8.2	6.8	30
1000	1.7	7.1	30

Table A2: Statistical comparison of satellite - radiosonde height difference fields (meters).

h LEVEL	REL DIF
16000 m	4.2%
14000	7.0
12000	14.5
10500	14.6
9000	11.9
7500	8.5
6000	3.8
4500	1.1
3000	-2.0
2000	-2.3
1250	-1.8
750	-1.0
375	-0.2
25	0.0
0	0.0

Table A3: Percent relative error of mean initial satellite height gradient with respect to initial radiosonde data for all model levels. Positive values indicate larger satellite gradients.

heights are compared in Table A3 using the balanced wind speed corresponding to geopotential gradient. Since kinetic energy of the wind is proportional to velocity squared, the numbers in the table express a percent change of the mean satellite height gradient relative to the radiosonde from:

$$(TKE_{sat}^{1/2} - TKE_{raob}^{1/2}) / TKE_{raob}^{1/2}$$

TKE is the sum of $\frac{1}{2} \rho |\bar{V}|^2$ over all horizontal grid points in the model domain. Although geostrophic winds

are more directly related to height gradients, the balanced winds suffice to illustrate that the satellite gradients are larger than those for the radiosonde at all levels above 3000 meters. Near 200 mb the satellite balanced speeds are about 14% faster than radiosonde balanced speeds.

Map comparisons of satellite and radiosonde initial height, temperature and moisture fields are shown in Figures A1 and A2. Although the patterns of the satellite and radiosonde height and temperature fields are similar, there are significant regional differences.

Figure A1: Satellite, radiosonde, and satellite - radiosonde height and temperature fields at 850, 700, 500, 300 and 200 mb (pages 170 through 174). The left hand side going down each page shows three panels for the radiosonde, satellite and difference fields of geopotential height (dekameters). On the right hand side of each page are the corresponding fields for temperature (°K).

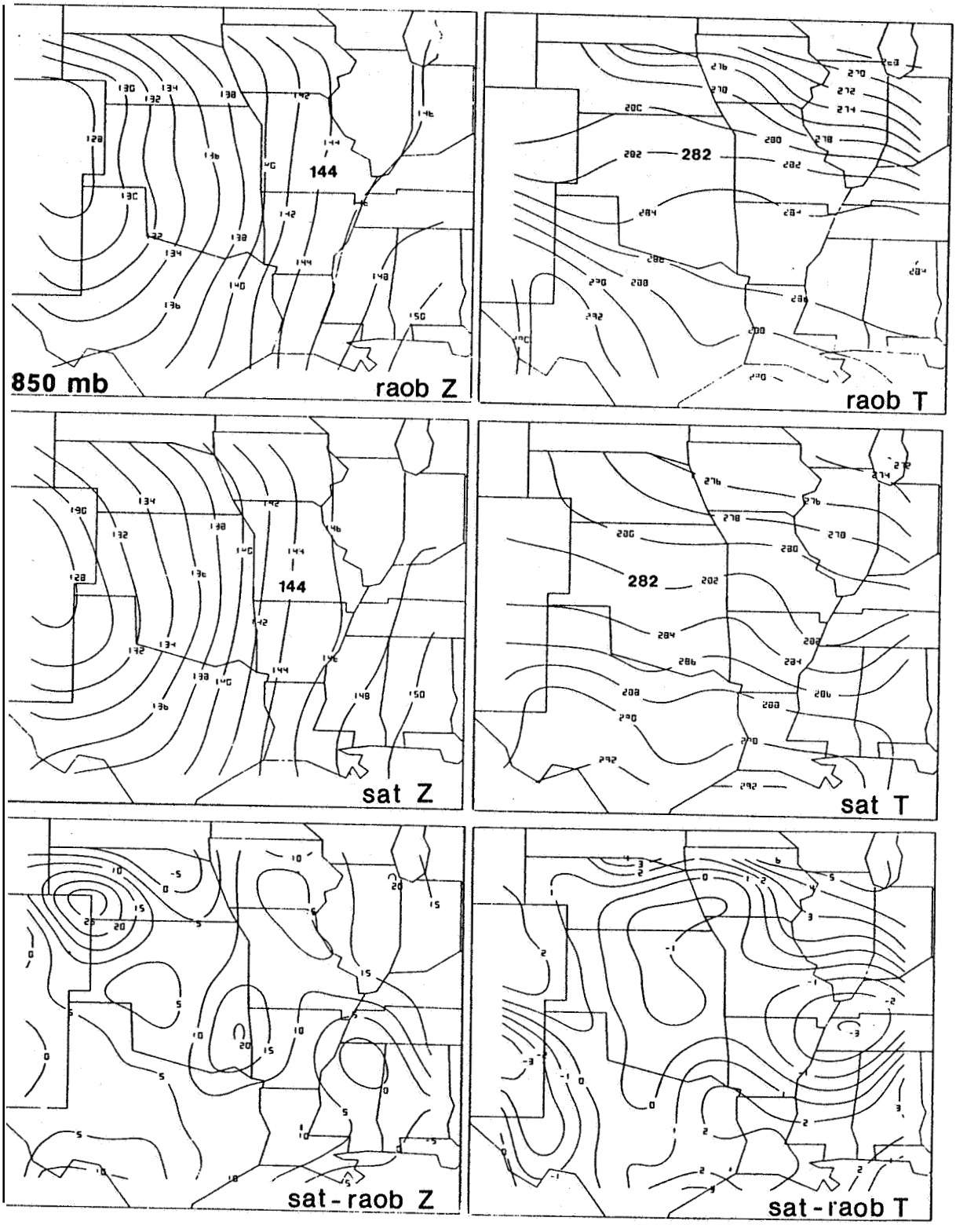
850 mb
raob Z
144
raob T
282
sat Z
144
sat T
282
sat-raob Z
sat-raob T

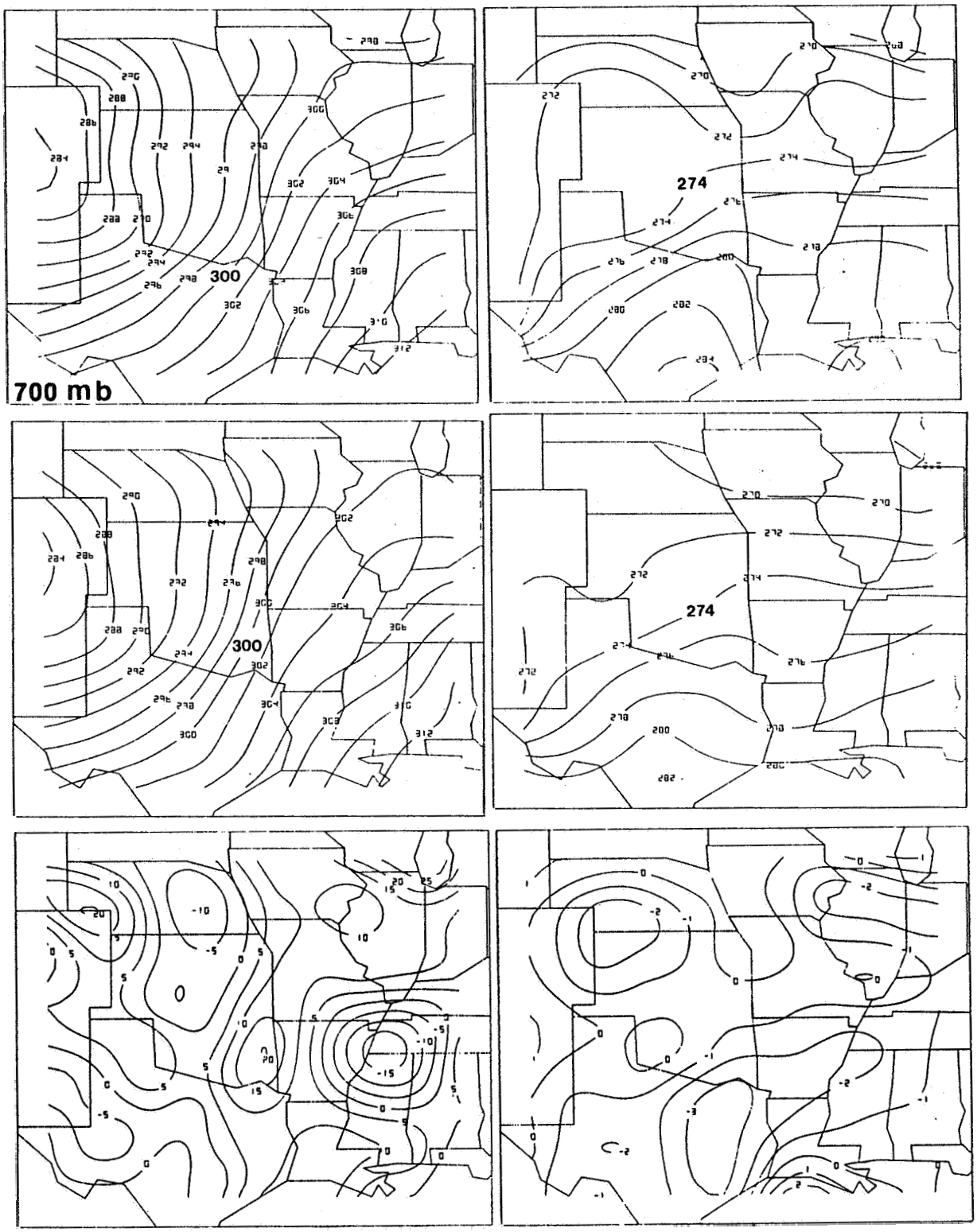

Figure *A1:* (continued)

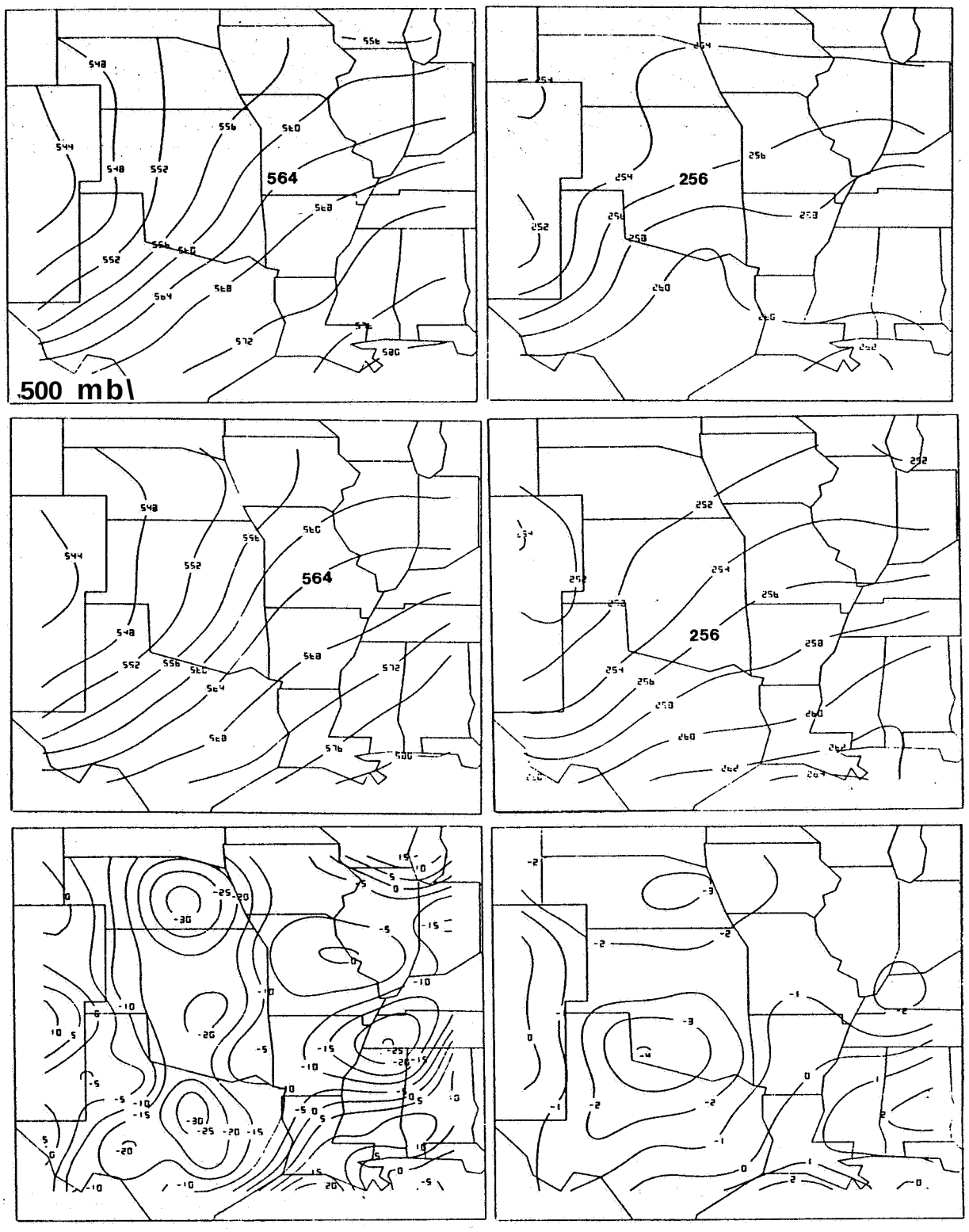

Figure A1: (continued)

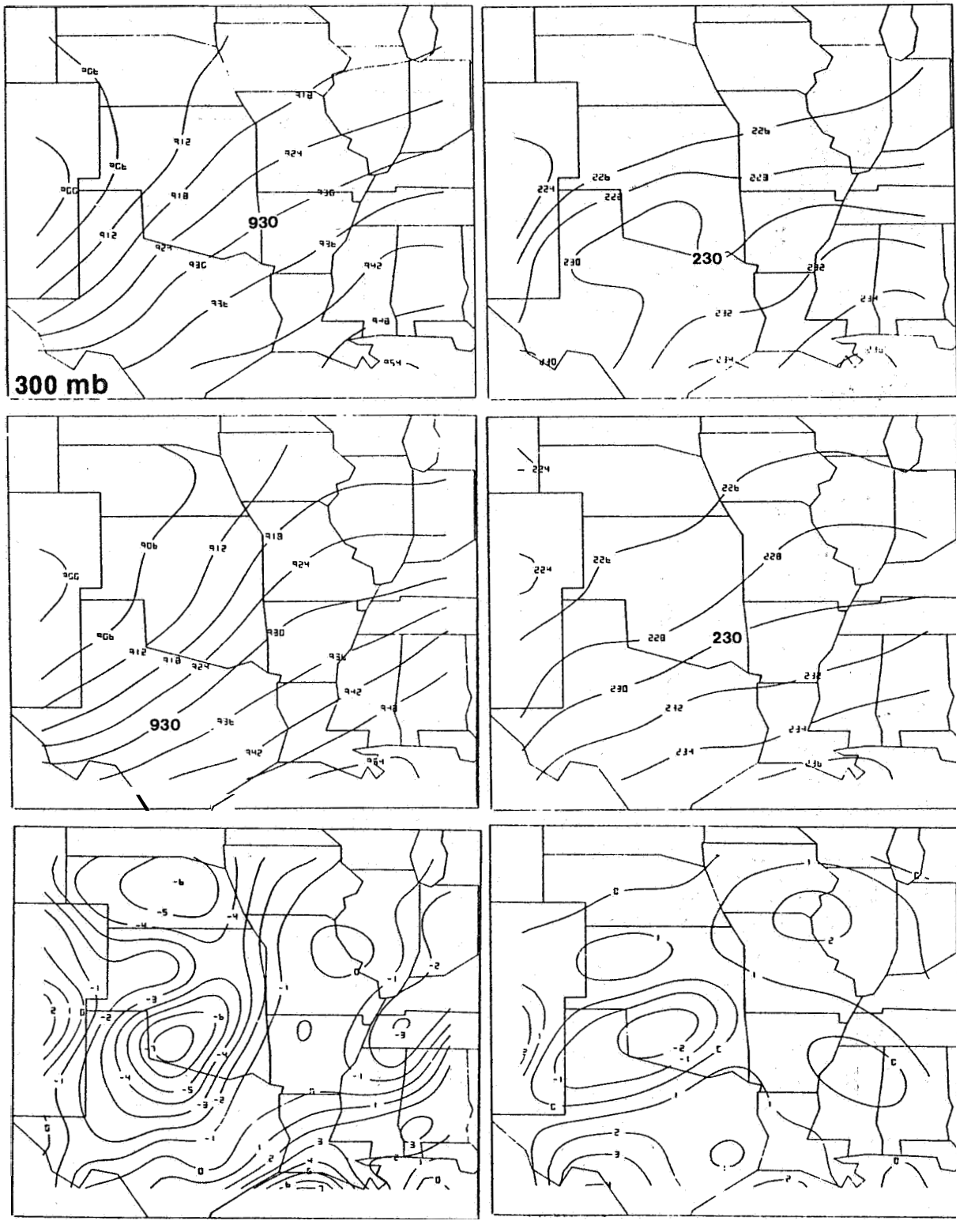

Figure A1: (continued)

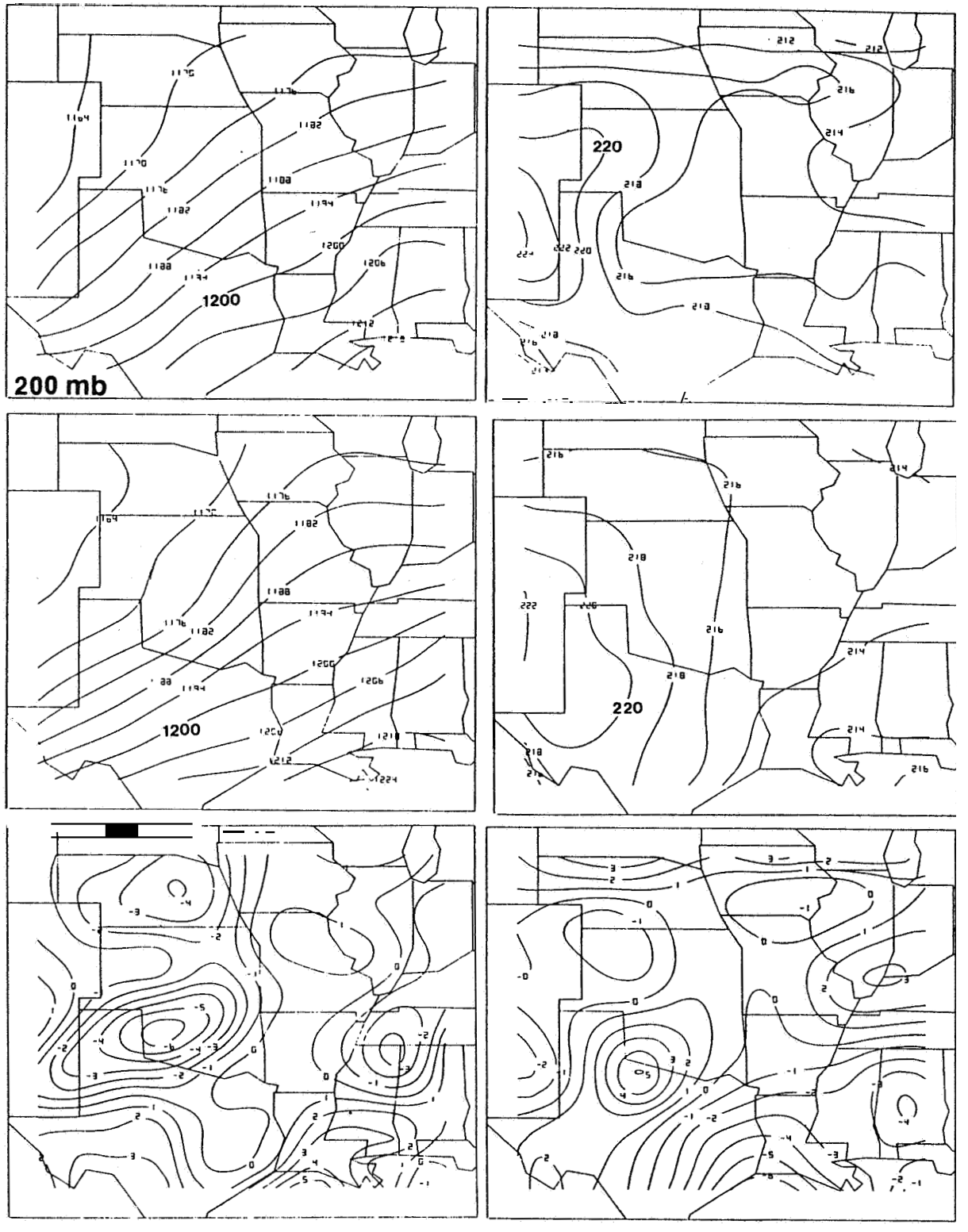

Figure A1: (continued)

Figure A2: Comparison of the initial satellite and radiosonde specific humidity analyses at the surface, 850, 700 and 500 mb (going left to right on successive pages). The top panel in each column shows the satellite specific humidity in tenths of gm / kg. The middle and bottom panels contain the radiosonde specific and relative (%) humidity analyses, respectively.

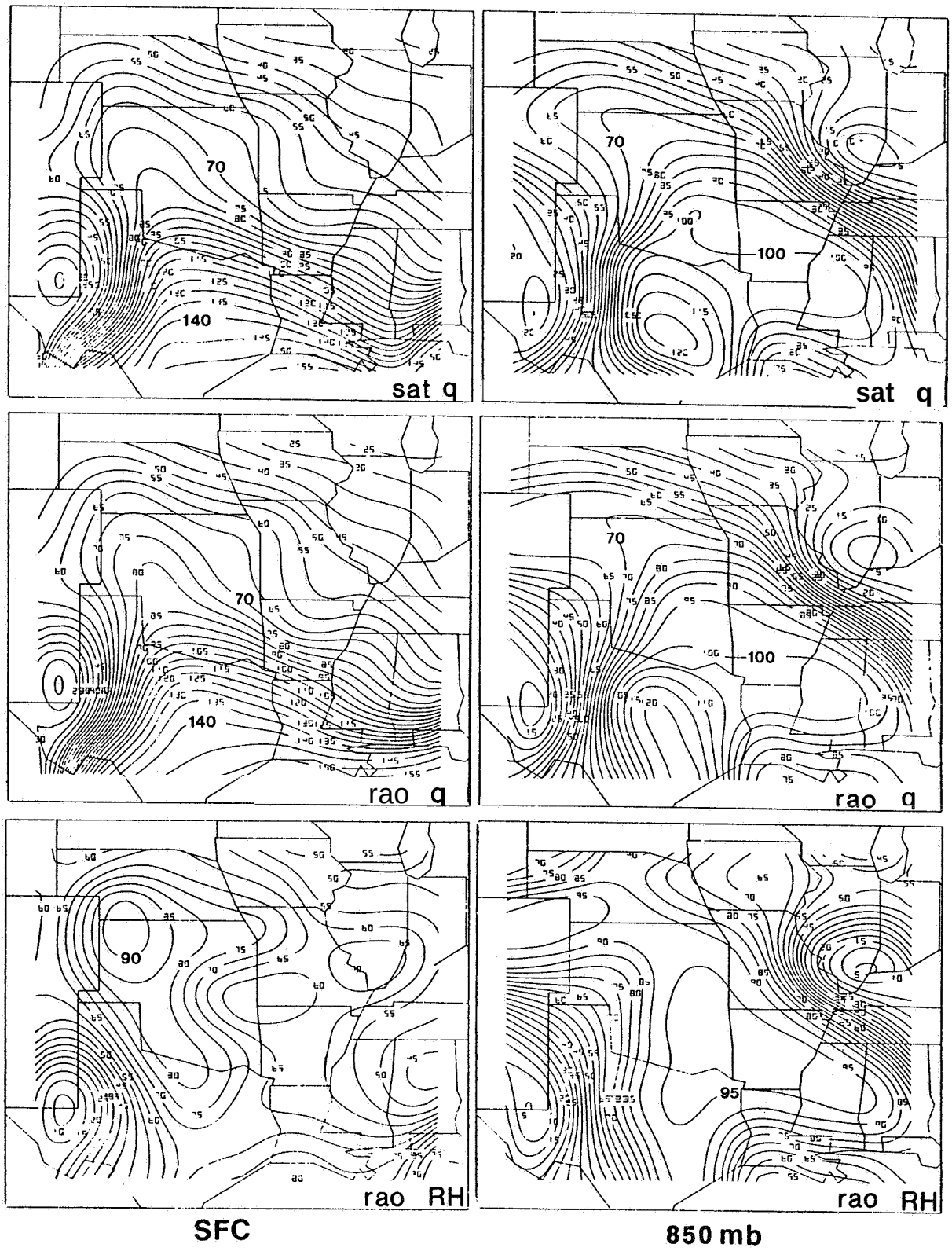
70
140
sat q
70
100
sat q
70
140
rao q
70
100
rao q
90
rao RH
95
rao RH
SFC
850 mb

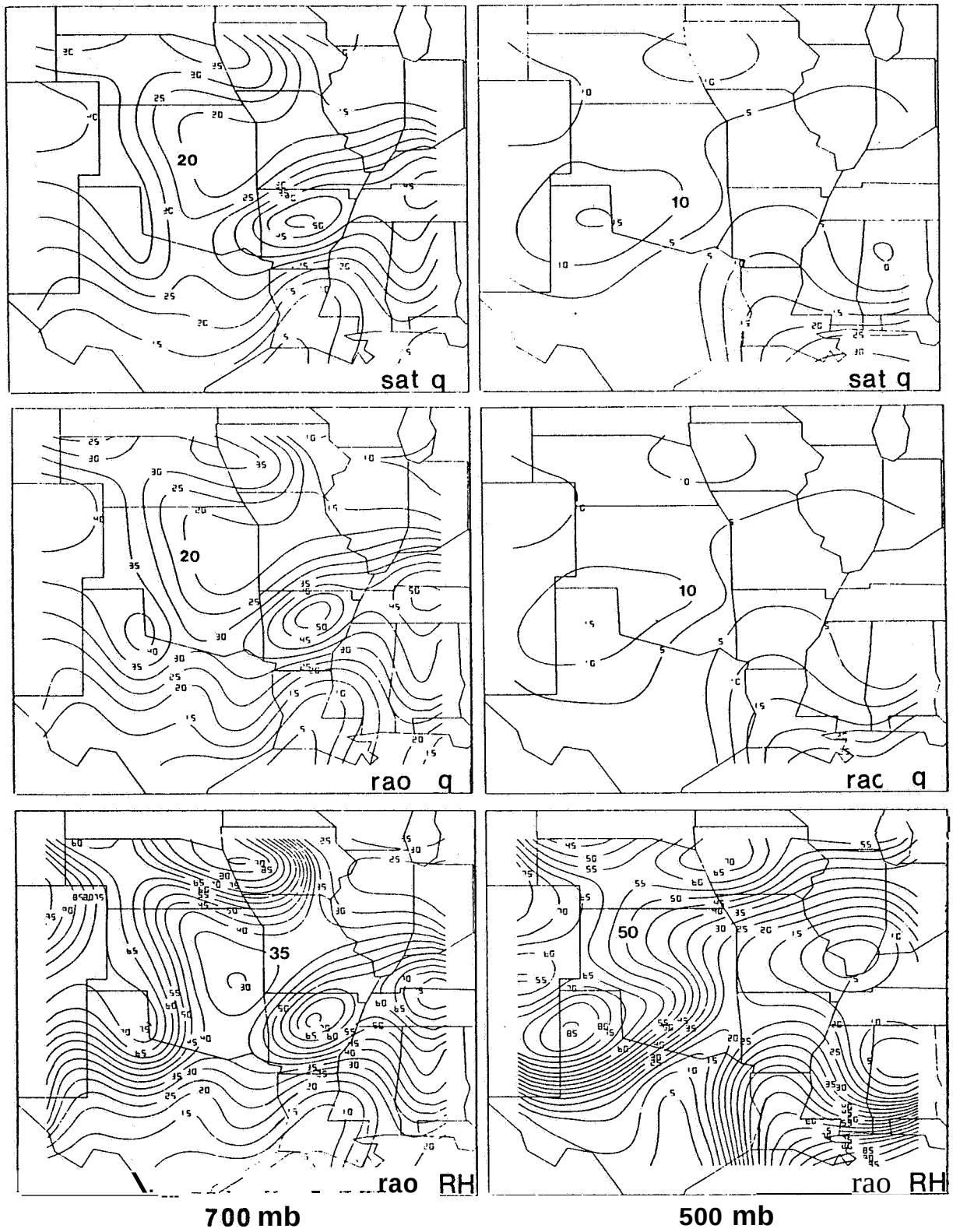

Figure A2: (continued)

Appendix B - Model Verification Data

This appendix contains analyses based on conventional meteorological observations. Figure B1 shows NMC mean sea level pressure patterns and frontal positions from 1800 (April 10) to 0900 GMT (April 11). Pages 181 to 185 contain **SESAME** geopotential height (dekameters) and temperature (^{o}C) analyses for 850, 700, 500, 300 and 200 mb. Each page has four panels corresponding to different times: 2100 GMT (upper left), 0000 GMT (upper right), 0300 GMT (lower left), and 0600 GMT (lower right). The format for the following five pages is the same except that the panels show radiosonde wind streamlines and isotachs (solid lines, m sec^{-1}). These SESAME analyses, which were provided by Mr. Thomas Q. Carney of Purdue University, were made using the Barnes method on a one degree latitude/longitude grid.

NMC hourly radar summaries are shown from **1735** to 0635 GMT April 10-11 in figure **B4.** These show the general spatial structure of the precipitation during the SESAME observing period, including the northward propagation of a mesoscale rain band from Oklahoma to Nebraska.

The precipitation rates in Figure **B5** (reproduced

from Vincent and Carney, 1982) are based on hourly surface observations averaged over one degree latitude/longitude boxes.

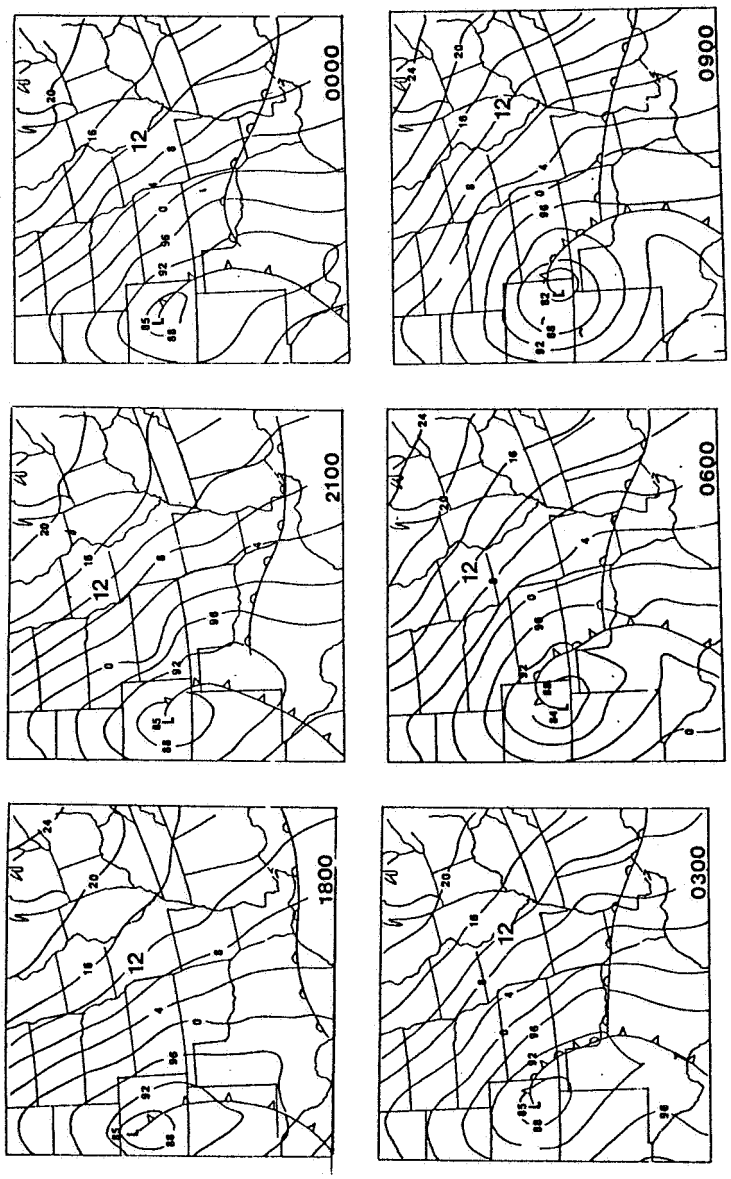

Figure B1: NMC analyzed mean sea level pressures (mb) and frontal positions.

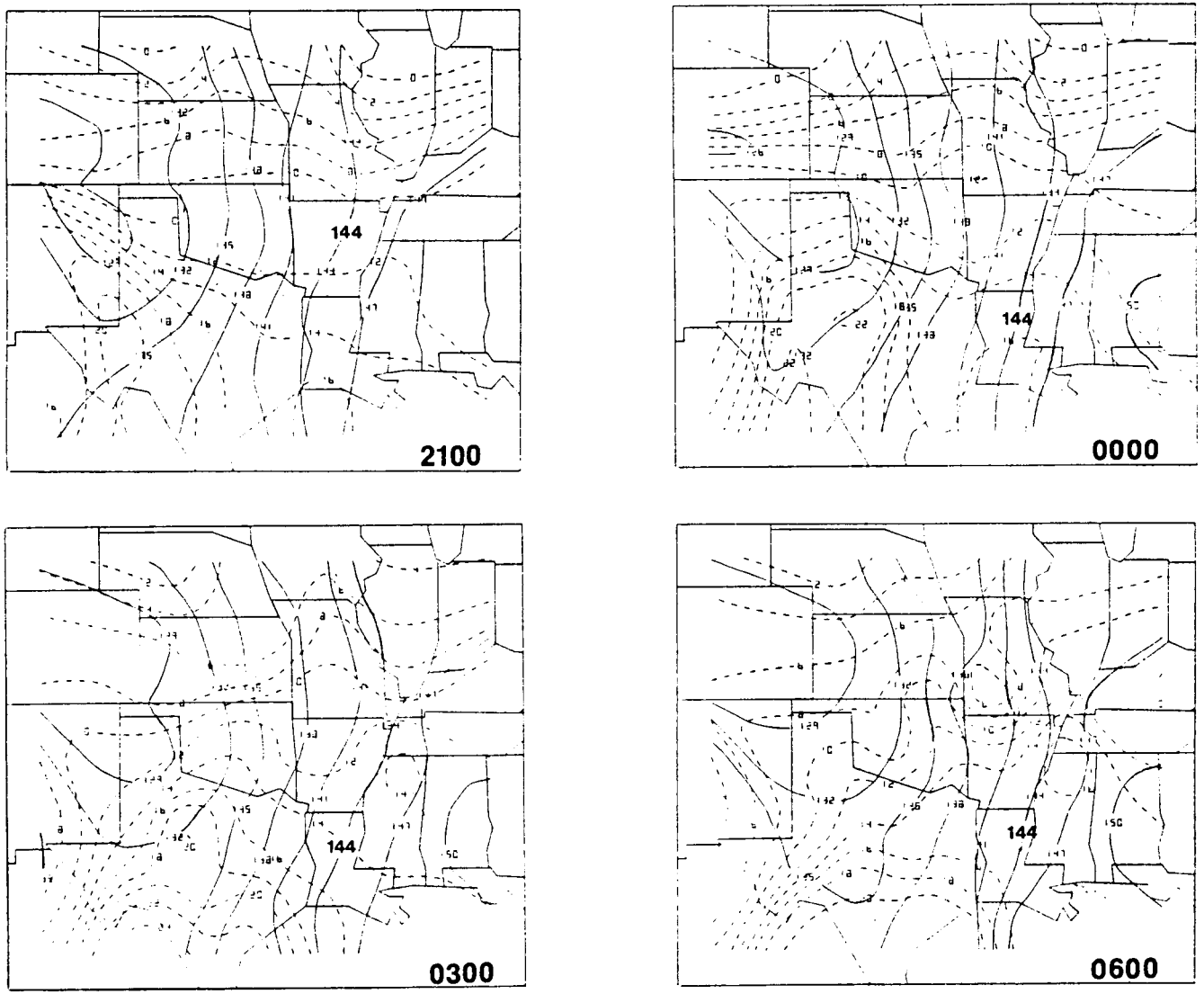

Figure B2: 850 mb SESAME height (dekameters) and temperature (°C, dashed lines) analyses for 2100 (UL), 0000 (UR), 0300 (LL) and 0600 GMT (LR) on April 10-11.

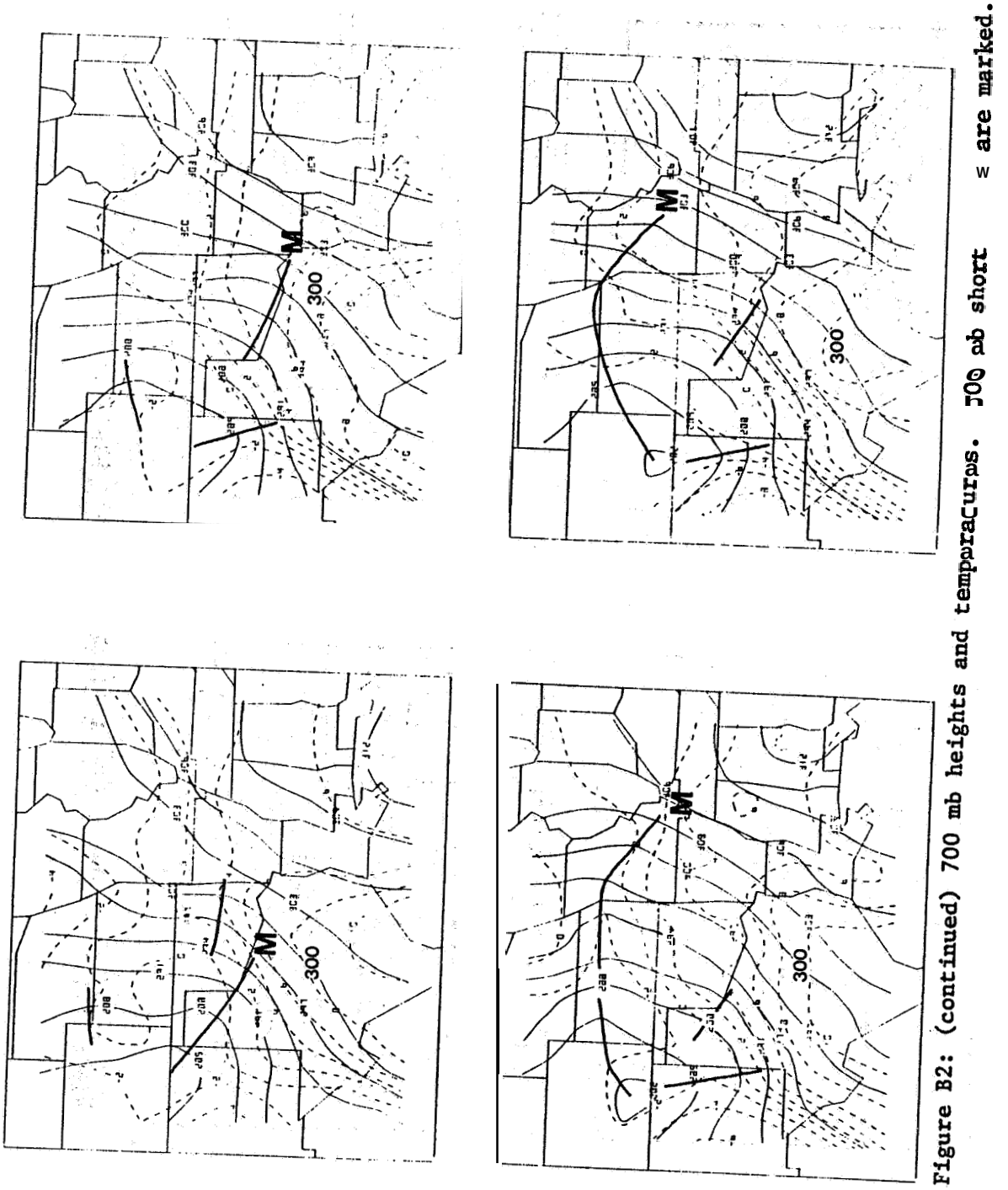

Figure B2: (continued) 700 mb heights and temperatures. 700 mb short wave are marked.

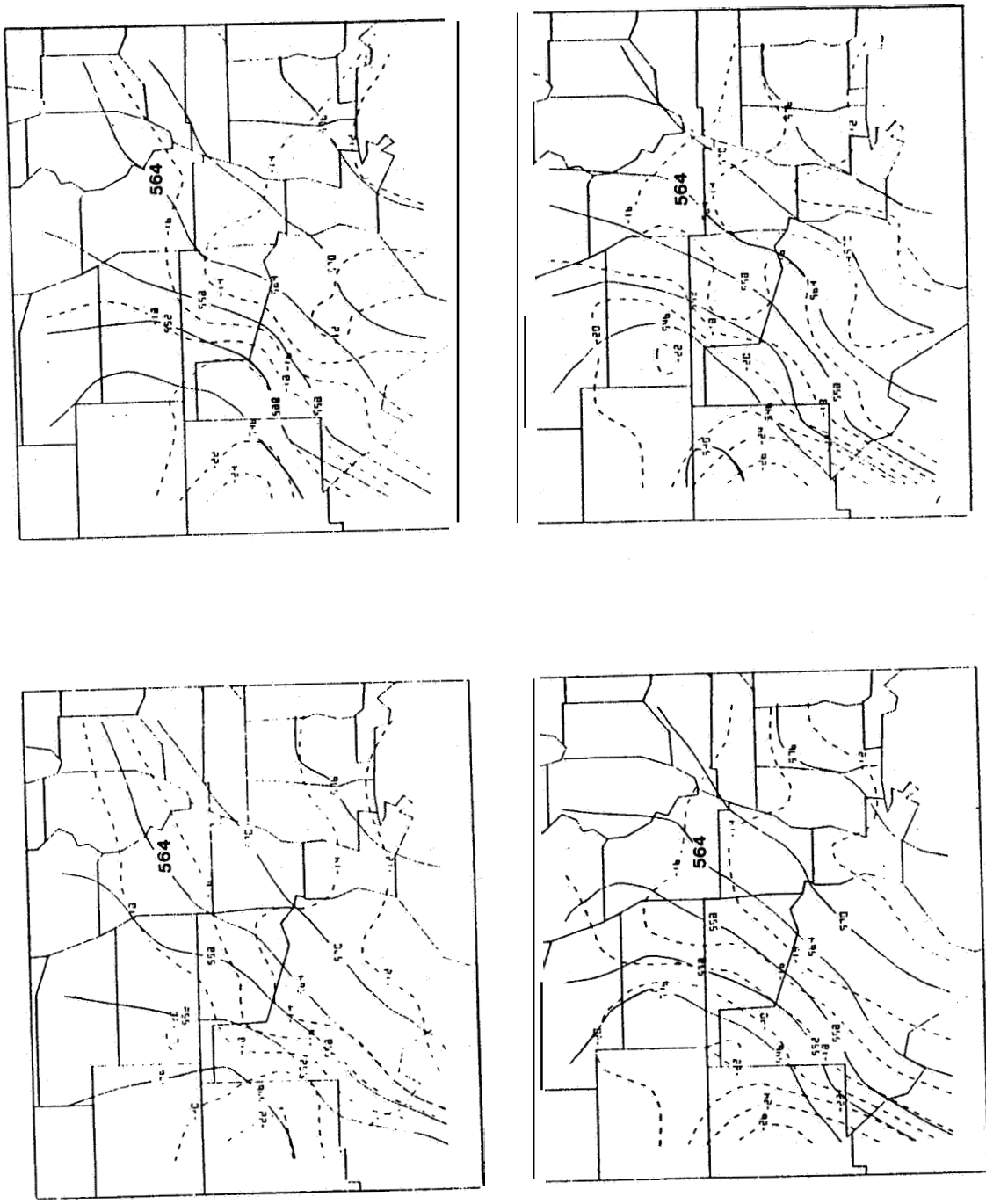

Figure B2: (continued) 500 mb heights and temperatures.

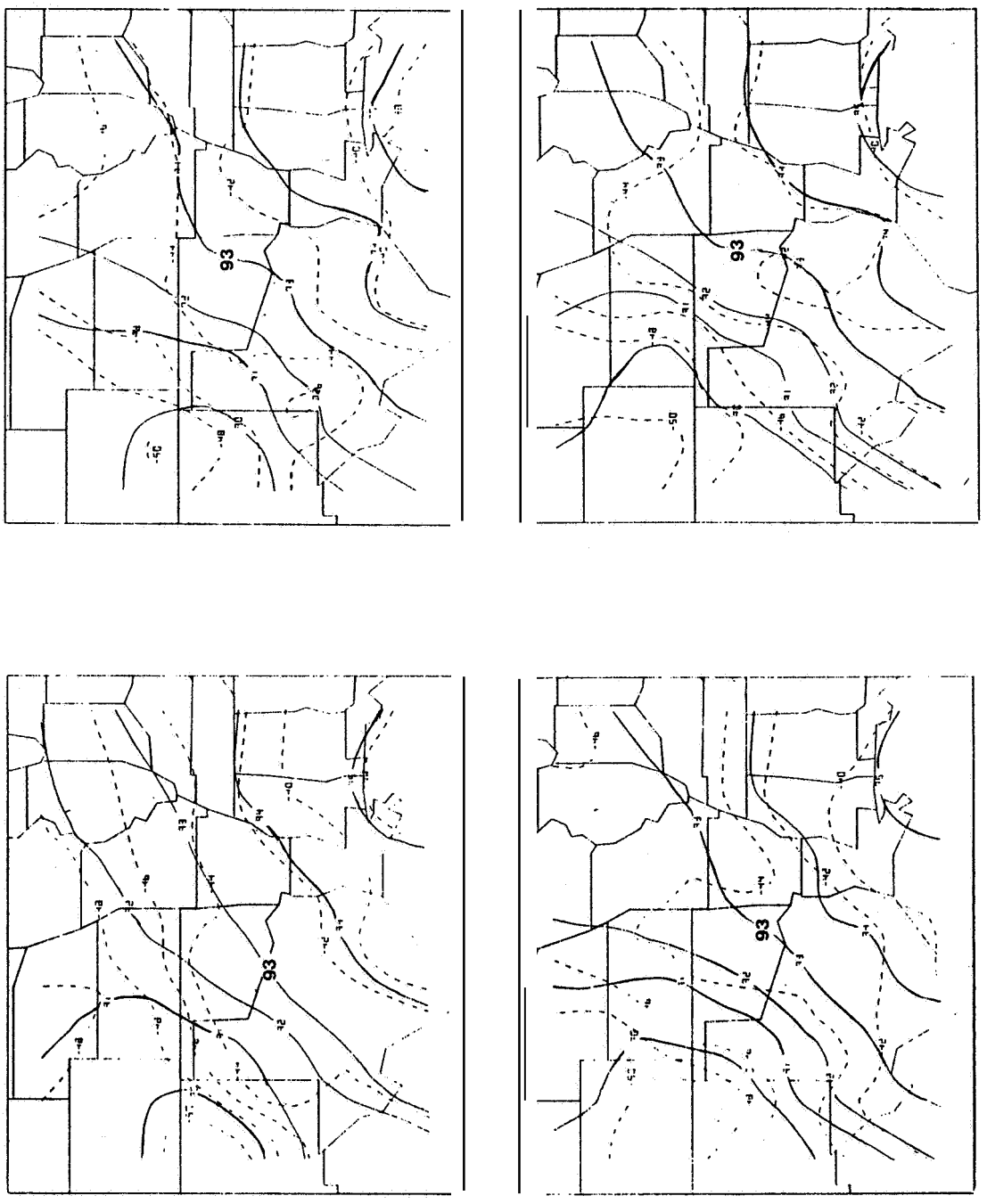

Figure B2: (continued) 300 mb heights and temperatures.

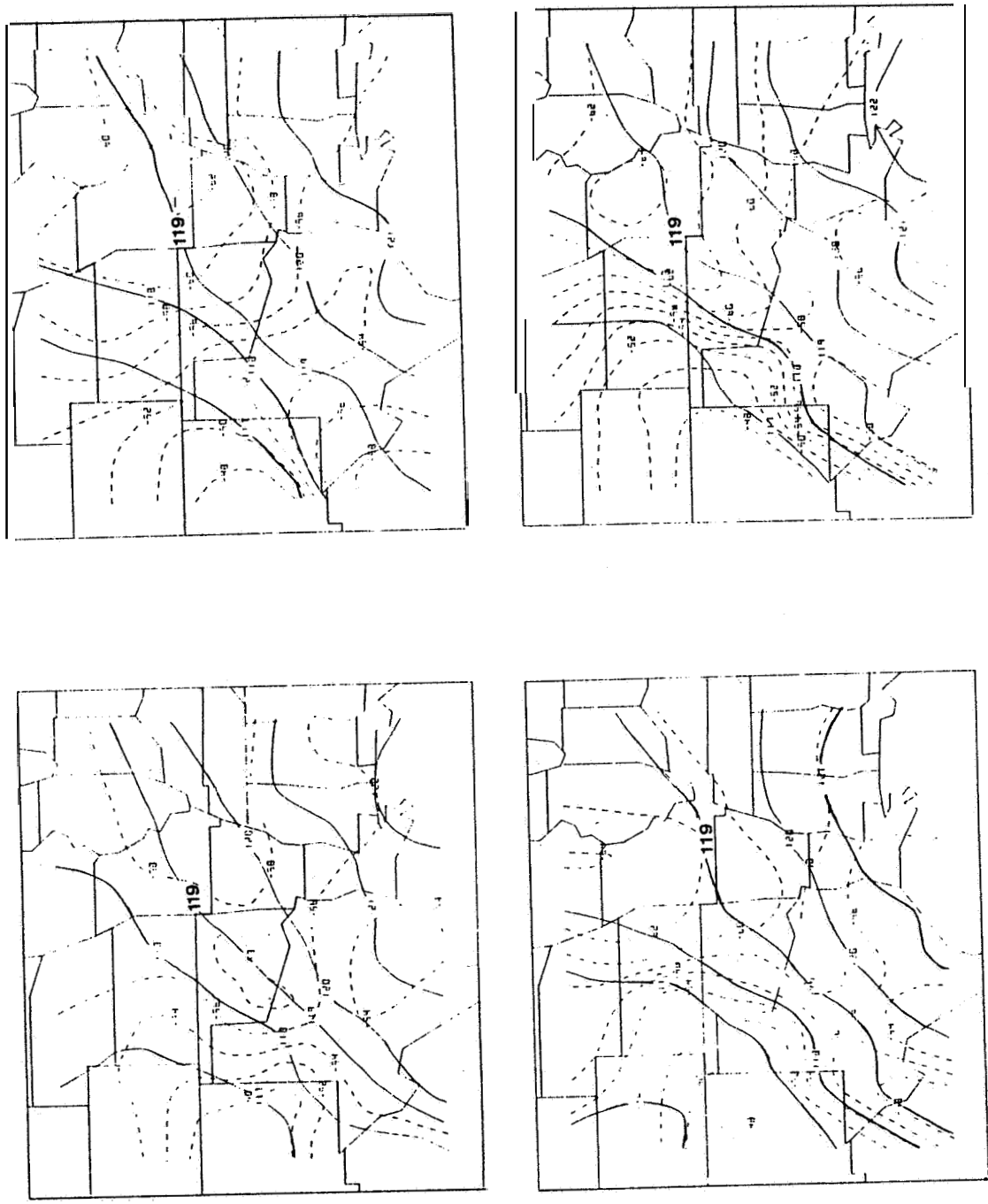

Figure B2: (continued) 200 mb heights and temperatures.

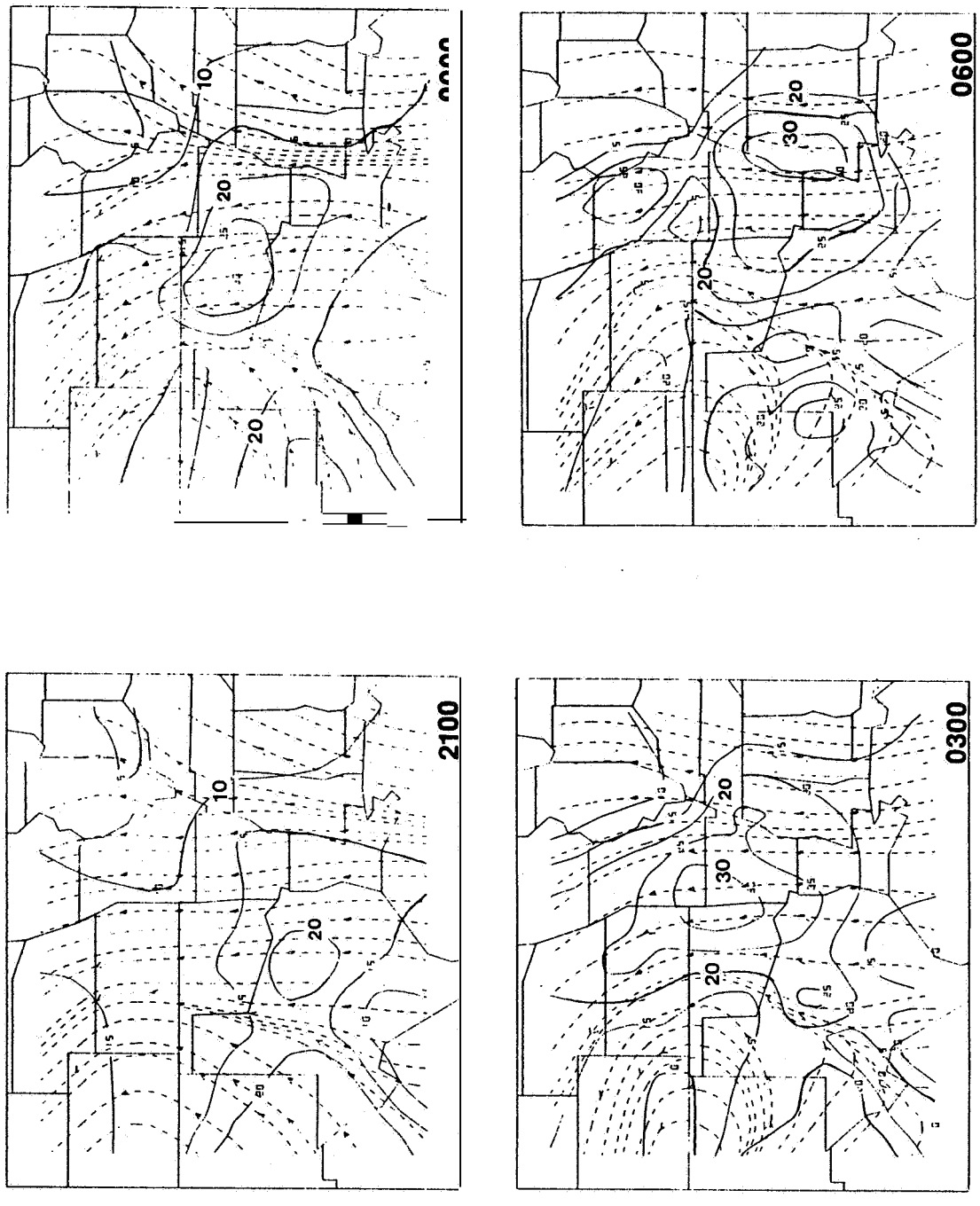

Figure B3: 850 mb SESAME radiosonde wind streamlines (dashed) and isotachs (m sec^{-1}). Times (GMT) are indicated on each panel.

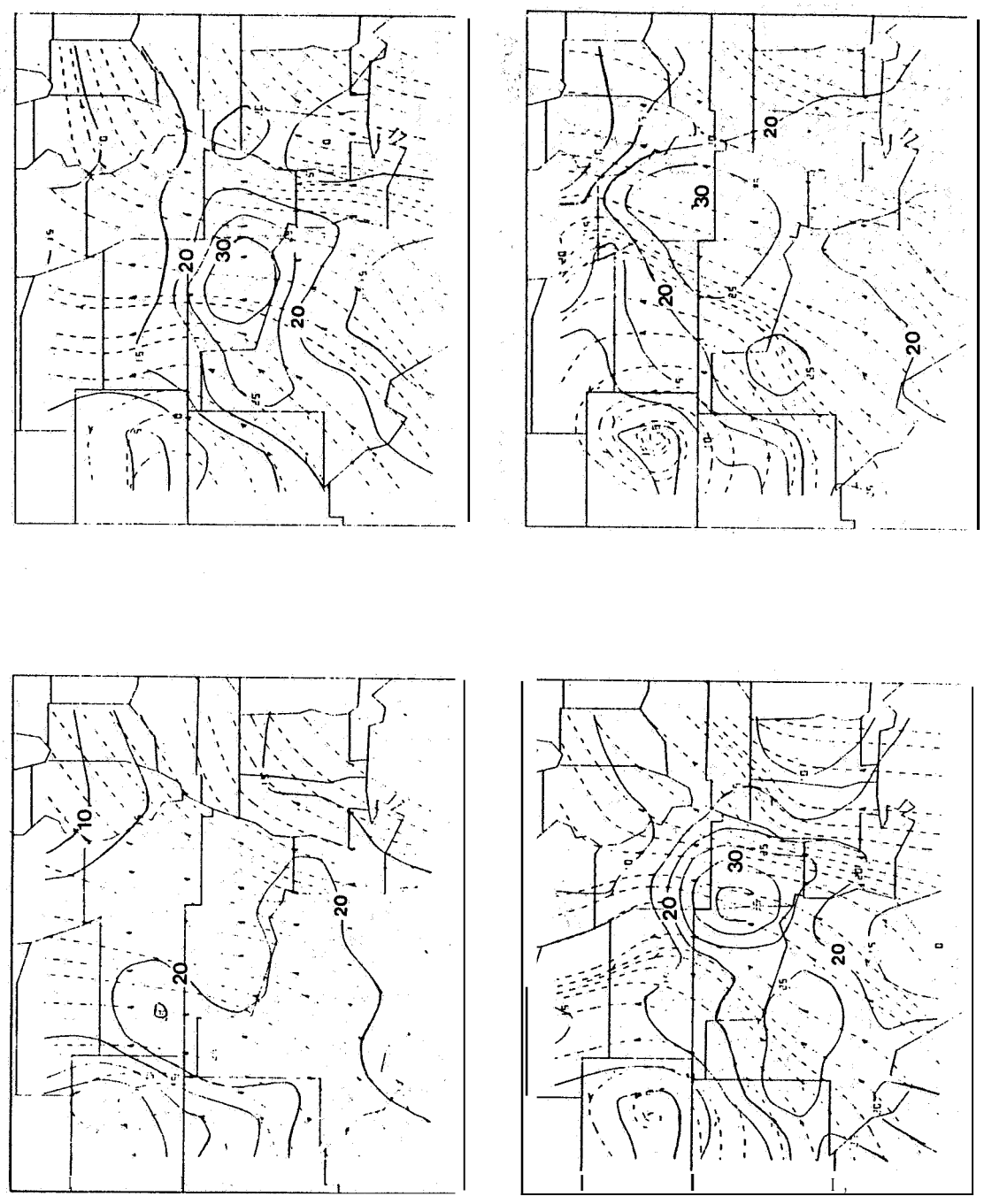

Figure B3: (continued) 700 mb streamlines and isotachs.

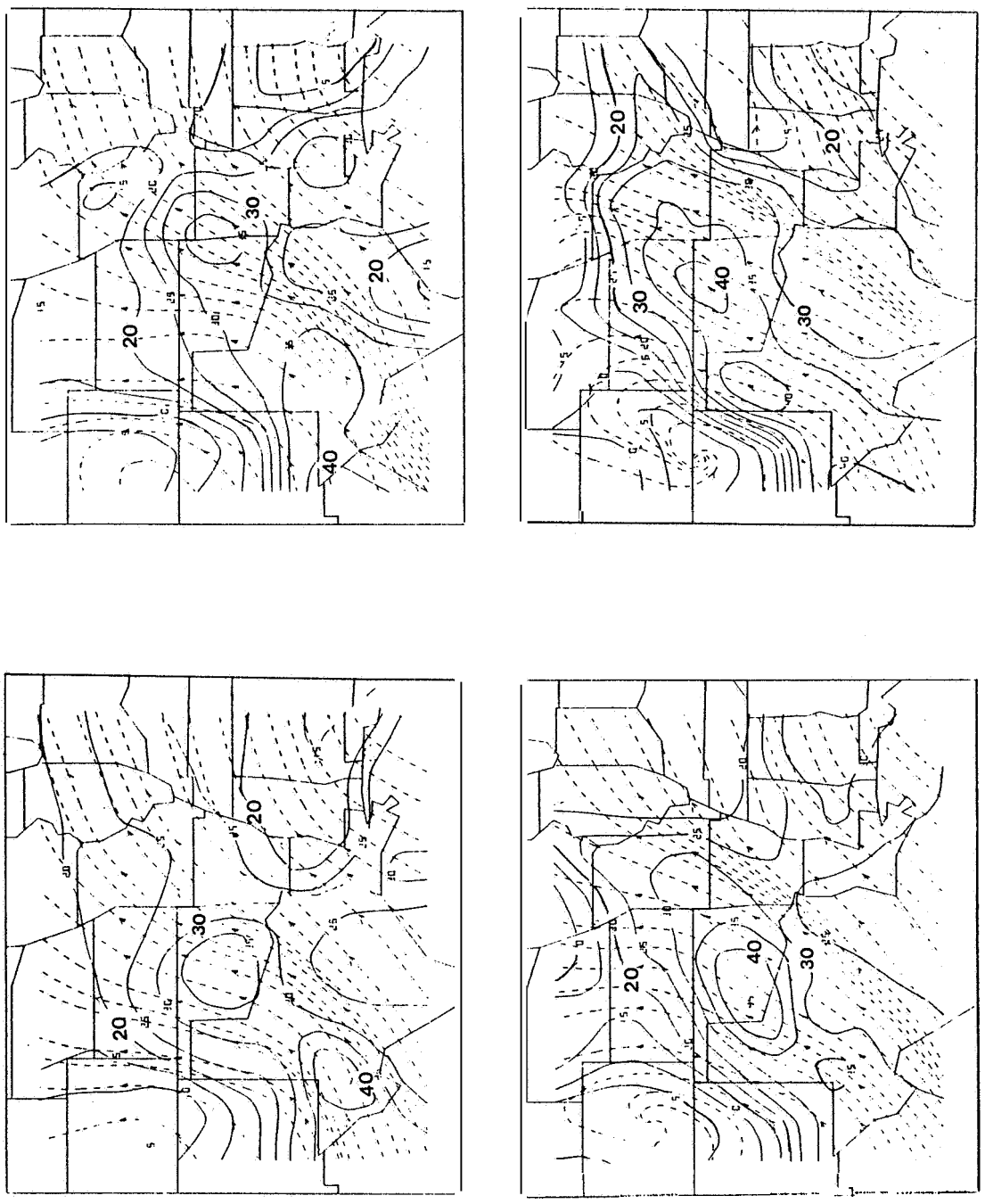

Figure B3: (continued) 500 mb streamlines and isotachs.

Figure B3: (continued) 300 mb streamlines and isotachs.

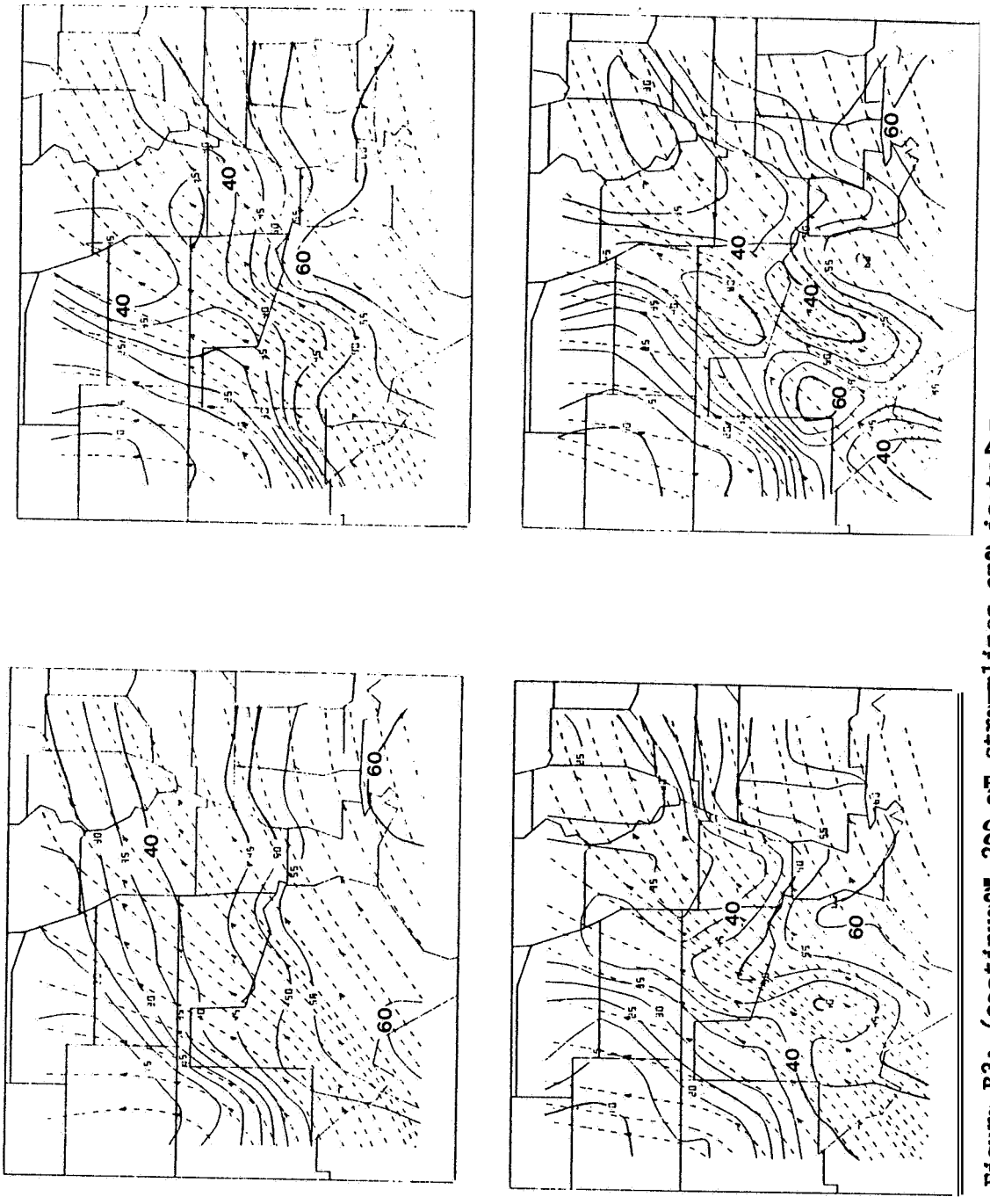

Figure B3: (continued) 200 mb streamlines and isotachs.

Figure B4: NMC hourly radar summaries. Times are indicated on each panel.

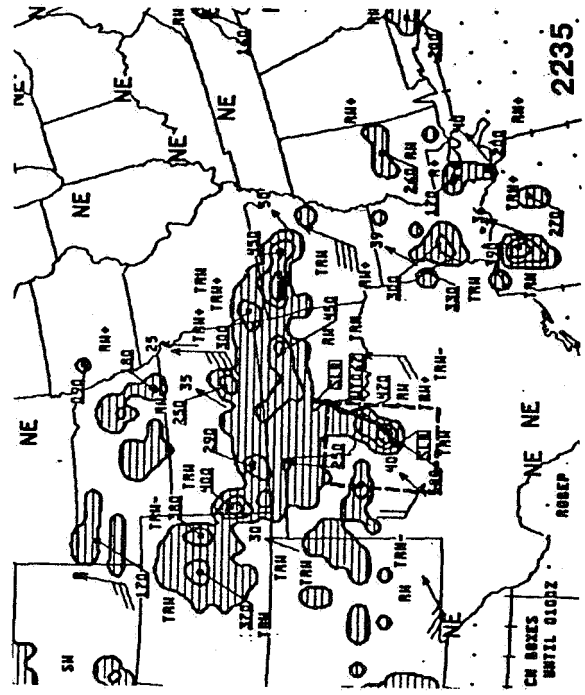
2235
NE
CH BOXES
UNTIL 0100Z

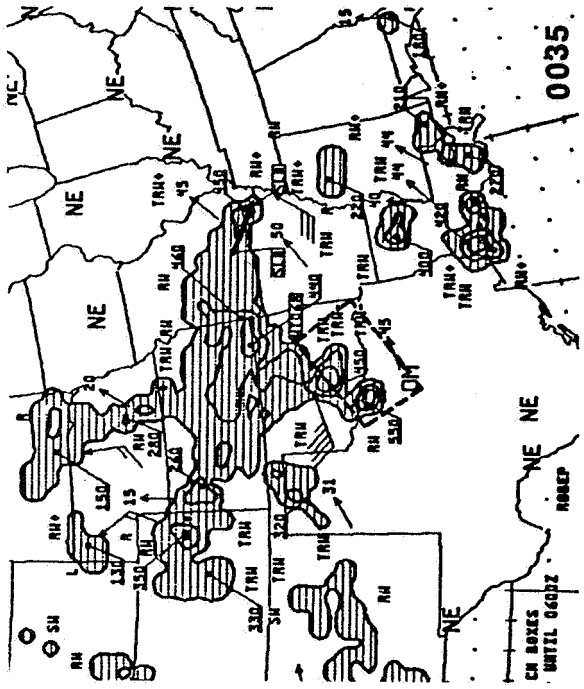
0035
NE
CH BOXES
UNTIL 0600Z

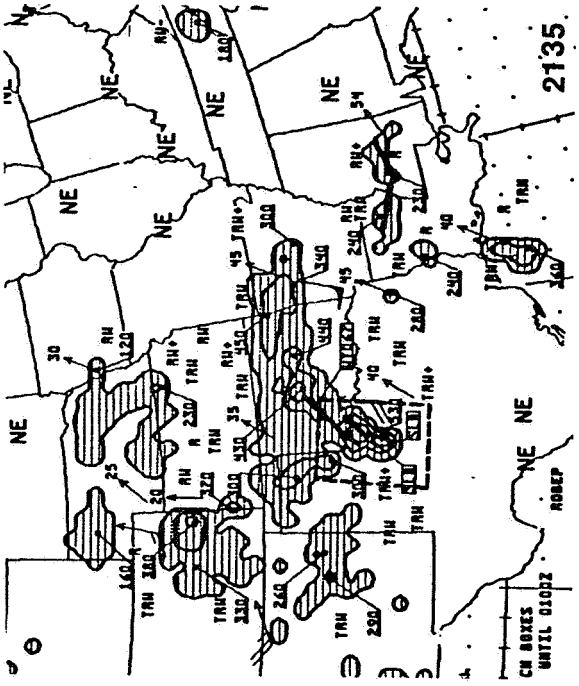
2135
NE
CH BOXES
UNTIL 0100Z

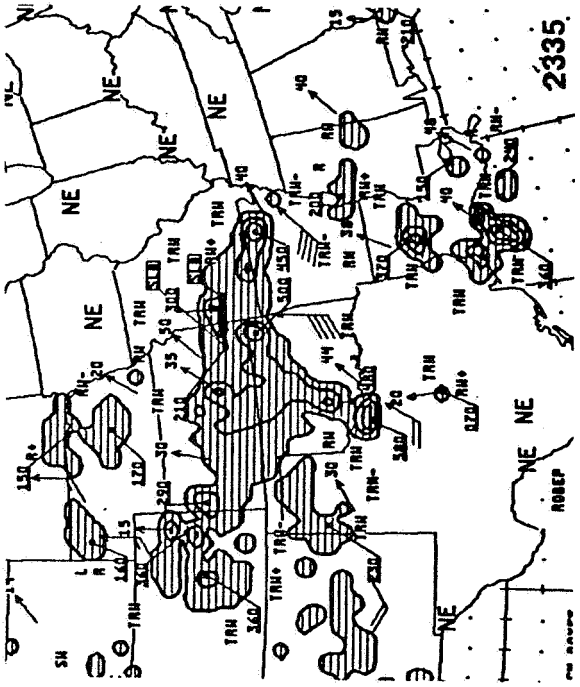
2335
NE

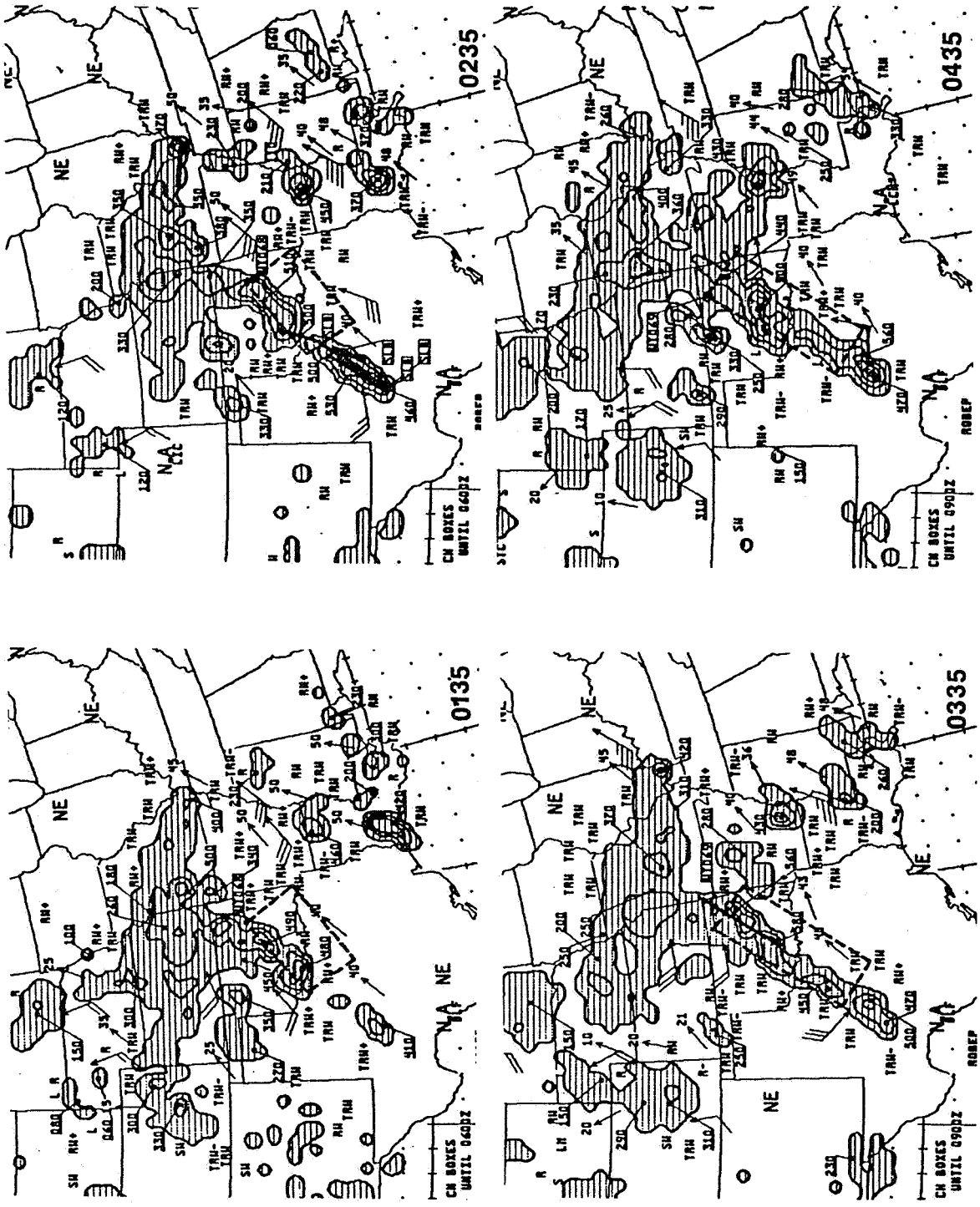
0235
0435
0135
0335
NE
NA
CH BOXES UNTIL 0600Z
CH BOXES UNTIL 0900Z

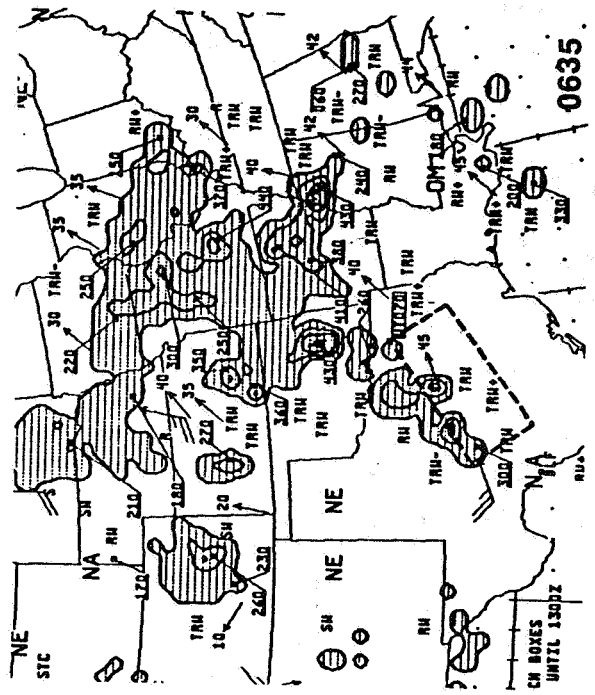
0635
NE
NA
NE
NE
CH BOXES
UNTIL 1300Z

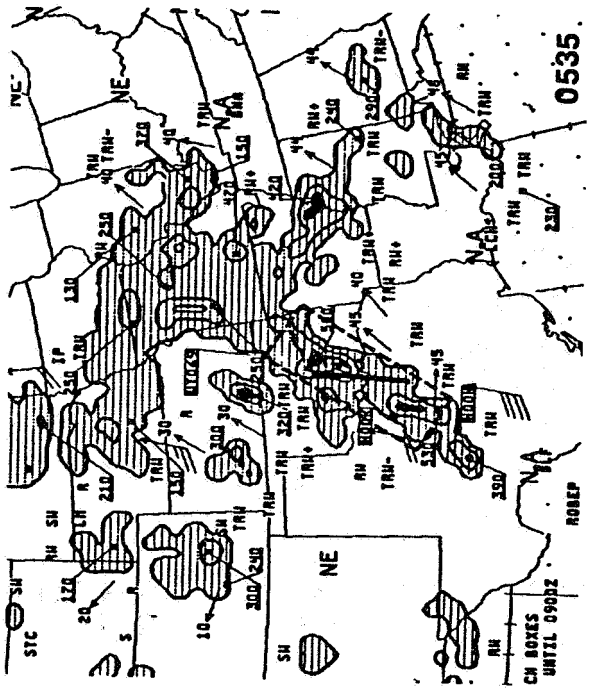
0535
NE
NA
NA
NE
CH BOXES
UNTIL 0900Z

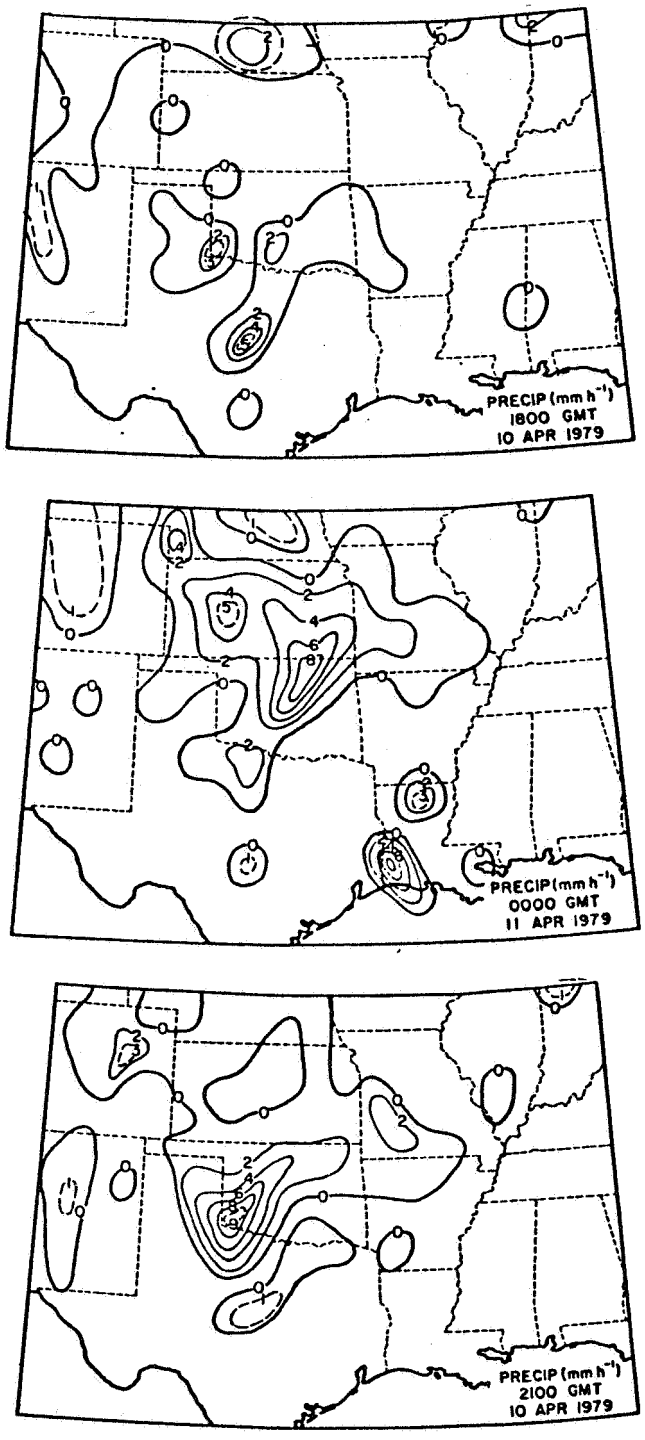

Figure B5: Observed surface precipitation rates for April 10 - 11, 1979. Units and times are shown on each panel. (Reproduced from Vincent and Carney, 1982).

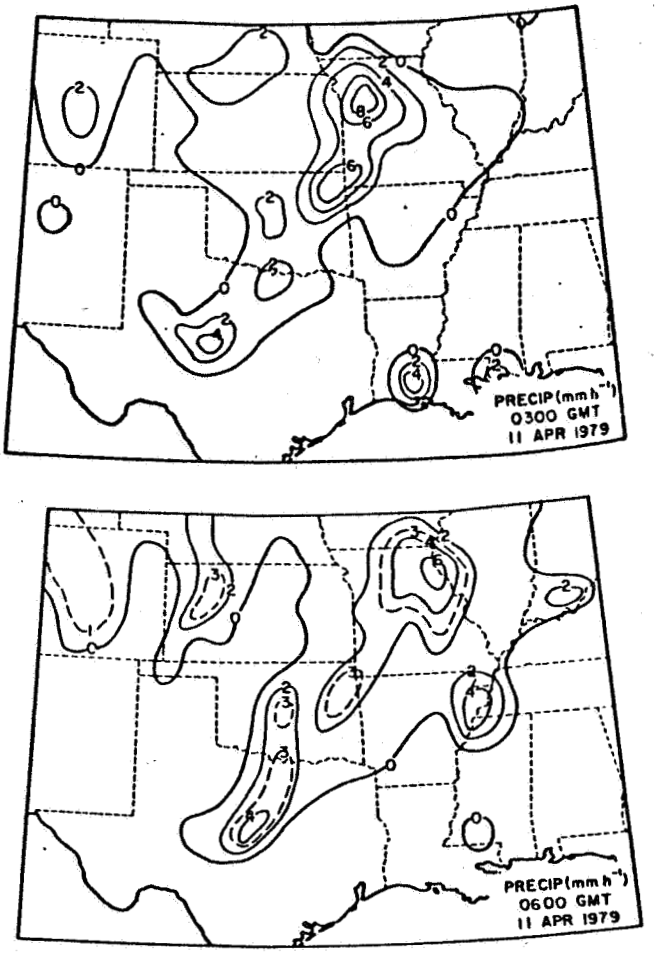

Figure B5: (continued)

Appendix C - Estimation of a Lower Bound on Relative Error in Radiosonde Specific Humidity Measurements

Using the relationship $q = RH \cdot q_s$ one can derive the following expression relating relative errors in q, RH and q_s:

$$(C\text{-}1) \qquad \frac{\Delta q}{q} = \frac{\Delta RH}{RH} + \frac{\Delta q_s}{q_s}$$

Solving $\frac{\Delta q_s}{q_s}$ using the definition of saturation specific humidity $q_s \simeq .622\ e_s/P$, and the Clausius Clapeyron equation $de_s/e_s = LdT/RT^2$, equation (C1) can be written as:

$$(C\text{-}2) \qquad \frac{\Delta q}{q} = \frac{\Delta RH}{RH} + \frac{L\ \Delta T}{RT^2} + \frac{\Delta p}{p}$$

which relates the relative error of q to those of relative humidity, temperature and pressure.

Typical RMS errors in relative humidity measurements are about 10% which implies a minimum relative error of about 10% in RH (i.e., 10%/ 100%). RMS errors for radiosonde temperature and pressure are at least 0.5 °C and 1.3 mb respectively. RMS error estimates are quoted from Fuelberg (1974) in Gerhard,

et al., (1979).

Plugging these error estimates into equation (C2) yields:

$$\frac{\Delta q}{q} = \pm .10 \pm \frac{2.5 \times 10^{10} \text{ erg/gm}}{\frac{8.317 \times 10^{7} \text{ erg/mole } ^{0}\text{K}}{18.016 \text{ gm/mole}}} \times \frac{0.5 \ ^{0}\text{K}}{(280 \text{ K})^{2}} \pm \frac{1.3 \text{ mb}}{850 \text{ mb}}$$

or $$\frac{\Delta q}{q} = \pm .10 \pm .0345 \pm .0015$$

Since any of the above terms may be positive or negative, the maximum lower bound relative error for q is ±13.6% and the minimum relative error is ± 6.4%. These values apply at levels around 850 mb. At higher levels where relative humidity is poorly measured, the relative errors for q may be much larger.

Furthermore, for the example presented, 74% of the total possible error is attributable to mis-measurement of relative humidity, 25% to temperature errors, and only about 1% to pressure errors.

Appendix D - Numerical Solution of the Balance Equation

The full non-linear balance equation is derived in this section as a quadratic equation in the variable $\nabla^2\psi$ where ψ is the stream function of the non-divergent balanced wind. This form facilitates the numerical solution and shows explicitly when the equation is non-elliptic. The derivation is similar to that of Pettersen **(1953)**.

Given the u and v component momentum equations **(Dl)** and **(D2)** in pressure coordinates (spherical terms are neglected)

$$\text{(Dl)} \qquad \frac{\partial u}{\partial t} + u\frac{\partial u}{\partial x} + v\frac{\partial u}{\partial y} + w\frac{\partial u}{\partial z} = -\frac{\partial \Phi}{\partial x} + fv$$

$$\text{(D2)} \qquad \frac{\partial v}{\partial t} + u\frac{\partial v}{\partial x} + v\frac{\partial v}{\partial y} + w\frac{\partial v}{\partial z} = -\frac{\partial \Phi}{\partial y} - fu$$

a divergence equation can be formed by taking $\frac{\partial}{\partial x}$ of (Dl) and $\frac{\partial}{\partial y}$ of **(D2)**, adding them and rearranging to get

$$\text{(D3)} \qquad \frac{d\delta}{dt} = -\nabla^2\Phi - \beta u - f\zeta - \left(\frac{\partial u}{\partial x}\right)^2 - \left(\frac{\partial v}{\partial y}\right)^2 - 2\frac{\partial v}{\partial x}\frac{\partial u}{\partial y}$$

where ζ is the relative vorticity equal to $\frac{\partial v}{\partial x} - \frac{\partial u}{\partial y}$, and

β is equal to $\frac{\partial f}{\partial y}$, and

δ is the horizontal divergence.

Using the definitions of shearing deformation A and stretching deformation B

$$A = \frac{\partial u}{\partial x} - \frac{\partial v}{\partial y} \quad ; \quad B = \frac{\partial v}{\partial x} + \frac{\partial u}{\partial y}$$

it is noted that

$$A^2 = \left(\frac{\partial u}{\partial x}\right)^2 - 2\,\frac{\partial u}{\partial x}\,\frac{\partial v}{\partial y} + \left(\frac{\partial v}{\partial y}\right)^2$$

$$B^2 = \left(\frac{\partial v}{\partial x}\right)^2 + 2\,\frac{\partial u}{\partial y}\,\frac{\partial v}{\partial x} + \left(\frac{\partial u}{\partial y}\right)^2$$

$$\zeta^2 = \left(\frac{\partial v}{\partial x}\right)^2 - 2\,\frac{\partial u}{\partial y}\,\frac{\partial v}{\partial x} + \left(\frac{\partial u}{\partial y}\right)^2$$

and thus

$$\zeta^2 - A^2 - B^2 = -4\,\frac{\partial u}{\partial y}\,\frac{\partial v}{\partial x} + 2\,\frac{\partial u}{\partial x}\,\frac{\partial v}{\partial y} - \left(\frac{\partial u}{\partial x}\right)^2 \left(\frac{\partial v}{\partial y}\right)^2 \tag{D4}$$

Furthermore,

$$(D5)\quad \frac{1}{2}\left(\zeta^2 - A^2 - B^2\right) - \frac{1}{2}\delta^2 = -\left(\frac{\partial u}{\partial x}\right)^2 - \left(\frac{\partial v}{\partial y}\right)^2 - 2\,\frac{\partial u}{\partial y}\,\frac{\partial v}{\partial x}$$

which are the last three terms of equation (D3).

Substituting (D5) into (D3) gives an alternate divergence equation:

$$(D6)\quad \frac{d\delta}{dt} + \frac{1}{2}\delta^2 = -\nabla^2\Phi + f\zeta + \frac{1}{2}\left(\zeta^2 - A^2 - B^2\right) - \beta u$$

Setting divergence equal to zero yields the balance equation in the form

$$(D7)\quad -\nabla^2\Phi + f\zeta + \frac{1}{2}\left(\zeta^2 - A^2 - B^2\right) - \beta u = 0$$

but using the relationship $\zeta = \nabla^2\psi$, one obtains

$$(D8)\quad f\nabla^2\psi - \nabla^2\Phi + \frac{1}{2}\left(\nabla^2\psi\right)^2 - \frac{1}{2}A^2 - \frac{1}{2}B^2 - \beta u = 0$$

which is quadratic in $\nabla^2\psi$.

Using the quadratic formula and $u = -\frac{\partial\psi}{\partial y}$, $v = \frac{\partial\psi}{\partial x}$

gives the final form of the balance equation as:

(D9)

$$\nabla^2\psi = - f \pm (f^2+2\nabla^2\Phi + 4(\frac{\partial^2\psi}{\partial x\partial y})^2 + (\frac{\partial^2\psi}{\partial x^2} - \frac{\partial^2\psi}{\partial y^2})^2 - \beta\frac{\partial\psi}{\partial y})^{1/2}$$

This equation is non-linear in ψ and is usually elliptic.

A negative square root corresponds to non-ellipticity and therefore to physically unreal solutions for the assumption of non-divergence. This condition occurs most frequently where $\nabla^2\Phi$ is strongly negative as in a high pressure area with strong anti-cyclonic curvature (see Figure D1). Paegle and Paegle (1974, 1976) claim to have found situations like that in Figure D1b which are associated with intense anomalous divergence. Therefore they have proposed a method to add just enough divergence to equation (D9) when necessary to insure ellipticity.

Another common approach to the ellipticity problem is based on the fact that the geostrophic stream function, $-\frac{\Phi}{f}$, is frequently close to the balance stream function. Thus, in non-elliptic areas (D9) can

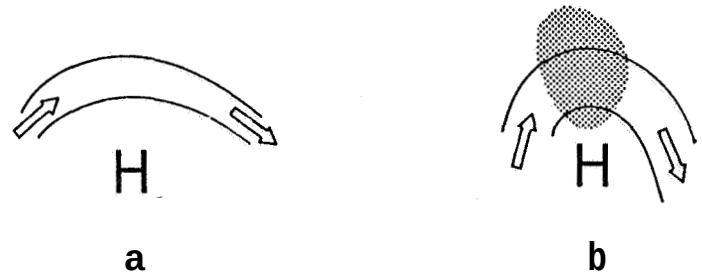

Figure D1: (a) Normal anticyclonic pressure and wind pattern. (b) flow and pressure pattern typically associated with non-elliptic areas (shaded) for the balance equation.

be solved by replacing ψ Balance by ψ geostrophic on the right hand side of the equation. Then the right had side is completely known and the equation may be solved by straight SOR (Krishnamurti, 1968).

As mentioned in chapter 3, the height fields can also be altered prior to numerical solution for ψ, to produce values of $\nabla^2\Phi$ which will guarantee that (D9) is elliptic everywhere. That procedure was not adopted because the height fields are the most reliable type of information provided by the satellite. Instead, in non-elliptic areas the equation $\nabla^2\psi = -f$ was solved which constrains the "balanced" winds to have non-negative absolute vorticity.

The solution of the balance equation involves an

iterative **SOR** technique for getting the quantity $\nabla^2\psi$ to converge over the domain. For each outer iteration for $(\nabla^2\psi)^{\nu+1}$ one inner iteration is required to obtain $\psi^{\nu+1}$. The outer iteration is given by

$$(D10) \qquad (\nabla^2\psi)^{\nu+1} = (\nabla^2\psi)^{\nu}(1-\omega) + (h(\psi^{\nu}))\ (\omega)$$

where ω is the relaxation factor and

$$h(\psi^{\nu}) = -f + (f^2 + 2\nabla^2\Phi + A^{2^{\nu}} + B^{2^{\nu}} + \beta u^{\nu})^{1/2}$$

The inner iteration is

$$(D11) \qquad \psi^{\nu+1} + \psi^{\nu}\ (1-\alpha) + (g(\psi^{\nu},\ (\nabla^2\psi)^{\nu+1}))\ (\alpha)$$

where α is the relaxation factor and the function g is given by

$$(D12) \qquad g(\psi^{\nu},\ (\nabla^2\psi)^{\nu+1} = (\nabla^2\psi)^{\nu+1} - \left(\frac{\psi^{\nu}_{i,j+1} + \psi^{\nu}_{i,j-1}}{\gamma^2}\right.$$

$$\left. + \psi^{\nu}_{i-1,j} - \psi^{\nu}_{i+1,j}\right)/\left(2 + \frac{2}{\gamma^2}\right) \ ;\ \gamma = \cos\ (\text{latitude})$$

The relaxation factor for the inner iteration, *a,* was chosen according to a formula from Haltiner and Williams (1980):

$$\alpha \text{ optimal} = 2 - \frac{2\pi}{\sqrt{2}}\left(\frac{1}{M^2} + \frac{1}{N^2}\right)^{1/2}$$

where **M** and **N** are the number of grid points in the x and y directions, The coefficient ω was determined experimentally. The test results are summarized in Figure D2. ω equal to **0.35** corresponds to under-relaxation and appears to be optimal for all levels. The lower levels (850 mb) converged much more rapidly than the upper levels. The range of convergent ω's was smaller for higher levels.

All derivatives were computed with second order finite differencing on a one degree latitude/longitude

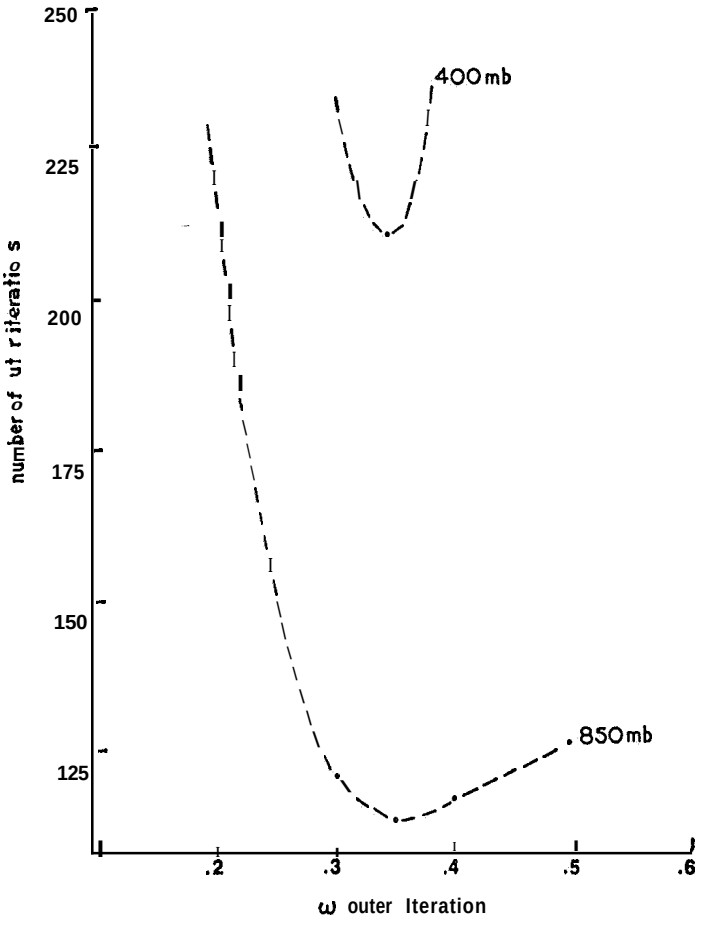

Figure D2: Graph of the relaxation factor for the outer iteration versus the number of iterations required for convergence at 850 and *400* mb. The optimal ω is about 0.35 corresponding to under-relaxation,

grid (see Figure D3). The mixed derivatives $\frac{\partial^2 \psi}{\partial x \partial y}$ were computed from this grid as $\frac{1}{2}\left(\frac{\partial}{\partial x}\left(\frac{\partial \psi}{\partial y}\right) + \frac{\partial}{\partial y}\left(\frac{\partial \psi}{\partial x}\right)\right)$. The term βu was calculated as $2\Omega_e \cos(\phi)\, u/a$ where Ω_e is the earth's angular velocity, "a" is the earth's radius and ϕ is latitude.

In order for the solution to converge, net

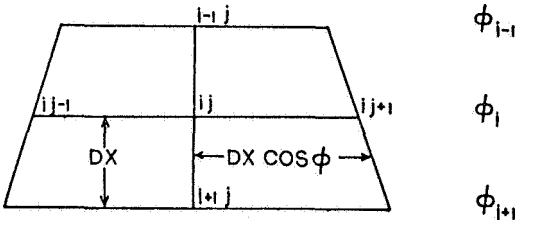

Figure D3: Grid stencil used for balance equation finite differencing. Φ refers *to* latitude.

divergence over the domain must be close to zero. This can be assured by choosing boundary values of ψ such that

$$\oint \frac{\partial \psi}{\partial s} \Delta S = 0$$

where **AS** is an interval of distance along the lateral boundaries. Since the geostrophic stream function $-\frac{\Phi}{f}$ calculated from the height fields is similar to the balance **stream** function, ψ , the former is used ***as*** a first guess on the boundaries and then adjusted to achieve zero outflow. The method is as described in Bengtsson and Temperton (1979, pg. **374).**

Since the balanced winds were computed on a one degree grid and horizontally interpolated to the finer mesh model grid, a test was made to determine how well the representation of the balanced winds is preserved after the interpolation. Panel a in Figure **D4** shows an

initial 850 mb height field from which balanced winds were computed. The resultant winds were interpolated to the model grid and the residual divergence removed as described in section 3.2. The balance equation was then reversed in order to regenerate a height field from the winds in the model coordinates. These heights (panel b) compared very well with the original heights indicating that the integrity of the original balanced winds is maintained after the horizontal interpolation. Panels c and d in Figure D4 show that the adjustments to the wind field after the removal of interpolation generated divergence are trivial.

Any imbalances between the mass and wind fields (as defined by the balance equation) in the model initial state must be due almost entirely to vertical interpolation. Such imbalances are inevitable since the winds and pressure-heights from which they were computed are interpolated to model coordinates independently of one another (Sundqvist, 1976). However, the largest errors are likely to be in the mass field because the heights from which the balanced winds were originally calculated are re-computed (as π on h_σ sufaces) by integrating upward hydrostatically

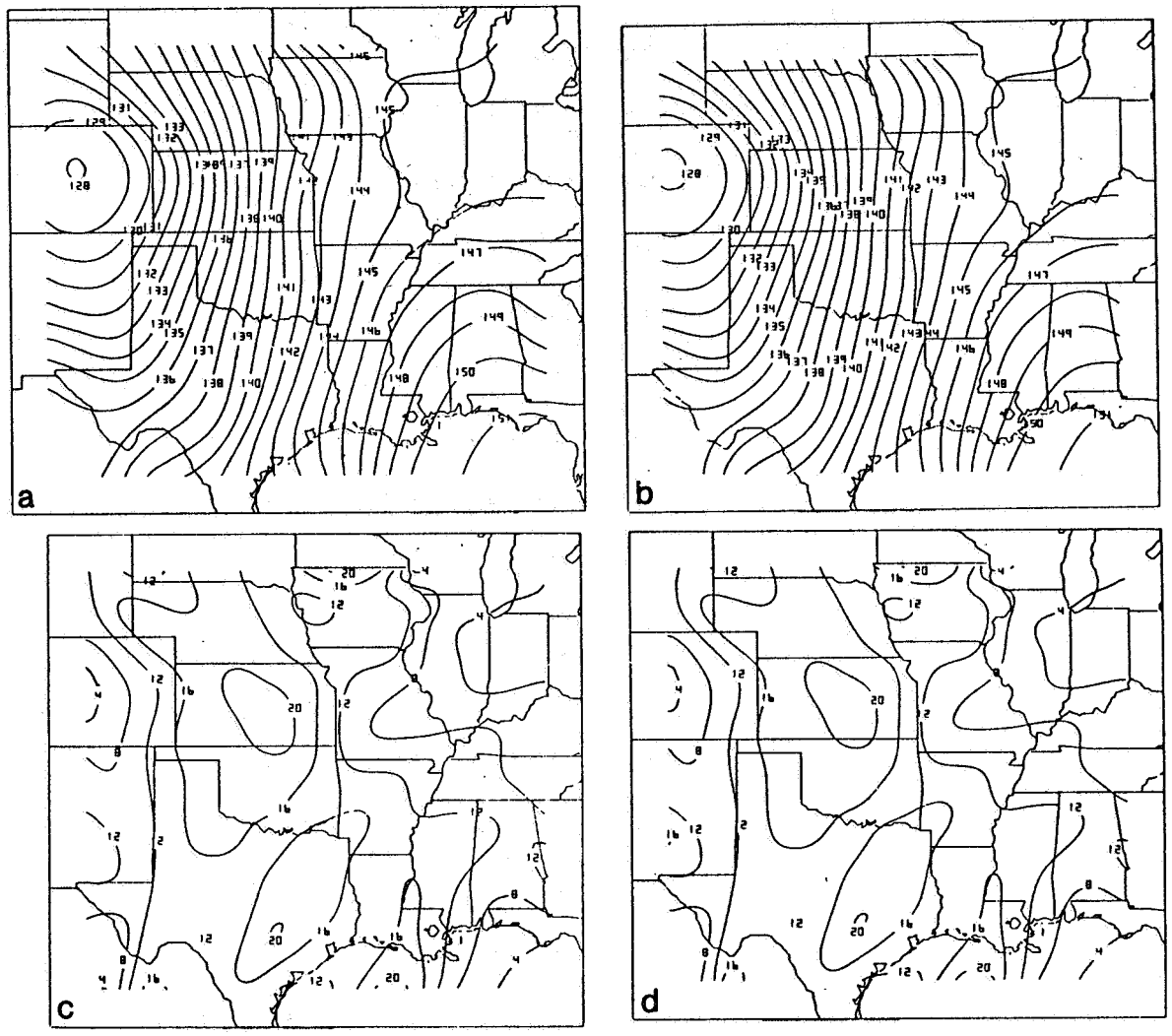

Figure D4: (a) original height field (1° grid) from which balanced winds were computed. (b) height field obtained by inverse solution of the balance equation from the balanced winds which had been interpolated to model coordinates. (c) balanced wind speeds in model coordinates. (d) same winds as in (c) except that small interpolation related divergence has been removed.

using independent linear vertical interpolated values of temperature and specific humidity (Barker, 1980).

Non-linear balanced winds and the non-divergent portion of the gradient winds for the same height field are compared in Figure D5. The strong likeness of the two wind fields suggests that considerable computer time can be saved by using the non-divergent gradient stream functions as a first guess for the balanced stream functions. It is also possible that the non-divergent gradient wind might be just as satisfactory as the balanced wind for initializing the LAMPS model. These winds have already been used for initializing the Australian numerical model (Mills and Hayden, 1982).

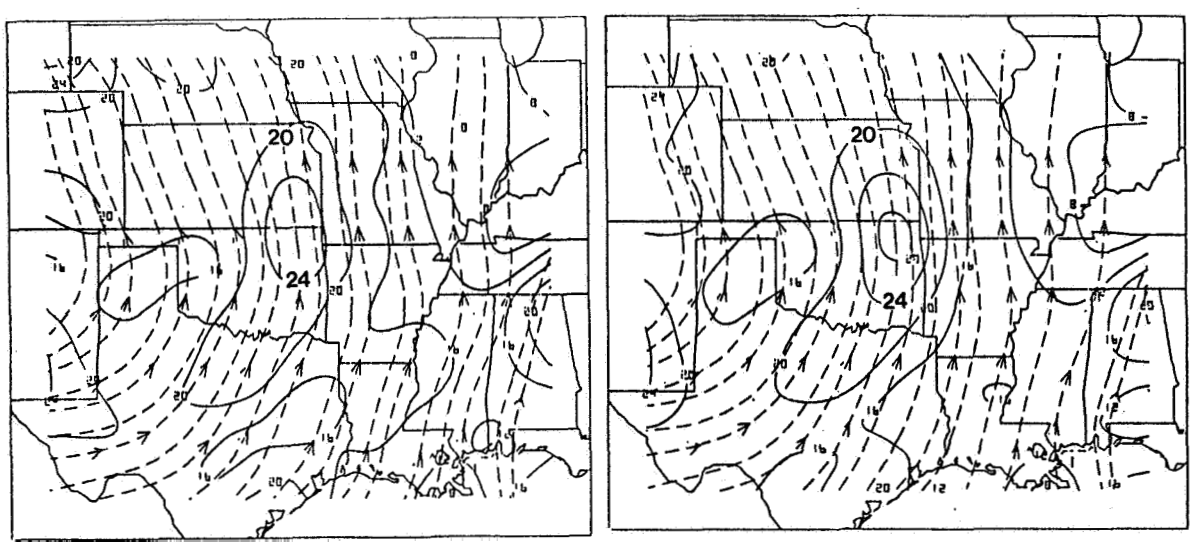

Figure D5: Comparison of non-linear balanced winds (left) and non-divergent gradient winds for the same 850 mb height analysis.

Appendix E - Numerical Solution of the Quasi-geostrophic Vertical Motion Equation and Continuity Equation in Model Coordinates

To solve the quasi-geostrophic vertical motion equation in h coordinates requires a similar equation in z coordinates which is to be transformed term by term so that derivatives on z surfaces can be calculated from values on the model h surfaces. The equation used is by Lee (1981):

(E1)

$$(\sigma_1-\sigma_2)\nabla_z^2(\rho w) + f_o^2\left(\frac{\partial^2}{\partial z^2}\rho w\right) = f_o\frac{\partial}{\partial z}\{(\rho\vec{V}_g\cdot(\nabla_z^2 p + f))\} + \frac{gR}{C_p}\nabla_z^2(\vec{V}_g\cdot\vec{\nabla}\rho)$$

where $\sigma_1 = g\frac{\partial \ln\theta}{\partial z}$ and $\sigma_2 = g\frac{C_p}{C_v}\frac{\partial \ln P}{\partial z}$. Other variables have their usual meteorological meanings.

The grid stencil used is as shown in Figure E1 where ϕ is a dummy varible. The subscripts N, S, e, and w refer to points on a compass and U and L refer to upper and lower levels. DY is the north - south distance between grid points. The east - west distance is DX = DY * cos (latitude). The finite differencing

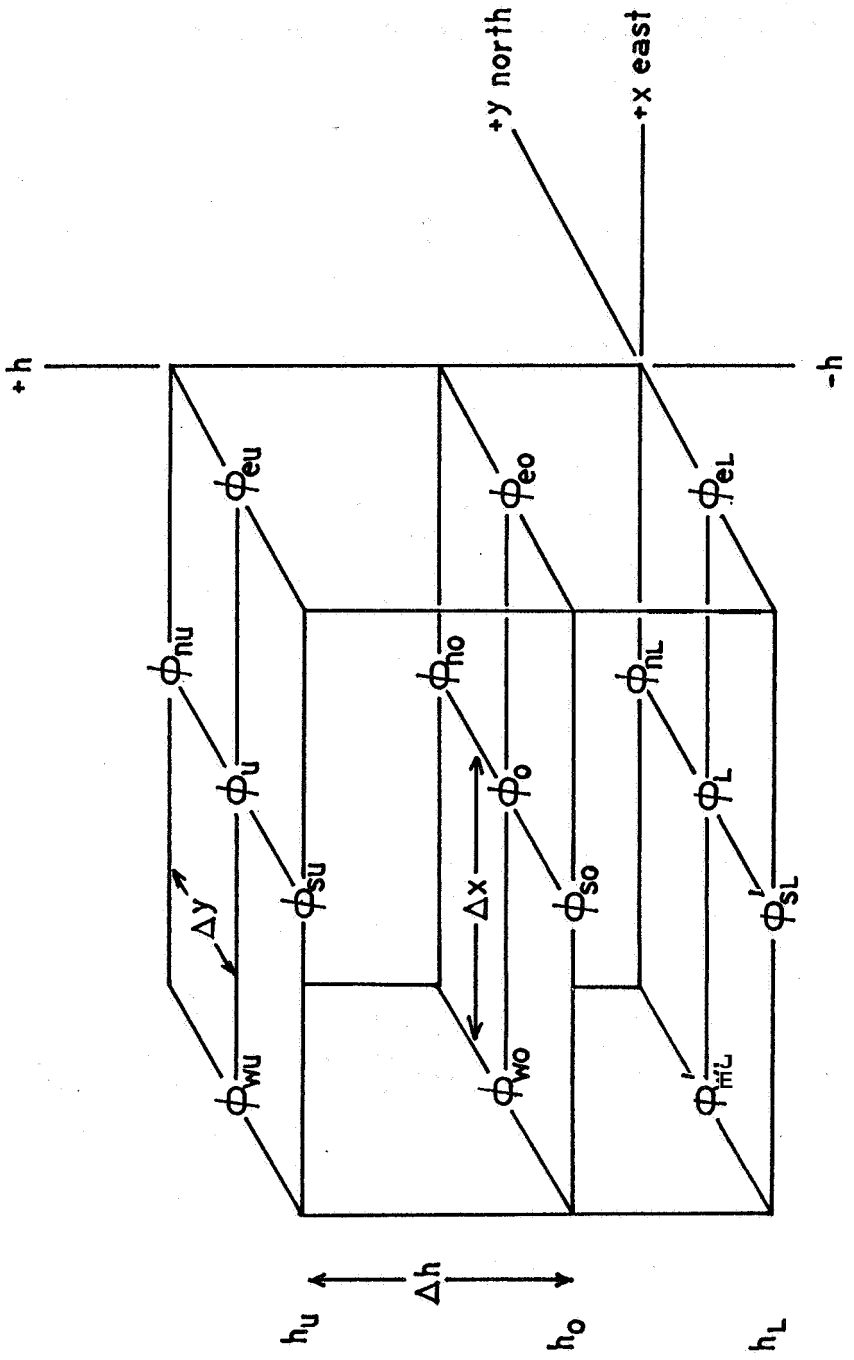

Figure E1: Grid stencil used in omega equation finite differencing.

employed **is** second under accurate. Spherical terms are neglected.

From the basic relations **for** the h_σ coordinate **sys**tem,

$$h_\sigma = \frac{E}{H-E} \mathbf{H6} + (1-6)Z \quad \text{and} \quad \frac{\partial \phi}{\partial x}\Big|_Z = \frac{\partial \phi}{\partial x}\Big|_h - \frac{\partial \phi}{\partial} \frac{\partial Z}{\partial X}\Big|$$

the following transformations can be derived:

$$\frac{\partial Z}{\partial X}\Big|_h = \delta \left(\frac{H-Z}{H-E}\right) \frac{\partial E}{\partial X}$$

$$\frac{\partial \phi}{\partial x}\Big|_Z = \frac{\partial \phi}{\partial x}\Big|_h - \delta \frac{\partial \phi}{\partial h} \frac{\partial E}{\partial X} \left(\frac{H-h}{H-E}\right)$$

$$\frac{\partial^2 \phi}{\partial X^2}\Big|_Z = \frac{\partial^2 \phi}{\partial X^2}\Big|_h - \delta \left(\frac{H-h}{H-E}\right) \left\{\frac{\partial E}{\partial X}\left(2\frac{\partial^2 \phi}{\partial X \partial h} - \frac{\partial E}{\partial X} \frac{H-h}{H-E} \frac{\partial^2 \phi}{\partial h^2}\right) + \right.$$

$$\left. \left(2\frac{\left(\frac{\partial E}{\partial X}\right)^2}{H-E} + \frac{\partial^2 E}{\partial X^2}\right) \frac{\partial \phi}{\partial h}\right\}$$

$$\frac{\partial \phi}{\partial Z} = \frac{\partial \phi}{\partial h} \left(1-\delta' + \delta' H/(H-E)\right)$$

$$\frac{\partial^2 \phi}{\partial Z^2} = \frac{\partial^2 \phi}{\partial h^2} \left(1-\delta' + \delta' H/(H-E)\right)^2$$

Also, given $p = 1000 \left(\frac{\pi}{C_p}\right)^{C_p/R}$ and $\rho = \frac{C_p}{R} \frac{p}{\pi\theta}$

the geostrophic wind components can be calculated as

$$u_g = - \frac{\theta}{f} \frac{\partial \pi}{\partial y}\bigg|_h - \delta \frac{g}{f} \frac{\partial E}{\partial y} \left(1- \frac{h}{H}\right)$$

$$v_g = \frac{\theta}{f} \frac{\partial \pi}{\partial X}\bigg|_h + \delta \frac{g}{f} \frac{\partial E}{\partial X} \left(1 - \frac{h}{H}\right)$$

The second order accurate finite difference formula required are

$$\frac{\partial \phi}{\partial X}\bigg|_h = \frac{\phi_e - \phi_w}{2\ DX}$$

$$\frac{\partial^2 \phi}{\partial X^2}\bigg|_h = \frac{\phi_e + \phi_w - 2\phi_o}{DX^2}$$

$$\frac{\partial \phi}{\partial h}\bigg|_o = \frac{\chi(\phi_u-\phi_o) + (\phi_o-\phi_L)/\chi}{h_u-h_L} = \frac{\chi(\phi_u-\phi_0) + (\phi_o-\phi_L)/\chi}{(\Delta h)\,(1+\chi)}$$

$$\left.\frac{\partial^2\phi}{\partial h^2}\right|_o = \frac{\chi\phi_u + \phi_L - (1+\chi)\phi_o}{\frac{1}{2}(h_u-h_o)^2(\chi^2+\chi)}$$

$$\left.\frac{\partial^2\phi}{\partial x\partial h}\right|_o = \frac{\chi(\phi_{eu}+\phi_{wo}-\phi_{wu}-\phi_{eo}) + \frac{1}{\chi}(\phi_{eo}+\phi_{wL}-\phi_{wo}-\phi_{eL})}{2(1+\chi)\,DX\,(h_u-h_o)}$$

The coordinate system parameters, δ and δ' (good for all x, y) are required to switch on ($\delta = 1$) or off ($\delta = 0$) terms in the equations related to sloped h_σ surfaces below **H** = 5250 meters. χ is a ratio relating the vertical distance Δh for a model layer to the depth of the model layer immediately below it, i.e.,

$$\chi = (h_o - h_L)/(h_u - h_o)$$

The following table lists values of δ, δ' and χ for each h level.

h	δ	δ'	X
0	1	1	0.000
25	1	1	0.071
375	1	1	0.933
750	1	1	0.750
1250	1	1	0.677
2000	1	1	0.750
3000	1	1	0.667
4500	1	0.75	1.000
6000	0	0.25	1.000
7500	0	0	1.000
9000	0	0	1.000
10500	0	0	1.000
12000	0	0	.750
14000	0	0	1.000
16000	0	0	0.000

Derivation of SOR formula

Let the right hand side of equation (El) equal F, and let

$$K1 = g(a_1 - \sigma_2) \; ; \; \phi = pw \text{ and } K2 = f_o^2$$

Then the equation can be written

$$K1 \, \nabla_z^2 \phi + K2 \, \frac{\partial^2 \phi}{\partial z^2} = F$$

By letting Q = (H-h)/(H-E) and

S = (1-6^{I}+δ^{1}H/(H-E)) and using the transformation for

the laplacian on a z surface we get

$$Kl\ \nabla_h^2\phi - QKl\delta\ 2\frac{\partial E}{\partial x}\frac{\partial^2\phi}{\partial x\partial h} + 2\frac{\partial E}{\partial y}\frac{\partial^z\phi}{\partial y\partial h}\ Q((\frac{\partial E}{\partial x})^2 + (\frac{\partial E}{\partial y})^2)\frac{\partial^2\phi}{\partial h^2}$$

$$+ (2((\frac{\partial E}{\partial x})^2 + (\frac{\partial E}{\partial y})^2/(H-E) + \nabla_h^2 E)\frac{\partial\phi}{\partial h} + K2\ S^2\ \frac{\partial^2\phi}{\partial h^2} = F$$

where the terms in **F** have been transformed into h_σ coordinates, By defining

$$I = 2\ Q\ Kl\ \delta\ \frac{\partial E}{\partial X},\quad J = 2\ Q\ Kl\ \delta\ \frac{\partial E}{\partial y}$$

$$N = Q^2\ Kl\delta\ ((\frac{\partial E}{\partial X})^2 + (\frac{\partial E}{\partial y})^2)/(H-E) + \nabla^2 E)$$

$$L = (-\ Q\ Kl\ \delta\ (2((\frac{\partial E}{\partial X})^2 + (\frac{\partial E}{\partial y})^2)/(H-E) + \nabla^2 E))/Kl$$

and dividing by Kl, the above equation can be expressed as

$$\nabla_h^2\phi + P\frac{\partial^2\phi}{\partial h^2} + L\frac{\partial\phi}{\partial h} = \frac{F}{K1} + \frac{I}{K1}\frac{\partial^2\phi}{\partial x\,\partial h} + \frac{J}{K1}\frac{\partial^2\phi}{\text{ayah}}$$

where P = N / K1.

The terms on the left hand side can be expanded into finite difference form yielding

$$\frac{\phi_e + \phi_w}{DX^2} + \frac{\phi_N + \phi_S}{DY^2} - \frac{2\phi_o}{DX^2} - \frac{2\phi_o}{DY^2} + \frac{2P(\chi\phi_u+\phi_L)}{(\Delta h)^2(\chi^2+\chi)} - \frac{2P(1+\chi)\phi_o}{(\Delta h)^2(\chi^2+\chi)}$$

$$+ L\left(\frac{\chi\phi_u - \phi_L/\chi}{\Delta h\ (1+\chi)}\right) + \frac{L(1-\chi)\phi_o}{\chi(\Delta h)} = \frac{F}{K1} + \frac{I}{K1}\frac{\partial^2\phi}{\partial x\partial h} + \frac{J}{K1}\frac{\partial^2\phi}{\partial y\partial h}$$

After moving all terms not involving ϕ_o to the right hand side, and multiplying both sides by DX2DY2(Ah)2χ , the equation becomes

$$(2(\Delta h)^2\chi(DX^2+DY^2) + DX2DY2(2P+(1-\chi)L\Delta h))\phi_o =$$

$$\left\{\frac{F}{K1} + \frac{I}{K1}\frac{\partial^2\phi}{\partial X\partial h} + \frac{J}{K1}\frac{\partial^2\phi}{\partial y\partial h} - \frac{(\phi_e+\phi_w)}{DX^2} - \frac{(\phi_N + \phi_S)}{Dy^2}\right.$$

a

$$- \frac{2P(\chi\phi_u+\phi_L)}{(\Delta h)^2(\chi^2+\chi)}$$

$$- \frac{L(\chi\phi_u - \phi_L/\chi)}{\Delta h(1+\chi)} \} \times DX^2DY^2(\Delta h)^2\chi$$

Finally, the SOR formula can be written as

$$\phi_o^{\nu+1} = (1-\gamma)\phi_o^{\nu} +$$

$$\gamma \{H\} \frac{DX^2DY^2(\Delta h)^2\chi}{2(\Delta h)^2\chi(DX^2+DY^2) + DX^2DY^2(2P+(1-\chi)L\Delta h)}$$

After solving for $\phi_o = (\rho w)_o$, dividing by density yields vertical motion dz/dt on the model h_σ surfaces. The relaxation factor, γ, which was optimal was determined experimentally to be about 1.2.

<u>solution of model continuity equation for the horizontal divergent wind components on model h surfaces</u>

The model continuity equation is

$$\frac{\partial}{\partial h}(P\dot{h}) = -\frac{\partial}{\partial x}(Pu) - \frac{\partial}{\partial y}(Pv)$$

$$-\frac{\partial P}{\partial t} + P\left(\frac{\dot{Q}}{\theta\pi} + \frac{v \tan \phi}{a} + \frac{\vec{V} \cdot \vec{\nabla} E}{H-E}\delta\right)$$

where $P = p/\pi$. Neglecting the diabatic and curvature terms and setting $\partial P/\partial t = 0$, the equation can be expanded to

$$P\frac{\partial \dot{h}}{\partial h} + \dot{h}\frac{\partial P}{\partial h} = -P\frac{\partial u}{\partial x}\Big|_h - P\frac{\partial v}{\partial y}\Big|_h -$$

$$u\frac{\partial P}{\partial x} - v\frac{\partial P}{\partial y} + \frac{P\delta}{H-E}(\vec{V}_\chi + \vec{V}_\psi) \cdot \vec{\nabla} E$$

where $\vec{V}$ has been expressed in terms of a divergent and non-divergent component. Using the relation

$\frac{\partial w}{\partial z} = \frac{\partial \dot{h}}{\partial h} = (1-\delta' + \delta' H/(H-E)) \frac{\partial w}{\partial h}$, the forcing function F is

$$F = P(1-\delta'+\delta' H/(H-E)) - \frac{P\delta}{H-E} \vec{V}_{\Psi} \cdot \vec{\nabla} E$$

Then using $u = -\frac{\partial \chi}{\partial X}$ and $v = -\frac{\partial \chi}{\partial Y}$, the continuity equation is written

$$-P \nabla^2 \chi - \vec{\nabla} \chi \cdot \vec{\nabla} P + \frac{P\delta}{H-E} \vec{\nabla} \chi \cdot \vec{\nabla} E = -F$$

or

$$-\nabla^2 \chi + \left(-\frac{\vec{\nabla} P}{P} + \frac{\delta}{H-E} \vec{\nabla} E\right) \cdot \vec{\nabla} \chi = -F/P = FF$$

which can be reformatted as

$$-\frac{\partial^2 \chi}{\partial x^2} - \frac{\partial^2 \chi}{\partial y^2} + \underbrace{\left(-\frac{1}{P} \frac{\partial P}{\partial x} + \frac{\delta}{H-E} \frac{\partial E}{\partial x}\right)}_{K1} \frac{\partial \chi}{\partial x} +$$

$$\underbrace{\left(-\frac{1}{P} \frac{\partial P}{\partial y} + \frac{\delta}{H-E} \frac{\partial E}{\partial y}\right)}_{K2} \frac{\partial \chi}{\partial y} = FF$$

Then with finite differencing

$$\frac{-(\chi_e + \chi_w)}{DX^2} - \frac{(\chi_N+\chi_S)}{DY^2} + \frac{2\chi_o}{DX^2} + \frac{2\chi_o}{DY^2} =$$

$$FF - K1\ \frac{\partial \chi}{ax} - K2\ \frac{\partial \chi}{\partial y}$$

Multiplying both sides by DX2DY2 gives

$$2(DX2+DY2)\chi_o = (FF-K1\ \frac{\partial \chi}{\partial x}-K2\ \frac{\partial \chi}{\partial y} +$$

$$\frac{\chi_e+\chi_w}{DX^2} + \frac{\chi N+\chi_S}{DY^2})\ DX^2DY^2$$

from which the SOR formula can be written:

$$\chi_o^{v+1} = \chi_o^v\ (1-\gamma) + \frac{\gamma DX^2DY^2}{2(DX^2+DY^2)}\ FF - K1\ \frac{\chi_e-\chi_w}{2DX}$$

$$- K2 \frac{\chi_N - \chi_S}{2DY} + \frac{\chi_N + \chi_S}{DY^2} + \frac{\chi_e + \chi_w}{DX^2}$$

where ν is the iteration index and γ is the relaxation factor. $\gamma = 1.8$ was used with good results. The u and v divergent components are derived from the gradients of the χ field.

REFERENCES

Alberty, R. L., Burgess, D. W., and Fujita, T. T., 1980: Severe weather events of April 10, 1979. BAMS, 61:9, pp. 1033-1034.

Anthes, R. A., Hsie, Eirh-yu, Keyser, D., and Kuo, Y-H., 1981: Impact of data and initialization procedures on variations of vertical motion and precipitation in mesoscale models. PROC. IAMAP Symposium. Hamburg. pp. 245-257.

Anthes, R., Kuo, Y.-H., Benjamin, S. G., and Li, Y.-F., 1982: The evolution of the mesoscale environment of severe local storms: Preliminary modeling results. MWR, 110:9, pp. 1187-1213.

Arnold, James E., 1982: Characteristics of ageostrophic flow in the vicinity of a severe weather outbreak (AVE-SESAME I). Preprints of 12th Conference on Severe Local Storms. AMS. pp. 205-208.

Asselin, Richard, 1967: The operational solution of the balance equation. Tellus, 19:1, pp. 24-31.

Atlas, R., Ghil, M., and Halem, M., 1982: The effect of model resolution and satellite sounding data on GLAS model forecasts. MWR, 110:7, pp. 662-681.

Barker, Edward H., 1980: Solving for temperature using unnaturally latticed hydrostatic equations. MWR, 108:8, pp. 1260-1268.

Barnes, Stanley L., 1973: Mesoscale objective map analysis using weighted series observations. NOAA Tech Memo. ERL-NSSL-62. 60 pp.

Barnes, Stanley L., 1981: SESAME 1979 Data User's Guide. Project SESAME, U.S. Department of Commerce, NOAA/ERL Building, Boulder, CO. 236 pp.

Bengtsson, L. and Temperton, C. Numerical Methods Used In Atmospheric Models. Volume II. GARP Publications Series no. 17. World Meteorological Organization, 1979, 499 pp.

Bolin, Bert, 1953: The adjustment of a non-balanced velocity field towards geostrophic equilibrium in a stratified fluid. Tellus, 5:3, pp. 373-385.

Broderick, Harold J., 1980: Structure of a baroclinic zone using TIROS-N retrievals. Preprints of 8th conference on weather forecasting and analysis. AMS, pp. 129-134.

Chang, C. B., Perkey, D. J., and Kreitzberg, C. W., 1982: A numerical case study of the effects of latent heating on a developing wave cyclone. JAS, 39:7, pp. 1555-1570.

Daley, Roger, 1981: Normal mode initialization. Review of Geophysics and Space Physics, 19:3, pp. 450-468.

Dey, C. H. and McPherson, R. D., 1977: An experiment in global divergent initialization. MWR, 105:11, pp. 1372-1383.

Doneaud, Andre, A., Miller, James R., Priegnitz, David L., and Engle, Thomas, 1981: The role of mesoscale surface motion in the life cycle of a convective storm in a dry contiental climate. Proceedings of IAMAP Symposium. Hamburg, pp. 188-191.

Ellsaeser, H. W., 1968: Comparative test of wind laws for numerical weather prediction. MWR, 96:5, pp. 277-285.

Fiorino, Michael and Warner, Thomas T., 1981: Incorporating surface winds and rainfall rates into the initialization of a mesoscale hurricane model. MWR, 109:9, pp. 1914-1929.

Fritsch, J. M. and Maddox, R. A., 1981: Convectively driven mesoscale systems aloft. Part I: Observations. JAM, 20:1, pp. 9-19.

Fritsch, J. M. and Brown, J. M., 1982: On the generation of convectively driven mesohighs aloft. MWR, 110:11, pp. 1554-1563.

Gerhard, M. L., Fuelberg, H. E., Williams, S. F., and Turner, R. E., 1979: AVE-SESAME I: 25-mb Sounding Data. NASA Tech. Memo. NASA TM-78256.

Ghil, M., Halem, Y., and Atlas, R., 1979: Time continuous assimilation of remote sounding data and its effect on weather forecasting. MWR, 107:2, pp. 140-171.

Gruber, Arnold and Watkins, Carmella D., 1982: Statistical assessment of the quality of TIROS-N and NOAA-6 satellite soundings.- MWR, 110:7, pp. 867-882.

Gyakum, J. R., 1981: On the nature of explosively developing cyclones in the northern hemisphere extratropical atmosphere. Ph.D. Thesis. Massachusetts Institute of Technology, Cambridge, MA, 225 pp.

Haltiner, G. J. and Williams, R. T., 1980: Numerical Prediction and Dynamic Meteorology. Wiley and Sons, Inc., New York, 477 pp.

Hayden, C. M., 1973: Experiments in four-dimensional assimilation of NIMBUS-4 SIRS data. JAM, 12:3, pp. 425-440.

Hillger, Donald W. and Vonder Haar, Thomas, H., 1979: An analysis of satellite infrared soundings at the mesoscale using statistical structure and conrelation functions. JAS, 36:2, pp. 287-305.

Homan, J. H. and Vincent, D. G., 1982: Mesoanalysis of the severe storm outbreak of 10-11 April 1979. Preprints of 12th conference on severe local storms. AMS, pp. 359-362.

Houghton, David D., Baumhefner, David P. and Washington, Warren M., 1971: On global initialization of the primitive equations: Part II. The divergent component of the horizontal wind. JAM, 10:8, pp. 626-534.

Kalb, Michael W., 1979: A technique for utilizing satellite derived geostrophic winds. M.S Thesis, Department of Meteorology, Univ. of Wisconsin, Madison, WI, 73 pp.

Kocin, Paul J., Uccellini, L. W., and Petersem, R. A., 1982: The role of jet streak "coupling" in the development of the 10-11 April 1979 Wichita Falls

tornado outbreak. Preprints of 12th conference on severe local storms. AMS. pp. 560-563.

Kreitzberg, C. W. and Perkey, D. J., 1976: Release of potential instablility: Part I. A sequential plume model with a hydrostatic preimitive equation model. JAS, 33:3, pp. 456-475.

Krishnamurti, T. N., 1968: A diagnostic balance model for studies of weather systems of low and high latitudes, Rossby number less than 1. MWR, 96:4, pp. 197-207.

Kuo, H. L., 1974: Further studies of the parameterization of the influence of cumulus convectin on large scale flow. JAS, 37:7, pp. 1232-1240.

Lee, Dong, Kyou, 1981: Impact of mesoscale satellite wind data on numerical model simulations. Ph.D. Thesis, Department of Meteorology. University of Wisconsin, Madison, WI, 110 pp.

Lejenas, H., 1977: Initialization of primitive equation models-some aspects of including a divergent wind component into the initial state. Beitrage zur Physik der Atmosphare, 50, pp. 154-168.

Maddox, R. A., 1980: Mesoscale convective complexes. BAMS, 61:11, pp. 1374-1387.

Miller, Robert C., 1972: Notes on analysis and severe-storm forecasting procedures on the Air Force Global Weather Central, USAF-Air Weather Service Technical Report 200.

Mills, G, A. and Hayden, C. M., 1982: The use of high horizontal resolution satellite temperature and moisture profiles to initialize a mesoscale numerical weather prediction model. A severe weather event case study. (unpublished)

Moller, Alan R., 1980: Mesoscale surface analysis of the 10 April 1979 tornadoes in Texas and Oklahoma. Preprints of 8th conference on weather forecasting and analysis. pp. 36-43.

Moore, James T., 1982: The forcing and evolution of the three dimensional moisture convergence during the 10-11 April 1979 severe weather outbreak. Preprints of 12th conference on severe local storms. AMS. pp. 209-212.

National STORM Program Document. 1983. University Corporation for Atmospheric Research. Boulder, CO.

Newman, W. R., 1972: The relationship between horizontal moisture convergence and severe storm occurrences. M.S. Thesis, Univ. of Oklahoma, 54 pp.

Orlanski, I., 1975: A rational subdivision of scales for atmospheric processes. BAMS, 56:5, pp.527-530.

Paegle, Jan and Paegle, Julia N., 1974: An efficient and accurate approximation to the balance wind with application to non-elliptic data. MWR, 102:12. pp. 838-846.

Paegle, Jan and Paegle, Julia N., 1976: On geopotential data and ellipticity of the balance equation: A data study. MWR, 104:10, pp. 1279-1288.

Perkey, D. J., 1976: Prediction of convective activity using a system of parasitic-nested numerical models. NASA contractor report. CR-2761. 160 pp.

Perkey, D. J. and Kreitzberg, C. W., 1976: A time-dependent lateral boundary scheme for limited area primitive equation models. MWR, 104:6, pp. 744-755.

Petterson, Sverre, 1953: On the relation between vorticity, deformation and divergence and the configuration of the pressure field. Tellus, 5:3, pp. 231-237.

Phillips, N. A., 1960: On the problem of initial data for the primitive equations, Tellus, 12:2, pp. 121-126.

Rao, G. W. and Fishman, J., 1975: An iterative initialization scheme for mesoscale studies. Tellus, 27:2, pp. 157-167.

Schlatter, Thomas! W., 1981: An assessment of operational TIROS-N temperature retrievals over the United States. MWR, 109:1, pp. 110-119.

Seaman! R. S., Falconer, R. E. and Brown, J., 1977: Application of a variational blending technique to numerical analysis in the Australian region. Australian Meteorological Magazine, 25:1, pp. 3-22.

Smith, W. L. and Woolf, H. M., 1976: The use of eigenvectors of statistical covariance matrices for interpreting satellite sounding radiometer observations. JAS, 33:7, pp. 1127-1140.

Smith, W. L., Woolf, H. M., Hayden, C. M., Wark, D. Q., and McMillin, L. M., 1979: The TIROS-N operational vertical sounder. BAMS, 60:10, pp. 1177-1187.

Smith, W. L., Nagle, F. W., Hayden, C. M., and Woolf, H. M., 1981: Vertical mass and moisture structure from TIROS-N. BAMS, 62:3, pp. 388-393.

Streit, David F., 1981: An intercomparison of the ability of TIROS-N satellite soundings, radiosonde soundings and NMC analyses to track upper tropospheric jet streaks. M.S. Thesis, Department of Meteorology. Univ. of Wisconsin, Madison, 47 pp.

Sundqvist, H., 1975: Initialization for models using sigma as the vertical coordinate. JAM, 14:3, pp. 153-158.

Sumi, Akimasa, 1977: Preliminary experiments of four-dimensional data assimilation. Journal of the Met. Soc. of Japan, 55:6, pp. 573-584.

Tarbell, Terry C., 1979: The initilization of the divergent component of the horizontal wind in mesoscale numerical weather prediction models and its effect on initial precipitation rates. Ph.D. Thesis, Department of Meteorology. Pennsylvania State University, University of Park, PA, 216 pp.

Ulanski, Stanley E. and Garstang, Michael, 1978: The role of surface divergence and vorticity in the life cycle of convective rainfall. Part II: A descriptive model, JAS, 35:6, pp. 1063-1069.

Vincent, D. G. and Carney, T. Q., 1982: Meso-synoptic scale circulation patterns during severe weather outbreak of April 10-11, 1979. Preprints of 12th conference on severe local storms. AMS. pp. 556-559.

Warner, Thomas T., Anthes, R. A., and McNab, Alan L., 1978: Numerical simulations with a three-dimensional mesoscale model. MWR 106:8, pp. 1079-1099.

Washington, Warren M. and Baumhefner, David P., 1975: A method of removing lamb waves from initial data for a primitive equation models. JAM, 14:2, pp. 114-119.

TECHNICAL REPORT STANDARD TITLE PAG

1. REPORT NO.	2. GOVERNMENT ACCESSION NO.	3. RECIPIENT'S CATALOG NO.
NASA CR-3826		

4. TITLE AND SUBTITLE	5. REPORT DATE
Initialization of a Mesoscale Model for April 10, 1979, Using Alternative Data Sources	August 1984
	6. PERFORMING ORGANIZATION CODE
7. AUTHOR(S)	8. PERFORMING ORGANIZATION REPORT #
Michael W. Kalb	
9. PERFORMING ORGANIZATION NAME AND ADDRESS	10. WORK UNIT, NO.
Universities Space Research Association The American City Building, Suite 311 10227 Wincopin Circle Columbia, Maryland 21044	M-460
	11. CONTRACT OR GRANT NO.
	NAS8-34767
	13. TYPE OF REPORT & PERIOD COVERED
12. SPONSORING AGENCY NAME AND ADDRESS	
National Aeronautics and Space Administration Washington, D. C. 20546	Contractor Report
	14. SPONSORING AGENCY CODE

15. SUPPLEMENTARY NOTES

Technical Monitor: Gregory S. Wilson, Atmospheric Science Division, Systems Dynamics Laboratory, George C. Marshall Space Flight Center, Alabama

16. ABSTRACT

A 35 km grid limited area mesoscale model was initialized with high density SESAME radiosonde data and high density TIROS-N satellite temperature profiles for April 10, 1979. These data sources were used individually and with low-level wind fields constructed from surface wind observations. The primary objective was to examine the use of satellite temperature data for initializing a mesoscale model by comparing the forecast results with similar experiments employing radiosonde data. The impact of observed low level winds on the model forecasts was also investigated with experiments varying the method of insertion. All forecasts were compared with each other and with mesoscale observations for precipitation, mass and wind structure. Preliminary forecasts initialized with radiosonde winds and balanced winds showed that balanced winds substantially reduced initial model shock and provided smoother and more accurate mass fields. The radiosonde and satellite precipitation forecasts differed significantly although both had some very realistic qualities. A low-level short wave which was present in both the radiosonde and satellite initial states was retained by the model and propagated around the synoptic scale trough from Oklahoma to Nebraska. The radiosonde short wave was associated with a mesoscale precipitation band that verified with a short wave band evident in radar and SESAME radiosonde observations. The satellite short wave showed a weaker association with a precipitation band; however, the satellite forecast gave a slightly better depiction of convective precipitation over Oklahoma, exhibiting the same general location and orientation as observed. Continuous insertion of low-level winds during the initialization period had impacts on mass, wind and precipitation fields. The most dramatic was an improvement in sea level pressure patterns by reducing the fast eastward propagation of the mass field experienced in other forecasts. The model simulated several additional mesoscale features including intensification of a low-level dry line and generation of a low-level jet. Several forecasts produced convective precipitation systems with characteristics satisfying criteria for a mesoscale convective complex. The study demonstrated that high density satellite temperature data and balanced winds can be used in a mesoscale model to produce forecasts which verify favorably with observations.

17. KEY WORDS	18. DISTRIBUTION STATEMENT
AVE-SESAME I Mesoscale Modeling Convective Precipitation Satellite Soundings	Unclassified - Unlimited

19. SECURITY CLASSIF. (of this report)	20. SECURITY CLASSIF. (of this page)	21. NO. OF PAGES	22. PRICE
Unclassified	Unclassified	244	All